Developing a Tileable Superconducting Circuit for Quantum Computation

Peter Anthony Spring

Jesus College

University of Oxford

A thesis submitted for the degree of

Doctor of Philosophy

Hilary 2021

Abstract

Superconducting circuits have been demonstrated at the ~ 50 qubit scale, with gate fidelities approaching the thresholds required for error correction using surface codes. It is generally considered that maintaining and improving this performance while scaling to $\gtrsim 100$ qubits will require 3D integration of control wiring, and techniques to prevent or mitigate the effects of unwanted electromagnetic modes which emerge in the circuit environment at larger scales. At the present time, no single design has emerged as the clear scaling "winner", and many different modalities are being explored. In this thesis, we describe one potential scaling architecture for superconducting circuits, which is based on a unit cell containing a set of controllable, measurable qubits. In analogy to the unit cell of a crystal, this unit cell can be tiled, in this case to form 2D arrays of individually controllable and measurable qubits. This is enabled by three key technologies: 3D integrated off-chip control wiring, reverse-side readout resonators, and inductive shunting of the device enclosure with micromachined pillars. To validate this approach, we design and build a demonstration device featuring four transmon qubits and containing within it a single unit cell of the architecture. The device construction involves the fabrication of reverse-side circuits and the use of novel CNC drilling of the circuit substrate. We measure coherence times and single-qubit gate fidelities comparable with the state-of-the-art for transmon qubits (avg. $T_1 = 149\,\mu s$, avg. echoed $T_2^* = 189\,\mu s$, avg. $F > 99.98\%$), establishing that the design is compatible with high coherence. An important feature of the design is that the infinite construct formed by tiling the plane with the unit cell possesses a cutoff frequency, below which the circuit environment cannot sustain any electromagnetic modes. We develop models to predict this cutoff frequency, and predict that environment mediated crosstalk between qubits inside this structure decays exponentially with spatial separation. This crosstalk can be viewed as being mediated by evanescent waveguide modes, or by bound states formed by the interaction of qubits with the environmental modes around the cutoff. Both models provide quantitative predictions for the rate of crosstalk decay, which are shown to be in good agreement. We propose this architecture as a promising candidate for building 2D arrays of hundreds or thousands of nearest neighbour coupled superconducting qubits, which could provide a testbed of quantum error correction schemes such as the surface code.

Contents

List of Figures

List of Tables

Acknowledgements

There are so many people I would like to thank for the last four and a half years. I would like to thank James Gates, Lewis Carpenter, and Paul Gow at the University of Southampton. Without your expert help in silicon machining, this project might have turned out very differently. At the Clarendon Laboratory, I would like to thank Jon Denton for all of your help in the workshop, Dave Sharp for keeping our fridges alive, and Jason Brown for making fabrication fun. In the Leeklab group I would like to thank everyone. Andy for your patience teaching me code, Joseph for your patience teaching me fabrication, and Brian for your patience teaching me everything else. Takahiro for teaching me Randomised Benchmarking, for many great physics chats, and for humouring my bad Japanese. Shuxiang for being a genius, and for your extraordinary ability to get things working. I still cannot believe you fixed that oscilloscope. Giulio for being a wonderful E-beam companion, counterbalancing my haphazard ways with a more measured approach. Our battles with the Raith were legendary. Simone for being a great HF buddy, for your fastidiousness in fabrication, and for forgiving me when I coated the evaporator window. James for teaching me the horrors of writing a driver, for building a brilliant control electronics setup, for carrying the HFSS torch, and for your desert dry sense of humour. Vivek for your help repeatedly opening and closing the fridge during a mad couple of weeks. Boris for your help with the paper. Mustafa for showing me how bottomless a subject microwave engineering is. I would especially like to thank Peter Leek, for tirelessly trying to teach me how to do science, and for encouraging me to think more critically. It goes without saying, but I have gained so much under your supervision. Outside the world of physics, there are many friends I would like to thank. The whole 2016 M3 Jesus boat, and in particular Piotr and Yiangos, for an unforgettable year on the Isis. Nadescha and Robbie for an amazing first year at Jesus college. Wouter for a great meal in Boston, and for an unforgettable game of Battle Sheep. Sam for inspiring me to keep learning Japanese, and for taking me out for gyutan in Sendai. Caro for your infectious laugh, and for being the ultimate Hank's dance partner. Arjun for your proficiency speaking Spanish. Priyav and Santiago, for being such great friends the whole way through, and for being the best lockdown amigos anyone could ask for. I have so many good memories from Kame house. Natascha, for your joy, adventure, and insatiable appetite for life. Finally, I would like to thank my whole family (including Rupert) and in particular my parents, Anna and Peter.

Chapter 1

Introduction

1.1 Motivation

Quantum Computation studies the possibilities for information processing with quantum mechanical systems [1]. It is a broad interdisciplinary field that integrates Physics and Computer Science, and which puts the connection between the two under the microscope. By viewing computation through the lens of physics, the field asks questions such as: what constraints do the laws of quantum mechanics impose on the processing of information? And conversely, by viewing physics through the lens of computation, the field asks questions such as: what computational resources are required to simulate quantum mechanical systems? As well as being of great practical interest, it is hoped that asking (and hopefully answering) questions of this sort could lead to insights into Quantum Mechanics, which is our best current theory for how nature behaves – excluding Gravitation.

Two major milestones in the field occurred in quick succession in mid 1990's. The first was the discovery of Shor's algorithm [2]. This is an efficient *quantum* algorithm for finding the prime factors of an integer. This result is interesting because no efficient *classical* algorithm is known for this problem, and it is generally believed one does not exist. The second milestone was the discovery of a quantum error correcting code, the CSS code [3, 4]. This led to the prediction that quantum information processing can still be carried out in the presence of realistic noise, so long as this noise is below a threshold [5]. Taken together, these results are powerful because they suggest that computers which compute using the rules of quantum mechanics can process information in a more efficient manner than computers which do not, so long as noise can be kept below a finite threshold. The importance of this finite

noise threshold is highlighted by the example of analogue computing; *classical analogue* algorithms have been found that are more efficient than known *classical digital* algorithms, however since they lack a noise threshold this speedup cannot be realised in any real physical system [1].

Results such as these have strongly motivated experimental efforts to build a quantum computer. The DiVincenzo criteria [6], proposed at the turn of the millennium, set out five necessary conditions for building a quantum computer (seven if it is also desired to carry out quantum communications). The first criteria states that the platform for quantum computing should be *a scalable physical system with well-characterised qubits* [6] – where a qubit is simply a two-level quantum system that can be described by the state vector $a\,|0\rangle + b\,|1\rangle$, obeying $|a|^2 + |b|^2 = 1$. Many different physical systems are being explored as potential candidates for building quantum computers, including photonic systems [7], systems of trapped ions [8], systems of neutral atoms [9], silicon quantum dots [10, 11], and superconducting circuits [12]. However, all of these physical systems still face challenges with regards to being scalable; i.e., being able to sustain increasingly large numbers of well-characterised qubits. This is for a myriad of reasons, and each physical system faces its own particular scaling challenges. As pointed out in Ref. [13]: *Declaring a* [quantum computing] *technology 'scalable' is a tricky business, because the resources used to define and control a qubit are diverse.*

The goal of this thesis is to build and characterise a superconducting circuit containing well-characterised qubits that is *tileable*. By tileable, it is meant that the device contains a unit-cell which can tile the plane in a simple 'copy-paste' fashion, into larger devices containing 2D arrays of well-characterised qubits that can be individually controlled and measured. The inherent periodicity of these devices allows tools such as Bloch's theorem and meta-material models to be used to predict their behaviour at scale. Since this definition does not say anything about the scalability of the resources required to perform control and measurement (e.g. microwave electronics, dilution refrigerator), it is not a claim that the device is scalable. Rather, we see circuit tileability as a useful property on the longer road to scalability.

1.2 Thesis structure

In Chapter 2, we give an introduction to the field of superconducting circuits, with a focus on a particular type of superconducting qubit known as the transmon. We

review some of the dominant decoherence mechanisms of transmon qubits, and some of the powerful simulation methods that have been developed for predicting their behaviour inside very general environments.

In Chapter 3, we provide a brief overview of some of the major scaling challenges encountered by superconducting circuits for quantum computation, and review some of the approaches being taken to address these challenges.

In Chapter 4, we introduce a superconducting circuit architecture that is being actively pursued in our lab. We review this architecture and contribute some new material towards understanding its behaviour.

In Chapter 5, we consider inductively shunting cavities as a means of rendering the architecture introduced in Chapter 4 tileable to grids of many qubits without the emergence of deleterious environmental EM modes. We develop models for predicting the mode frequencies of periodically inductively shunted cavities, and then use these models to predict the spatial dependence of deleterious couplings between transmon qubits enclosed in such cavities. We test the predictions against finite-element (FE) simulations and find good agreement.

In Chapter 6, we describe the methodology we have developed to practically construct tileable devices integrating the architecture described in Chapter 4 and the inductively shunted cavities of Chapter 5. We use this methodology to construct a four-qubit demonstration device.

In Chapter 7, we describe experiments on a four-qubit demonstration device built according to Chapter 6. We assess the device performance in the context of quantum computing by characterising qubit coherence times, circuit crosstalk, and single-qubit gate fidelities. We then discuss the experimental results.

In Chapter 8, we summarise the main results of the thesis, some key limitations, the near-term outlook, and some of the possible directions for future work.

Chapter 2

Superconducting Circuits

In this chapter, we give an introduction to the field of superconducting circuits and circuit quantum electrodynamics (circuit QED). We quickly focus on the transmon qubit [14], which is the type of qubit used in this thesis, and review some of its major decoherence mechanisms. We conclude with an overview of some of the simulation methods that can be used to model the behaviour of transmon qubits embedded in very general electromagnetic environments.

2.1 Introducing superconducting circuits

Superconducting circuits are electrical circuits cooled to temperatures where they transition into a superconducting state and behave according to quantum mechanics. These circuits are typically made of aluminium or niobium-titanium alloys, and fabricated on silicon or sapphire substrates. We start by discussing the typical frequency and length scales.

2.1.1 Frequency and length scales

Superconducting circuits are constrained to operate in a relatively narrow frequency range. The lower limit on frequency is set by the ability to cool the circuits to prevent thermal excitations. For a circuit behaving as a qubit, the thermal excited state population p_e follows a Boltzmann distribution and is given by $p_e = \exp(-\hbar\omega/k_B T)$ in the limit $p_e \ll p_g$, where ω is the qubit transition frequency and p_g is the ground state population. For a maximum tolerated thermal excited state population $p_{e,max}$, the limit imposed on the qubit frequency is then $\hbar\omega > k_B T \ln(1/p_{e,max})$. Superconducting circuits are operated inside dilution refrigerators with a base stage temperature of around $\sim 20\,\mathrm{mK}$, and so a reasonable maximum value of $p_{e,max} = 0.1\%$ then sets

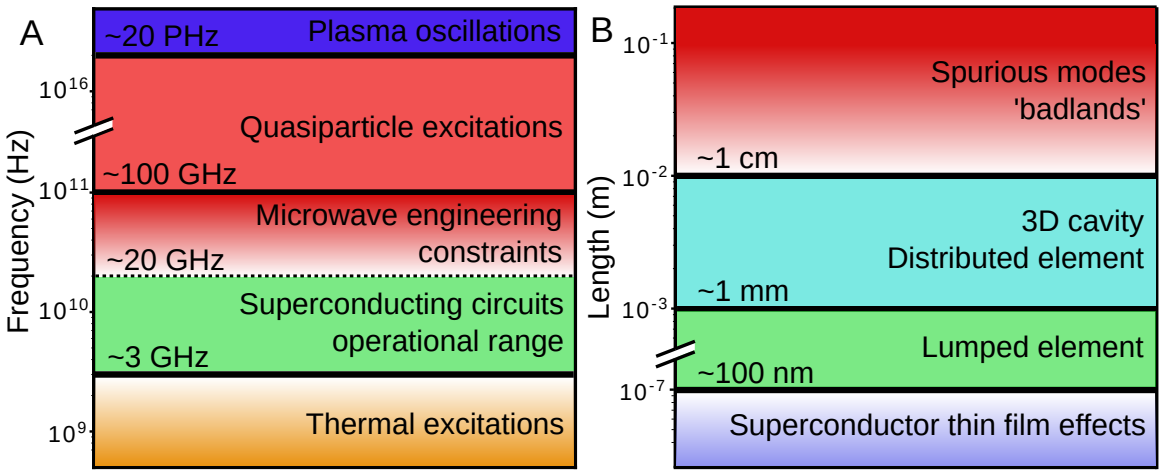

Figure 2.1: **Frequency and length scales: (A)** Relevant energy scales for superconducting circuits. **(B)** Relevant length scales for superconducting circuits.

a bound of $\omega/2\pi \gtrsim 3\,\text{GHz}$.

An upper limit on superconducting circuit frequencies is set by the superconducting energy gap of the material the circuits are made from. Incident excitations (photons, phonons, etc.) with energy above the superconducting gap will be able to break Cooper-pairs and excite Bogoliubov quasiparticles in the superconductor. These quasiparticles are not protected from dissipation and limit the coherence times of superconducting qubits, see section 2.2.2.3. Photons will effectively break Cooper-pairs when $\hbar\omega > 2\Delta$, where Δ is the superconducting energy gap. For thin film aluminium $\Delta \approx 200\,\mu\text{eV}$ [15, 16], which sets an upper bound on qubit frequencies of $\omega/2\pi \approx 100\,\text{GHz}$. However, for frequencies $\omega/2\pi \gtrsim 20\,\text{GHz}$, the increased physical tolerances required on all equipment (generators, filters, connectors, etc.) leads to increased costs. Due to the lack of strong motivation to operate above 20 GHz, this pragmatically sets a narrower operational frequency range of around $3\,\text{GHz} - 20\,\text{GHz}$, which is in the microwave frequency range. In practice, superconducting circuits are generally operated in the still narrower range of $4\,\text{GHz} - 10\,\text{GHz}$, in part due to the $1/\omega$ scaling of dielectric relaxation times discussed in section 2.2.2.2.

Another relevant frequency is the plasma oscillation frequency in the superconducting material [17]. If this is near the resonant frequencies of the circuit, the ability to excite plasma oscillations (plasmons) in the superconductor will prevent a simple description of the circuit dynamics in terms of only a few degrees of freedom [17, 18]. However, for aluminium, the plasma frequency ω_p satisfies $\omega_p/2\pi \approx 20\,\text{PHz}$, and

so these plasma oscillations can be safely ignored. The typical frequency scales are summarised in Fig. 2.1(A).

Length scales are set by the behaviour of superconducting circuit structures at microwave frequencies. Circuits with a longest physical length $s < 1\,\text{mm}$ can typically be described as lumped-elements, because the wavelength of excitations at typical $4\,\text{GHz} - 10\,\text{GHz}$ superconducting circuit frequencies and substrate permittivities $\epsilon_r \sim 10$ is $\lambda \gtrsim 1\,\text{cm}$, and so $s \ll \lambda$. In the $1\,\text{mm} < s < 1\,\text{cm}$ range, a distributed-element treatment is often more appropriate as s become comparable to the wavelength of circuit excitations. The rich behaviour of microwaves in structures at this length scale is the subject of microwave engineering [19]. At length scales $s > 1\,\text{cm}$, many electromagnetic structures (2D circuits, 3D cavities, etc.) carry modes with frequencies close to typical superconducting circuit frequencies, that are detrimental to superconducting circuit operation. In superconducting circuit devices containing element with $s \gtrsim 1\,\text{cm}$ in scale, care must therefore be taken to prevent or mitigate these spurious modes. This is an important subject in this thesis, and is the main topic of Chapter 5.

Finally, superconducting circuits are made out of thin film (typically $\sim 100\,\text{nm}$) superconductors, and so the superconducting coherence length (ξ_0) and the London penetration depth (λ_L) of the materials are important. For aluminium, $\xi_0 \approx 1500\,\text{nm}$ – far larger than the superconducting circuit thickness. This means that while bulk aluminium is a type-I superconductor, superconducting circuits made of aluminium exhibit properties of type-II superconductors – for instance they can trap flux vorticies [20]. The superconducting energy gap is also different compared to bulk aluminium, and dependent on the circuit thickness. Kinetic inductance effects, as predicted by the Mattis-Bardeen equation [21, 22], also become important for thin film superconductors, and can contribute significantly to the inductance of superconducting circuit elements, see e.g. Ref. [23].

2.1.2 Lumped-element ingredients

The electrical response of superconducting circuits can be described in terms of the following lumped elements: capacitors, inductors, ideal transformers, resistors and Josephson junctions, shown in Fig. 2.2. Remarkably, this is true even where the real circuit contains distributed elements and 3D cavities, so long as the qubits exist in a passive, linear electromagnetic environment [24], which is discussed further in section

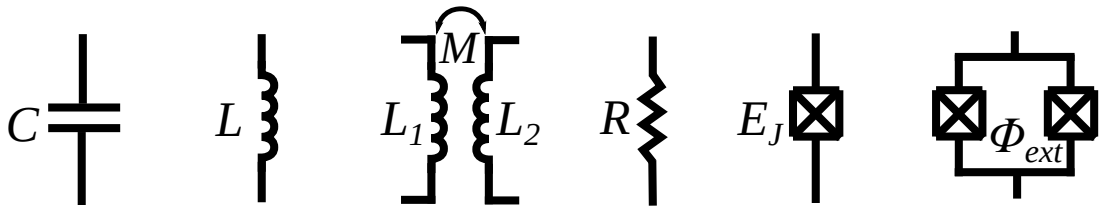

Figure 2.2: **Superconducting circuit lumped-elements:** Circuit symbols for a capacitor (C), inductor (L), ideal transformer (mutual inductance $M = L$), resistor (R), Josephson junction (Josephson energy E_J), and SQUID (external flux Φ_{ext}).

2.3. Here, we consider the lumped elements in turn. Capacitors and inductors are linear lossless components that store electric and magnetic field energy respectively. They have frequency dependent impedances given by $Z_C = 1/(i\omega C)$ and $Z_L = i\omega L$. It is useful to express the voltage in terms of flux, defined as

$$\Phi(t) = \int_{-\infty}^{t} V(\tau) d\tau \tag{2.1}$$

The capacitance is then defined $C = Q/\dot{\Phi}$ and the inductance defined $L = \Phi/\dot{Q}$ where the differentiation is with respect to time. The electric and magnetic field energy stored in capacitors and inductors is related to the flux across them as

$$E_C = \int_0^Q \dot{\Phi}(q) dq = \frac{C\dot{\Phi}^2}{2} \tag{2.2}$$

$$E_L = \int_0^\Phi \dot{Q}(\phi) d\phi = \frac{\Phi^2}{2L} \tag{2.3}$$

Ideal transformers are linear lossless transformers with a coupling coefficient of $k = 1$ such that the mutual inductance $M = k\sqrt{L_1 L_2}$ reduces to $M = \sqrt{L_1 L_2}$. They represent inductive coupling between different circuits. Resistors are linear components that have real impedance $Z = R$. They represent energy dissipation in the circuit.

Josephson junctions behave as non-linear lossless circuit elements. They are formed by spatially separating two superconducting materials by a distance far smaller than the superconducting coherence length, such that Cooper pairs can tunnel between them without dissipation [25]. The current and voltage across the junction are related to the superconducting phase ϕ across the junction by the Josephson equations [26]

$$I = I_0 \sin(\phi) \tag{2.4}$$

$$V = \varphi_0 \frac{d\phi}{dt} \tag{2.5}$$

where φ_0 is the reduced flux quantum $\varphi_0 = \hbar/2e$ and I_0 is the critical current of the junction above which normal electrons flow with dissipation. Notice that the second equation implies the superconducting phase ϕ and the flux defined in eq. 2.1 are related by $\phi = \Phi/\varphi_0 \bmod 2\pi$, where the mod 2π is due to ϕ being defined over $[0, 2\pi]$. From the Josephson equations and the definition of inductance $L = V/\dot{I}$, it follows immediately that Josephson junctions have an effective inductance

$$L = \frac{\varphi_0}{I_0 \cos(\Phi/\varphi_0)} \tag{2.6}$$

The associated inductive energy is given by

$$E = \int_0^\Phi \dot{Q}(\phi) d\phi = E_J[1 - \cos(\Phi/\varphi_0)] \tag{2.7}$$

where $E_J = I_0\varphi_0$, and we have used $\dot{Q} = I$. The junction inductance can be expanded into the form

$$L = \frac{\varphi_0}{I_0}[1 + \frac{1}{2}(\frac{\Phi}{\varphi_0})^2 + \mathcal{O}((\frac{\Phi}{\varphi_0})^4)] \tag{2.8}$$

In the small flux limit $\Phi \ll \varphi_0$, the junction behaves as a linear inductor with inductance $L_J = \varphi_0/I_0$, with a small quadratic perturbation. Likewise, the energy can be expanded into the form

$$E = \frac{\Phi^2}{2L_J}[1 - \frac{1}{12}(\frac{\Phi}{\varphi_0})^2 + \mathcal{O}((\frac{\Phi}{\varphi_0})^4)] \tag{2.9}$$

which in the small flux limit is the inductive energy stored in the linear junction inductor L_J with a small quadratic perturbation.

Josephson junctions can be made by separating two superconductors by a thin (roughly $\sim 1\,\text{nm}$ scale) insulator [27] or normal metal [28] layer, referred to as S-I-S and S-N-S junctions respectively. Alternatively, they can be formed by a narrow constriction in the superconductor such that it loses its superconductivity in the constriction [29], referred to as an S-c-S junction. In this thesis, all junctions are S-I-S junctions, also known as tunnel junctions. The critical current I_0 (and hence L_J and E_J) is determined by the normal state resistance R_n of the oxide barrier through the Ambegaokar-Baratoff formula [30]

$$I_0(T) = \frac{\pi\Delta}{2eR_n} \tanh(\frac{\Delta}{2k_BT}) \tag{2.10}$$

where R_n and Δ (the superconducting gap) are evaluated at temperature T. Importantly, $I_0 \propto 1/R_n$, where R_n depends on the junction area A and thickness t as

$R_n \propto t/A$. The Josephson energy E_J and linear inductance L_J can thus be set by the experimenter by choice of the junction dimensions.

There is one more important ingredient to superconducting circuits, which is the behaviour exhibited by two Josephson junctions when joined together by superconductor to form a loop (Fig. 2.2). We assume both junctions have the same Josephson energy for simplicity, although similar results follow if the junctions are asymmetric [14]. Dropping the constant term, the energy of the circuit element formed by this arrangement, known as a SQUID [31], is simply the sum of the junction energies

$$E = -E_J[\cos(\Phi_1/\varphi_0) + \cos(\Phi_2/\varphi_0)] \tag{2.11}$$

$$= -2E_J \cos(\frac{\Phi_1 + \Phi_2}{2\varphi_0}) \cos(\frac{\Phi_1 - \Phi_2}{2\varphi_0}) \tag{2.12}$$

The fluxes across the two junctions Φ_1 and Φ_2 and the externally applied magnetic flux Φ_{ext} are constrained by the requirement that the total magnetic flux enclosed in the loop be quantised, which follows from the requirement that the macroscopic wave function of the superconductor be single valued everywhere, leading to

$$\Phi_1 - \Phi_2 = \varphi_0 2\pi n + \Phi_{\text{ext}} \tag{2.13}$$

The energy of the SQUID can therefore be expressed

$$E = -(-1)^n 2E_J \cos(\Phi_{\text{ext}}/2\varphi_0) \cos(\tilde{\Phi}/\varphi_0) \tag{2.14}$$

where $\tilde{\Phi} = (\Phi_1 + \Phi_2)/2\varphi_0$. This is the energy of a single junction with effective Josephson energy $E_{Jeff} = (-1)^n 2E_J \cos(\Phi_{\text{ext}}/2\varphi_0)$ and flux $\tilde{\Phi}$ across it. It is as if we can dynamically change the area of this junction's oxide barrier just by adjusting an external magnetic field! This effect is used extensively to create circuits whose parameters can be dynamically changed by magnetic flux control knobs.

2.1.3 Circuit quantisation

Just like any quantum system, the behaviour of superconducting circuits can be determined from their Hamiltonian. In general, the Hamiltonian of any circuit containing the lumped elements discussed earlier – including resistors – can be found algorithmically [32, 33]. The resistors can be treated by replacing them with infinitely long transmission lines that funnel energy out of the system without explicitly involving dissipation [32, 34]. Here, we will consider the Hamiltonian of two very simple lossless circuits, a linear LC oscillator and a nonlinear "JC" oscillator, shown in Fig. 2.3.

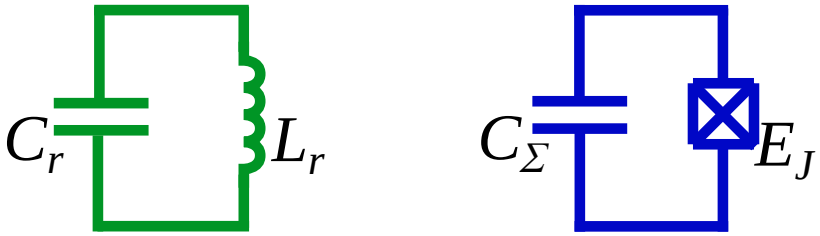

Figure 2.3: **Oscillator circuits:** Linear LC oscillator formed of a capacitor and inductor, and non-linear JC oscillator formed of a capacitor and Josephson junction.

The classical Hamiltonian for the LC oscillator is just the sum of the inductive and capacitive energy, given by

$$H = \frac{C\dot{\Phi}^2}{2} + \frac{\Phi^2}{2L} \tag{2.15}$$

Written in this form, the Hamiltonian can be directly associated with that of a mass on a spring. The flux Φ plays the part of position x, the capacitance C takes the role of mass m, and the inductance maps to the spring constant through $L = 1/k$ (a smaller inductance equates to a stiffer spring). The classical Hamiltonian may equivalently be written

$$H = \frac{Q^2}{2C} + \frac{\Phi^2}{2L} \tag{2.16}$$

In this form the charge Q plays the role of momentum p in the mechanical analogy. To perform quantisation, we replace the charge and flux variables with quantum operators, expressed symbolically by $Q \to \hat{Q}$, $\Phi \to \hat{\Phi}$. Crucially, just as momentum and position are conjugate variables, so charge and flux are conjugate variables, and their quantum operators will obey the commutation relation [32]

$$\left[\hat{\Phi}, \hat{Q}\right] = i\hbar \tag{2.17}$$

The quantum Hamiltonian ($H \to \hat{H}$) is then given by

$$\hat{H} = \frac{\hat{Q}^2}{2C} + \frac{\hat{\Phi}^2}{2L} \tag{2.18}$$

which has an identical form to the quantum harmonic oscillator [35]. Just as it is useful to define the following annihilation operator for the quantum harmonic oscillator

$$\hat{a} = \frac{1}{\sqrt{2\hbar\omega}}(\sqrt{k}\hat{x} + i\frac{\hat{p}}{\sqrt{m}}) \tag{2.19}$$

it is useful to define the equivalent annihilation operator for the circuit oscillator

$$\hat{a} = \frac{1}{\sqrt{2\hbar\omega}}(\frac{\hat{\Phi}}{\sqrt{L}} + i\frac{\hat{Q}}{\sqrt{C}}) \tag{2.20}$$

through which the Hamiltonian can be re-expressed

$$\hat{H} = \hbar\omega(\hat{n} + 1/2) \tag{2.21}$$

where $\hat{n} = \hat{a}^\dagger\hat{a}$ is the number operator and $\omega = 1/\sqrt{LC}$ is the resonant frequency of the classical LC circuit. The flux and charge operators can be expressed in terms of the creation ($\hat{a}^\dagger$) and annihilation operators as

$$\hat{Q} = i\sqrt{\frac{\hbar}{2Z}}(\hat{a}^\dagger - \hat{a}) \tag{2.22}$$

$$\hat{\Phi} = \sqrt{\frac{\hbar Z}{2}}(\hat{a}^\dagger + \hat{a}) \tag{2.23}$$

where $Z = \sqrt{L/C}$ is the characteristic impedance of the classical LC oscillator. Considering eq. 2.21, the quantised LC circuit has equally spaced energy levels separated by energy $\hbar\omega$. This fact alone makes such oscillators unsuitable as qubits, as all neighbouring state transitions $|n\rangle \to |n+1\rangle$ are energy degenerate.

The JC circuit likewise has a Hamiltonian given by the sum of its capacitive and inductive energy

$$\hat{H} = \frac{\hat{Q}^2}{2C} - E_J\cos(\hat{\Phi}/\varphi_0) \tag{2.24}$$

where we have dropped the constant E_J term and moved straight to the quantum operator picture. Following Ref. [36], we slightly complicate the circuit by allowing the JC oscillator to couple to external voltage sources V_i. This will have the effect of modifying the charge across the junction $\hat{Q} \to \hat{Q} - \sum_i C_i V_i$, where C_i is the coupling capacitance to voltage source i. It will also adjust the shunt capacitance $C \to C_\Sigma = C + \sum_i C_i$, which is a small adjustment for weak coupling capacitances. Next, we substitute the Cooper-pair number operator for the charge operator $\hat{Q} \to 2e\hat{n}$, and the superconducting phase operator for the flux operator $\hat{\Phi}/\varphi_0 \bmod 2\pi \to \hat{\phi}$, to arrive at

$$\hat{H} = 4E_C(\hat{n} - n_g)^2 - E_J\cos(\hat{\phi}) \tag{2.25}$$

where $E_C = e^2/2C_\Sigma$, $n_g = \sum_i C_i V_i/2e$ and $\hat{\phi}$ is defined over $[0, 2\pi]$. This Hamiltonian is known as the Cooper-pair box Hamiltonian [37, 38]. Due to the non-linearity of the inductive energy, the energy levels will be anharmonic, making this circuit a possible qubit candidate. The term n_g allows for coupling to other circuits and external drives, presenting possibilities for qubit control and readout. However, this n_g term also makes the circuit sensitive to any uncontrolled voltage fluctuations in the circuit environment, introducing a possible dephasing mechanism, which leads us to the next section.

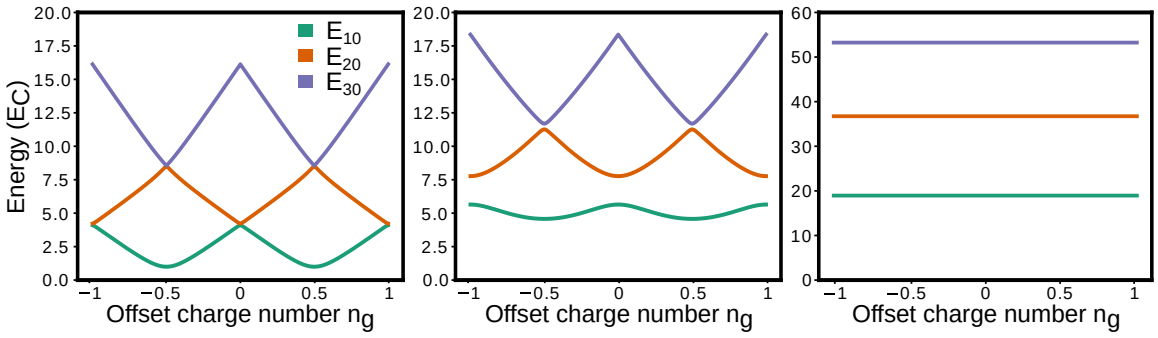

Figure 2.4: **Transmon charge dispersion:** First three eigenenergies E_{m0} for the Cooper-pair box Hamiltonian in eq. 2.25, solved in the charge basis for $E_J/E_C = 1, 5$ and 50. Figure reproduced from Ref. [36].

2.2 Transmon qubit

The lowest three energy levels $E_{m0} = E_m - E_0$ of the Cooper-pair box Hamiltonian are shown in Fig. 2.4, for different values of E_J/E_C and n_g. These energy levels are found numerically by diagonalising the truncated Cooper-pair box Hamiltonian in the charge basis [36], here truncated to the lowest 30 energy levels. For small values of E_J/E_C, the transition energies have a strong dependence on the offset charge n_g, which presents a clear dephasing mechanism for qubits defined between any pair of energy levels. How this translates into a characteristic dephasing time T_2 is quantified in section 2.2.3. For $E_J/E_C = 50$, it is apparent that the n_g dependence of the energy levels is greatly reduced. Defining the charge dispersion of the mth level ε_m as

$$\varepsilon_m = E_{m0}(n_g = 1/2) - E_{m0}(n_g = 0) \tag{2.26}$$

a WKB approximation can be used to derive the following analytical expression for the energy levels in the limit $E_J/E_C \gg 1$ [14]

$$E_{m0}(n_g) \approx E_{m0}(n_g = 1/4) - \frac{\varepsilon_m}{2}\cos(2\pi n_g) \tag{2.27}$$

with the charge dispersion given by

$$\varepsilon_m = (-1)^m E_C \frac{2^{4m+5}}{m!}\sqrt{\frac{2}{\pi}}\left(\frac{E_J}{2E_C}\right)^{\frac{m}{2}+\frac{3}{4}} e^{-\sqrt{8E_J/E_C}} \tag{2.28}$$

Importantly, the charge dispersion is exponentially suppressed with respect to E_J/E_C. A physical understanding for this is also provided in Ref. [14]: the charge dispersion is fundamentally caused by tunnelling through the periodic $-E_J\cos(\hat{\phi})$ potential. A higher E_J/E_C barrier will exponentially suppress such tunnelling events and therefore result in exponentially smaller ε_m. Qubits operated between the ground and

first excited state in the limit $E_J/E_C \gtrsim 50$ are known as transmon qubits [14], and are protected from dephasing due to slowly varying charge noise as a result of the exponentially suppressed charge dispersion.

A large E_J/E_C ratio will result in the lowest energy wavefunctions residing near the bottom of the $-E_J\cos(\hat{\phi})$ potential. To solve for the energy levels, it is thus sufficient to expand the cosine potential and keep only the first few terms, resulting in the Hamiltonian

$$\hat{H} \approx 4E_C\hat{n}^2 + \frac{1}{2}E_J\phi^2 - \frac{1}{24}E_J\phi^4 \tag{2.29}$$

where we have dropped the n_g term in the limit $E_J/E_C \gg 1$. This is just a perturbed quantum harmonic oscillator. Substituting in the ladder operator expressions for $\hat{n}$ and $\hat{\phi}$ (from eqs. 2.22 & 2.23), the Hamiltonian becomes

$$\hat{H} = \hbar\omega(\hat{m} + 1/2) - \frac{1}{12}E_C(\hat{a}^\dagger + \hat{a})^4 \tag{2.30}$$

where $\hat{m} = \hat{a}^\dagger\hat{a}$ and $\omega = 1/\sqrt{L_J C_\Sigma} = \sqrt{8E_C E_J}/\hbar$. Expanding and normal ordering the quartic term using the commutator $\left[\hat{a}, \hat{a}^\dagger\right] = 1$ and dropping constant terms results in

$$\hat{H} = \hbar\omega\hat{m} - \frac{1}{2}E_C\hat{m}(\hat{m}-1) - \frac{1}{12}E_C(\hat{a}^{\dagger 4} - 6\hat{a}^{\dagger 2} - 4\hat{a}^\dagger(\hat{a}^{\dagger 2} + \hat{a}^2)\hat{a} - 6\hat{a}^2 + \hat{a}^4) \tag{2.31}$$

Assuming the perturbation is small, we can then use first order perturbation theory to find the lowest energy levels. The eigenstates of the unperturbed harmonic oscillator circuit are just $|m\rangle$, so these energy levels are given by

$$E_n = \hbar\omega m - \frac{1}{2}E_C m(m-1) \tag{2.32}$$

The first few transition energies are then $E_{10} = \hbar\omega$, $E_{12} = \hbar\omega - E_C$, $E_{23} = \hbar\omega - 2E_C$. Single photon transitions between non-neighbouring levels are forbidden to first order perturbation as $\langle i+j|\,\hat{n}\,|i\rangle = 0$ for $j \neq \pm 1$. Defining the qubit anharmonicity $\alpha = (E_{12} - E_{01})/\hbar$, we see that for the transmon

$$\alpha \approx -E_C/\hbar \tag{2.33}$$

$$\alpha/\omega \approx (\frac{8E_J}{E_C})^{-\frac{1}{2}} \tag{2.34}$$

This is the second important point of the transmon – while charge dispersion is exponentially suppressed with respect to E_J/E_C, relative anharmonicity is only inverse square-root suppressed [14]. For physical values $E_J/h = 16\,\text{GHz}$ and $E_C/h =$

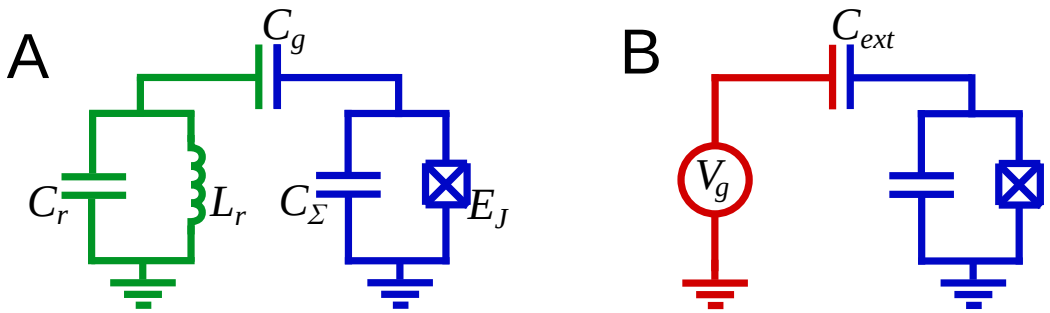

Figure 2.5: **Transmon coupled to resonator and voltage source:** (**A**) Effective circuit of a transmon coupled to a resonator. (**B**) Effective circuit of a transmon coupled to a voltage source.

0.19 GHz – corresponding to $L_J = 10\,\text{nH}$, $C_\Sigma = 100\,\text{fF}$, and $E_J/E_C = 84$, we find: $\omega/2\pi = 5\,\text{GHz}$, $\alpha/2\pi \approx -190\,\text{MHz}$ and $\varepsilon_1/h = -45\,\text{Hz}$. The transmon qubit thus remains sufficiently anharmonic that it can be controlled with fast $\sim 10\,\text{ns}$ pulses without significantly driving higher transitions, even as the charge dispersion is heavily suppressed.

In Chapter 7 we must find E_C and E_J from measured values of ω and α to predict the charge dispersion. To do this we use more accurate expressions found from higher order perturbation theory [39]

$$\omega \approx \sqrt{8E_JE_C} - E_C(1 + \eta + 21\eta^2/2^3 + 608\eta^3/2^6 + 5319\eta^4/2^7) \tag{2.35}$$

$$\alpha \approx -E_C(1 + 9\eta/2^2 + 81\eta^2/2^3 + 3645\eta^3/2^6 + 46899\eta^4/2^7) \tag{2.36}$$

$$\eta = (\frac{8E_J}{E_C})^{-\frac{1}{2}} \tag{2.37}$$

2.2.1 Readout and control

Readout of superconducting qubits is typically achieved by coupling qubits to LC oscillators, which may be formed from 2D planar circuits or 3D cavities. A basic circuit representation is shown in Fig. 2.5 (A). Performing circuit quantisation results in the following Hamiltonian [40]

$$\hat{H} = 4E_C(\hat{n} + (C_g/C_r)\hat{n}_r - n_g)^2 - E_J\cos\hat{\phi} + \hbar\omega_r\hat{a}^\dagger\hat{a} \tag{2.38}$$

where $\hat{a}^\dagger$ and $\hat{a}$ are the ladder operators of the LC resonator, frequency $\omega_r = 1/\sqrt{L_rC_r}$, and $\hat{n}_r = \hat{Q}_r/2e$ is the charge operator of the resonator. Here we have taken the limit $C_g \ll C_r, C_\Sigma$. In this form, the coupling between qubit and resonator is expressed

as a voltage bias on the qubit $n_g \to n_g - (C_g/C_r)\hat{n}_r$. Taking the transmon limit, we drop the constant offset charge term and expand out the flux and charge terms to get

$$\hat{H} \approx 4E_C\hat{n}^2 + \frac{1}{2}E_J\phi^2 - \frac{1}{24}E_J\phi^4 + \hbar\omega_r\hat{a}^\dagger\hat{a} + 2(C_g/C_r)\hat{n}_r\hat{n} \tag{2.39}$$

where the $\hat{n}_r^2$ term has been absorbed into the resonator frequency $\omega_r \to \omega_r(1 + (C_g/C_r)^2)^{1/2}$, which is a small change for $C_g \ll C_r$. Introducing ladder operators and making a rotating wave approximation results in

$$\hat{H} = \hbar\omega_q\hat{b}^\dagger\hat{b} - \frac{1}{2}E_C\hat{b}^\dagger\hat{b}(\hat{b}^\dagger\hat{b} - 1) + \hbar\omega_r\hat{a}^\dagger\hat{a} + \hbar g(\hat{b}^\dagger\hat{a} + \hat{b}\hat{a}^\dagger) \tag{2.40}$$

where $\hat{b}^\dagger$ and $\hat{b}$ are the ladder operators of the transmon, $\omega_q = \sqrt{8E_JE_C}$ and g represents the coupling strength between the transmon and resonator and can be expressed in the following form [41]

$$g = \omega_r\frac{C_g}{C_\Sigma}(\frac{E_J}{2E_C})^{\frac{1}{4}}\frac{Z_r}{Z_{vac}}\sqrt{2\pi\alpha} \tag{2.41}$$

Here, $Z_r = \sqrt{L_r/C_r}$, $Z_{vac} = \sqrt{\epsilon_0/\mu_0} \approx 377\,\Omega$ and α is the fine structure constant $\approx 1/137$. For physical circuit parameters, g can be large $\sim 0.1\omega_r$, and increases with larger values of E_J/E_C. This is the third important point of the transmon – while it is insensitive to slowly varying voltage sources, its coupling to fast $\sim$ GHz voltage sources actually *increases* with E_J/E_C, allowing it to couple effectively to GHz frequency circuits and drive lines [14]. The coupling g can also be expressed in the following forms which are often more convenient

$$g = \frac{1}{2}\frac{1}{\sqrt{Z_qZ_r}}\frac{C_g}{C_\Sigma C_r} \tag{2.42}$$

$$= \frac{1}{2}(\frac{\omega_q\omega_r}{C_\Sigma C_r})^{\frac{1}{2}}C_g \tag{2.43}$$

where $Z_q = \sqrt{L_J/C_\Sigma}$. Truncating the transmon to the ground and first excited state in eq. 2.40 leads to the Jaynes-Cummings Hamiltonian [42]

$$\hat{H} = \frac{\hbar\omega_q}{2}\hat{\sigma}_z + \hbar\omega_r\hat{a}^\dagger\hat{a} + \hbar g(\hat{b}^\dagger\hat{\sigma}_- + \hat{b}\hat{\sigma}_+) \tag{2.44}$$

where $\hat{\sigma}_+ = \hat{\sigma}_x + i\hat{\sigma}_y$ and $\hat{\sigma}_- = \hat{\sigma}_x - i\hat{\sigma}_y$ and $\hat{\sigma}_{x,y,z}$ are the Pauli matrices. Instead, making a Schrieffer-Wolff transformation on eq. 2.40 before truncating the qubit levels results in the following [40]

$$\hat{H} \approx \frac{\hbar\omega_q}{2}\hat{\sigma}_z + \hbar(\omega_r + \chi\hat{\sigma}_z)\hat{a}^\dagger\hat{a} \tag{2.45}$$

where we have neglected small changes to ω_q and ω_r and where

$$\chi = -\frac{g^2 E_C/\hbar}{\Delta(\Delta - E_C/\hbar)} \approx \frac{g^2\alpha}{\Delta(\Delta+\alpha)} \tag{2.46}$$

Here, $\Delta = \omega_q - \omega_r$. This Schrieffer-Wolff transformation is valid in the *dispersive limit* $|g| \ll |\Delta|$ and for low photon numbers in the resonator $n \ll n_{crit}$, where $n_{crit} = (\Delta/2g)^2$ [43]. As is clear from eq. 2.45, the resonator inherits a 2χ frequency shift depending on the qubit state. This is known as the single-photon Stark shift. Therefore, by sending a microwave pulse to the resonator near resonance and measuring the reflected signal, the state of the qubit can be inferred. This is the basis of superconducting qubit dispersive readout [40, 44]. Importantly, the back-action on the qubit is small in the dispersive regime for low power readout pulses and so the measurement also initialises the qubit in the measured state, making this readout method quantum non-demolition (QND), see e.g. Refs. [36, 41, 45, 46].

A circuit representation of a superconducting qubit coupled to an external voltage source is shown in Fig. 2.5 (B). The effect of the drive is to introduce a voltage bias to eq. 2.25, so that $n_g \to n_g - C_g V_g/2e$. Expanding in the transmon limit, this becomes

$$\hat{H} \approx 4E_C\hat{n}^2 + \frac{1}{2}E_J\phi^2 - \frac{1}{24}E_J\phi^4 + 8E_C C_g/(2e)V_g\hat{n} \tag{2.47}$$

where we have neglected the V_g^2 term as it does not bear on the qubit dynamics. The first three terms are the quartic order transmon Hamiltonian, and the last term is the interaction between the qubit and drive. Introducing ladder operators, this term can be expressed [43]

$$\hat{H}_{dr} = i\frac{2e}{\sqrt{2}}\frac{C_g}{C_\Sigma}\left(\frac{E_J}{8E_C}\right)^{\frac{1}{4}} V_g(\hat{b}^\dagger - \hat{b}) \tag{2.48}$$

Again, the strength of the interaction increases as $(E_J/E_C)^{1/4}$. Assuming a driving voltage of the form $V_g(t) = V_x(t)\cos(\omega_d t) + V_y(t)\sin(\omega_d t)$ and on changing frame such that $i(\hat{b}^\dagger - \hat{b}) \to \hat{b}^\dagger + \hat{b}$ eq. 2.48 becomes

$$H_{dr} = \hbar\Omega(t)(\hat{b}^\dagger + \hat{b}) \tag{2.49}$$

$$\Omega(t) = \frac{2e}{\sqrt{2}}\frac{C_g}{C_\Sigma}\left(\frac{E_J}{8E_C}\right)^{\frac{1}{4}} V_g(t) = \Omega_x(t)\cos(\omega_d t) + \Omega_y(t)\sin(\omega_d t) \tag{2.50}$$

Following closely Ref. [36], by moving to a frame rotating at the drive frequency, making a rotating wave approximation and truncating the transmon to its lowest two energy levels, eq. 2.47 is recast as

$$\hat{H}^R = \frac{\hbar}{2}[\Delta(t)\hat{\sigma}_z + \Omega_x(t)\hat{\sigma}_x + \Omega_y(t)\hat{\sigma}_y] \tag{2.51}$$

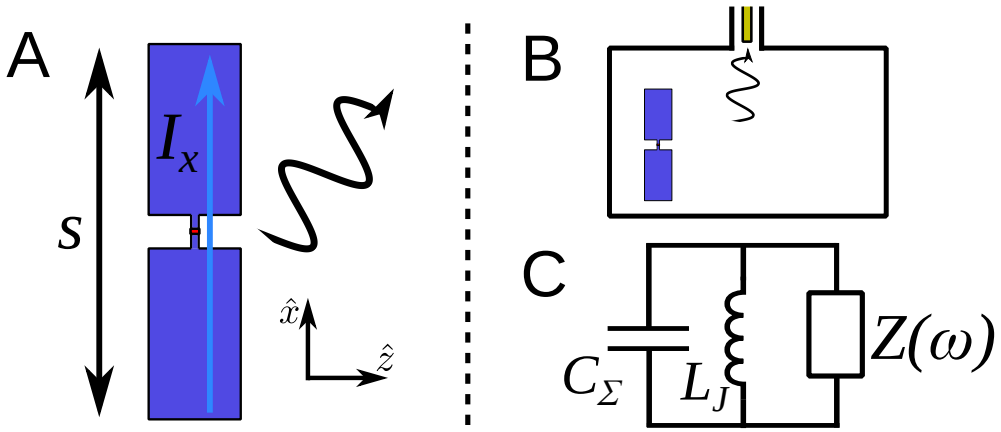

Figure 2.6: **Radiative relaxation:** (**A**) Dipole transmon qubit with length s depicted radiating into free space. (**B**) Dipole transmon placed inside a 3D cavity and radiating through an external control line. (**C**) A general circuit representation of a transmon qubit coupled to an environment represented by the impedance $Z(\omega)$.

where $\Delta = \omega_d - \omega_q$. In this form, it is clear that the qubit can be manipulated independently around each axis of the Bloch sphere by varying the drive amplitudes $\Omega_x(t)$ and $\Omega_y(t)$, and the drive frequency ω_d, and therefore that the microwave drive can generate arbitrary single qubit gates.

2.2.2 Relaxation mechanisms

Transmon qubits will exchange energy with uncontrolled environmental degrees of freedom, resulting in the qubit evolving into a mixed state. This process can be described by the following Master equation [41]

$$\dot{\rho} = -i[\hat{H}_q, \rho] + \gamma \mathcal{D}[\hat{b}]\rho \tag{2.52}$$

where $\mathcal{D}$ is the dissipator operator [41], $\hat{H}_q$ is the transmon Hamiltonian given in eq. 2.31, ρ is the density matrix of the transmon, and $\hat{b}$ is the annihilator operator acting on the transmon. Here, we have neglected dephasing and assumed that the number of thermal photons in the environment $\bar{n}_\gamma \to 0$ [41]. In this case $\gamma = 1/T_1$, where T_1 is the characteristic relaxation time of the qubit defined

$$T_1 = \frac{1}{\kappa} = \frac{1}{\kappa_\downarrow + \kappa_\uparrow} \tag{2.53}$$

We now review three major sources of relaxation in transmon qubits: radiative relaxation, dielectric relaxation, and quasiparticle relaxation. Under the assumption these decay channels act independently, the total relaxation rate is given by

$$\kappa = \kappa_{rad} + \kappa_{diel} + \kappa_{qp} \tag{2.54}$$

2.2.2.1 Radiative relaxation

It is instructive to first approximate the classical radiative loss of a standard dipole transmon into the vacuum. To do this we start from the vector potential [47]

$$\boldsymbol{A}(\boldsymbol{r},t) = \frac{u_0}{4\pi}\int \frac{[\boldsymbol{j}]}{|\boldsymbol{r}-\boldsymbol{r'}|}d^3\boldsymbol{r'} \tag{2.55}$$

Here, the vector potential at position $\boldsymbol{r}$ is found by integrating over the retarded current density $[\boldsymbol{j}]$, weighted by the separation $|\boldsymbol{r}-\boldsymbol{r'}|$. For a dipole transmon length s oriented along the $\hat{x}$ axis (Fig. 2.6)(A) the vector potential in the far field can be approximated as

$$A_x(r,t) = \frac{u_0}{4\pi r}\int_0^s I_x dx = \frac{u_0}{4\pi r} I_x s \tag{2.56}$$

where $I_x = i\omega Q$ and where we assumed $s \ll \lambda$ to replace the retarded current density $[\boldsymbol{j}]$ with the current density $\boldsymbol{j}$. This is the vector potential of a Hertzian Dipole [47]. Using this vector potential to work out the electric and magnetic far-fields, then the Poynting vector, and then integrating over a spherical shell, the average power radiated is found to be given by [47]

$$P = \frac{Q^2\omega^4 s^2}{12\epsilon_0 \pi c^3} \tag{2.57}$$

The first excited state of the transmon corresponds to the oscillation of a single Cooper pair through this dipole $Q \to 2e$. Taking $E = \hbar\omega$ and $T_{rad} = E/P$ results in [14]

$$T_{rad} = \frac{12\pi\hbar\epsilon_0 c^3}{(2e)^2\omega^3 s^2} \tag{2.58}$$

For a realistic transition frequency of 5 GHz and transmon length $s = 0.5$ mm, $T_{rad} \approx 1$ µs. This is orders of magnitude below current state-of-the-art qubit relaxation times, demonstrating that large dipole transmons must be prevented from radiating into free-space. This result illustrates that dipole transmons make good antennas, due both to their macroscopic size, and the path of current flow when excited.

In an arbitrary linear electromagnetic (EM) environment, T_{rad} can be accurately found through a simple semi-classical formula [48]. As shown in Fig. 2.6, the transmon qubit and its environment are represented by a classical LC oscillator connected to an impedance $Z(\omega)$. The quality factor of the classical circuit is given by $Q = \omega RC$ where $R = 1/\mathrm{Re}[Y(\omega)]$ is the effective resistance of the environment. Where this resistance is entirely due to external loss (i.e. through control ports), this leads to the

following expression for the radiative lifetime [48]

$$T_{rad} = RC = \frac{C}{\mathrm{Re}[Y(\omega)]} \tag{2.59}$$

This formula can be derived by treating the transmon as a two level system and using Fermi's golden rule, see Ref [49]. For simple circuits, the admittance Y can be found analytically. In general, it can be accurately simulated using finite element classical electromagnetism simulation tools such as ANSYS HFSS [50] or COMSOL [51]. As discussed in section 2.3, the qubit capacitance C can also be accurately simulated using classical EM simulation tools. This simple equation is therefore very powerful and has been experimentally verified for a variety of transmon qubits coupled to different environments [48].

By placing a transmon qubit in a 3D cavity, its EM environment is dramatically changed and it cannot radiate into the far-field (as its vector potential will be 0 outside the cavity) [52]. In this case, radiative loss will solely be through the external control lines that couple to the circuits. Considering eq. 2.59, it is possible to engineer the admittance Y such that the qubit decouples from certain control lines. For example, in the case where the qubit is dispersively coupled to a readout-resonator, it is beneficial to increase the radiative (i.e. external) decay rate of the resonator κ_{ext} and increase the single-photon Stark shift 2χ to be able to perform fast readout [53, 54]. However, in the simple circuit shown in Fig. 2.5(A), the qubit will inherit some of this loss through its coupling g to the resonator, in the dispersive limit given by [41]

$$\kappa_q = (g/\Delta)^2 \kappa_r \tag{2.60}$$

This seems to suggest fast readout and high qubit relaxation times are incompatible. However, since the radiative lifetime is in fact dictated by the electrical response of the circuit through eq. 2.59, it is possible to introduce circuit elements that invalidate eq. 2.60, resolving this apparent problem. This is known as Purcell filtering [41, 55], and allows for fast readout alongside high qubit relaxation times. The required suppression of the real part of the admittance has been demonstrated using $\lambda/4$ CPW resonators [55], broadband CPW filters [56], and by 'stacking' $\lambda/2$ CPW resonators in series [53].

Because radiative loss can be accurately predicted and controlled by microwave engineering the coupling of superconducting qubits to their environment, it is relatively

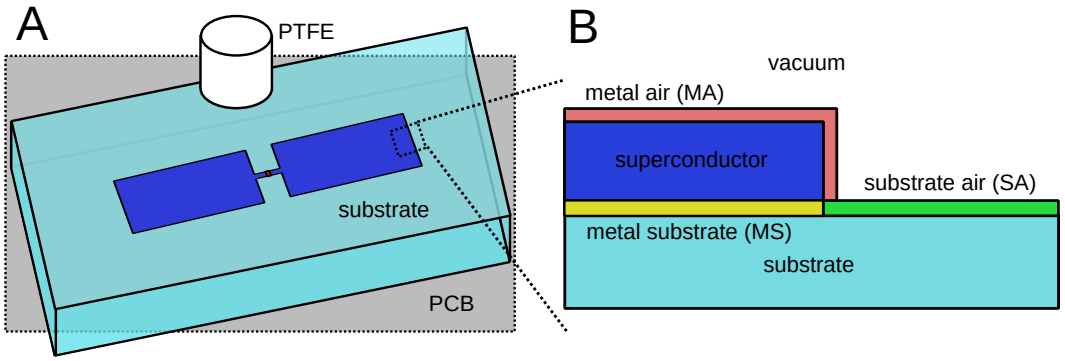

Figure 2.7: **Dielectric relaxation:** (**A**) Illustration of possible dielectric relaxation sources in a transmon's environment. Here, the environment contains a substrate, a PCB board and a piece of PTFE. (**B**) Cross-section of the transmon pad edge, depicting the different interfaces that are thought to contribute significantly to dielectric relaxation. Figure (B) is adapted from Ref. [59].

straightforward to design devices such that $\kappa_{rad} \ll \kappa_{other}$. As such, radiative loss is generally not a limiting factor of state-of-the-art superconducting qubit relaxation times. However, as other decay channels are reduced, qubits must be increasingly decoupled from their control lines to ensure that they are not radiatively limited. This then requires that more powerful drives be used to perform quantum logic gates at the same rate, resulting in an increased power load on the dilution refrigerator [57]. Methods to break this trade-off by giving the control lines a non-linear power response have been explored, see Ref. [58].

2.2.2.2 Dielectric relaxation

Dielectric relaxation refers to an internal loss channel where the electric field of an excited qubit exists inside dissipative materials. The microscopic source of the dissipation is consistent with a discrete distribution of two-level-systems (TLS) residing inside the dielectric that each possess an electric dipole moment [60]. The physical origin of these TLS is not conclusively known, and a review of proposed mechanisms is given in Ref. [61]. In very small volumes, the discrete nature of the TLS becomes important, whereas over larger volumes it is valid to treat them as a continuous distribution, resulting in the bulk loss tangent of the material δ. Where the loss tangent concept is meaningful, the associated dielectric loss limited quality factor of the material is given by [19]

$$Q = 1/\tan\delta \tag{2.61}$$

The associated relaxation rate of a superconducting qubit in proximity to various materials with quality factors Q_i is given by [59]

$$\kappa_{diel} = \omega_q \sum_i \frac{p_i}{Q_i} = \omega_q \sum_i p_i \tan\delta_i \tag{2.62}$$

where p_i is the electric field participation ratio of the qubit, defined as the fraction of the qubit's electric field energy stored in material i

$$p_i = \frac{\int_{V_i} \epsilon_i |\boldsymbol{E}|^2 dV}{\sum_j \int_{V_j} \epsilon_j |\boldsymbol{E}|^2 dV} \tag{2.63}$$

These expressions predict that regions with a large participation ratio will disproportionately contribute to dielectric losses, and also that the dielectric relaxation time scales inversely with the qubit frequency (since $T_1 = Q/\omega$ and Q is frequency independent in eq. 2.61). The strongest electric field of an excited transmon will be inside the oxide material used to form the Josephson junction barrier. However, the density of TLS in thin SiO_2 interfaces has been found to be $\sim 1\,\mu m^{-2} GHz^{-1}$[59, 60]. For Josephson junctions with area $\sim 0.04\,\mu m^2$ (as used in this thesis) the probability of harbouring a single TLS in a 1 GHz range is then just a few percent. This implies the oxide barrier inside the junction is unlikely to contribute to dielectric relaxation, so long as the junction is small enough. In devices with many hundreds of qubits however, sporadic junction TLS may cause a notable percentage of qubits to have a significantly reduced relaxation time.

Outside of the Josephson junction, the most obvious candidate for dielectric relaxation is the substrate the circuit is fabricated on. Considering circuits fabricated on silicon, which has a high relative permittivity $\epsilon_r = 11.45$ at $\sim 10\,K$ [62] (which we take as the cryogenic permittivity throughout), the participation ratio inside the substrate is generally $p_{sub} \sim 90\%$ – largely independent of the qubit and enclosure design. Recent experimental work on superconducting resonators have found loss tangent $\tan\delta$ values for cryogenic silicon of $2.6 \pm 0.4 \times 10^{-7}$ [63], $1.3 \pm 1.7 \times 10^{-7}$ [64], and $1.2 \pm 0.3 \times 10^{-7}$ [65], while a study of transmon qubits on silicon found an upper bound $\tan\delta < 5 \times 10^{-7}$ [66]. A value of 1.2×10^{-7} corresponds to a substrate loss limited qubit lifetime of around 300 µs for a qubit at $\omega_q/2\pi = 5\,GHz$, using $p_{sub} = 0.9$. This is close to the relaxation times of state-of-the-art transmon qubits (100 µs – 200 µs [12]), and suggests that substrate limited loss may soon be a dominant relaxation mechanism for transmon qubits. This limit could be increased by using higher quality substrates [67].

There is a large body of experimental evidence that another significant (often dominant) contributor to dielectric relaxation is from 1 nm−10 nm thick dielectric interface layers that reside on the surfaces of the qubit and the substrate [59, 63, 65, 66]. While the participation in these interfaces is small ($p_i \sim 10^{-4} - 10^{-3}$), they can have high loss tangents ($\tan\delta_i \sim 10^{-4} - 10^{-3}$, under assumptions about the interface thicknesses and relative permittivities), limiting qubit relaxation times to 10 µs − 100 µs. These interfaces are often divided into three categories: between the qubit and the substrate (MS), between the qubit and the vacuum ('air') (MA), and between the substrate and the vacuum (SA) [59]. Unlike the participation in the substrate bulk, the participation in these interfaces is strongly dependent on both the qubit geometry and the qubit fabrication process. In large part, the qubit geometry dependence is due to the behaviour of electric fields at the edge of a thin metal sheet - where the field strength diverges like $|E| \propto 1/\sqrt{x}$ as a function of distance from the metal edge [47, 59]. This means that qubits with a large perimeter to surface area ratio will tend to have increased participation in these critical interfaces. Reducing the perimeter to surface ratio by adjusting the qubit geometry – and by simply making the qubit larger – is therefore an effective way to reduce qubit loss in interfaces [59, 66, 67].

The loss tangent and participation in these interfaces is dependent on the circuit fabrication process. For instance, performing an HF dip immediately prior to superconducting qubit fabrication on silicon can significantly reduce losses in the MS interface, by removing the thin oxide layer on the silicon surface [68]. HMDS passivation may further decrease loss at this interface [69]. 'Trenching' circuits by etching the silicon substrate away after circuit fabrication can significantly reduce participation in the MS and SA interfaces – and also inside the substrate, by reducing field participation at the circuit edges where fields are strongest [63–65, 70].

Additionally, any other dielectrics used in the packaging of the device can contribute to dielectric relaxation, for instance the PTFE inside coaxial cables or the epoxy in PCB boards. It is therefore important to minimise the field participation of qubits inside such materials.

In summary, there is strong experimental evidence that dielectric relaxation is a limiting factor in state-of-the-art transmon qubit relaxation times. Qubits with a larger

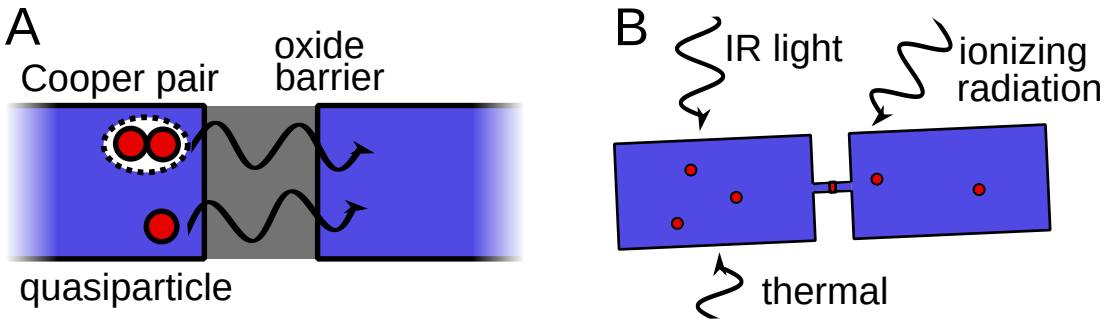

Figure 2.8: **Quasiparticle relaxation:** (**A**) Illustration of Cooper pair tunnelling and quasiparticle tunnelling through a transmon qubit tunnel junction. (**B**) Illustrating some of the key quasiparticle generation mechanisms in transmon qubits.

physical footprint are less sensitive to interface loss, although it may still be a significant relaxation mechanism. Interface loss can also be reduced through improvements to fabrication processes. Separate to interface loss, transmon qubits fabricated on silicon substrates may have substrate loss limited relaxation times $\lesssim 0.5\,\text{ms}$, suggesting higher quality substrates may be needed to reach 1 ms relaxation times. Finally, it is important to ensure that potentially lossy dielectrics in the device packaging are sufficiently separated from qubits to prevent additional dielectric relaxation.

2.2.2.3 Quasiparticle relaxation

Quasiparticles here refer to Bogoliubov excitations above the superconducting ground state. Such quasiparticles are not protected from scattering like Cooper-pairs and so their motion through the superconductor is dissipative. In transmon qubits, the dominant quasiparticle relaxation mechanism is from quasiparticle tunnelling events through the Josephson junctions [71]. At low temperature $k_B T \ll \Delta$ (here Δ is the superconducting gap), the thermal quasiparticle population density in a superconductor is given by [71]

$$x_{qp}^{th} = \sqrt{\frac{2\pi k_b T}{\Delta}} e^{-\frac{\Delta}{k_b T}} \tag{2.64}$$

where the density x_{qp} is the fraction of quasiparticles to the total number of electrons in the material N_{qp}/N_e. For thin film aluminium $\Delta \approx 200\,\mu\text{eV}$ [15, 16] and so at 50 mK $x_{qp}^{th} \sim 2.5 \times 10^{-21}$. The associated relaxation rate due to dissipative quasiparticle junction tunnelling events in a transmon qubit is given by [20, 71]

$$\kappa_{qp} = \sqrt{\frac{2\omega_q \Delta}{\pi^2 \hbar}} x_{qp}^{th} \tag{2.65}$$

which corresponds to a quasiparticle limited lifetime of $\sim$ 250 years (!) at 50 mK. This suggests quasiparticle related relaxation should be negligible, as superconducting circuit devices are thermalised to dilution refrigerators operating at $\lesssim 20\,\text{mK}$.

However, far higher quasiparticle densities between $10^{-6} - 10^{-8}$ have been experimentally detected in superconducting qubits [15]. A thermal density of $x_{qp} = 10^{-7}$ corresponds to a QP limited relaxation time of $\sim 220\,\mu s$ using eq. 2.65 (again taking $\Delta = 200\,\mu eV$) [15], making this loss channel significant. Additionally, the distribution of these quasiparticles has been found not to follow a thermal distribution, and to cause qubit excitation and decay events with approximately equal frequency [15]. Therefore, as well as causing qubit relaxation through decay and excitation events, quasiparticle tunnelling can also result in a significant residual excited state population (around $p_e \sim 10\%$ in Ref. [15]).

The source of these 'hot' non-equilibrium quasiparticles has been found to be high frequency light $\omega/2\pi \gtrsim 100\,GHz$ that is able to break Cooper-pairs efficiently [15]. This light can leak into the device from black body radiation at the 4 K stage of the dilution refrigerator. This leads to the requirement to carefully shield superconducting qubit devices from infra-red light. When carefully shielded [72, 73], residual excited state populations and quasiparticle densities of $p_e \sim 1\%$ and $x_{qp} \sim 10^{-9}$ have been measured [72]. This is still well above the prediction of a thermal distribution.

Another quasiparticle generation mechanism is Cooper-pair breaking by ionising radiation [16, 74]. A recent experiment involving transmon qubits irradiated by a radioactive source found a quasiparticle population due to background radiation $x_{qp} \approx 7 \times 10^{-9}$ [16], in fair agreement to the residual density mentioned above and corresponding to a quasiparticle limited relaxation time of a few ms [16]. Radiation shielding should therefore further reduce the density of quasiparticles and increase this limit.

It is also possible to reduce the density of quasiparticles by increasing the rate of quasiparticle removal from the superconductor. Assuming a constant generation rate g, the dynamics of non-thermal quasiparticle density can be modelled by the following simple equation [20]

$$\frac{dx_{qp}}{dt} = -rx_{qp}^2 + -sx_{qp} + g \tag{2.66}$$

where r ($\sim 1/(100\,ns)$ [20]) is the standard recombination rate through quasiparticles pairing up to form a Cooper-pair (hence $\propto x_{qp}^2$), and s is the trapping rate due to removal of individual quasiparticles from the superconductor $\propto x_{qp}$. Importantly, recombination is a factor of x_{qp} less efficient than trapping due to its quadratic scaling. Effective quasiparticle traps can be made by depositing a normal metal onto

superconducting qubit pads [75], by trapping magnetic flux voticies inside these pads [20], and by engineering the superconducting energy gap of these pads by composing them of multiple superconductors [76].

In summary, quasiparticles can be a significant relaxation mechanism for transmon qubits if the device is not properly IR shielded. A signature of significant quasiparticle density as a result of poor IR shielding is a high residual qubit excited state population $p_e \sim 10\%$. Once effectively shielded, there is evidence that the remaining quasiparticle population is due to ionising radiation, limiting transmon qubit lifetimes to a few ms [16]. This limit could be increased by improved radiation shielding, or by employing quasiparticle traps. Finally, we note that since radiation induced quasiparticles may cause correlated errors over large physical distances $\sim 1\,\text{cm}$ and long times $\sim 1\,\text{ms}$, they might pose a significant threat to quantum error correction codes [74, 77].

2.2.3 Dephasing mechanisms

As well as causing relaxation, interactions with the environment can perturb the energy levels of the transmon, resulting in noise on its qubit transition frequency. This can be described by adjusting the Master equation in eq. 2.52 to include a dephasing term [41]

$$\dot{\rho} = -i[\hat{H}_q, \rho] + \gamma\mathcal{D}[\hat{b}]\rho + 2\gamma_\varphi\mathcal{D}[\hat{b}^\dagger\hat{b}]\rho \tag{2.67}$$

where again this assumes $\bar{n}_\gamma \to 0$ and also includes assumptions about the dephasing mechanism [41]. Here, $\gamma_\varphi = 1/T_2^*$ is the pure dephasing rate, related to the characteristic T_2 dephasing time by

$$T_2 = \frac{1}{\kappa_2} = \frac{1}{\kappa/2 + \gamma_\varphi} \tag{2.68}$$

Note that T_2 is bounded by the relaxation time $T_2 \leq 2T_1$, whereas the pure dephasing time T_2^* is independent of T_1. To relate γ_φ to a noise source $f(t)$ on the qubit transition frequency ω_q, we express the total accumulated phase $\phi(t)$ of the off-diagonal density matrix elements $\rho_{01}, \rho_{10} \propto \exp(\phi(t))$ in terms of a Taylor series expansion in $f(t)$ [36]

$$\phi(t) = \int_0^t \omega(f(t'))dt' = \omega_{q,0}t + \frac{\partial\omega_q}{\partial f}\int_0^t f(t')dt' + ... \tag{2.69}$$

To first order, the effect of the noise source on the accumulated phase is then given by

$$\Delta\phi(t) = \frac{\partial\omega_q}{\partial f}\int_0^t f(t')dt' \tag{2.70}$$

Following closely Ref. [36], if this phase is Gaussian distributed then

$$< e^{i\Delta\phi(t)} >= e^{-<\Delta\phi^2(t)>/2} = e^{-\gamma_\varphi(t)t} \tag{2.71}$$

Therefore, the pure dephasing rate $\gamma_\varphi(t)$ can be expressed

$$\gamma_\varphi(t) = \frac{1}{2t}(\frac{\partial\omega_q}{\partial f})^2\int_0^t\int_0^t < f(t')f(t'') > dt'dt'' \tag{2.72}$$

Introducing the power spectral density $S_f(\omega)$ defined as the mean-squared amplitude of f at frequency ω per 1 Hz bandwidth, this evaluates to [36, 78]

$$\gamma_\varphi(t) = \frac{1}{2t}(\frac{\partial\omega_q}{\partial f})^2\int_{-\infty}^{\infty} S_f(\omega)\frac{\sin(\omega t/2)}{\omega t/2}\frac{d\omega}{2\pi} \tag{2.73}$$

To proceed further requires knowledge of the power spectral density. Many noise sources, including charge noise, are modelled as having a $1/\omega$ frequency dependence $S_f(\omega) = 2\pi A^2/\omega$, where A represents the noise amplitude. It is also necessary to provide cutoff frequencies for the noise ω_{c0} and ω_{c1} ($\omega_{c0} < \omega_{c1}$). For charge noise, the resultant pure dephasing time is given by [36]

$$T_\varphi \approx \frac{2e\hbar}{|\epsilon_1|\pi A\sin(2\pi n_g)} \tag{2.74}$$

For $E_J/E_C = 69$ and $\varepsilon_1/h = -394\,\text{Hz}$ (taken from one of the qubits characterised in Chapter 7), and taking $A = 10^{-3}e$ as a reasonable worst case scenario [36, 79, 80], and also $\sin(2\pi n_g) = 1$, we find $T_\varphi \approx 250\,\text{ms}$, demonstrating the effect of the exponentially suppressed charge noise of the transmon on dephasing times.

Another important dephasing mechanism is due to thermal photons inside a qubit's readout resonator. This can be understood by considering that adding or removing a photon from the resonator shifts the qubit frequency by 2χ. In the limit $\bar{n}_{th} \ll 1$, where $\bar{n}_{th}$ is the average thermal photon population of the resonator, the associated dephasing time is given by [81, 82]

$$\frac{1}{T_\varphi} = \frac{\bar{n}_{th}\kappa_r\chi^2}{\kappa_r^2/4 + \chi^2} \tag{2.75}$$

where κ_r is the total decay rate of the resonator. In a recent experiment on a transmon device with special steps taken to reduce n_{th} to a very low value $n_{th} \approx 2\times10^{-4}$,

pure dephasing times of $T_\varphi \sim 10\,\text{ms}$ were measured [81], indicating that remaining dephasing mechanisms were very small in this device compared to the relaxation limited dephasing time $T_2 = 2T_1 \approx 200\,\mu\text{s}$. Possible remaining dephasing mechanisms are thermally fluctuating TLS [83, 84], and quasiparticles due to the weak dependence of qubit frequency on quasiparticle density [71].

2.3 Simulating transmon circuits

The low anharmonicity of transmon qubits means the Hamiltonian can be separated into a linear part and a nonlinear perturbation. Furthermore, the charge dispersion of the energy levels can be ignored. In section 2.2 we used this to solve the Hamiltonian of a transmon capacitively coupled to an LC oscillator. This technique can be generalised to solve the Hamiltonian of a transmon coupled to an arbitrary linear electromagnetic (EM) environment, so long as the electrical response of the linear environment can be found and an equivalent circuit synthesised. Advanced classical electromagnetism simulation tools can be used to determine the electrical response of linear EM environments; and various techniques exist to synthesise an equivalent circuit, which makes these methods very powerful.

2.3.1 Black-box quantisation

Here, we review black-box quantisation [24, 85, 86] for a single transmon as described in Ref. [85], in which a method is given for finding the Hamiltonian of transmons embedded in linear EM environments with low dissipation. A schematic of a single transmon embedded in an unspecified linear EM environment is shown in Fig. 2.9(A). In fig. 2.9(B), we imagine open circuiting the Josephson junction of the transmon, placing probe tips on either side, and measuring the impedance response defined $Z(\omega) = V(\omega)/I(\omega)$ where $V = V_+ + V_-$ and $I = I_+ - I_-$. This response can be simulated accurately using classical EM simulation software for a given environment. The circuit representation of the junction embedded in this EM environment is shown in Fig. 2.9(C). The junction can be split into a linear and non-linear part as shown in fig. 2.9(D), where the energy of the non-linear portion is given by

$$E_{nl} = -E_J\left(\frac{\phi^4}{4!} - \frac{\phi^6}{6!} + \mathcal{O}(\phi^8)\right) \tag{2.76}$$

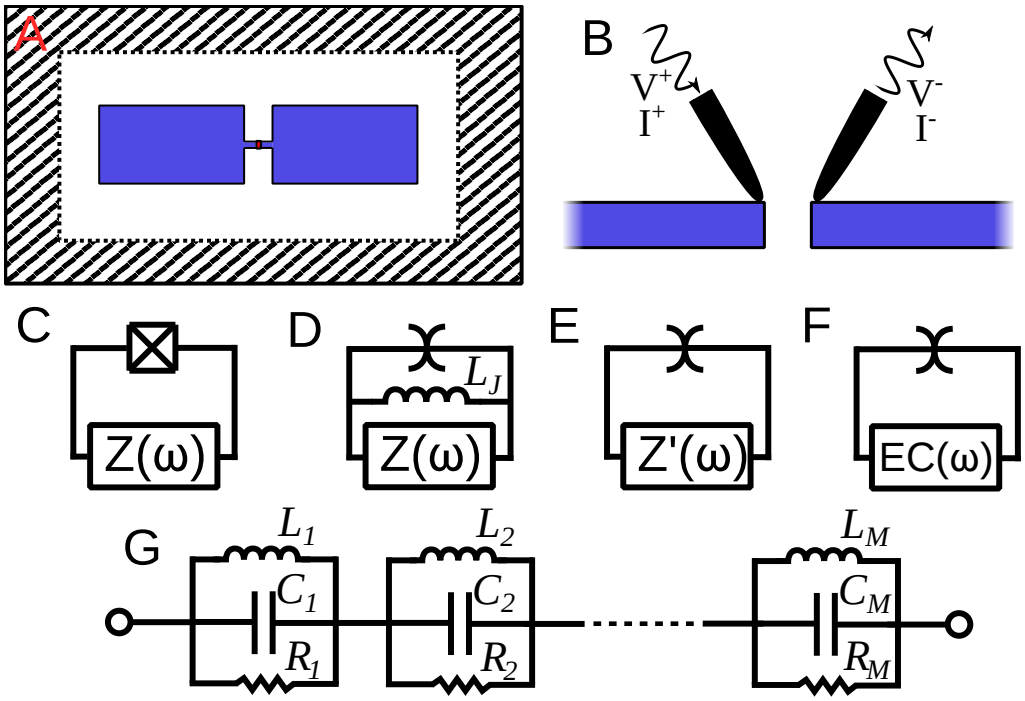

Figure 2.9: **Black-box quantisation:** (**A**) Transmon qubit inside a linear EM environment. (**B**) The junction is removed, and the impedance response $Z(\omega)$ across the junction measured with probe tips. (**C**) Circuit representation of (A). (**D**) The junction is divided into a linear inductance L_J and a non-linear inductance depicted by the semi-circle symbol. (**E**) The linear inductance is absorbed into the impedance $Z(\omega)$. (**F**) The impedance $Z'(\omega)$ is replaced with an equivalent circuit. (**G**) The Fosters equivalent circuit. Figures (C,D,E,F,G) are adapted from Ref. [85].

The linear junction inductance L_J is then absorbed into the environment $Z(\omega) \rightarrow Z'(\omega)$ by the transformation

$$\frac{1}{Z'(\omega)} = \frac{1}{Z(\omega)} + \frac{1}{i\omega L_J} \tag{2.77}$$

Here we have neglected the capacitance of the junction itself, C_J [85], assuming it is small for a transmon. At this stage, we have a purely non-linear circuit element with energy given by eq. 2.76, connected to a linear circuit element with impedance $Z'(\omega)$, as shown in Fig. 2.9(E). To proceed further, we must synthesise an equivalent circuit composed of lumped-elements that reproduces the impedance $Z'(\omega)$, as shown in Fig. 2.9(F). Under the condition that dissipation is low, an approximate equivalent circuit is the Foster's equivalent circuit [87] shown in Fig. 2.9(G), whose impedance is given by

$$Z_F(\omega) = \sum_{p=1}^{M} (i\omega C_p + \frac{1}{i\omega L_p} + \frac{1}{R_p})^{-1} \tag{2.78}$$

The condition for low dissipation is $R_p \gg Z_p$ where $Z_p = \sqrt{L_p/C_p}$ [85]. If the impedance $Z'(\omega)$ is only known over a finite frequency range, as must be the case when it is determined by FE simulation methods, an approximate solution can be found by setting M equal to the number of modes in this range, where the modes are defined by the poles $\mathrm{Im}\big[Z'(\omega_p)\big] \to \infty$. C_p, L_p and R_p can then be found from the behaviour of the admittance spectrum $Y(\omega) = 1/Z'(\omega)$ at these poles, using the relations [85]

$$C_p = \frac{1}{2}\mathrm{Im}\Big[\frac{dY(\omega)}{d\omega}\Big]\Big|_{\omega=\omega_p} \tag{2.79}$$

$$R_p = \frac{1}{\mathrm{Re}\big[Y(\omega_p)\big]} \tag{2.80}$$

$$L_p = \frac{1}{\omega_p^2 C_p} \tag{2.81}$$

More properly, the Foster's equivalent circuit can be found by fitting the complex function $Z_f(s)$ to the simulated $Z'(\omega)$ spectrum, where $Z_f(s)$ is given by [86]

$$Z_f(s) = \sum_{k=1}^{M} \frac{R_M}{s - s_k} + D + Es \tag{2.82}$$

as can be done by Vector-fitting methods [88]. The Foster's equivalent circuit can then be synthesised from the fitted pole residues R_M, see Ref. [86]. In the case of no dissipation, this Foster's equivalent circuit can exactly synthesise the impedance $Z'(\omega)$, up to very small fitting errors [86]. Note that because the capacitive transmon pads and linear junction inductance L_J are included in $Z'(\omega)$, one of the modes p will correspond to the linearised transmon qubit (this mode should lie inside the simulated frequency range). We call this mode q. In the case dissipation is due to external losses, the radiative relaxation time of each mode (including the qubit mode) can be approximated by

$$T_{rad,p} = R_p C_p \tag{2.83}$$

In the case dissipation is small, we can proceed by taking $R_p \to \infty$. The circuit in Fig. 2.9(F) can then be quantised to give the following simple Hamiltonian [85]

$$\hat{H} = \sum_{p}^{M} \hbar\omega_p \hat{a}_p^\dagger \hat{a}_p - E_J\Big(\frac{\hat{\phi}_J^4}{4!} - \frac{\hat{\phi}_J^6}{6!} + \mathcal{O}(\hat{\phi}_J^8)\Big) \tag{2.84}$$

where $\hat{\phi}_J$ is the superconducting phase across the junction given by

$$\hat{\phi}_J = \frac{1}{\varphi_0}\sum_{p}^{M} \sqrt{\frac{\hbar Z_p}{2}}(\hat{a}_p^\dagger + \hat{a}_p) \tag{2.85}$$

where $Z_p = \sqrt{L_p/C_p}$ and φ_0 is the reduced flux quantum. This form can be solved numerically, or analytically up to first order [85]. It consists of M uncoupled harmonic oscillators and a non-linear perturbation that introduces coupling between them. Considering the generality of Fig. 2.9(A), this result is perhaps surprising – the transmon environment could contain a mixture of lumped-elements, distributed elements, and 3D cavities; and yet it can be described by this simple Hamiltonian.

The black-box quantisation method described above, while powerful for environments with low dissipation, is approximate because the Foster's equivalent circuit cannot exactly synthesise an impedance $Z'(\omega)$ featuring dissipation. Remarkably, an exact (up to very small fitting errors) equivalent circuit can still be found where $Z'(\omega)$ features arbitrary dissipation using Brune synthesis [86, 89]. The resulting Brune equivalent circuit can also be quantised [86], rigorising black-box quantisation methods for transmons in linear EM environments with dissipation.

Black box quantisation methods can also in principle be generalized to find the Hamiltonian of multiple transmon qubits embedded in a passive linear EM environment featuring voltage sources [24, 85], discussed in the next section.

2.3.2 Impedance response formulas

Fig. 2.10(A) shows a system of transmon qubits embedded in a linear EM environment containing external control lines. Ports are defined at the location of transmon Josephson junctions as in Fig. 2.9(B), and also across the control ports at the boundary of the system. The resulting $N_q + N_d$ port network is shown in Fig. 2.10(B), having N_q qubit ports and N_d control line ports.

In principle, black-box quantisation can be performed on this network. However, this can be computationally expensive. First, the $(N_q + N_d) \times (N_q + N_d)$ impedance matrix of the network needs to be simulated or numerically solved over a frequency range $\Delta\omega$ that includes all transmon frequencies and the frequencies of other modes that are desired in the Hamiltonian. The frequency step should be sufficiently small that important features (e.g. poles) in the impedance response are not missed. Next, this $(N_q + N_d) \times (N_q + N_d)$ impedance matrix must be fit to a multiport extension of the complex function in eq. 2.82. After this, an equivalent circuit must be found using the fitted parameters, in general using multiport Brune synthesis [24, 90]. To find a Hamiltonian including radiative losses, the control line ports must be terminated

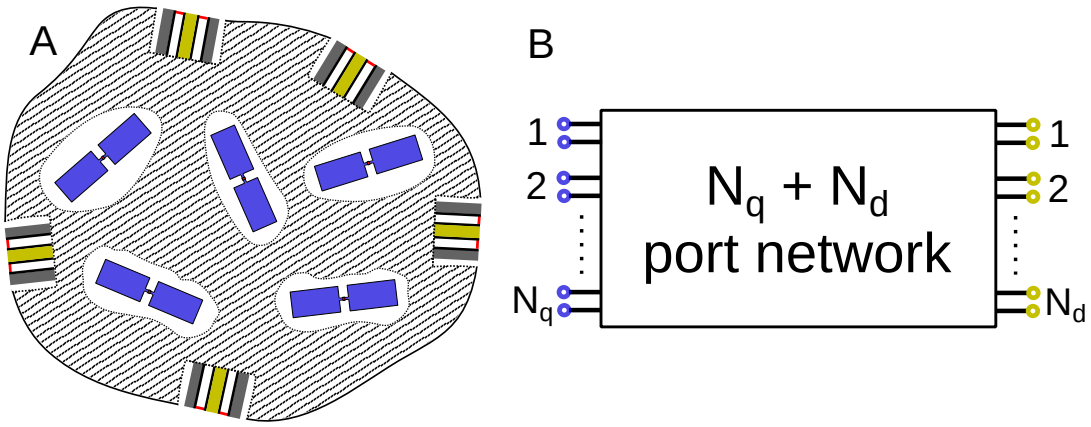

Figure 2.10: **Network representation for transmon circuits:** (**A**) Depiction of transmon qubits embedded in a linear EM environment featuring external control lines. (**B**) An equivalent $N_q + N_d$ port network for the linear electrical response, where N_q is the number of transmons and N_d the number of drives.

with their characteristic impedance, resulting in a N_q port circuit with a $N_q \times N_q$ impedance matrix. Finally, the non-linear junction energies should be placed across their respective qubit ports and circuit quantisation performed on the resultant circuit [24, 33, 91]. This process may be computationally prohibitive for large values of N_q, N_d and for many frequency steps, and the resultant Hamiltonian may be complicated [24].

Remarkably, in Ref. [92] it is shown that under appropriate conditions and approximations key Hamiltonian terms for the circuit in Fig. 2.10(A) can be found instead using simple impedance formulas. Only specific elements of the impedance matrix need to be known to evaluate these formulas – and crucially they only need to be known at specific frequencies of interest. The conditions for these formulas to apply are: (1) qubits have low anharmonicity (a condition met by transmon qubits), and (2) qubits have dispersive interactions with the internal modes of the environment:

$$|g_{ij}| \ll |\omega_i^q - \omega_j^I| \tag{2.86}$$

where ω_i^q are the qubit frequencies, ω_j^I the internal mode frequencies, and g_{ij} are the couplings between qubits and internal modes. Here, we simply state some of the key results given these conditions. The transverse coupling J_{ij} between qubits i and j, defined $\hat{H} = J_{ij}(\hat{a}_i\hat{a}_j^\dagger + \hat{a}_i^\dagger\hat{a}_j)$, is given by [92]

$$J_{ij} = -\frac{1}{4}\sqrt{\frac{\omega_i\omega_j}{L_iL_j}}\mathrm{Im}[\frac{Z_{ij}(\omega_i)}{\omega_i} + \frac{Z_{ij}(\omega_j)}{\omega_j}] \tag{2.87}$$

where $Z_{ij}(\omega)$ is the transfer impedance between qubit ports i and j, ω_i is the frequency of qubit i, and the inductance L_i is related to the bare junction inductance of qubit i by $L_i = L_{J_i}/(1 - 2E_{C_i}/\hbar\omega_i)$. The key approximations are that dissipation and the effect of $\mathcal{O}(\hat{\phi})^4$ terms in the circuit Hamiltonian are neglected. Under the same assumptions, the drive coupling ε_{ij} between qubit i and control line j, defined $\hat{H} = \varepsilon_{ij}(\hat{a}_i - \hat{a}_i^\dagger)V_j$, where V_j is the voltage on control line j, is given by [92]

$$\varepsilon_{ij} = \sqrt{\frac{\omega_i}{2\hbar L_i}}\mathrm{Im}[Z_{ij}(\omega_i)]\frac{e^{i\theta_j}C_j}{\sqrt{1+\omega_j^2 Z_0^2 C_j^2}} \tag{2.88}$$

where C_j is the shunting capacitance of control line j, Z_0 is the characteristic impedance of the control lines (here assumed the same for all control lines), and $\theta_i = (\pi/2) - \arctan(\omega_d Z_0 C_j)$. The contribution of control line j to the radiative relaxation time of qubit i can also be found [92]

$$\frac{1}{T_{rad}^{ij}} = \frac{2}{L_i}\mathrm{Im}[Z_{ij}(\omega_i)]^2\frac{\omega_i^2 C_j^2 Z_0}{1+\omega_j^2 Z_0^2 C_j^2} \tag{2.89}$$

$$= 4\omega_i Z_0 |\varepsilon_{ij}|^2 \tag{2.90}$$

Notice that $T_{rad}^{ij} \propto 1/|\varepsilon_{ij}|^2$. For an otherwise closed environment, the total radiative relaxation time of qubit i is then given by

$$\frac{1}{T_{rad}^{i}} = \sum_{j=1}^{N_d}\frac{1}{T_{rad}^{ij}} \tag{2.91}$$

Importantly, these expressions can be used where the network between qubits and control ports is described by a circuit model, in which case Z_{ij} may be found analytically – providing analytical predictions for qubit couplings and control line couplings. We will use these expressions in this manner in Chapter 5. As an example, here we use eq. 2.87 to predict the transverse coupling between two capacitively coupled transmons. This is shown in Fig. 2.11, where we have replaced the Josephson junctions with ports as prescribed by the method. The transfer impedance is given by

$$Z_{12}(\omega) = \left.\frac{V_2}{I_1}\right|_{I_2=0} = \frac{1}{i\omega C_{q1}C_{q2}}\frac{C_g}{1+C_g(1/C_{q1}+1/C_{q2})} \approx \frac{C_g}{i\omega C_{q1}C_{q2}} \tag{2.92}$$

where the final approximation is in the limit $C_g \ll C_q$. By reciprocity, $Z_{21} = Z_{12}$, and on inserting into eq. 2.87 we find

$$J_{12} = \frac{1}{4}\sqrt{\frac{\omega_1\omega_2}{L_1L_2}}\frac{C_g}{C_{q1}C_{q2}}[\frac{1}{\omega_1^2}+\frac{1}{\omega_2^2}] \tag{2.93}$$

$$= \frac{1}{4}\sqrt{\frac{\omega_1\omega_2}{C_{q1}C_{q2}}}C_g[\frac{\omega_1}{\omega_2}+\frac{\omega_2}{\omega_1}] \tag{2.94}$$

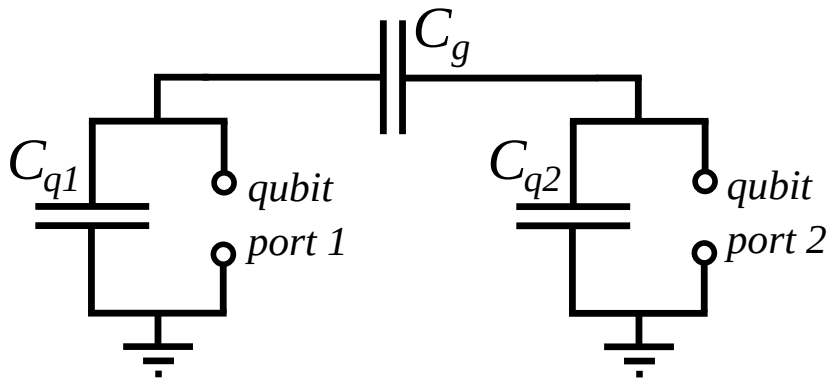

Figure 2.11: **Capacitively coupled transmons:** Effective circuit for two capacitively coupled transmons, with the junctions replaced by ports.

where we used $\omega_1 = 1/\sqrt{L_1 C_{q1}}$, $\omega_2 = 1/\sqrt{L_2 C_{q2}}$ in the second line. Next, we make the substitutions $\omega_1 = \omega - (\Delta/2)$, $\omega_2 = \omega + (\Delta/2)$, to find

$$J_{12} = \frac{1}{4}\sqrt{\frac{\omega_1\omega_2}{C_{q1}C_{q2}}}C_g[2 + (\frac{\Delta}{\omega})^2 + \mathcal{O}(\frac{\Delta}{\omega})^4] \tag{2.95}$$

In the limit $\Delta \ll \omega$ we arrive at

$$J_{12} = \frac{1}{2}\sqrt{\frac{\omega_1\omega_2}{C_{q1}C_{q2}}}C_g \tag{2.96}$$

which is the same transverse coupling between a transmon and a resonator in eq. 2.43, determined by circuit quantisation.

Chapter 3

Scaling Superconducting Circuits

In this chapter, we discuss some of the scaling challenges faced by superconducting circuits for quantum computing, and review some of the approaches being taken to address these challenges. We conclude with a discussion of what we mean by a tileable superconducting device.

3.1 General considerations

Quantum computers are highly sensitive to physical errors, which must be sufficiently small and local in nature to enable fault tolerance to be encoded using quantum error correction codes. Fault tolerance is essential for quantum algorithms which have gate depths corresponding to computation times that far exceed the decoherence timescales and gate error rate of the quantum computing hardware [6]. Considering superconducting circuits, surface codes have emerged as the most promising family of error correction codes [93–97], as they require a 2D array of physical qubits with nearest neighbour couplings – which is a natural configuration for lithographically defined circuits on 2D substrates. Surface codes have physical qubit error thresholds as high as $\sim 1\%$ [94] (or even 5% under biased noise [98]). Smaller physical error rates $\lesssim 1 \times 10^{-3}$ are required for logical qubits with error rates $\lesssim 10^{-14}$, using ~ 1000 physical qubits per logical qubit [94]. Importantly, this assumes that physical errors are uncorrelated. Error correcting codes can in general tolerate correlated errors so long as they obey certain scaling laws. For instance, for a d dimensional physical qubit array, two qubit correlated errors must decay faster than $1/r^d$, where r parametrises the distance between physical qubits [99].

The very low physical errors and high physical qubit overhead that is required for fault tolerant quantum computing makes scaling up quantum computers difficult.

Achieving the required low error rates is challenging enough in small scale devices, and scaling will introduce new error channels and exacerbate existing ones. In contrast, digital computers can make use of voltage thresholding and efficient classical error correction routines to achieve significant robustness against internal imperfections, i.e. gate voltage, crosstalk, broken transistors; and external environment, i.e. temperature, physical vibrations, stray EM fields.

Superconducting circuits have their own particular set of scaling challenges. While their strong coupling to light allows for fast $10\,\text{ns} - 100\,\text{ns}$ quantum gates [12], it makes them particularly vulnerable to decoherence and crosstalk (undesired couplings). Increasing the physical size of the qubits can reduce their sensitivity to interface losses (discussed in Chapter 2), while increasing their spatial separation can help reduce crosstalk. A consequence of this is that while digital computers have successfully scaled by getting smaller, from $\sim 10\,\mu\text{m}$ gate length MOS transistors in 1971 [100] to $\sim 5\,\text{nm}$ today [101], superconducting quantum computers might instead scale by physically getting bigger. Purely for interest's sake, scaling *up* superconducting circuits by an equivalent factor in their linear dimensions would mean going from the $\sim 5\,\text{mm} \times 5\,\text{mm}$ devices of today to $\sim 10\,\text{m} \times 10\,\text{m}$ devices by 2070.

3.2 Challenges to scaling

Here we will discuss some of the scaling challenges that superconducting circuits face in more detail.

3.2.1 Control and cooling

For a circuit with n qubits, it is necessary to be able to generate n independent qubit control waveforms if qubits are to be simultaneously controllable. Similarly, the number of independent waveforms for qubit readout pulse generation must also scale $\propto n$. If the circuit contains flux tunability, the number of independent flux biases must also scale $\propto n$. Currently, waveform signals for superconducting qubit control and resonator readout pulses are typically provided by room temperature rack mounted digital-to-analogue converters (DACs) or arbitrary waveform generators (AWGs) combined with local oscillators (LO), see e.g. Refs. [53, 102, 103]. The DAC/AWG output and LO output are combined in IQ mixers to produce the control signals (see Appendix F for an example control electronics setup). Importantly, DACs, AWGs, LO generators, and IQ mixers all have a significant physical size. For instance, in the

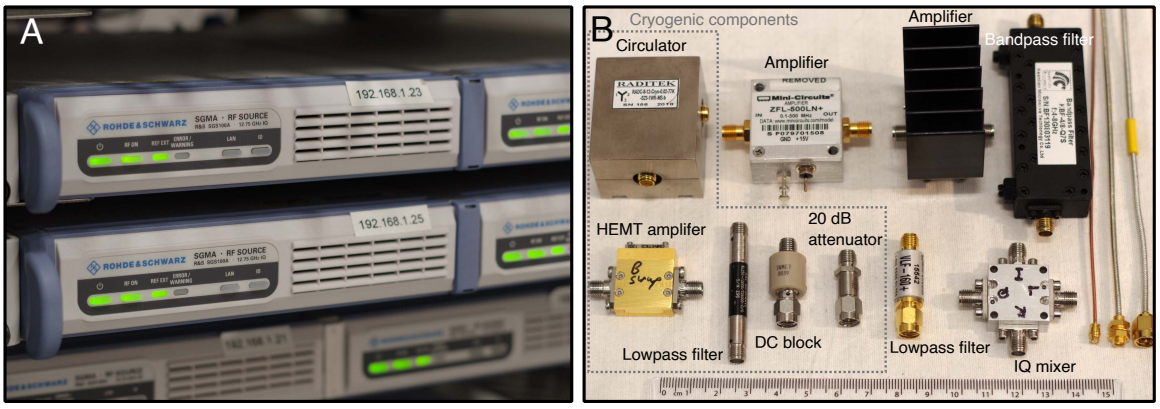

Figure 3.1: **Microwave components:** (**A**) Optical image of rack mounted R&S SGS100A SGMA RF Sources (6 visible). (**B**) Optical image of a selection of some of the microwave components typically used in superconducting circuit control. Components inside the grey dotted line are mounted inside the dilution refrigerator.

experiments in this thesis, the LO signal and IQ mixing for each qubit signal are provided by R&S SGS100A SGMA RF sources, each having 25 cm × 5.25 cm × 40.1 cm dimensions (see fig. 3.1(A)). The instructions for the waveform shapes that are given to the DACs/AWGs are provided by field-programmable gate arrays (FPGAs), which are also used to store the returning readout signal to memory, after digitisation using analogue-to-digital converters (ADCs). These FPGAs and ADCs have similarly large physical dimensions. Significant miniaturisation would be desirable for the control of devices featuring many thousands of qubits.

Another consideration is the size of microwave components inside the dilution refrigerator used to route, filter, and amplify control and readout signals. The qubit readout chain in particular involves bulky microwave circulators, band-pass filters and HEMT amplifiers, see e.g. Refs. [15, 53, 102, 103], all having ∼ cm scale linear dimensions (see Fig. 3.1(B)). Here, significant miniaturisation will be a necessity in order to be able to control devices featuring many thousands of qubits.

Another important consideration is the increased heat load on the dilution refrigerator as the number of control lines increases [57]. First, these control lines directly thermally link the different stages of the dilution refrigerator, introducing a 'passive' heat load on the lower stages. Secondly, additional power will be dissipated in these lines when control signals are sent through them, introducing an 'active' heat load onto the dilution refrigerator stages. Under reasonable assumptions, a modern dilution refrigerator with reasonable cooling power might control a quantum processor

with up to 1000 superconducting qubits while maintaining a mixing chamber temperature $\leq 30\,\mathrm{mK}$ [57]. Interestingly, in this simulated scenario the dominant heat load on the mixing chamber stage was the active load on the control lines [57]. To go beyond this, the active heat load on control lines will need to be reduced, or the cooling power of the dilution refrigerator increased.

3.2.2 Wiring

Small scale superconducting circuit devices have used either: (1) Planar architectures where signals are routed to qubits and planar-resonators using on-chip coplanar waveguides that extend to the edges of the circuit substrate where they are carried off by wirebonds [40, 104]; (2) 3D transmon architectures where signals are routed to qubits and 3D cavity resonators through coaxial cables that aperture couple to the cavity [52]. Both approaches face challenges to scaling. In the case of (1), signals cannot easily be routed off the circuit substrate edge through wirebonds at large scale, simply because the available space for qubits scales like the substrate area and for wirebonds like the substrate perimeter. Packing the wirebonds more densely will result in increased crosstalk between them [104, 105]. Additionally, in order to reach the circuit edge, coplanar waveguides must cover further distances – circumnavigating qubits, resonators, qubit coupling circuitry, and other coplanar waveguides – while also avoiding crosstalk. The wirebonds carry the signals onto PCBs where they are carried along further planar transmission lines to 3D interconnects. These PCB planar transmission lines themselves have crosstalk that will increase with qubit number as they become more tightly packed [104]. In 3D transmon architectures (2), if multiple qubits are placed in the same resonant cavity, they can be difficult to control addressably, meaning signals sent to one qubit might significantly perturb the dynamics of other qubits. If qubits are each placed in separate cavities, the effective qubit pitch can be large $\sim 1\,\mathrm{cm}$, due to the dimensions of readout cavities with fundamental modes at $\sim 10\,\mathrm{GHz}$.

3.2.3 Spurious modes

Superconducting circuits operate in a microwave frequency range $4\,\mathrm{GHz} - 10\,\mathrm{GHz}$ where the characteristic wavelength is approximately $1\,\mathrm{cm} - 10\,\mathrm{cm}$ for relative permittivity ϵ_r between 1 and 10. 3D cavities enclosures and finite sections of planar transmission line can then harbour modes at circuit frequencies when the overall circuit dimensions reach the $1\,\mathrm{cm} - 10\,\mathrm{cm}$ scale. Various circuit features can act as

unintended planar transmission lines [106], such as slotlines formed by divided ground planes [107]. As the circuit gets larger, unless preventative steps are taken, the density of these spurious modes near qubit frequencies will increase, and their effects will become more pronounced.

For instance, assuming for the sake of simplicity that two qubits (labelled 1 and 2) both transverse couple to a single spurious mode (labelled s), an effective direct transverse coupling J appears between them given by [36]

$$J_{12} = \frac{g_{1s}g_{2s}}{2} \frac{(\omega_1 + \omega_2 - 2\omega_s)}{(\omega_1 - \omega_s)(\omega_2 - \omega_s)} \tag{3.1}$$

There are two important points to this expression. First, the coupling diverges when either qubit is resonant with the spurious mode. Second, due to the standing wave nature of spurious modes, g_{1s} and g_{2s} do not in general decrease with the physical separation between qubits 1 and 2 – depending on mode s, they may have a maximum when the qubits are at opposite ends of the circuit. This means that frequency collision with spurious modes can cause large undesired couplings between distant qubits.

Another consequence of coupling to spurious modes is coherent exchange with the spurious mode itself. In the case that a qubit is resonant with a spurious mode, they will hybridise and undergo coherent exchange interactions [108], meaning that an excited qubit's energy will periodically be entirely stored in the spurious mode. In the dispersive limit $\Delta \gg g$, the qubit and spurious mode will not undergo complete exchange, and the maximum population leakage p_s to the spurious mode will scale like $p_s \approx (g/\Delta)^2$ [108].

While these mediated qubit-qubit interactions and direct spurious mode interactions are in principle coherent, in practice it may be hard to operate a large array of qubits that are all coupled to one another through spurious modes with long-range spatial distributions, and which also individually undergo coherent exchange interactions with these modes.

Even if this were possible, spurious modes also introduce relaxation mechanisms for qubits. If a spurious mode has total decay rate κ_s due to both external and internal losses, then coupled qubits will inherit this loss as $\kappa_q \approx (g/\Delta)^2\kappa_s$ for $\Delta \gg g$ [40], and like $\kappa_q \approx g^2/\kappa_s$ on resonance [41].

Spurious modes are thus a significant cause for concern when scaling superconducting circuit devices.

3.2.4 Qubit entanglement and frequency collisions

Quantum computation requires spreading entanglement among qubits through controlled interactions between them. Increased qubit connectivity allows entanglement to be spread throughout the processor faster and allows for more efficient error correction schemes [109–111]. Nearest neighbour couplings are a natural form of interaction to implement in superconducting qubit arrays due to the fact they can be engineered with tailored coupling circuitry lithographically defined in the spaces between neighbouring qubits; see e.g. Refs. [103, 112, 113]. Such coupling circuity is essential to enable entangling gates, however it can present its own scaling challenges. As well as coupling neighbouring qubits, the network formed by coupling circuitry will in general also cause undesirable couplings (crosstalk) between more distant qubits [92]. These couplings, while in principle coherent, may add significant complexity to implementing error correction schemes such as surface code that ideally involve only nearest neighbour couplings.

Additionally, entangling gates impose constraints on the allowed energy level spacings of interacting qubits. Unlike quantum computing platforms that use indistinguishable physical systems as qubits, such as ion traps [8], superconducting qubit systems inevitably feature device-to-device variation in their Hamiltonian. Practically, the dominant source of this variation is the critical current I_0 of Josephson junctions. This means that there is always some probability of 'frequency collisions' between interacting qubits, that will introduce unacceptably large errors to entangling gates [114]. As the number of qubits on a single substrate increases, the probability of any such frequency collisions increases [114], which can result in a subset of defective qubits across the circuit.

3.3 Approaches to scaling

Here, we review some of the ways that the challenges discussed above are being tackled in current experimental superconducting circuit research.

3.3.1 Miniaturised and cryogenic control

An established and effective way of reducing the number of circulators, filters, quantum limited amplifiers and HEMTs inside the dilution refrigerator is to multiplex qubit readout [115, 116]. By reading out k qubits through a single readout control setup, the total number of such setups in an n qubit device is reduced from n to n/k. This multiplexing does not in general have to sacrifice the ability to perform simultaneous qubit readout. For instance, in Ref. [103], a 54 qubit device was demonstrated featuring $k = 6$ qubit readout multiplexing. All qubits could be read out simultaneously, and yet the cryogenic setup required 9 readout control setups rather than 54.

Qubit control can also in principle be multiplexed. In one proposal, fast cryogenic switches at the 4K stage of the dilution refrigerator are used to rapidly route waveforms generated outside of the refrigerator to different qubits [117]. Advantages of this scheme are it reduces the total number of waveform generators, the number of control lines that must travel to the 4K stage, and the active heat load on the mixing chamber stage. This comes at the cost of sacrificing simultaneous qubit control.

Another promising proposal to massively multiplex qubit control signals and readout input signals is to use a 'photonic link' to carry signals between the room temperature generators and the mixing chamber of the dilution refrigerator [118]. Here, room-temperature electro-optical modulators are used to convert the microwave control signals to optical frequency signals $\sim 100\,\mathrm{THz}$. These optical frequency signals are then routed to the mixing chamber stage through optical fibres rather than coaxial cables, where the microwave signals are recovered using photodiodes, and sent to the superconducting circuit device. Due to the large bandwidth at optical frequencies, many control signals can be carried along a single optical fibre, greatly reducing the passive heat load on the dilution refrigerator and taking up far less space than the many coaxial cables that would otherwise be required. Recently, such a control scheme using a photonic link was demonstrated in a single transmon qubit device [118].

All these proposals still require circulators, filters, and amplifiers inside the dilution refrigerator as part of each readout control setup. Typically, the ferrite circulators are the largest elements, and smaller circulator designs will likely be necessary in devices with many thousands of qubits. Cryogenic on-chip circulators using Josephson junctions have been demonstrated that could be far more compact [119, 120], at the

cost of requiring active pumping with microwave drives and/or flux control.

Alongside multiplexing and reducing the size of microwave components inside the dilution refrigerator, it may still be necessary to increase the effective size and cooling power of the dilution refrigerator itself. This could be done by simply making larger dilution refrigerators, potentially featuring multiple dilution units in order to increase the cooling power; or by cryogenically linking different dilution refrigerators which contain separate superconducting circuit devices coupled through the link, as was recently demonstrated in Ref. [121].

3.3.2 3D wiring

In order to avoid the wiring issues described in the previous section, one approach is to retain on-chip wiring and route signals off the substrate away from its edge. This can be achieved with vertical interconnects that galvanically connect to contact pads on the qubit substrate [122, 123]: either by the use of through silicon vias (TSVs) that carry signals through the qubit substrate or interposer substrates [124–126]; or through indium bump bonds that physically contact the qubit substrate [103, 112, 127]. Examples of these methods of 3D integration are shown in Fig. 3.2.

We comment that all of these schemes involve some form of inductive connection between out of plane wiring and planar wiring on the qubit substrate, and so are vulnerable to substrate heating due to contact resistance [128], and will fail if physical contact is broken. Additionally, we note that the schemes shown in Fig. 3.2(D) & (E) still use edge connected wirebonds at some stage - and so are still affected by the area to perimeter scaling considerations discussed previously.

3.3.3 Spurious mode suppression

In order to avoid slotline modes appearing due to finite sections of slotline transmission line, low inductance superconducting airbridges can be used to inductively shunt divided ground planes. This will raise the cutoff frequency of the slotline transmission lines, making transmission evanescent at qubit and resonator frequencies and preventing the emergence of low frequency slotline modes [107]. Alternatively, divided ground planes can be inductively shunted using TSVs that connect to a common ground on the reverse side of the substrate. These TSVs can also be used to suppress spurious cavity modes, so long as the TSVs inductively connect to both sides of the cavity (this

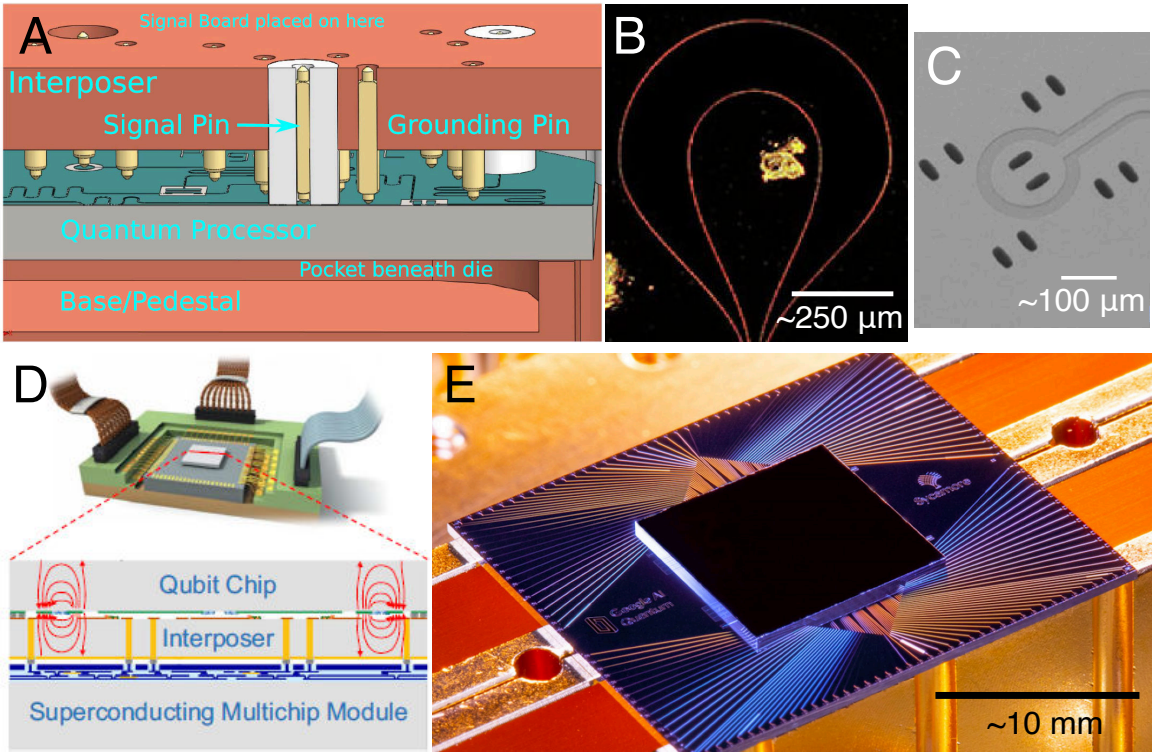

Figure 3.2: **3D wiring review:** (**A**) Schematic of a 3D 'pogo-pin' interconnect contacting CPW wiring on the qubit substrate [122]. (**B**) Microscope image of 3D interconnect contact pad, showing the point of contact of a 'quantum-socket' 3D interconnect [123] (approximate scale bar added). (**C**) SEM image of CPW that is inductively connected to circuitry on the reverse side of the substrate through superconducting TSVs [124] (approximate scale bar added). (**D**) Concept of packaging and wiring for a superconducting quantum processor, using an interposer substrate with TSVs and indium bump bonds to route signals to the qubit substrate [124]. (**E**) Optical image of a superconducting qubit processor (black) with 54 qubits and 88 couplers, which is indium bump bonded to a larger wiring substrate [103] (approximate scale bar added).

is the topic of Chapter 5). Examples of these methods of spurious mode suppression are shown in Fig. 3.3.

Spurious modes can also be mitigated by taking a non-monolithic approach, dividing the device into sub-systems, each consisting of circuits housed in separate enclosures having $\sim$ cm scale dimensions [126, 130]. In one proposal, these devices are realised by a multi-layer stack of etched silicon substrates, which are bonded together using indium [126]. Extremely high quality ($Q > 300 \times 10^6$) 'micromachined' cavities have been demonstrated with this technique [131], but high coherence qubits inside such an architecture have yet to be demonstrated [132].

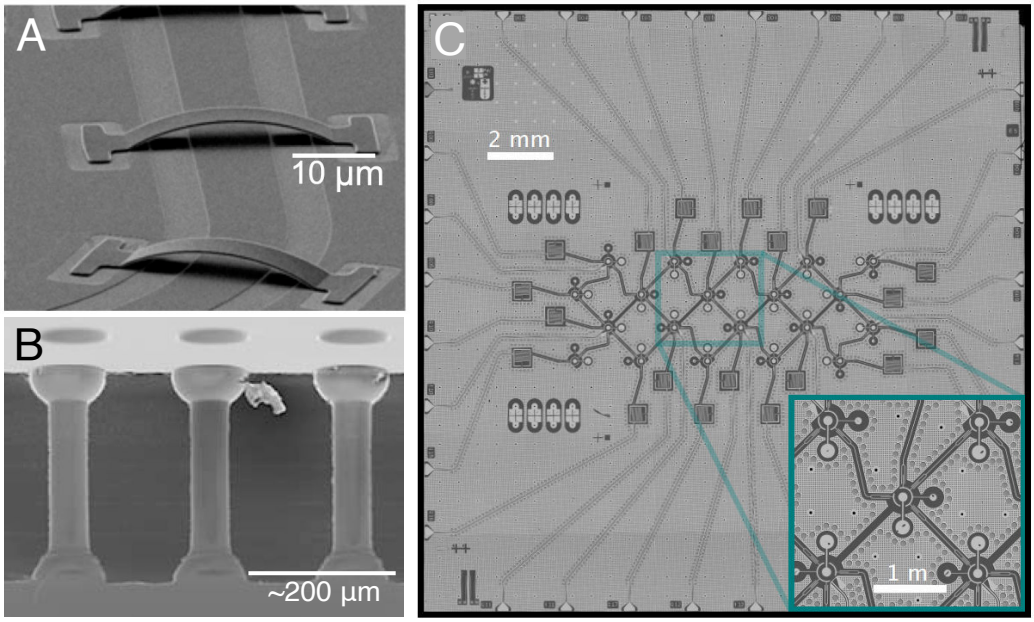

Figure 3.3: **Spurious mode suppression review:** (**A**) SEM image of airbridges used to prevent spurious slotline modes [107]. (**B**) SEM image of superconducting TSVs in silicon [129] (approximate scale bar added). (**C**) Optical image of superconducting qubit processor with 19 qubits, featuring an array of TSVs (visible in inset) to reduce crosstalk in the circuit [113].

We comment that a possible disadvantage in using superconducting airbridges and superconducting TSVs is that they necessitate their own multistage fabrication processes involving lithography, evaporation/sputtering, and etching steps. These can present opportunities for contamination of the circuit substrate, which may increase dielectric relaxation rates.

3.3.4 Frequency tunability and dynamical decoupling

One approach to reduce the crosstalk mediated by qubit coupling circuitry is to introduce frequency tunable couplers and/or frequency tunable qubits to engineer couplings with a large on-off ratio and/or suppressed ZZ crosstalk [103, 133–137], where all of these schemes make use of flux tunable SQUIDs. Another approach is to use fixed frequency qubits with fixed capacitive couplings and to activate gates with microwave drives [102, 138] (a notable example being the cross-resonance gate [138–140]), and to mitigate the resulting crosstalk between qubits through dynamical decoupling schemes [112, 141]. An advantage of the former approach is the ability to switch off interactions between qubits when not performing two qubit gates, in the ideal case eliminating crosstalk mediated by coupling circuitry. This comes at the

significant cost of increased numbers of control lines to the device, increased control electronics overhead, and sensitivity to flux noise. The fixed frequency approach has the advantage of not requiring flux control and the associated control lines and electronics, at the cost of relying on dynamical decoupling schemes to suppress errors related to coupling circuitry crosstalk. These schemes may place constraints on the ability to perform simultaneous two-qubit gates on different pairs of qubits in close proximity, see e.g. Ref. [112].

Introducing frequency tunability to qubits also significantly mitigates the issue of frequency collisions, since variation in the critical current of junctions can be compensated for with DC flux offsets [103]. In order to reduce the probability of frequency collisions when using fixed frequency circuits, it is necessary to improve the precision with which the critical current of Josephson junctions can be set by the experimenter. Improvements to waferscale junction fabrication have recently demonstrated $\sim 2\%$ [142] relative standard deviations in the critical current of nominally identical junctions fabricated across 4 inch silicon wafers. This should translate to $\sim 1\%$ standard deviation in transmon qubit transition frequencies across waferscale devices. The use of post fabrication laser-annealing to selectively 'age' individual Josephson junctions has been used to achieve even lower transmon frequency standard deviations of 0.25% [114]. To further reduce the likelihood of frequency collisions, qubits can be arranged in layouts with reduced connectivity compared to the nearest-neighbour square array [110, 114]. This comes at the cost of less efficient topological error correction protocols than the surface code [110].

3.4 Discussion

In this chapter, we have attempted to give an brief overview of some of the main scaling issues faced by superconducting circuits and some of the approaches being taken to address them. In the following chapters we will aim to demonstrate a device that addresses in particular two of these challenges: (1) the device-level wiring limitations and (2) the emergence of spurious modes. The goal is to demonstrate a device that can scale to large 2D arrays of well-characterised, individually controllable and measurable qubits, by tiling a unit cell in a simple copy-paste fashion. As discussed in the Introduction, we call this kind of device design tileable.

Chapter 4

The Coaxmon Architecture

In this chapter, we provide an overview of a superconducting circuit architecture being pursued in our lab. We call this the 'coaxmon architecture', as it uses transmon qubits that are individually addressed by stripped back coaxial cables. This architecture is designed to be a tileable architecture for making 2D transmon qubit arrays with nearest neighbour couplings. Qubits were first demonstrated in the architecture in a single qubit device [143], and then in a four qubit device [144]. Entangling gates between two directly capacitively coupled qubits in a coaxmon architecture have been demonstrated using the cross-resonance gate [140]. Here, we will review the architecture, and make some new contributions to understanding its behaviour with simulations and analytical models.

4.1 Overview

Fig. 4.1(A) shows a schematic of a unit cell, featuring a transmon qubit (blue), a readout resonator (green), a qubit control line (red), and a resonator control line (yellow). This is a colour code we maintain throughout this thesis. The four components are concentrically aligned along the $\hat{z}$ axis, and excepting the Josephson junctions and spiral inductors have cylindrical symmetry. The resonator used for dispersive qubit readout is fabricated on the opposite side of the circuit substrate to the qubit, which we refer to as 'reverse-side readout'. The control lines never contact the circuit substrate, which we refer to as 'off-chip wiring'. There are no ground planes on either side of the circuit substrate, and instead the enclosure acts as the circuit ground. The qubit and resonator are both floating, i.e. have no inductive links to ground.

The key motivators for this architecture are as follows: (1) Each concentrically aligned set of qubit, readout resonator and control wiring forms a compact unit cell containing

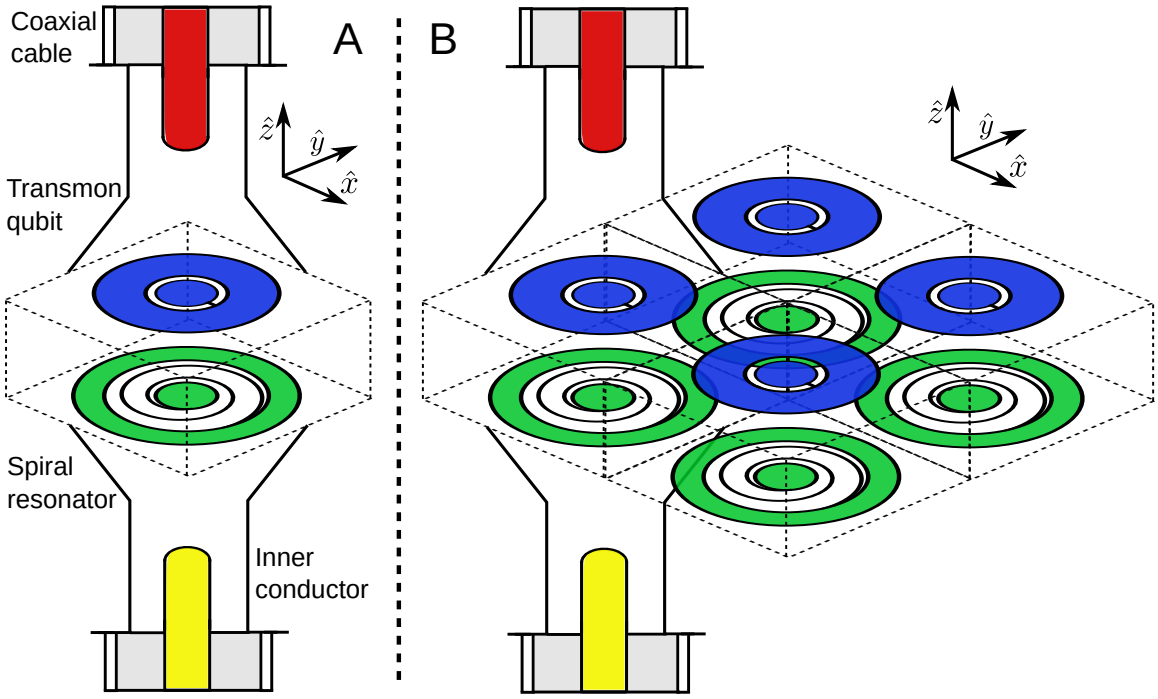

Figure 4.1: **Coaxmon architecture:** (**A**) Schematic of single qubit unit cell. (**B**) 2D qubit arrays can be formed by tiling the unit cell.

a single qubit with addressable control and readout functionality. Due to the 3D nature of the wiring, this unit cell can be repeatedly copied and pasted in the $\hat{x}-\hat{y}$ plane to form large arrays of individually controllable and measurable qubits, as shown in Fig. 4.1(B). (2) The off-chip wiring removes the need to galvanically connect control wiring to the substrate, which eliminates contact resistance and associated substrate heating [128]. It also removes all on-chip wiring, such as coplanar-waveguides, which frees up space on the qubit-side of the substrate and eliminates a source of parasitic couplings. (3) The reverse-side readout unlocks further space on the qubit-side of the substrate. (4) The lack of airbridges, wirebonds, bump-bonds, through silicon vias, epoxy, or fibreglass PCB's simplifies the fabrication process and device packaging, and removes possible dielectric loss channels for superconducting qubits.

We now discuss each element of the architecture in more detail.

4.2 Concentric qubit

The architecture features transmon qubits with pads consisting of a concentric circle and ring, joined by a thin bridge containing a Josephson junction. This is shown in Fig. 4.2(A), where the island dimensions are labelled. This qubit design has been

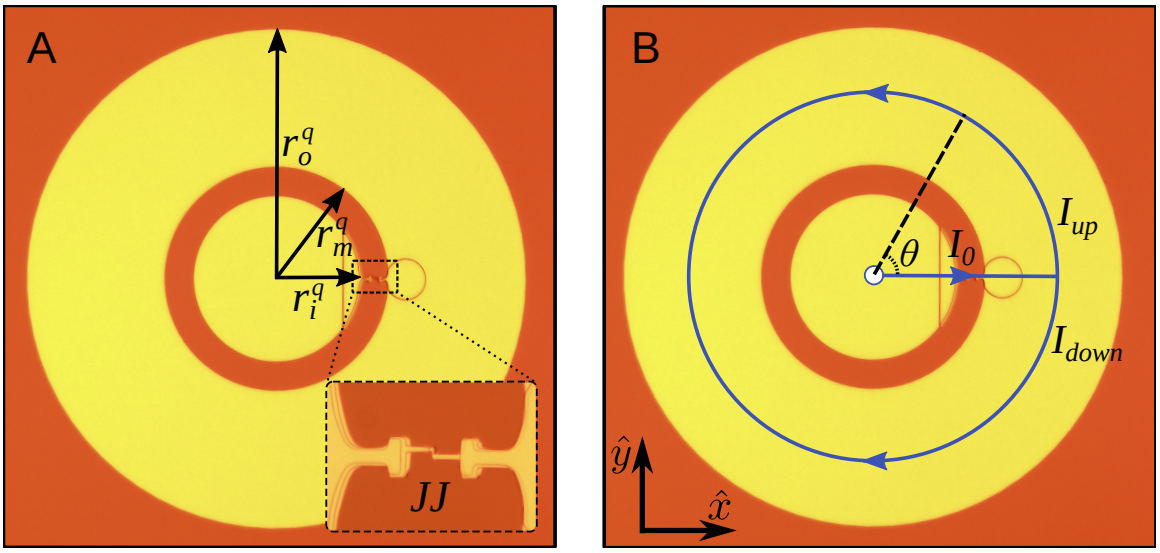

Figure 4.2: **Concentric transmon qubit:** Optical image of a concentric transmon qubit with: (**A**) Island dimensions and an inset showing the bridge containing the Josephson junction. (**B**) An idealised model of the current flow overlaid.

used in Ref. [145], where the qubit frequency was flux tunable. We adopt the name 'concentric qubit' that was used in this reference. We use relatively large qubits, with a typical outer radius $r_o^q \sim 0.5\,\text{mm}$, to reduce their sensitivity to interface loss (see Chapter 2). This size matches well to the use of UT47 coaxial cables (having 0.6 mm outer radius) for the qubit and resonator off-chip control wiring.

4.2.1 Suppressed dipole moment

In Chapter 2, following Ref. [14], we modelled the radiative relaxation time of a dipole transmon in free space by treating it as a classical antenna and calculating the power radiated into the far field. Using the same treatment, we now show that the relaxation time of the concentric transmon qubit in free space is greatly enhanced. The current flow in an excited concentric transmon is idealised as shown in Fig. 4.2(B). Here, a current $I_0 e^{i\omega_q t}$ flows between the qubit islands through the joining bridge, and a current I_{up} and I_{down} flows through the outer island. We approximate the central island as a point. Assuming that the charge in the outer island is uniformly distributed, I_{up} and I_{down} are given by

$$\boldsymbol{I}_{up}(\theta) = \frac{I_0}{2}(1 - \frac{\theta}{\pi})\hat{\boldsymbol{\theta}} \tag{4.1}$$

$$\boldsymbol{I}_{down}(\theta) = -\frac{I_0}{2}(1 - \frac{(2\pi - \theta)}{\pi})\hat{\boldsymbol{\theta}} \tag{4.2}$$

Similar to the dipole transmon treatment, we again start from the vector potential

$$\boldsymbol{A}(\boldsymbol{r},t) = \frac{u_0}{4\pi}\int \frac{[\boldsymbol{j}]}{|\boldsymbol{r}-\boldsymbol{r'}|}d^3\boldsymbol{r'} \tag{4.3}$$

We make the same approximations that in the far field $\boldsymbol{r}-\boldsymbol{r'} \rightarrow \boldsymbol{r}$, and that for antennas much smaller than the wavelength $[\boldsymbol{j}] \rightarrow \boldsymbol{j}$. We consider the components of $\boldsymbol{A}$ along $\hat{\boldsymbol{x}}$ and $\hat{\boldsymbol{y}}$ separately. From our simple model for the current flow, the component along $\hat{\boldsymbol{x}}$ becomes

$$A_x(r,t) = \frac{u_0}{4\pi r}[\int_0^{r_0} I_0 dx - r_0\int_0^{\pi} I_0(1-\frac{\theta}{\pi})\sin\theta d\theta] \tag{4.4}$$

The first term is due to current through the bridge, and the second term is due to current through the outer island. Both terms evaluate as the vector potential of a Hertzian dipole of length r_0 oriented along $\hat{\boldsymbol{x}}$, but with opposite phase, and so the total vector potential along $\hat{\boldsymbol{x}}$ is 0. In other words, in the far field, the vector potential due to the current through the bridge has cancelled with the vector potential due to current through the outer island. We next consider the component along $\hat{\boldsymbol{y}}$, given by

$$A_y(r,t) = \frac{u_0}{4\pi r}[r_0\int_0^{\pi} \frac{I_0}{2}(1-\frac{\theta}{\pi})\cos\theta d\theta - r_0\int_0^{\pi} \frac{I_0}{2}(1-\frac{\theta}{\pi})\cos\theta d\theta] \tag{4.5}$$

The first term is due to the current I_{up} while the second is due to the current I_{down}. Both of these terms evaluate to be the vector potential for Hertzian dipoles of length r_0/π oriented along $\hat{\boldsymbol{y}}$, but with opposite phase, and so similarly the total vector potential along $\hat{\boldsymbol{y}}$ is 0. The vector potential is therefore 0 everywhere in the far field and so the concentric transmon qubit has no dipole moment (or multipole moments) and will not radiate at all in this approximation. This perfect cancellation would not occur if we used the proper retarded current density $[\boldsymbol{j}]$ instead of the approximation $\boldsymbol{j}$. Nevertheless, the results demonstrate that concentric qubits are poor antennas with suppressed radiative decay in the vacuum.

4.3 Spiral resonator

One of the key distinguishing features of the coaxmon architecture is the use of reverse-side resonators. These resonators have a similar footprint to the concentric qubits, as shown in fig 4.3(A). A concentric circle and ring form the two islands, which are joined by a thin spiral. We call these spiral resonators. The capacitance between the pads and the inductance of the spiral define the fundamental mode frequency

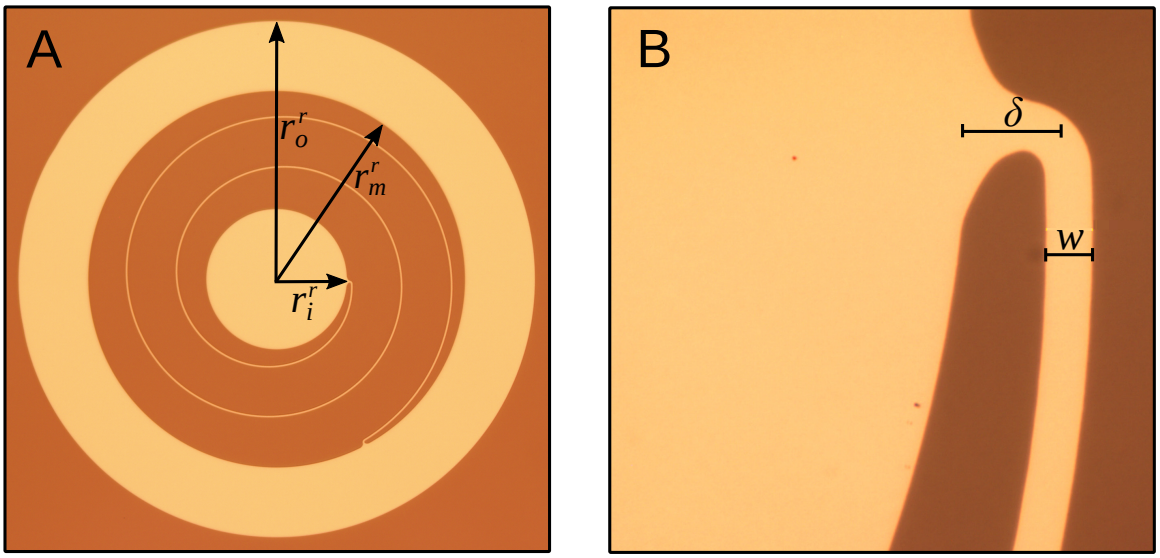

Figure 4.3: **Spiral resonator:** Optical images of a spiral resonator. (**A**) Island dimensions overlaid. (**B**) A zoomed in view of the smooth join between the spiral (width w) and the inner island.

$\omega_r = 1/\sqrt{LC}$. The inductance can be estimated as the self inductance of a flat wire length l, width w, and thickness t, approximately given by [106]

$$L = 2l(0.5 + \ln(\frac{2l}{w+t}) + 0.2235(\frac{w+t}{l})) \times 10^{-7} \text{ H} \tag{4.6}$$

where l, w, t are in meters. We use spiral resonators with $w \sim 5\,\mu\text{m}$, $t \sim 100\,\text{nm}$, and $l \sim 4\,\text{mm}$, resulting in $L \sim 6\,\text{nH}$. For simplicity, we use Archimedean spirals defined in polar coordinates by

$$r = a\theta \tag{4.7}$$

Given the spiral coefficient a, and the boundary angles θ_{start} and θ_{stop}, the arc length of the spiral is given by

$$l(\theta_{start}, \theta_{stop}) = l(\theta_{stop}) - l(\theta_{start}) \tag{4.8}$$

$$l(\theta) = \frac{1}{2}a[\theta\sqrt{1+\theta^2} + \ln(\theta + \sqrt{1+\theta^2})] \tag{4.9}$$

For the spiral resonators in this thesis, $\theta_{start} = (r_i^r + \delta)/a$, $\theta_{stop} = (r_m^r - \delta)/a$, where δ is a small $\sim 10\,\mu\text{m}$ separation. Practically, this slight separation of the spirals from the main islands is to prevent sharp edges at the intersection, and they are instead joined with smooth transition features as shown in Fig. 4.3(B).

4.3.1 Higher modes

The spiral resonators will have higher modes, and we briefly consider the first two here. An HFSS eigenmode simulation of a spiral resonator with fundamental frequency

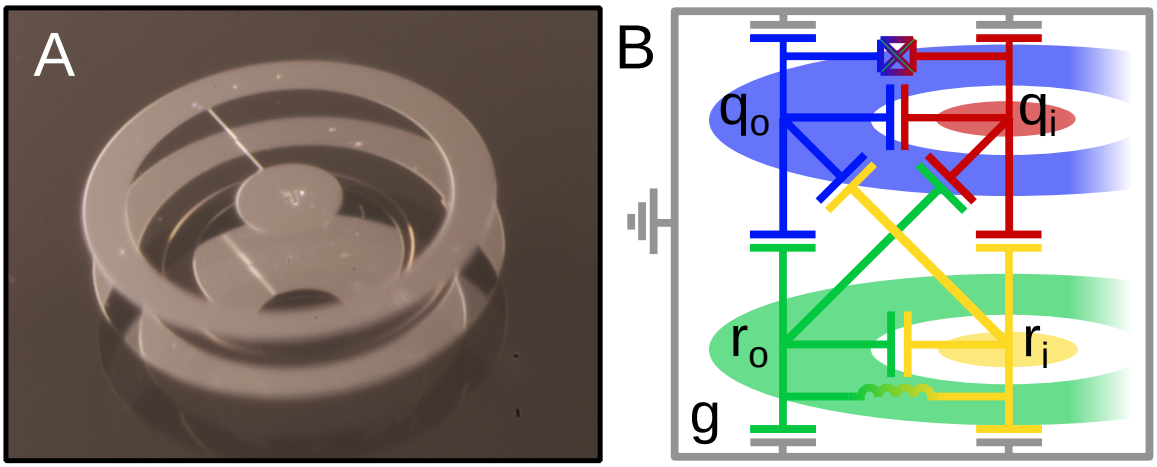

Figure 4.4: **Qubit resonator interaction:** (**A**) Optical image of a concentric qubit and reverse-side resonator, having 1 mm diameter, fabricated on sapphire. Image used with permission from [144]. (**B**) Circuit diagram of the through substrate interaction between the qubit and resonator.

$f_0^r = 9.1\,\text{GHz}$ finds the next two modes at $f_1^r = 21.9\,\text{GHz}$ and $f_2^r = 35.7\,\text{GHz}$. In the f_1^r mode, the charge in the two main pads oscillate in phase, and an antinode appears in the middle of the spiral. This charge configuration will not couple effectively to the concentric qubit, and we conclude that higher modes can be safely neglected when considering the qubit-resonator interaction.

4.4 Qubit-resonator coupling

The concentric qubit and reverse side resonator couple through the circuit substrate. Due to the relatively large qubit and spiral resonator islands, and the large permittivity of silicon and sapphire substrates $\epsilon_r \sim 10$, the coupling is dominantly capacitive. Very large transverse couplings of $g/2\pi = 460\,\text{MHz}$ ($g/\omega_q = 0.06$) have been measured in a coaxmon device with the pad geometry shown in 4.4(A) [143]. Such large couplings are possible due to the large substrate permittivity. The coupling strength is determined by the capacitance network shown in Fig. 4.4(B). This circuit contains 10 capacitances, a linear inductance, and the non-linear Josephson junction (JJ). We can perform circuit quantisation to find the transverse coupling g between the qubit and resonator. Here g is defined as in eq. 2.40: $\hat{H}_{int} = \hbar g(\hat{b}^\dagger\hat{a} + \hat{b}\hat{a}^\dagger)$. We perform the circuit quantisation using Mathematica [146]. The solution for g can be expressed $g = (1/2)\sqrt{(\omega_q\omega_r)/(C_qC_r)}C_g$, where C_q and C_r have complicated forms but are always greater than 0, and C_g also has a complicated form but can be factored $C_g = \alpha\beta$

where β is also always greater than zero and α is given by

$$\alpha = [C_{Q_iR_o}C_{Q_oR_i}(C_{GQ_i}+C_{GQ_o}+C_{GR_i}+C_{GR_o})+C_{GQ_o}C_{GR_i}C_{Q_iR_o}+C_{GQ_i}C_{GR_o}C_{Q_oR_i}]$$
$$-[C_{Q_iR_i}C_{Q_oR_o}(C_{GQ_i}+C_{GQ_o}+C_{GR_i}+C_{GR_o})+C_{GQ_o}C_{GR_o}C_{Q_iR_i}+C_{GQ_i}C_{GR_i}C_{Q_oR_o}] \tag{4.10}$$

This is formed of a positive term and a negative term, which swap places on exchanging the nodes $r_i \leftrightarrow r_o$ or $q_i \leftrightarrow q_o$. The important point is that g can be positive, negative, and also 0. This means that although very large values such as $g/2\pi = 460\,\text{MHz}$ are possible due to the capacitive interaction through the $\epsilon_r \sim 10$ substrates, small values of g are also accessible due to the cancellation between direct and diagonal capacitances.

In the case one of the capacitances to ground dominates, the condition for cancellation takes a simpler form. For instance, if $C_{GR_o} \to \infty$, C_g can still be factored as before, where now

$$\alpha = C'_{GQ_o}C_{Q_iR_i} - C'_{GQ_i}C_{Q_oR_i} \tag{4.11}$$

Here, C'_{GQ_o} and C'_{GQ_i} are the adjusted capacitances of the qubit islands to ground

$$C'_{GQ_o} = C_{GQ_o} + C_{Q_oR_o} \tag{4.12}$$
$$C'_{GQ_i} = C_{GQ_i} + C_{Q_iR_o} \tag{4.13}$$

In this case, the condition for $g = 0$ is simply $C_{Q_oR_i}/C'_{GQ_o} = C_{Q_iR_i}/C'_{GQ_i}$.

4.5 Off-chip control wiring

The coaxmon architecture uses stripped back coaxial cables to address qubits and resonators, as shown in Fig. 4.5. A coaxial cable with characteristic impedance $Z_{0,1}$ is aligned concentrically to each qubit and resonator, along the $\hat{z}$ axis. The inner conductor of the cable extends out a distance d_2 into a cylindrical hole in the enclosure, forming a coaxial waveguide with characteristic impedance $Z_{0,2}$. The inner conductor then terminates, leaving a d_{pin} length section of cylindrical waveguide between the inner conductor and a qubit/resonator on the circuit substrate. Following Ref. [18], cylindrical symmetry means the TM_{0m} modes of the cylindrical waveguide will be dominantly excited. These modes have cutoff frequencies given by [18, 19]

$$\beta = \sqrt{k^2 - (\frac{p_{0m}}{r_2})^2} \tag{4.14}$$

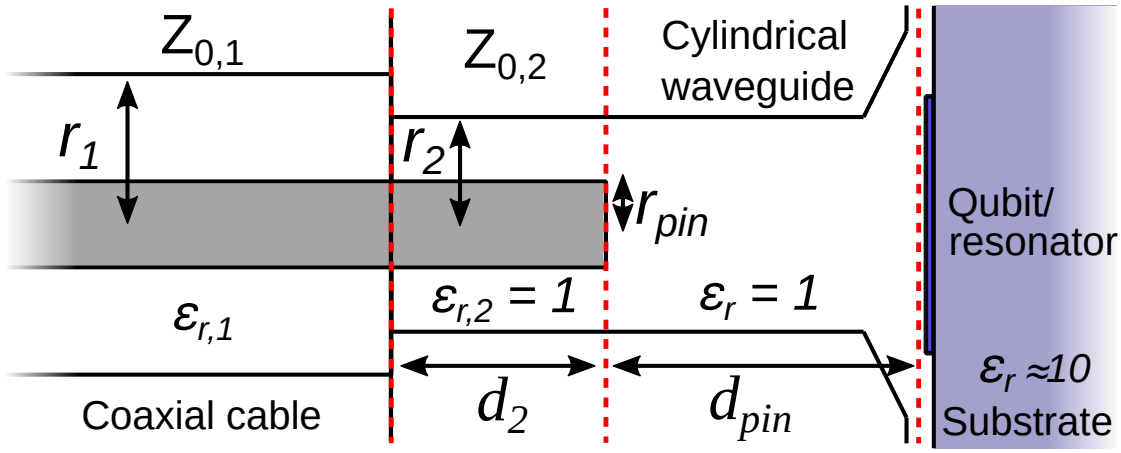

Figure 4.5: **Off-chip control line coupling:** Cross-section of the control setup used to address qubits and resonators in the coaxmon architecture. The inner conductor of a coaxial cable with characteristic impedance $Z_{0,1}$ extends into a cylindrical hole in the device enclosure, that leads to a qubit/resonator.

Here, r_2 is the radius of the waveguide and p_{0m} is the mth solution to the Bessel function $J_0(x) = 0$. The first three solutions are $x \approx 2.40, 5.52, 8.65$. p_{01} has the lowest cutoff frequency and so TM_{01} will be the dominant mode. For 10 GHz signals and $\epsilon_r = 1$: $k \approx 200\,\mathrm{m}^{-1}$. On the other hand, in our off-chip control scheme $r_2 \sim 0.5\,\mathrm{mm}$ and so $p_{01}/r \approx 5000\,\mathrm{m}^{-1}$. In this case, β is to a good approximation frequency independent, and given by $\beta \approx ip_{01}/r$. Hence, signals will be evanescent through the cylindrical waveguide and the coupling strength ε of qubits and resonators to their control lines will scale like

$$\varepsilon \propto e^{-d_{pin}/\delta_{guide}} \tag{4.15}$$

$$\delta_{guide} = \frac{r_2}{p_{01}} \approx \frac{r_2}{2.40} \tag{4.16}$$

It is desirable that qubits and resonators all have nominally the same coupling to their control lines, and δ_{guide} sets the relevant length scale for misalignment tolerance on the inner conductors. For the device characterised in Chapter 7, $r_2 = 0.35\,\mathrm{mm}$ and so $\delta_{guide} \approx 150\,\mu\mathrm{m}$. In this case, even $\sim 50\,\mu\mathrm{m}$ variation in d_{pin} will result in significant variation in the coupling strengths, highlighting the importance of good alignment of the off-chip wiring.

Another aspect of the off-chip wiring to consider is the impedance matching between the coaxial cable, having impedance $Z_{0,1}$, and the coaxial waveguide formed between the protruding inner conductor and the cylindrical hole in the enclosure, having impedance $Z_{0,2}$. The reason for extending the inner conductor out a distance

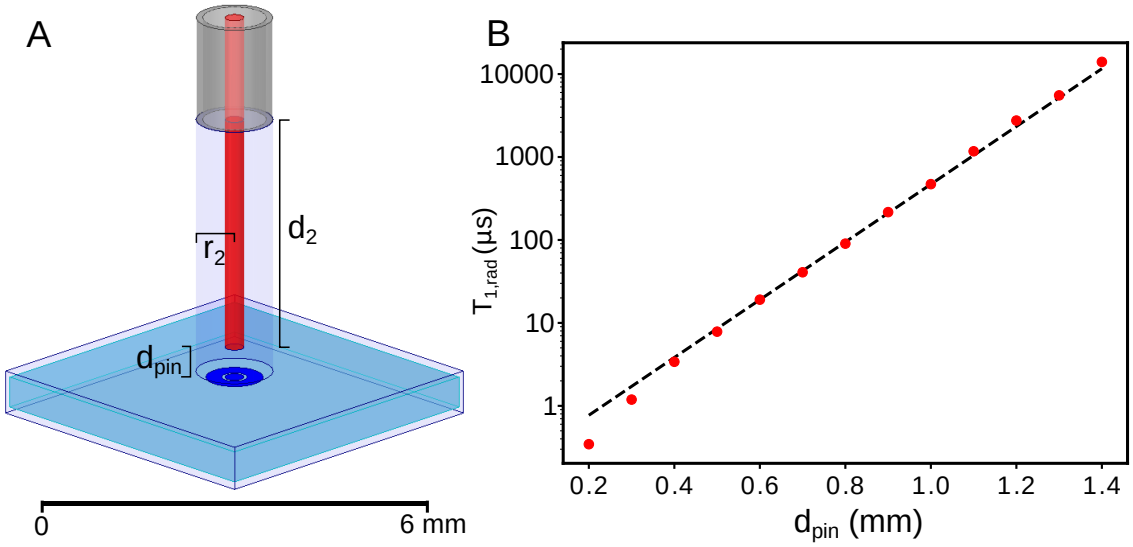

Figure 4.6: **Radiatively limited relaxation time:** (**A**) HFSS model for simulating radiative loss of the qubit through its control line. A 50 Ω termination is defined at the end of the coaxial cable. $r_{pin} = 0.15\,\text{mm}$, $r_1 = 0.5\,\text{mm}$, $\epsilon_{r,1} = 2.1$, $r_2 = 0.6\,\text{mm}$ and $d_2 = 4.2\,\text{mm}$. (**B**) Simulated radiative lifetime $T_{1,rad}$ (using method [48] described in Chapter 2) for qubit frequency 5.2 GHz, along with fit to eq. 4.18.

d_2 is to retract the PTFE dielectric in the coaxial cable away from the qubits, independent of d_{pin}. The characteristic impedance of the dominant mode of a coaxial waveguide is given by [19]

$$Z_0 = \frac{1}{2\pi}\sqrt{\frac{\mu}{\epsilon}}\ln(\frac{r_{outer}}{r_{inner}}) \tag{4.17}$$

We use UT47 coaxial cables with $Z_{0,1} = 50\,\Omega$ and $r_{pin} = 0.15\,\text{mm}$, and so the condition for impedance matching such that $Z_{0,2} = Z_{0,1}$ is $r_2 \approx 0.35\,\text{mm}$, considering that the cylindrical hole contains no dielectric during measurement ($\epsilon_{r,2} = 1$). A large impedance mismatch may result in distorted qubit control pulses due to significant reflections back at the device at the transition $Z_{0,2} \to Z_{0,1}$.

4.5.1 Decoherence contributions

The radiatively limited relaxation time of the qubits will clearly depend on their coupling to the off-chip control wiring. The radiative relaxation time can be generally expressed $T_1 = (\text{Qubit energy})/(\text{Power radiated})$. The power an excited qubit sends into its control line satisfies $P_{rad} \propto 1/\varepsilon^2$. Hence, from eq. 4.15 it follows that

$$T_{1,rad} \propto e^{2d_{pin}/\delta_{guide}} \tag{4.18}$$

Fig. 4.6 shows simulations of the radiatively limited lifetime for a transmon qubit in a coaxmon architecture, varying d_{pin}. For the purpose of illustrating the dependence of

radiative T_1 on d_{pin}, the reverse-side resonator and resonator control line are excluded from the model. The loss tangent of the coaxial cable dielectric is also set to 0. The fit to eq. 4.18 is shown with $\delta_{guide} = 0.254\,\text{mm}$ found from eq. 4.16 using $r_2 = 0.6\,\text{mm}$, which is the value used in the simulation model. The fit is good for $d_{pin} > 0.5\,\text{mm}$, below which the radiative lifetime decreases faster than predicted. We expect this is because the simple waveguide coupling model breaks down at such short separations as direct capacitive coupling to the inner conductor becomes significant. In this particular model, values of $d_{pin} > 1.1\,\text{mm}$ will result in $T_{1,rad} > 1\,\text{ms}$, significantly larger than state-of-the-art transmon qubit relaxation times.

We briefly consider some of the other possible relaxation mechanisms the off-chip wiring presents to qubits and resonators. Any field participation of the qubit inside the PTFE dielectric of the coaxial cables may contribute to dielectric losses in the qubit. However, we retract this dielectric $\sim 5\,\text{mm}$ from the qubits, where the near-field of the excited qubits will be negligible. Hence we conclude that this loss channel is negligible. Current induced in the inner conductors of the coaxial cables by an excited qubit or resonator will present another internal loss channel. We do not quantitatively predict this conductor loss for the coaxmon architecture, but note that in this thesis, we have used coaxial cables with silver plated copper inner conductors which are not superconducting at $\sim 10\,\text{mK}$. Using a superconducting material such as NiTb would minimise this loss channel.

Finally, the extended inner conductors of the coaxial cables are not anchored at the device facing end and may vibrate in response to physical vibrations in the dilution refrigerator. Such movement will result in variation in the external quality factor of qubits and resonators, and therefore affect their loaded resonance frequencies. This will result in a dephasing mechanism on qubits. Here, we briefly consider the sensitivity of qubit frequency to variations δx in d_{pin}. Treating the qubit as a harmonic oscillator, using results in Ref. [147], the change to its frequency due to the external coupling to the qubit control line can be expressed as

$$\omega_L - \omega_0 \approx -(\frac{\kappa_{ext}}{4C_q Z_0})^{\frac{1}{2}} \tag{4.19}$$

where κ_{ext} is the external decay rate of the qubit through its control line (characteristic impedance Z_0), and C_q is the effective shunting capacitance of the qubit. Here we have assumed $C_k^q \ll 1/(\omega_q Z_0)$, where C_k^q is the effective external coupling capacitance

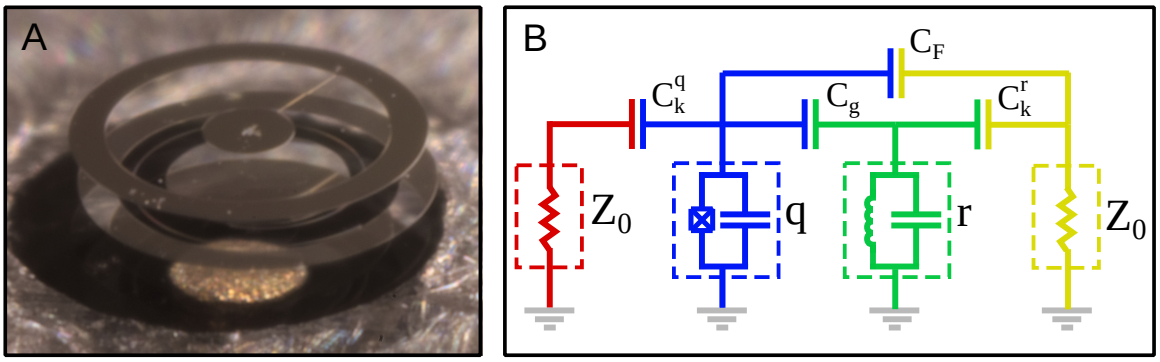

Figure 4.7: **Intrinsic Purcell filtering:** (**A**) Optical image of a qubit and reverse-side resonator with 1 mm diameter, fabricated on sapphire and mounted in an enclosure for measurement. The inner conductor of the resonator control line is visible. Image used with permission from [144]. (**B**) Toy circuit model of qubit radiative loss, incorporating Purcell filtering effect.

of the qubit as defined in Fig. 4.7(B). Using eq. 4.18 and $\kappa_{ext} = 1/T_{1,rad}$, the change in qubit frequency due to a change δx in d_{pin} is then given by

$$\delta\omega_q = \left(\frac{\kappa_{ext}}{4C_q Z_0}\right)^{\frac{1}{2}} \frac{1}{\delta_{guide}} \delta x \tag{4.20}$$

For reasonable values $\kappa_{ext}/2\pi \approx 100\,\text{Hz}$, $C_q = 100\,\text{fF}$, $\delta_{guide} = 150\,\mu\text{m}$ and $Z_0 = 50\,\Omega$; we find $\delta f_q/\delta x \approx 6\,\text{kHz}/\mu\text{m}$.

The resonator will similarly acquire frequency noise due to vibrations in the inner conductor of its control line. Assuming reasonable values $\kappa_{ext}/2\pi \approx 2\,\text{MHz}$, $C_r = 100\,\text{fF}$, $\delta_{guide} = 150\,\mu\text{m}$ and $Z_0 = 50\,\Omega$; we find $\delta f_r/\delta x \approx 800\,\text{kHz}/\mu\text{m}$, where we have also assumed $C_k^r \ll 1/(\omega_r Z_0)$. The qubit will inherit this noise through its coupling to the resonator, given by $\delta f_q \approx (g/\Delta_{r,q})^2 \delta f_r$ in the dispersive limit. Assuming a reasonable qubit coupling $g/\Delta_{r,q} = 0.05$; we find $\delta f_q/\delta x \approx 2\,\text{kHz}/\mu\text{m}$.

We do not know the scale of δx noise nor the spectral density, however, we cannot rule out sub µm scale oscillations in the unanchored inner conductors of the control lines. This section highlights that such physical vibrations may present a dephasing mechanism to qubits in the coaxmon architecture.

4.6 Intrinsic Purcell filtering

A benefit to integrating both reverse-side readout and off-chip wiring is that the capacitance network formed by the geometric arrangement of qubit, reverse-side resonator, and off-chip resonator control line naturally implements a notch-type Purcell

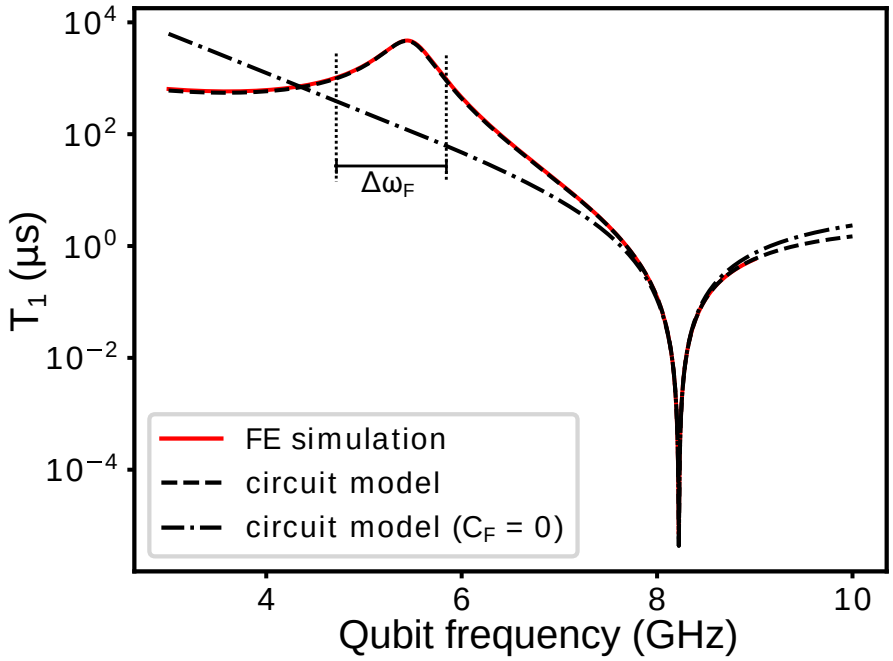

Figure 4.8: **Intrinsic Purcell filtering simulation:** FE simulation prediction for the radiatively limited T_1 time of a qubit in a device with identical dimensions to that measured in Chapter 7, along with fits using the circuit model in Fig. 4.7(B).

filter of the kind described in Ref. [148], that can protect the qubit from radiative loss down the resonator control line. An image of the physical arrangement of qubit, reverse-side resonator and resonator control line is shown in Fig. 4.7(A) and the effective circuit model is shown in Fig. 4.7(B). The coupling of qubit and resonator to their respective control lines is modelled by the capacitances C_k^q and C_k^r, and the coupling between qubit and resonator is represented by the single capacitance C_g. The important feature for the Purcell filter is the direct capacitance C_F between the qubit and the resonator control line. At the filter frequency ω_F, this coupling and the coupling through the resonator destructively interfere and decouple the qubit from the resonator control line. The filter frequency is given by [148]

$$\omega_F = 1/\sqrt{L_r(C_r + C_r')} \tag{4.21}$$

$$C_r' = \frac{C_F C_g + C_g C_k^r + C_k^r C_F}{C_F} \tag{4.22}$$

Fig. 4.8 shows the radiatively limited T_1 time of a coaxmon qubit as a function of frequency as found by Ansys HFSS simulation. The simulation model is shown in Appendix B. The enclosure dimensions and qubit and resonator pad geometry in the simulation model are set to be identical to those in the real device measured in Chapter 7. The exception is the resonator pin distance d_{pin}^r, which is 0.2 mm in

Table 4.1: **Purcell filter circuit model parameters:** Fitted parameters to the circuit model in Fig 4.7.

C_q (fF)	C_r (fF)	L_r (nH)	C_g (fF)	C_k^q (fF)	C_k^r (fF)	C_F (fF)	Z_0 (Ω)
109	100	3.46	3.85	0.02	4.42	0.123	50

simulations compared to $\sim 0.4\,\text{mm}$ in the real device. The simulated T_1 values are here found from the real admittance spectrum using eq. 2.59 [48], with $C_q = 109\,\text{fF}$ found from BBQ. Also shown is the radiatively limited T_1 predicted by applying eq. 2.59 to the circuit model in Fig. 4.7(B) with fitted parameters, showing good correspondence. For consistency between the simulation and circuit model, the fitted circuit parameters are constrained by the requirement [147]

$$(C_k^r)^2 Z_0/(C_r^2 L_r) = \kappa_{ext}^r \tag{4.23}$$

where $\kappa_{ext}^r/2\pi = 4.5\,\text{MHz}$ is the external decay rate of the resonator found from simulation. The fitted values are given in table 4.1. The Purcell filter effect is clearly visible by the maximum in T_1. This maximum occurs at the filter frequency ω_F. We additionally show the prediction of the circuit model taking $C_F = 0$, showing that the filter disappears. We define the filter bandwidth $\Delta\omega_F$ as the frequency range where the radiative T_1 exceeds 1 ms. The filter has a predicted bandwidth of 1.14 GHz, between 4.70 GHz and 5.83 GHz. In the absence of the filter, the predicted radiative T_1 varies between 400 µs and 60 µs over this range. The filter is thus expected to significantly enhance the radiative T_1 time of the qubit over a wide range of relevant qubit frequencies, making it an attractive feature of the architecture. By tuning the geometry of the qubit, reverse-side resonator, and off-chip wiring, the filter frequency can be adjusted for purpose. Importantly, this filter exists intrinsically in the circuit, without requiring the addition of specific Purcell filtering CPW resonators as in Refs. [53, 55, 56]. We mention that in Ref. [148], the authors note the sub fF C_F values required to utilise this intrinsic filter can be difficult to realise with fully planar circuit designs.

4.7 Enclosure

In the coaxmon architecture, there are no on-chip ground planes on either side of the circuit substrate. Instead, the cavity enclosure acts as the circuit ground. An advantage of removing ground planes from the circuit substrate is that on-chip circuitry such as qubit coupling circuitry will not result in divided ground planes. As discussed

in Chapter 3, these can harbour spurious slotline modes that mediate crosstalk.

While using the cavity enclosure as the circuit ground removes the risk of divided on-chip ground planes, spurious cavity modes can still mediate crosstalk between circuits. If we assume the cavity tightly encloses a circuit substrate with permittivity $\epsilon_r \sim 10$, and set a minimum allowed cavity mode frequency of 10 GHz, then using eq. 5.1 (taken from next chapter), a square cavity is limited to have 6.7 mm side lengths, limiting a qubit array with 2 mm qubit pitch to just 9 qubits! These cavity modes thus present an obstacle to claiming that the coaxmon architecture is tileable.

In the next chapter, we will study how cavities can be modified to remove these spurious modes. In analogy with the use of airbridges to inductively link divided ground planes to suppress slotline modes, we will model how inductively linking the upper and lower halves of the cavity enclosure can suppress low frequency cavity modes, allowing the cavity enclosure to behave as a good ground to enclosed qubits and resonators at any scale.

Chapter 5

Superconducting Circuits in Inductively Shunted Cavities

In this chapter we consider the problem of building an enclosure that will provide a clean electromagnetic environment to enclosed superconducting circuits at any scale. Simple contiguous cavities are very good at doing this for small devices – but fail beyond a certain scale due to the modes of the cavity encroaching on circuit frequencies. This places tight constraints on the dimensions of circuits that can be effectively shielded, and ultimately on the number of superconducting qubits that can be housed in simple contiguous cavity enclosures.

In integrated circuits (IC), it is standard practice to use through silicon vias (TSVs) to enable 3D integration of signal routing and to reduce crosstalk between circuits [149–151]. Recently, superconducting TSVs have been developed for these purposes in superconducting circuits [124, 129, 152]. In this chapter we consider how a generalisation of TSVs, conducting cylinders, behave when placed inside a cavity. By drawing on results from photonic crystals and meta-materials, we show how such a structure can form an enclosure that provides a clean electromagnetic environment to 2D qubit arrays at any scale.

This structure behaves differently to a simple contiguous cavity, and so the question arises how enclosed qubits behave and interact in their new electromagnetic environment. We use a plasma meta-material description to predict the form of inter-qubit coupling and other crosstalk quantities mediated by this structure. We then compare these predictions with those of a bound states model that instead considers the coupling as arising from the band structure of the new distribution of cavity modes, and show that these two different ways of considering the system are in good agreement.

Much of the work in this Chapter was published in Ref. [153].

5.1 Contiguous cavity modes

First, we review how the modes of a contiguous cavity behave as the cavity dimensions increase. We focus on rectangular cavities to keep the equations simple, however, the general conclusions hold irrespective of the cavity shape. Consider a rectangular cavity with dimensions ℓ_x, ℓ_y, ℓ_z. The mode frequencies of this cavity are given by [19]

$$f_{nml} = \frac{1}{2\sqrt{\epsilon\mu}} \sqrt{\frac{n^2}{\ell_x^2} + \frac{m^2}{\ell_y^2} + \frac{l^2}{\ell_z^2}} \tag{5.1}$$

where n, m, l take integer values, and physical solutions permit only one of n, m, l to be zero. We now consider whether these modes exhibit a cutoff frequency as we unbound the cavity dimensions one by one. We impose the hierarchy $\ell_z \leq \ell_y \leq \ell_x$. First, we take $\ell_x \to \infty$, and so replace the discrete n/ℓ_x variable with the continuous variable k_x/π, where k_x is the wave-vector, leading to

$$f_{k_x,ml} = \frac{1}{2\sqrt{\epsilon\mu}} \sqrt{\frac{k_x^2}{\pi^2} + \frac{m^2}{\ell_y^2} + \frac{l^2}{\ell_z^2}} \tag{5.2}$$

This cavity is characterised by a cutoff frequency, $f_{cutoff} = 1/(\sqrt{\epsilon\mu} 2\ell_y)$, below which no modes can exist irrespective of the value of k_x. Thus, contiguous cavities *can* in fact scale to have an infinite area $\ell_x \ell_y$ and have a cutoff frequency – *if* all the scaling is done in one dimension. However, such long thin cavities are likely to be of limited use as superconducting circuit enclosures, as many of the most promising applications of superconducting circuits (such as surface code) require 2D grids of qubits. To model this scenario, we further take $\ell_y \to \infty$, and substitute in the continuous variable k_y/π for m/ℓ_y, leading to

$$f_{k_x,k_y,l} = \frac{1}{2\sqrt{\epsilon\mu}} \sqrt{\frac{k_x^2}{\pi^2} + \frac{k_y^2}{\pi^2} + \frac{l^2}{\ell_z^2}} \tag{5.3}$$

Now, there is no longer a cutoff frequency for the contiguous cavity, as $k_x, k_y \to 0$, $l = 0$ is a physical mode solution with frequency $f_{k_x,k_y,l} \to 0$. Frequency collisions with enclosed circuits are guaranteed in this case. For instance, setting $k_y \to 0, l = 0$ results in $\omega_{k_x} = k_x/\sqrt{\epsilon\mu}$, which is the linear dispersion of a plane-wave propagating along the $\hat{x}$ direction. The implication for superconducting circuits is that simple contiguous cavities cannot provide a clean EM environment to circuits that scale in 2D, as the modes of the enclosure will collide with qubit frequencies.

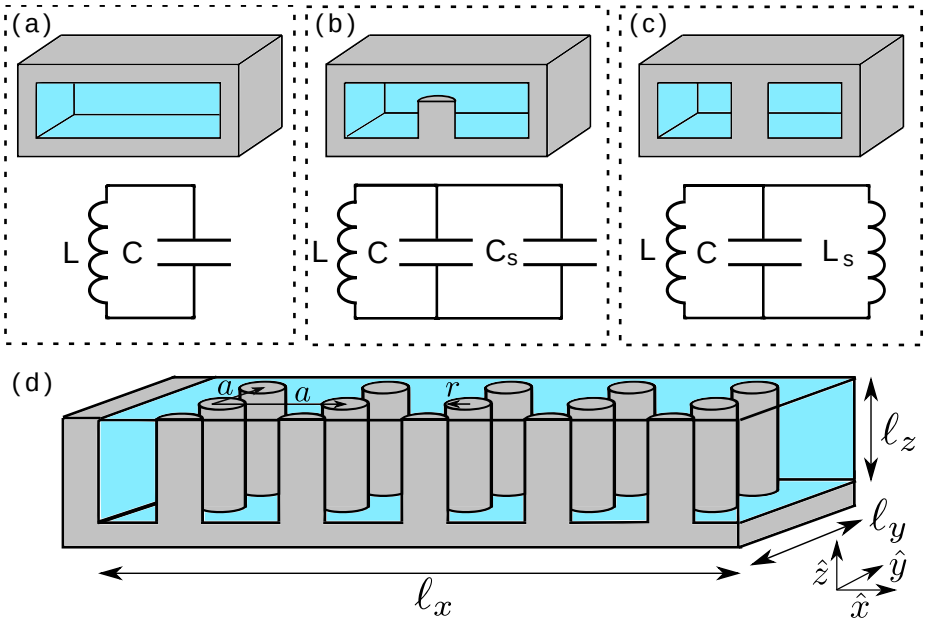

Figure 5.1: **Modifying rectangular cavities: (A) - (C)** Cross-sections of rectangular cavities along with circuit representations of their fundamental mode. **(D)** A cavity filled with a dielectric and inductively shunted by a square array of conducting cylinders, spacing a and radius r (cavity top and sides not shown).

5.2 Inductively shunted cavity modes

Here, we consider how a rectangular cavity might be modified to reintroduce a cutoff frequency even as it scales in 2D. Fig. 5.1 shows cross-sections of rectangular cavities containing metal cylindrical protrusions, along with circuit representations. In Fig. 5.1(A), the cavity contains no protrusions, and the fundamental mode is represented by a simple LC oscillator. The capacitance and inductance of this oscillator can be expressed as [154]

$$C = \frac{1}{\pi^4 \alpha^2} \frac{\epsilon \ell_x \ell_y}{\ell_z} \quad L = \pi^2 \alpha \mu \ell_z \tag{5.4}$$

where

$$\alpha = \frac{\ell_y}{\ell_x} + \frac{\ell_x}{\ell_y} \tag{5.5}$$

The capacitance takes the form of a parallel-plate capacitance (scaled by the dimensionless parameter $1/\pi^4\alpha^2$) between the two largest area walls of the cavity, while the inductance is proportional to the distance separating these walls. This matches with the EM fields and charge dynamics in the fundamental mode: the electric field is oriented along $\hat{\boldsymbol{z}}$, and the charge oscillates back and forth between the largest area walls, travelling though the side walls.

In Fig. 5.1(B), a perfectly conducting cylindrical stub is introduced to the cavity, protruding from the lower wall. It is clear that this stub will have a strong capacitance to the upper wall, and increase the total capacitance of the mode. Treating the stub as a perturbation, the adjusted fundamental mode frequency can be expressed $f_0 = 1/2\pi\sqrt{L(C + C_s)}$, where C_s is the shunting capacitance of the stub [155]. The effect is to reduce the fundamental mode frequency. As the separation of the stub from the upper wall decreases, its frequency can be reduced continuously down to zero. This can be a useful property where it is desirable to decrease cavity mode frequencies without increasing the dimensions of the cavity. The effect can also be utilised to make frequency tunable 3D cavities [156].

In Fig. 5.1(C), the perfectly conducting cylinder now contacts both the lower and upper wall of the cavity. Since it electrically connects the walls, it presents a new path for current to flow between them, represented by the shunting inductance L_s. Now, the fundamental frequency of the cavity can be expressed $f_0 = 1/2\pi\sqrt{LC/(1 + L/L_s)}$. The cylinder now reduces the total inductance of the fundamental mode, hence increasing the fundamental mode frequency. This makes inductively shunting the cavity a promising candidate for introducing a cutoff frequency even as the cavity scales in 2D.

To see this, one can imagine removing the side walls of the cavity entirely. In the simple circuit model, this means taking $L \to \infty$. The capacitance will also change $C \to C'$. The fundamental mode still exists, as current can still oscillate back and forth through the pillar, with a frequency $f_0 = 1/2\pi\sqrt{L_s C'}$. One can then imagine tiling this 'unit cell' to create an arbitrarily large structure, with each independent unit cell having the fundamental frequency $f_0 = 1/2\pi\sqrt{L_s C'}$, which then becomes the cutoff frequency of the whole structure.

This discussion implies that a cutoff frequency can be introduced by inductively shunting the cavity with an array of perfectly conducting cylinders, which theoretical and experimental work regarding metallic photonic crystals show is indeed the case [157–159]. Such a cavity is shown in Fig. 5.1(D). The array is formed of cylinders radius r and equal spacing a in $\hat{\boldsymbol{x}}$ and $\hat{\boldsymbol{y}}$. The cavity is perfectly conducting, has dimensions ℓ_x, ℓ_y, ℓ_z, and is filled with a uniform material with dielectric permittivity ϵ_r.

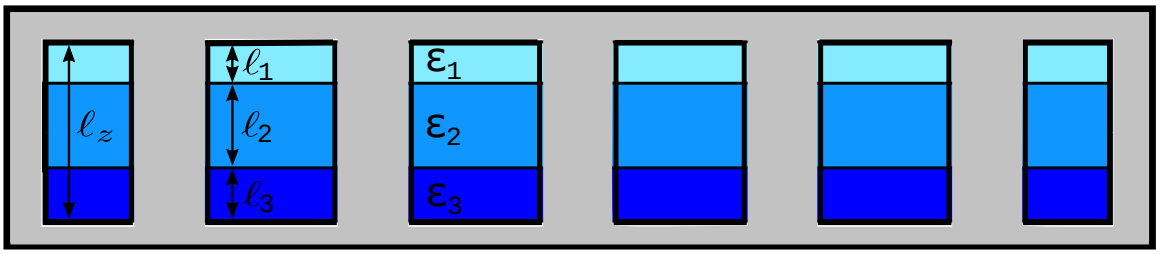

Figure 5.2: **Inductively shunted cavity with dielectric stack:** Cross-section of the inductively shunted cavity, now containing a stack of different dielectric materials.

In order to create large 2D superconducting qubit arrays, this cavity enclosure will only need to scale in two dimensions, i.e. ℓ_z does not need to scale with the array size. Superconducting circuit substrate thicknesses are typically ~ 0.5 mm, and so ℓ_z can be ~ 1 mm. In this case, $f(l > 0) > 44$ GHz (taking $\epsilon_r = 11.45$ and using eq. 5.1). This is well above the typical range of qubit and resonator frequencies in superconducting circuits, and so we will only consider $l = 0$ cavity modes in the remainder of this chapter.

Here, we comment that the cavity might contain a stack of dielectrics as shown in Fig. 5.2. Particularly relevant for superconducting quantum circuits is the three layer case: vacuum, substrate, vacuum. The magnetic properties of the cavity will be unaltered, so the introduction of multiple dielectric layers will only affect the capacitance of the $l = 0$ modes, which take the form of a parallel plate capacitance between the top and bottom of the cavity

$$C = k \times \frac{\epsilon_r}{\ell_z} \tag{5.6}$$

where k is a constant. The capacitance in the presence of multiple dielectric layers C' is the series sum of the parallel plate capacitances across each layer

$$C' = k \times 1/\Sigma_{i=1}^{n}(\frac{\ell_i}{\epsilon_i}) = k \times \frac{\epsilon'_r}{\ell_z} \tag{5.7}$$

$$\epsilon'_r = \ell_z/\Sigma_{i=1}^{n}(\frac{\ell_i}{\epsilon_i}) \tag{5.8}$$

Thus, the only effect of a dielectric stack is to replace the relative permittivity ϵ_r wherever it appears, with the effective relative permittivity ϵ'_r in eq. (5.8).

For an crude estimate of the cutoff frequency, we imagine replacing the array of

inductive shunts with a grid of thin conducting walls, with spacing a. This breaks the cavity up into an array of smaller uncoupled cavities, and results in a fundamental frequency for the whole system

$$f_a = 1/(a\sqrt{2\epsilon_0\epsilon_r\mu_0}) \tag{5.9}$$

This primitive model gives a prediction for the cutoff frequency, but is clearly an oversimplification. It fails to take into account the ability for EM waves to travel between the pillars, and gives a prediction which is independent of the shunt radius r. In the limit $r \to 0$, where the shunts disappear, the modes of the rectangular cavity in eq. 5.1 should be recovered. For a better model, we will make use of a celebrated meta-material description of conducting cylinder arrays.

5.3 Plasma model

The plasma frequency represents the frequency of simple harmonic motion that free electrons in a neutral medium will undergo if they are collectively displaced, given by [26]

$$\omega_p = \sqrt{\frac{ne^2}{\epsilon m_{eff}}} \tag{5.10}$$

where n is the electron density and m_{eff} the effective mass of the electrons in the medium. The ability of the elections to undergo collective simple harmonic motion results in the following frequency dependent contribution to the relatively permittivity of the medium [26]

$$\epsilon_p(f) = (1 - (\frac{f_p}{f})^2) \tag{5.11}$$

Above the plasma frequency, the permittivity is positive and travelling waves can propagate, whereas below the plasma frequency the permittivity is negative and waves are evanescent.

In Ref. [160], it was shown how a periodic array of long thin metal cylinders behaves like a plasma in response to low frequency electromagnetic waves – but with the possibility of having an extremely low plasma frequency in the GHz range as opposed to the PHz range common for metals. The conditions for this to apply are the following: (1) The electric field of the EM waves should be parallel to the axis of the cylinders. (2) The metal cylinders should be sufficiently long that it is valid to assume a uniform current through them and ignore charging effects at the ends. (3)

The wavelength of the EM waves must be long enough ($\lambda \gg a$) that Bragg scattering effects due to the cylinder periodicity is small. To avoid confusion, here λ is the wavelength of the EM wave *before* applying a permittivity modification due to the plasma, i.e. $\lambda = 1/(\sqrt{\mu\epsilon_0\epsilon_r}f)$. Given these conditions, the plasma frequency can be found by considering the electron density and effective mass of the effective medium. If the metal cylinders have electron density n_0, the electron density of the effective medium is simply scaled down by the fraction of the medium the cylinders occupy

$$n = \frac{\pi r^2}{a^2} n_0 \tag{5.12}$$

where r and a are defined as in Fig. 5.1. The effective mass of the electrons, on the other hand, is greatly increased, dominated by the self-inductance of the cylinders. For $r \ll a$ it is approximately given by [160]

$$m_{eff} = \frac{\mu_0 r^2 e^2 n_0}{2\pi} \ln(a/r) \tag{5.13}$$

Inserting these expressions into eq. 5.10 results in the following plasma frequency for the effective medium

$$f_p = \frac{f_a}{\sqrt{\pi \ln(\frac{a}{r})}} \tag{5.14}$$

where we have substituted in eq. 5.9 from the simple boundary model. Far more detailed analyses [161, 162] provide a slightly modified, more accurate expression for the plasma frequency, again valid in the regime $r \ll a$

$$f_p = \frac{f_a}{\sqrt{\pi}(\ln(\frac{a}{r}) - \Pi)^{0.5}} \tag{5.15}$$

$$\Pi = \ln(2\pi) - \pi/6 - \Sigma_{n=1}^{\infty}(\coth(n\pi) - 1)/n \approx 1.31$$

5.3.1 Applied to the inductively shunted cavity

We would like to apply this plasma model to the inductively shunted cavity in Fig. 5.1 to predict the frequencies of the $l = 0$ modes. It is not immediately clear we can do this, considering the three conditions given above. Condition (1) is satisfied for the $l = 0$ modes of the cavity, as these all have their electric field oriented along $\hat{\boldsymbol{z}}$ (parallel to the cylinder axis). However condition (2) appears not to be satisfied, as the cylinders have length ℓ_z, which can be small for superconducting device enclosures. However, the method of image charges can be used to show that if the cylinders connect to both walls of the cavity, then under the reasonable assumption of uniform current flow through the cylinders, they behave as if they are infinitely long. This

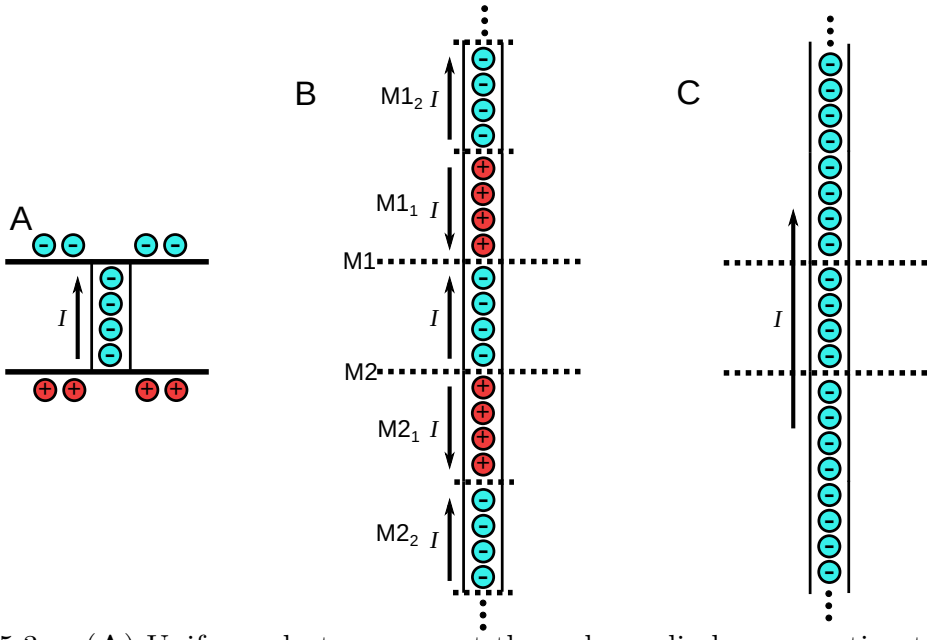

Figure 5.3: **:** (**A**) Uniform electron current through a cylinder connecting two cavity walls, where charge builds up. (**B**) The walls are replaced with an infinite array of mirror charges, generated by repeatedly reflecting the charge distribution through the mirror planes M1 and M2 (changing the charge sign and current flow direction on each reflection). (**C**) Identical fields are produced by a uniform current of electrons in an infinitely long cylinder.

is shown in Fig. 5.3. Here, we have replaced the upper and lower walls of the cavity with mirror planes, valid under the reasonable condition $\ell_x, \ell_y \gg r, \ell_z$. Therefore, we can apply eqs. 5.11 & 5.15 to the $l = 0$ modes of the inductively shunted cavity so long as the solutions also satisfy condition (3) that $\lambda \gg a$.

We note that the image charge model makes it clear that the cylinders must electrically connect to both walls of the cavity. In the case they are disconnected, the cylinders will instead behave like an infinite array of disconnected cylinders stacked along the $\hat{\boldsymbol{z}}$ axis. Arrays of such severed cylinders do *not* behave like a plasma [163] and so it would not be valid to apply the plasma meta-material model to the cavity in this case.

We are now ready to predict the mode frequencies of the inductively shunted cavity. Defining f_{nm} as the $l = 0$ mode frequencies of the cavity without the shunt array, and f'_{nm} as the frequencies with the array, the effect of the cylinder array is simply a modification to the permittivity of the cavity, $\epsilon_r \to \epsilon_r \epsilon_p$, resulting in the following

$$f'_{nm} = \frac{f_{nm}}{\sqrt{\epsilon_p(f'_{nm})}} \tag{5.16}$$

Inserting eq. (5.11) and rearranging, the mode frequencies of the inductively shunted cavity are given by

$$f'_{nm} = \sqrt{f_{nm}^2 + f_p^2} \tag{5.17}$$

This expression has two important properties: (1) As the cylinder radii become very small ($r/a \to 0$), $f_p \to 0$ and the mode frequencies reduce to those of a simple rectangular cavity. (2) In the limit $f_{11} \ll f_p$, substituting the wavenumbers $n\pi/\ell_x \to k_x$, $m\pi/\ell_y \to k_y$ and expanding results in the following quadratic mode spectrum around the plasma frequency

$$f = f_p(1 + \frac{1}{2}k^2/k_p^2) \tag{5.18}$$

where $k^2 = k_x^2 + k_y^2$ and $k_p = \sqrt{\epsilon_0\epsilon_r\mu_0}\omega_p$ (and $\omega_p = 2\pi f_p$). The cavity now has a cutoff frequency, the plasma frequency f_p, that exists even as $\ell_x, \ell_y \to \infty$. This makes sense considering we are treating the cavity as if it is filled with a plasma, as no standing EM waves should be able to form below the plasma frequency. We note that eq. 5.17 has previously been used empirically as a fit to FE simulations of cavities containing arrays of thin conducting cylinders [164].

We performed HFSS eigenmode simulations to verify eq. 5.17 over a range of r/a. The HFSS models are shown in Appendix B. The results are shown in Fig. (5.4), demonstrating good agreement for $r \ll a$. As r/a increases beyond around 0.1, the predictions diverge with simulation. The wavelength λ in condition (3) can be expressed $\lambda = \sqrt{2}(f_a/f)a$. For $r/a = 0.1$, $f_a/f \approx 2$, and so $\lambda \approx 2.8a$, which does not satisfy the condition $\lambda \gg a$. Therefore, this breakdown is expected, as Bragg scattering has become significant.

As the HFSS simulations show, with respect to the $l = 0$ modes, the periodically inductively shunted cavity does indeed behave as if filled with a plasma with a very low plasma frequency. This makes such cavities an attractive candidate for enclosures for large-scale superconducting circuits. Qubits and resonators that are well below the plasma frequency will reside in a clean EM environment that will be free of cavity modes at any scale (when scaling in $\hat{\boldsymbol{x}}$ and $\hat{\boldsymbol{y}}$). Furthermore, intuitively it seems that crosstalk between circuit elements will be exponentially suppressed, as any excitations below the plasma frequency cannot propagate and will decay away evanescently. These ideas will be developed in section 5.5.

First, we develop a model to predict the mode frequencies in the region $r/a > 0.1$.

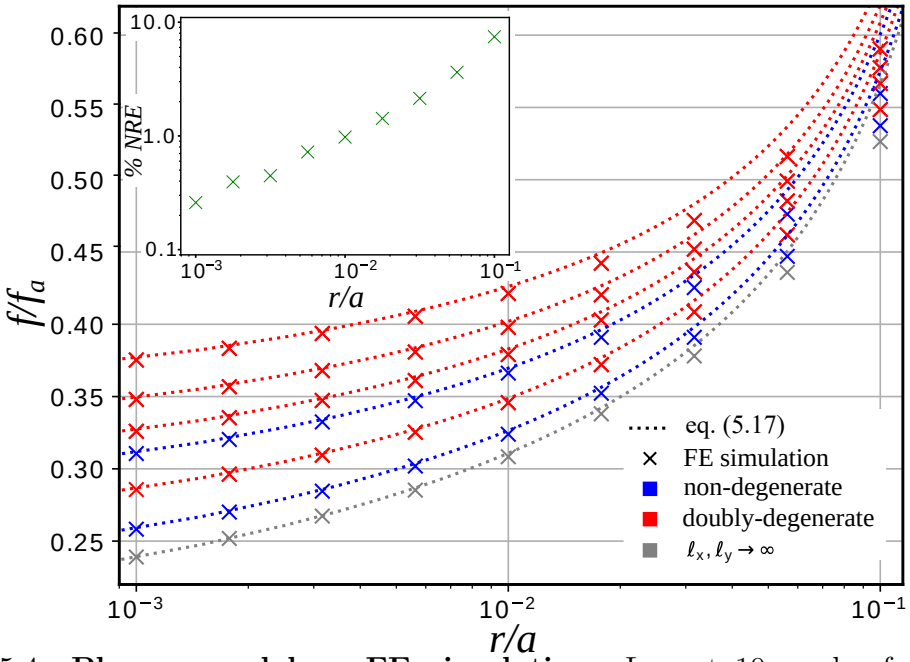

Figure 5.4: **Plasma model vs FE simulation:** Lowest 10 modes for a cavity containing an inductive shunt array, with $\ell_x, \ell_y = 10a$. The mode frequencies and degeneracies are accurately predicted by the plasma model. Also included in grey are results for the fundamental mode when $\ell_x, \ell_y \to \infty$, with simulation values found using a method described in Ref. [165]. Inset shows the normalised relative error (NRE) between simulation and eq. (5.17) $\Sigma_{i=1}^{10} |f_{i_{\mathrm{FE}}} - f_{i_{\mathrm{eq}}}| / 10 f_{i_{\mathrm{FE}}}$.

5.4 Circuit model

In this section, we develop a circuit model for the inductively shunted cavity valid for $r/a > 0.1$, where the plasma model has broken down. This is done mainly for completeness, as the plasma model is sufficient to predict the form of cavity-mediated crosstalk. In the limit $r/a > 0.1$, we will model the array of shunts as breaking up the cavity into an array of smaller cavities, taking the gaps between the shunts into account by allowing neighbouring cavities to magnetically couple to one another.

The tight-binding model has been used to model such coupled-cavity arrays [166], and circuit-models have also been used to model one dimensional coupled-cavity arrays [167, 168]. Here, we extend the circuit-model treatment to two dimensional arrays, and verify that, for $r/a > 0.1$, it provides an accurate model for the inductively shunted cavity.

Fig. 5.5 shows a section of the circuit, from which we construct the impedance matrix $\mathbf{Z_{2D}}$ using mesh analysis. We find this matrix can be mapped exactly into the simpler

impedance matrix $\mathbf{Z_{1D}}$ of the one dimensional coupled-cavity array shown in Fig. 5.6 through the relation

$$\boldsymbol{Z_{2D}}_{nm\times nm} = \boldsymbol{Z_{1D}}_{n\times n} \oplus \boldsymbol{Z_{1D}}_{m\times m} - Z_0 \boldsymbol{I}_{nm\times nm} \tag{5.19}$$

$$Z_0 = i\omega L_0 - \frac{i}{\omega C_0} \tag{5.20}$$

where $\oplus$ is the Kronecker sum. The derivation is provided in Appendix A. For the three specific inductance ratios $L_b/L_g = 0, 1, 2$ the circuit has simple, exact closed-form solutions. Taking $L_b = 0$ (corresponding to there being no edge effects for cavities at the border of the array), we find the mode frequencies of the inductively-shunted cavity to be

$$f_{ij} = \frac{f_0}{\sqrt{1 + 4\beta(1 + \frac{1}{2}(\cos(\frac{i\pi}{n}) + \cos(\frac{j\pi}{m})))}} \tag{5.21}$$
$$f_0 = 1/(2\pi\sqrt{L_0 C_0}) \quad \beta = L_g/L_0 \quad (1 \leq i \leq n, 1 \leq j \leq m)$$

where f_0 is the frequency of each uncoupled cavity in the circuit model, and β is the inductive coupling parameter between nearest neighbour cavities. Taking $n, m \to \infty$ results in a new cutoff frequency for the inductively-shunted cavity, $f_c = f_0/\sqrt{1+8\beta}$.

The field distribution of modes is now significantly altered by the inductive shunt array. We can find the relative field amplitude inside each cavity from the eigenvectors of $\mathbf{Z_{2D}}$. For $L_b = 0$, the relative field amplitudes are given by

$$E_{ij}(a,b) = E_0 \sin(\frac{i(2a-1)\pi}{2n}) \sin(\frac{j(2b-1)\pi}{2m}) \tag{5.22}$$
$$(1 \leq a, i \leq n) \quad (1 \leq b, j \leq m)$$

where E_{ij} is the relative electric field amplitude in each cavity, a and b index these cavities, and i and j index the modes. The lowest mode ($i, j = 1$) is symmetric, and the highest mode ($i = n, j = m$) is anti-symmetric, as would be expected for hybridised modes.

Note that this circuit model tends to the tight-binding model for $\beta \ll 1$. A series expansion of eq. 5.21 in powers of β results in

$$f_{ij} \approx f_0 - 2t(2 + \cos(k_x a) + \cos(k_y a)) \tag{5.23}$$
$$t = \beta f_0/2 \quad k_x = i\pi/\ell_x \quad k_y = j\pi/\ell_y$$

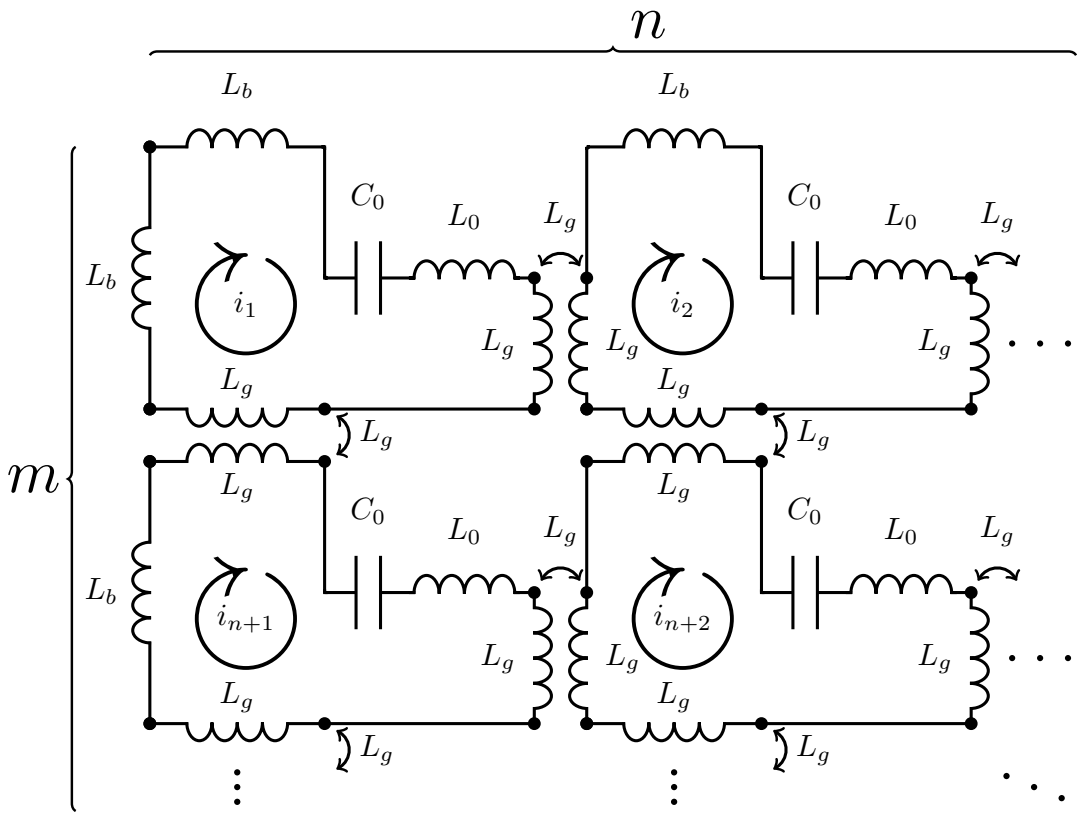

Figure 5.5: **2D coupled cavity circuit model:** Circuit representation for the lowest $n \times m$ modes of a $n \times m$ array of nearest neighbour magnetically coupled cavities formed by an array of $(n-1) \times (m-1)$ inductive shunts. The isolated fundamental mode of each cavity is represented by L_0 and C_0. The magnetic coupling between cavities is represented by ideal transformers with mutual inductance L_g. The boundary conditions in the outermost cavities are represented by the boundary inductance L_b.

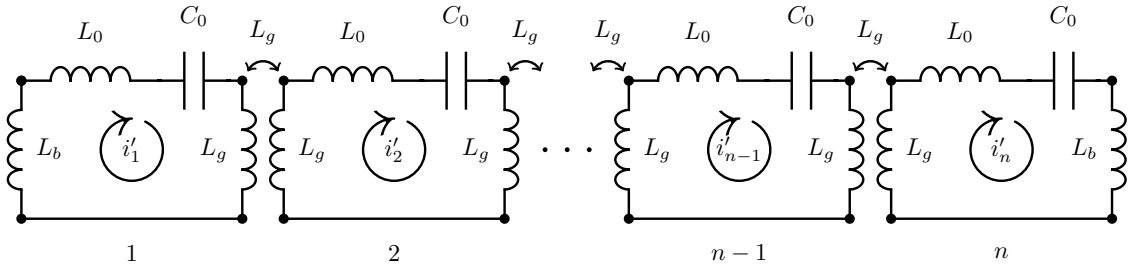

Figure 5.6: **1D coupled cavity circuit model:** Circuit representation for the lowest n modes of a chain of n magnetically coupled cavities.

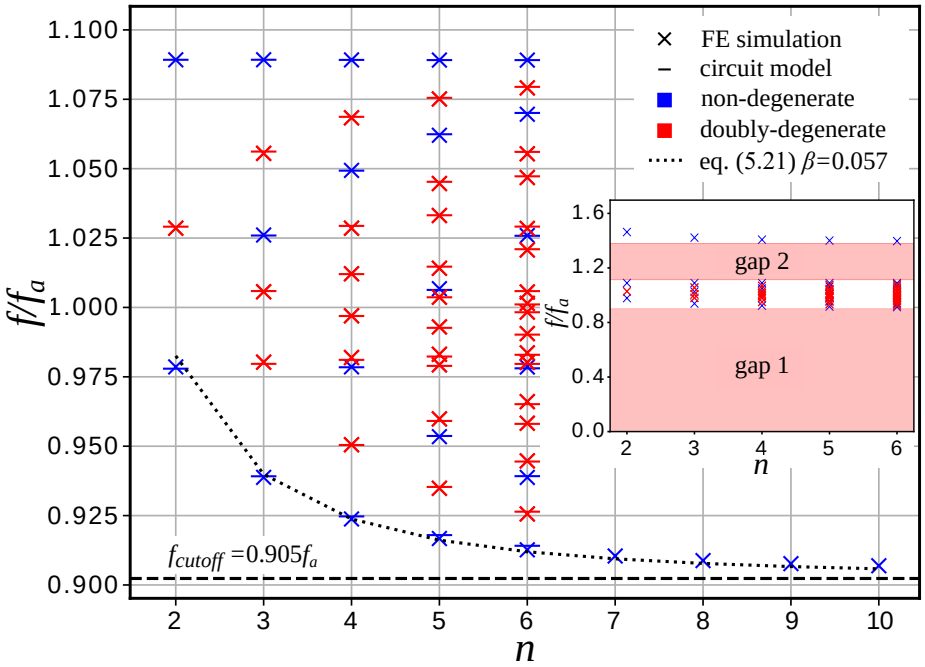

Figure 5.7: **Circuit model vs FE simulation:** Lowest n^2 modes for a cavity with size $\ell_x = \ell_y = a \times n$, containing $n-1 \times n-1$ inductive shunts, with $r = 0.25a$. For n between 2-6, the fit to the next-nearest neighbour circuit model is shown for all n^2 modes, fitted with nearest and next-nearest neighbour couplings β and β_1 as free parameters. For n between 7-10, only the fundamental frequency from FE simulation is shown. Dotted line shows the fundamental frequency decreasing towards a bound in agreement with eq. 5.21. Inset shows the lowest n^2+1 modes, showing two band gaps, below mode 1 and between modes n^2 and n^2+1.

which is the tight-binding model dispersion for a square lattice. A series expansion of the cosine terms in eq. 5.21 instead results in the following quadratic mode spectrum near the cutoff frequency

$$f = f_c(1 + \frac{1}{2}k^2/k_0^2) \tag{5.24}$$

where $k^2 = k_x^2 + k_y^2$, $k_0^2 = 1/(\beta a^2)$, and k_x and k_y are defined in eq. 5.23.

In Fig. 5.7 we show results of HFSS eigenmode simulations of cavities containing inductive shunt arrays with $r/a = 0.25$. The HFSS model for $n = 6$ is shown in Appendix B. We find good agreement to the circuit model, which improves further when we include a next-nearest neighbour coupling parameter β_1.

This is shown in Fig. 5.8, where the agreement of the nearest and next-nearest neighbour circuit models, as well as the tight binding model in eq. 5.23, are compared to a FE simulation. The agreement for all models increases as r/a increases. Note that the circuit model offers a better fit than the tight binding model for a single free

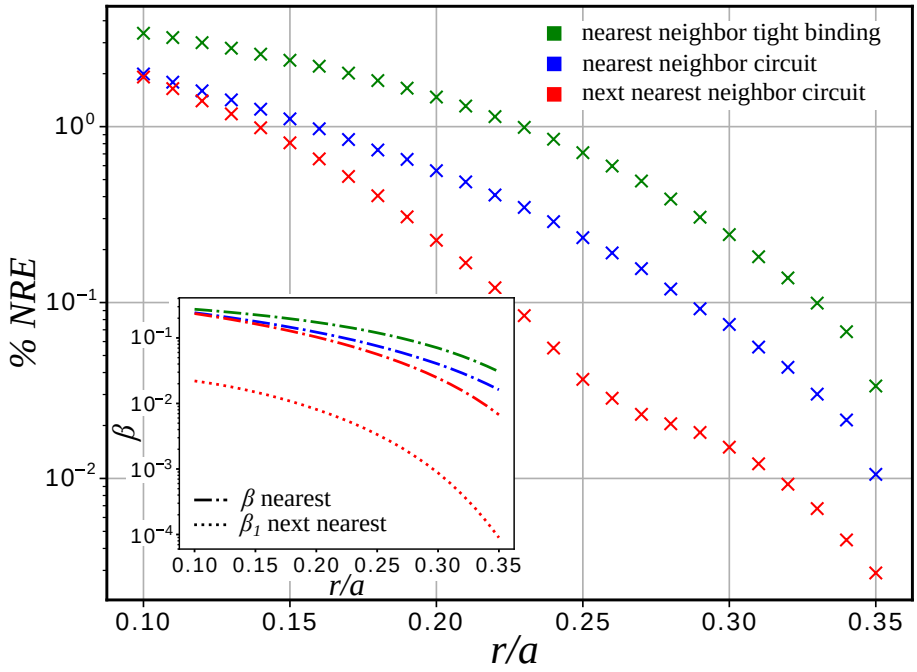

Figure 5.8: **Residuals of different model fits to FE simulation:** Normalised relative error (NRE) $\Sigma_{i=1}^{16}|f_{i_{\mathrm{FE}}} - f_{i_{\mathrm{model}}}|/16f_{i_{\mathrm{FE}}}$, between a FE simulation and three different fit models, for the lowest 16 modes of a cavity containing a 3×3 inductive shunt array, changing shunt radius r. Inset shows the fitted coupling parameters decreasing smoothly with increasing inductive shunt radius.

parameter.

While it is satisfying that the circuit in Fig. 5.5 shows good agreement with FE simulations of inductively shunted cavities, the model does not predict simple analytical formulas for f_0 or β, and so cannot predict the cutoff frequency as a simple function of a and r like the plasma model. Also, cylinders with $r/a > 0.1$ may be of limited practical use for superconducting circuits, as the cylinders start to take up a considerable fraction of the available real estate on the substrate. As such, the model developed in this section may be of more use for modelling actual 2D coupled cavity arrays.

5.5 Behaviour of embedded superconducting circuits

Having developed accurate models for the mode frequencies of inductively shunted cavities and shown that they exhibit a cutoff frequency, we now consider using these cavities to enclose large-scale superconducting circuits. In particular, we consider the

form of cavity-mediated crosstalk for superconducting circuits in such cavities. In the absence of any inductive shunts, this crosstalk is mediated through the standing-wave EM modes of the cavity. However, in the presence of the inductive shunt array, no standing-waves can form below the cutoff frequency, and there is a divergence in the density of cavity modes around the cutoff frequency. This results in a different form of cavity-mediated crosstalk.

The plasma model of periodic inductive shunts provides an intuitive framework for predicting the cavity-mediated crosstalk in this case. An excited superconducting qubit or control line, with a frequency below the plasma frequency, can only send out evanescent waves. So long as this qubit or control line is sufficiently distant from the edges of the cavity, edge effects will be highly attenuated. In this case, the qubit or control line will not 'see' the edges of the cavity, and it can be treated as if it is in a parallel-plate waveguide, with plates formed by the lower and upper walls of the cavity.

5.5.1 Parallel-plate waveguide modes

Parallel-plate waveguides can carry both radial modes and plane-wave modes. We only consider the radial modes, since qubits and localised drive-lines will not be able to excite plane waves. The radial modes of a parallel-plate waveguide can be divided into TE modes and TM modes. The field solutions are most naturally expressed in cylindrical coordinates (r, z, ϕ), in terms of an outward travelling wave and an inward travelling wave propagating along $\hat{\boldsymbol{r}}$. The field solutions for the TE_{nm} modes are [169]

$$E_r = \omega\mu_0 \frac{m}{r}[A^{(+)}H_m^{(2)}(k_n r) - A^{(-)}H_m^{(1)}(k_n r)]\sin(\frac{n\pi z}{\ell_z})\sin(m\phi) \tag{5.25}$$

$$E_\phi = \omega\mu_0 k_n[A^{(+)}H_m^{(2)\prime}(k_n r) - A^{(-)}H_m^{(1)\prime}(k_n r)]\sin(\frac{n\pi z}{\ell_z})\sin(m\phi) \tag{5.26}$$

$$E_z = 0 \tag{5.27}$$

$$H_r = -i\frac{n\pi}{\ell_z}k_n[A^{(+)}H_m^{(2)\prime}(k_n r) + A^{(-)}H_m^{(1)\prime}(k_n r)]\cos(\frac{n\pi z}{\ell_z})\cos(m\phi) \tag{5.28}$$

$$H_\phi = i\frac{n\pi}{\ell_z}\frac{m}{r}[A^{(+)}H_m^{(2)}(k_n r) + A^{(-)}H_m^{(1)}(k_n r)]\cos(\frac{n\pi z}{\ell_z})\sin(m\phi) \tag{5.29}$$

$$H_z = -ik_n^2[A^{(+)}H_m^{(2)}(k_n r) - A^{(-)}H_m^{(1)}(k_n r)]\sin(\frac{n\pi z}{\ell_z})\cos(m\phi) \tag{5.30}$$

Here, $H_m^{(2)}$ and $H_m^{(1)}$ are Hankel functions, $A^{(+)}$ and $A^{(-)}$ are the amplitudes of the outward and inwardly travelling waves, $H_m^{(2)\prime}(kr) = \frac{dH_m^{(2)}(kr)}{d(kr)}$, and k_n is the propagation wavenumber given by

$$k_n = \sqrt{k^2 - (n\pi/\ell_z)^2} \tag{5.31}$$

where k is the wavenumber of the medium and l_z is the distance separating the parallel plates along $\hat{\boldsymbol{z}}$. The field solutions for the TM_{nm} modes are [169]

$$E_r = -\frac{n\pi}{\ell_z} k_n [B^{(+)} H_m^{(2)\prime}(k_n r) + B^{(-)} H_m^{(1)\prime}(k_n r)] \sin(\frac{n\pi z}{l}) \cos(m\phi) \tag{5.32}$$

$$E_\phi = \frac{n\pi}{\ell_z} \frac{m}{r} [B^{(+)} H_m^{(2)}(k_n r) + B^{(-)} H_m^{(1)}(k_n r)] \sin(\frac{n\pi z}{l}) \sin(m\phi) \tag{5.33}$$

$$E_z = k_n^2 [B^{(+)} H_m^{(2)}(k_n r) + B^{(-)} H_m^{(1)}(k_n r)] \cos(\frac{n\pi z}{\ell_z}) \cos(m\phi) \tag{5.34}$$

$$H_r = -j\omega\epsilon_0 \frac{m}{r} [B^{(+)} H_m^{(2)}(k_n r) + B^{(-)} H_m^{(1)}(k_n r)] \cos(\frac{n\pi z}{\ell_z}) \sin(m\phi) \tag{5.35}$$

$$H_\phi = -j\omega\epsilon_0 k_n [B^{(+)} H_m^{(2)\prime}(k_n r) + B^{(-)} H_m^{(1)\prime}(k_n r)] \cos(\frac{n\pi z}{\ell_z}) \cos(m\phi) \tag{5.36}$$

$$H_z = 0 \tag{5.37}$$

where $B^{(+)}$ and $B^{(-)}$ are the amplitudes of the outward and inwardly travelling waves. Note that the TE modes have no electric field component along $\hat{\boldsymbol{z}}$, and similarly the TM modes have no magnetic field component along $\hat{\boldsymbol{z}}$. Along the direction of propagation $\hat{\boldsymbol{r}}$, the modes in general have both electric and magnetic field components, and so are hybrid with respect to this axis. For the TM modes, solutions exist for integer values $n, m \geq 0$, and for the TE modes for integer values $n \geq 1$, $m \geq 0$.

We now aim to determine the propagation wavenumbers k_n for the different modes inside the inductively shunted cavity. Using the plasma meta-material model to describe the cylinder array, the wavenumber of this medium is anisotropic due to the orientation of the cylinders along $\hat{\boldsymbol{z}}$. For modes with electric fields parallel to the cylinder axis, the wavenumber of the medium is given by $k = \sqrt{\mu\epsilon_0\epsilon_r\epsilon_p}\omega$, where ϵ_p is as defined in eq. 5.11; whereas for modes with electric fields orthogonal to the cylinder axis $k \approx \sqrt{\mu\epsilon_0\epsilon_r}\omega$ [170], where this approximation is valid for $r \ll a$. This leads to the following propagation wavenumbers for the TE_{nm} modes, which all have $E_z = 0$

$$k_n^{TE} = \sqrt{\mu\epsilon_0\epsilon_r\omega^2 - (n\pi/\ell_z)^2} \tag{5.38}$$

For the TM_{0m} modes having $E_r = 0, E_\phi = 0, E_z \neq 0$, we find

$$k_0^{TM} = \sqrt{\mu\epsilon_0\epsilon_r(\omega^2 - \omega_p^2)} \tag{5.39}$$

where we have substituted in eq. 5.11 for ϵ_p. In superconducting circuit enclosures ℓ_z can be as small as $\sim 0.5\,\mathrm{mm}$, even in circuits that scale in 2D. If we take $\ell_z = 1\,\mathrm{mm}$, then $\pi/\ell_z \approx 3100$, whereas for a qubit at $5\,\mathrm{GHz}$ on a silicon substrate with $\epsilon_r = 11.45$, $\sqrt{\mu\epsilon_0\epsilon_r}\omega \approx 350$. In this case k_n^{TE} will always be imaginary, and so long

Table 5.1: **Parallel-plate waveguide radial mode penetration depths:** For parameter values $\omega/2\pi = 4$ GHz, $\omega_p/2\pi = 34.4$ GHz, $\epsilon_r = 3.6$, $\ell_z = 0.6$ mm. These parameters are chosen to match those of the construct formed by tiling the device measured in Chapter 7.

n	0	1	2	3
δ_n^{TE} (mm)	-	0.19	0.10	0.06
δ_n^{TM} (mm)	0.74	≤ 0.19	≤ 0.10	≤ 0.06

as $\omega_p/2\pi > 5\,\text{GHz}$, k_0^{TM} will also always be imaginary. For superconducting circuits inside inductively shunted cavities with reasonable dimensions, the TE_{nm} and TM_{0m} modes will therefore be evanescent, with penetration depths given by

$$\delta_n^{TE} = 1/\sqrt{(n\pi/\ell_z)^2 - \mu\epsilon_0\epsilon_r\omega^2} \tag{5.40}$$

$$\delta_0^{TM} = 1/\sqrt{\mu\epsilon_0\epsilon_r(\omega_p^2 - \omega^2)} \tag{5.41}$$

Note that $\delta_0^{TM} = \delta_p$, where δ_p is the standard plasma penetration depth for EM waves in a plasma medium. For the TM_{nm} modes with $n \neq 0$, the situation is more complicated due to the fact there exist components of the electric field both parallel and perpendicular to the cylinder axis. However, these modes will decay at least as fast as the TE_{nm} modes, as the polarizability of the cylinders can only reduce the penetration depth, leading to $\delta_n^{TM} \leq \delta_n^{TE}$ for $n \neq 0$. The penetration depths for the first few values of n, for a realistic set of parameters, are summarised in table 5.1. Clearly, the TM_{0m} modes travel the furthest, and so will be the dominant modes for mediating crosstalk. We note that in the absence of the inductive shunt array, these modes would have propagating solutions at all frequencies.

At this stage, we wish to move from a description of electric and magnetic fields in waveguides to a description of voltages and currents along transmission lines. This is in order to arrive at a circuit representation for the couplings between circuit elements mediated by these waveguide modes. Following Refs. [171, 172], each waveguide mode can be represented by voltage and current waves travelling along a well defined 1D transmission line. General field solutions inside the waveguide can then be represented by voltages and currents along an infinite number of these transmission lines. The voltage and current obey the transmission line equations [171]

$$\frac{dV}{dr} = -i\kappa Z I \tag{5.42}$$

$$\frac{dI}{dr} = -i\frac{\kappa}{Z}V \tag{5.43}$$

where κ is the propagation wavenumber of the transmission line and Z is the characteristic impedance of the transmission line. For the radial TM modes of a parallel-plate waveguide, these are given by [171]

$$\kappa = \sqrt{k^2 - (\frac{n\pi}{\ell_z})^2 - (\frac{m}{r})^2} \tag{5.44}$$

$$Z_{nm}^{TM}(r) = \sqrt{\frac{\mu}{\epsilon}} \frac{\ell_z \alpha_m}{2\pi r \alpha_n} \frac{k_n^2}{\kappa k} \tag{5.45}$$

$$\alpha_i = \begin{cases} 1, & \text{if } i = 0 \\ 2, & \text{otherwise} \end{cases} \tag{5.46}$$

Notice that the propagation constant and characteristic impedance vary with distance r along these transmission lines, which is a consequence of the radial waveguide being nonuniform [171]. The phase velocity of these transmission lines are given by $v_{nm}^{TM} = \omega/\kappa$. We focus on the TM_{0m} transmission lines, as these correspond to the dominant modes. The characteristic impedances of these transmission lines are given by

$$Z_{0m}^{TM}(r) = \sqrt{\frac{\mu}{\epsilon}} \frac{\ell_z \alpha_m}{2\pi r} \frac{1}{\sqrt{1 - (m/kr)^2}} \tag{5.47}$$

The voltage and current solutions along these transmission lines can be expressed in terms of incident and reflected waves as [169, 172]

$$V_{0m}^{TM}(r) = -\ell_z k^2 [B^{(+)} H_m^{(2)}(kr) + B^{(-)} H_m^{(1)}(kr)] \tag{5.48}$$

$$I_{0m}^{TM}(r) = -i\sqrt{\frac{\epsilon}{\mu}} \frac{2\pi r}{\alpha_m} k^2 [B^{(+)} H_m^{(2)\prime}(kr) + B^{(-)} H_m^{(1)\prime}(kr)] \tag{5.49}$$

The input impedances of these transmission lines in the absence of reflected waves are therefore given by

$$Z_{in,0m}^{TM}(r) = i\sqrt{\frac{\mu}{\epsilon}} \frac{\ell_z \alpha_m}{2\pi r} \frac{2H_m^{(2)}(kr)}{[H_{m+1}^{(2)}(kr) - H_{m-1}^{(2)}(kr)]} \tag{5.50}$$

where we have used the identity $H_m^{(2)\prime} = (H_{m-1}^{(2)} - H_{m+1}^{(2)})/2$. Surprisingly, even in the absence of reflected waves, the input impedances do not equal the characteristic impedances in eq. 5.47! This is a consequence of the radial waveguide being nonuniform [171].

Inside the inductively shunted cavity and below the plasma frequency, ϵ_p is negative for the TM modes and k is imaginary. In this case, the input impedances of the

TM_{0m} transmission lines for outward travelling evanescent waves become

$$Z^{TM}_{in,0m}(r) = i\sqrt{\frac{\mu}{\epsilon_0\epsilon_r|\epsilon_p|}}\frac{\ell_z\alpha_m}{2\pi r}\frac{2K_m(r/\delta_p)}{[K_{m+1}(r/\delta_p)+K_{m-1}(r/\delta_p)]} \tag{5.51}$$

Here we have used that k is imaginary to transform $H^{(2)}_m$ into K_m using the identity $K_m(x) = (\pi/2)(-i)^{m+1}H^{(2)}_m(-ix)$, where $K_m(x)$ is the modified Bessel function of the second kind, which takes real arguments and is real everywhere. For $r/\delta_p \ll \sqrt{m+1}$, these input impedances simplify to

$$Z^{TM}_{in,0m}(r) \approx i\sqrt{\frac{\mu}{\epsilon_0\epsilon_r|\epsilon_p|}}\frac{\ell_z\alpha_m}{2\pi r}\frac{r/\delta_p}{m+1} \tag{5.52}$$

where we have used the identity $K_m(x) \approx (m!/2)(2/x)^m$, valid for $x \ll \sqrt{m+1}$. Thus the input impedance of these modes scales like $1/(m+1)$. In the next section, we find that the coupling between circuit elements mediated by these modes is linearly proportional to the input impedance $J, \varepsilon \propto Z^{TM}_{in,0m}(\delta_0)$, where δ_0 is the interaction length of qubits or control lines with the waveguide modes, taken to satisfy $\delta_0 < \delta_p$. Therefore, couplings mediated by the TM_{0m} waveguide modes having $m \gg 1$ are suppressed. Furthermore, the rotationally symmetric field solutions of the TM_{00} mode will couple more strongly to the rotationally symmetric qubits and control lines of the coaxmon architecture. We therefore conclude the TM_{00} mode is the dominant mode for mediating crosstalk, and will only consider the transmission line representation of this mode when evaluating the couplings in the next section. Below the plasma frequency, the characteristic and input impedance of this transmission line are given by

$$Z^{TM}_{00}(r) = i\sqrt{\frac{\mu}{\epsilon_0\epsilon_r|\epsilon_p|}}\frac{\ell_z}{2\pi r} \tag{5.53}$$

$$Z^{TM}_{in,00}(r) = \frac{K_0(r/\delta_p)}{K_1(r/\delta_p)}Z^{TM}_{00}(r) \tag{5.54}$$

Note that these are imaginary, and so this transmission line cannot radiate power into the far field. The phase velocity satisfies

$$v^{TM}_{00} = i/\sqrt{\mu\epsilon_0\epsilon_r|\epsilon_p|} \tag{5.55}$$

Finally, the voltage and current solutions for outwardly travelling evanescent waves along this transmission line are given by

$$V^{TM}_{00}(r) = -i\ell_z k^2 B^{(+)}(\frac{2}{\pi})K_0(r/\delta_p) = V_{inc}K_0(r/\delta_p) \tag{5.56}$$

$$I^{TM}_{00}(r) = -\sqrt{\frac{\epsilon_0\epsilon_r|\epsilon_p|}{\mu}}2\pi r k^2 B^{(+)}(\frac{2}{\pi})K_1(r/\delta_p) = \frac{V_{inc}}{Z^{TM}_{00}}K_1(r/\delta_p) \tag{5.57}$$

5.5.2 Predictions for cavity-mediated couplings

Having determined that the dominant coupling mechanism between qubits is the TM_{00} radial waveguide mode and found a transmission line representation for this mode, we are equipped to make some quantitative predictions about crosstalk in the inductively shunted cavity. In particular, we consider the transverse exchange coupling J_{ij} between qubits i and j, and the drive coupling ε_{ij} of localised drive-line i to qubit j. The corresponding Hamiltonian operators are as follows

$$\hat{H}^J_{ij} = J_{ij}(\hat{a}_i\hat{a}^\dagger_j + \hat{a}^\dagger_i\hat{a}_j) \tag{5.58}$$

$$\hat{H}^D_{ij} = \varepsilon_{ij}(\hat{a}_j - \hat{a}^\dagger_j)V_i \tag{5.59}$$

Here $\hat{a}^\dagger_i$ and $\hat{a}_i$ are the creation and annihilation operators of qubit mode i, V_i is the voltage on drive-line i, and 'localised drive-line' refers to a drive that interacts with the enclosure from a localised source.

To find the transverse coupling J_{ij} between qubits i and j, we will make use of the impedance formula [92] discussed in Chapter 2 (eq. 2.87) and restated below

$$J_{ij} = -\frac{1}{4}\sqrt{\frac{\omega_i\omega_j}{L_iL_j}}\mathrm{Im}[\frac{Z_{ij}(\omega_i)}{\omega_i} + \frac{Z_{ij}(\omega_j)}{\omega_j}] \tag{5.60}$$

To find the transfer impedance Z_{ij} we solve the effective circuit model in Fig. 5.10. Two transmon qubits, with their Josephson-junctions replaced by ports, are each capacitively coupled to a transmission line representation of the TM_{00} radial mode of the parallel plate waveguide, with δ_0 representing the interaction length between the qubits and the waveguide. Using eq. 5.56, the expression for the incident voltage wave along this transmission line is

$$V(d) = a \times V_0K_0(d/\delta_p) \tag{5.61}$$

where δ_p is the plasma penetration depth given in eq. 5.41, and a is a normalisation factor $a = 1/K_0(\delta_0/\delta_p)$. The voltages along the transmission line at the positions of qubit 1 and qubit 2 are then

$$V(\delta_0) = V_0 \tag{5.62}$$

$$V(d_{12} - \delta_0) = a \times V_0K_0(d_{12}/\delta_p) \tag{5.63}$$

where we have taken $d_{12} \gg \delta_0$. This leads to the required voltage and current relations

$$V_{d_{12}}/V_0 = a \times K_0(d_{12}/\delta_p) \tag{5.64}$$

$$V_0/I_0 = Z_{in}(\delta_0) \tag{5.65}$$

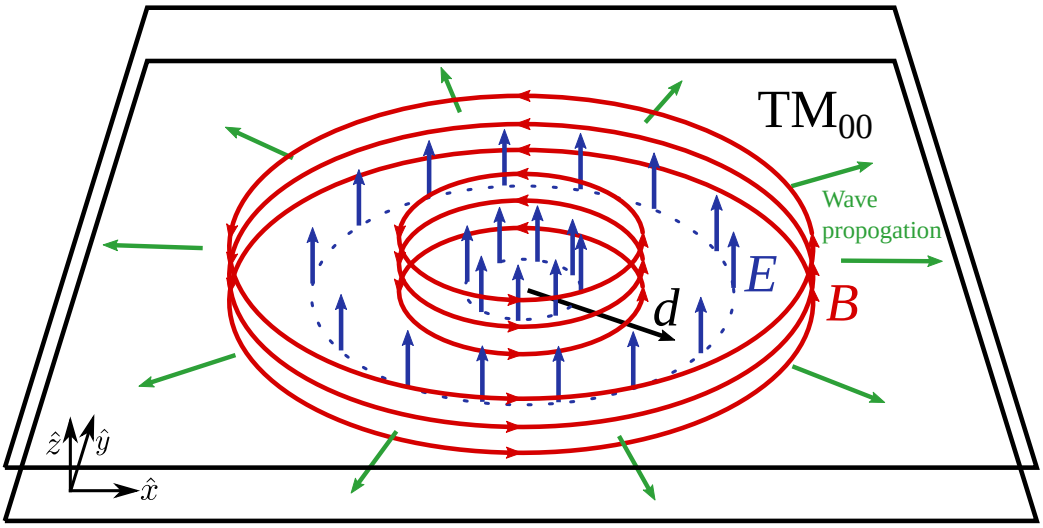

Figure 5.9: **Parallel-plate waveguide radial TM_{00} mode:** Visualisation of the outward travelling radial TM_{00} mode of a parallel plate wave-guide, having $E \propto H_0^{(2)}(kd)$, $B \propto H_1^{(2)}(kd)$.

Here, $Z_{in}(\delta_0)$ is the input impedance of this transmission line to outward travelling waves given in eq. 5.54 (the subscript and superscript have been dropped). The circuit can now be solved for the transfer impedance Z_{12}. Defining $Z_g = 1/i\omega C_g, Z_{q1} = 1/i\omega C_{q1}$ and $Z_{q2} = 1/i\omega C_{q2}$, we find

$$Z_{12} = \frac{Z_{q1}Z_{q2}Z_{in}(\delta_0)}{(Z_g + Z_{q2})(Z_g + Z_{in}(\delta_0))} \times aK_0(d/\delta_p) \tag{5.66}$$

where we have used $I_{q1} \approx V_{q1}/Z_{q1}$ (valid for $C_{q1} \gg C_g$), where I_{q1} is the current applied at port 1. Notice that since Z_{in} is imaginary, Z_{12} is also imaginary. For large coupling impedance $Z_g \gg Z_{q2}, Z_{in}(\delta_0)$, eq. (5.66) simplifies to

$$Z_{12} = \frac{Z_{q1}Z_{q2}Z_{in}(\delta_0)}{Z_g^2} \times aK_0(d/\delta_p) \tag{5.67}$$

We use the following expression for the coupling strength between transmon qubits and the TM_{00} transmission line

$$g = \frac{C'_g}{2}\sqrt{\frac{\omega_q v}{C_q C'_r(\delta_0)}} = \frac{C'_g}{2}\sqrt{\frac{\omega_q Z_{00}^{TM}(\delta_0)}{C_q}}v \tag{5.68}$$

where v is the phase velocity of the TM_{00} transmission line in eq. 5.55 (the subscript and superscript have been dropped); $C'_r(\delta_0) = 1/(vZ_{00}^{TM}(\delta_0))$ is the capacitance per unit length of the transmission line at δ_0; and C'_g is the coupling capacitance per unit length between the qubit and the transmission line, where $C_g = C'_g\delta_0$. Substituting

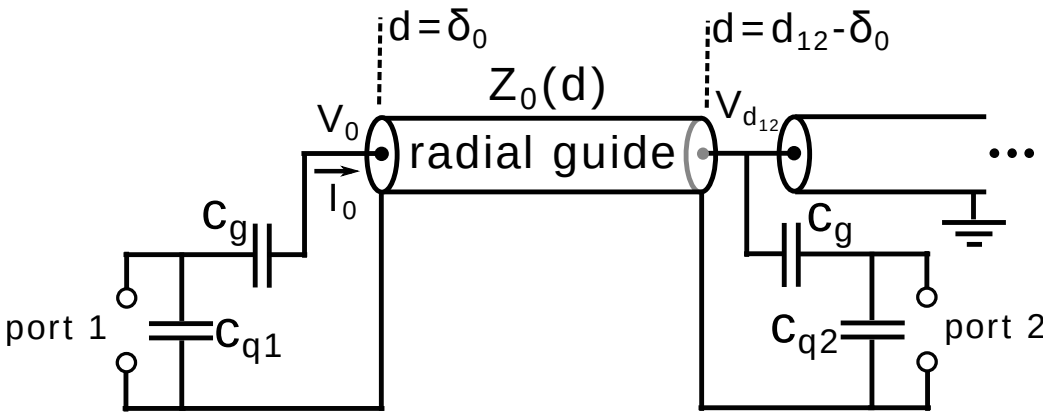

Figure 5.10: **Circuit model for qubits coupled by radial TM_{00} mode:** Two transmon qubits (with junctions replaced by ports), separated by distance d_{12} and coupled by the transmission line representation of the TM_{00} mode of a radial parallel-plate waveguide.

eqs. (5.67) & (5.68) into eq. (5.60), and using eq. (5.54) to relate the characteristic and input impedance, we find

$$J_{12} = -2\mathrm{Im}[g^2]\frac{\omega_q}{(v/\delta_0)^2}K_0(d_{12}/\delta_p)/K_1(\delta_0/\delta_p) \tag{5.69}$$

where g^2 and v are both negative imaginary. Here, we have used reciprocity to set $Z_{21} = Z_{12}$. Finally, we redefine $g \to |g| \times (K_1(\delta_0/\delta_p))^{1/2}$ to arrive at the general expression for qubits i and j

$$J_{ij} = -2g^2\frac{\omega_q}{(|v|/\delta_0)^2}K_0(d_{ij}/\delta_p) \tag{5.70}$$

This is the main result of this chapter. The spatial dependence of the coupling is all contained in the $K_0(d_{ij}/\delta_p)$ term. For $d_{ij} \gg \delta_p$, it has the simple asymptotic form

$$K_0(d_{ij}/\delta_p) \to \sqrt{\pi/2} \times e^{-d_{ij}/\delta_p}/\sqrt{d_{ij}/\delta_p} \tag{5.71}$$

The J coupling decays exponentially at a rate given by the plasma penetration depth, with an extra $1/\sqrt{d}$ dependence. This is what we would intuitively expect – excitations decay away exponentially below the plasma frequency, with an extra $1/\sqrt{d}$ dependence that takes into account that the waves are travelling radially outwards in 2D. We would also expect the same spatial dependence for other cavity-mediated crosstalk quantities. To show this is true for the coupling ε_{ij} of drive line j to qubit i, we use another impedance formula from Ref. [92], discussed in Chapter 2 (eq. 2.88), and restated below

$$\varepsilon_{ij} = \sqrt{\frac{\omega_i}{2\hbar L_i}}\mathrm{Im}[Z_{ij}(\omega_i)]\frac{e^{i\theta_j}C_j}{\sqrt{1+\omega_j^2 Z_0^2 C_j^2}} \tag{5.72}$$

Importantly, $\varepsilon_{ij} \propto \mathrm{Im}[Z_{ij}(\omega_i)]$, from which it directly follows that

$$\varepsilon_{ij} \propto K_0(d_{ij}/\delta_p) \tag{5.73}$$

This is because the coupling ε_{ij} will also be mediated by the TM_{00} mode, and so the transfer impedance between drive line j and qubit i will have a similar form to eq. 5.67. Since the radiative relaxation time of qubit i through control line j satisfies $T_{rad}^{ij} \propto 1/|\varepsilon_{ij}|^2$ (eq. 2.90), it also follows that

$$T_{rad}^{ij} \propto (K_0(d_{ij}/\delta_p))^{-2} \tag{5.74}$$

The contribution to the radiative relaxation of a qubit from distant control lines drops off exponentially.

We now discuss some of the main implications of these results. From eq. 5.41, it follows that for $\omega \ll \omega_p$

$$\delta_p \approx 1/\sqrt{\mu\epsilon_0\epsilon_r}\omega_p \tag{5.75}$$

Thus, if the frequencies of qubits, resonators and drives are much less than the plasma frequency, the penetration depth of their excitations are approximately frequency independent. Substituting in eq. 5.15 for ω_p results in the following

$$\delta_p \approx \frac{a}{\sqrt{2\pi}}[\ln(\frac{a}{r}) - \Pi] \tag{5.76}$$

where Π is a numerical factor defined in eq. 5.15, with value $\Pi \approx 1.31$. This provides a very simple analytical prediction for the penetration depth, that depends only on r and a. It is proportional to the shunt separation a, and decreases significantly with increasing r. For $\omega \ll \omega_p$, δ_p is also independent of ϵ_r. This is interesting, as it tells us that engineering the relative permittivity inside inductively shunted cavities (for instance with vacuum regions) will not help to decrease the penetration depth of cavity-mediated crosstalk. Finally, while eq. 5.76 is only valid for $r/a < 0.1$, we expect the description of cavity-mediated crosstalk (including eqs. 5.70, 5.73 & 5.75) developed in this section to remain valid for $r/a > 0.1$ so long as $\lambda \gg a$, where λ is the wavelength of the excitation defined in condition (3). For example, for a qubit at $\omega_q/2\pi = 5\,\mathrm{GHz}$ inside a cavity with $\epsilon_r = 11.45$, $\lambda \approx 18\,\mathrm{mm}$, and so, if $a = 2\,\mathrm{mm}$, we expect the plasma model to remain valid even if $r/a > 0.1$.

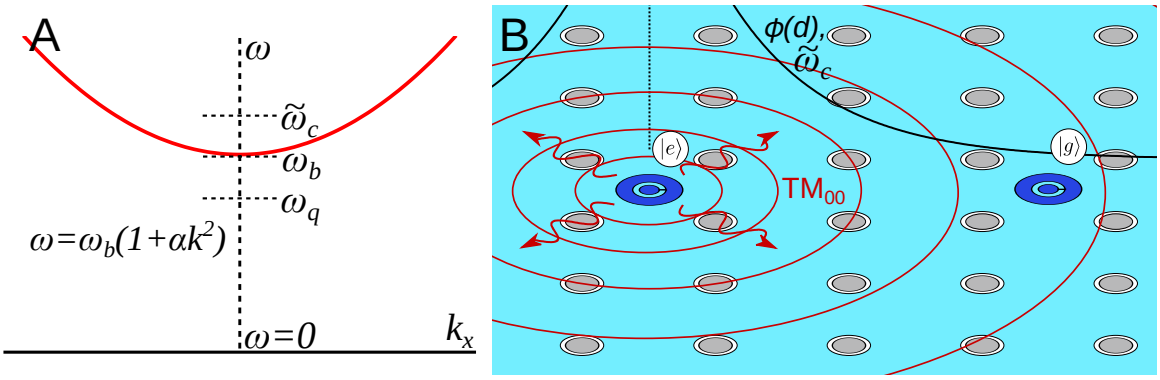

Figure 5.11: **Bound state mediated qubit coupling:** (**A**) 2D quadratic dispersion curve projected along $k_y = 0$. A qubit with frequency $\omega_q < \omega_b$ 'seeds' an effective cavity with frequency $\tilde{\omega}_c$. (**B**) An excited qubit can interact with distant qubits through the effective cavity, which has an exponentially decaying wave function $\phi(d)$. Alternatively the interaction can be viewed classically as mediated by the radial TM_{00} waveguide mode of a parallel-plate waveguide.

5.5.3 Bound states model for qubit-qubit coupling

A similar expression for J can be derived by instead considering the interaction between qubits meditated by the new distribution of modes in the inductively shunted cavity.

Using the plasma model, the mode spectrum inside the inductively shunted cavity is given by eq. 5.18, valid for $r \lesssim 0.1a$. Using the circuit model, the mode spectrum is given by eq. 5.24, valid for $r \gtrsim 0.1a$. Both spectrums are characterised by a 2D quadratic dispersion around a cutoff at $k_x = k_y = 0$. We restate eq. 5.18 below in terms of angular frequency

$$\omega_k = \omega_p(1 + \frac{1}{2\mu_0\epsilon_0\epsilon_r\omega_p^2}|\boldsymbol{k}|^2) \tag{5.77}$$

where ω_k denotes the cavity mode frequency. This is just like a band curve of a photonic crystal, having a band-gap below ω_p (Fig. 5.11(A)). In fact, the inductively shunted cavity can be thought of as a photonic crystal in the limit $\ell_x/a, \ell_y/a \to \infty$, with the metal cylinders behaving as the periodic variation of the dielectric constant, having permittivity $\epsilon \to \infty$. This kind of periodic metallic structure is sometimes called a metallic photonic crystal [157, 159].

The dispersion is characterised by a van Hove singularity at $k_x = k_y = 0$, where there is a singularity in the density of states $g(\omega)$. If qubits are close in frequency to

the van Hove singularity, their interaction with it will dominate over their interaction with the modes further away, and so the quadratic dispersion in eq. 5.77 can be used to approximate the dispersion everywhere. Modelling the qubits as two level systems, the Hamiltonian for a single qubit at position $\boldsymbol{d} = 0$ inside the inductively shunted cavity is given by [173]

$$\hat{H} = \frac{\hbar\omega_q}{2}\hat{\sigma}_z + \hbar\int d\boldsymbol{k}\omega_k \hat{a}^\dagger_{\boldsymbol{k}}\hat{a}_{\boldsymbol{k}} + \hbar g\int d\boldsymbol{k}(\hat{\sigma}^+\hat{a}_{\boldsymbol{k}}E_{\boldsymbol{k}}(0) + \hat{a}^\dagger_{\boldsymbol{k}}\hat{\sigma}^- E^*_{\boldsymbol{k}}(0)) \tag{5.78}$$

where $\hat{a}^\dagger_k$ and $\hat{a}_k$ are the creation and annihilation operators of the photonic modes, g is the interaction of the qubit with these modes (assumed to be independent of k), and $E_k(\boldsymbol{d})$ are the spatial wave functions of the photonic modes, which have Bloch form due to the periodicity of the cylinder array $E_{\boldsymbol{k}}(\boldsymbol{d}) = e^{i\boldsymbol{k}\cdot\boldsymbol{d}}u_{\boldsymbol{k}_0}(\boldsymbol{d})$, where $\boldsymbol{k}_0$ is the wave vector at the cutoff frequency. The integration is carried out over the Brillouin zone.

Following very closely Ref. [173], which considers this Hamiltonian in the context of cold-atoms in photonic crystals, for a single excitation in the system and for qubits inside the band-gap, the Schrödinger equation $\hat{H}\left|\Psi\right\rangle = \hbar\omega\left|\Psi\right\rangle$ has the following dressed state solution [173]

$$\left|\phi\right\rangle = \cos(\theta)\left|e\right\rangle\left|0\right\rangle + \sin(\theta)\left|g\right\rangle\left|1\right\rangle \tag{5.79}$$

where $\left|g\right\rangle$, $\left|e\right\rangle$ are the qubit states, and $\left|0\right\rangle$, $\left|1\right\rangle$ are the ground state and effective excited state of the photonic modes, $\left|1\right\rangle = \int d\boldsymbol{k}c_{\boldsymbol{k}}\hat{a}^\dagger_{\boldsymbol{k}}\left|0\right\rangle$. Here, $c_{\boldsymbol{k}}$ are the amplitudes for the different photonic modes in the effective mode $\left|1\right\rangle$, and the angle θ determines how qubit-like or photon-like the excitation is. For a 1D photonic crystal with a quadratic band dispersion, the solutions for $c_{\boldsymbol{k}}$ and θ are provided in the supplementary material of Ref. [173]. The dressed state $\left|\phi\right\rangle$ is a bound state. Importantly, the photonic component has an exponentially decaying spatial wave function, in the 1D case given by [173]

$$\phi(d) = \int d\boldsymbol{k}c'_{\boldsymbol{k}}E_{\boldsymbol{k}}(d) = \sqrt{\frac{2\pi}{\delta_b}}e^{-|d|/\delta_b}E_{\boldsymbol{k}_0}(d) \tag{5.80}$$

where $c'_{\boldsymbol{k}} \propto c_{\boldsymbol{k}}$ and δ_b is the bound state length given by

$$\delta_b = \sqrt{\alpha\omega_b/(\omega_b - \omega_q)} \tag{5.81}$$

Here, α characterises the curvature of the band-edge, which we define $\omega_k = \omega_b[1 + \alpha(k - k_0)^2]$. Note that in Ref. [173] α is instead defined $\omega_k = \omega_b[1 + \alpha(k - k_0)^2/k_0^2]$,

which is divergent in our case since $k_0 = 0$. We have also made the assumption $(\omega_b - \omega_q) \gg \beta$ to arrive at this form for the bound state length, where $\beta = (\pi g^2 |u_{k_0}|^2 / \sqrt{4\alpha\omega_b})^{2/3}$ [173]; the general expression can also be found in this reference. The photonic component of this bound state behaves like a single photonic mode that is localised on the qubit with an exponentially decaying envelope. Physically, this can be understood as follows: the qubit acts like a defect in the periodic photonic crystal that induces a localised cavity. The effective frequency of this cavity is given by the average participating photonic mode frequency $\tilde{\omega}_c = \int d\boldsymbol{k} |c_{\boldsymbol{k}}|^2 \omega_k$. For a 1D photonic crystal $\tilde{\omega}_c \approx 2\omega_b - \omega_q$, again assuming $(\omega_b - \omega_q) \gg \beta$ [173]. The dressed state solution in eq. 5.79 can be mapped exactly to the single excitation dressed state solution of the Jaynes Cummings Hamiltonian (eq. 2.44) of this qubit and effective cavity mode [173], which allows for an intuitive description.

In the case multiple qubits are inside the photonic crystal, they can exchange excitations through their induced cavity modes, just as two qubits coupled to a single cavity can exchange excitations in the Jaynes Cummings model, as illustrated in Fig. 5.11(B). The result, found by tracing out the photonic modes in the multi-qubit extension of eq. 5.78, is a transverse coupling $\hat{H}_{int} = J_{ij}(\sigma_i^+ \sigma_j^- + \sigma_j^+ \sigma_i^-)$ between qubits i and j with the following spatial dependence in a 2D photonic crystal with quadratic dispersion around the cutoff [173, 174]

$$J_{ij} \propto E_{\boldsymbol{k}_0}(\boldsymbol{d}_i) E_{\boldsymbol{k}_0}(\boldsymbol{d}_j) K_0(d_{ij}/\delta_b) \tag{5.82}$$

This result is valid for $(\omega_b - \omega_q) \gg \beta$. In the inductively shunted cavity, $\boldsymbol{k}_0 = \{0, 0\}\mathrm{m}^{-1}$, while for qubits positioned in the same location in each unit cell $u_{\boldsymbol{k}_0}(\boldsymbol{d}_i) = u_{\boldsymbol{k}_0}(\boldsymbol{d}_j)$. In this case the spatial dependence simplifies to

$$J_{ij} \propto K_0(d_{ij}/\delta_b) \tag{5.83}$$

Interestingly, eq. 5.83 has exactly the same spatial dependence as we found by considering the cylinder array as an effective plasma medium and treating the inductively shunted cavity as a parallel-plate waveguide with a dominant radial TM_{00} mode. To test the agreement further, we read α off from eq. (5.77) and compare the predicted bound state length δ_b with the plasma penetration depth δ_p in eq. (5.41). We find

$$\delta_b = 1/\sqrt{\epsilon_0 \epsilon_r \mu_0 2\omega_p(\omega_p - \omega_q)} \tag{5.84}$$

This result holds for qubits close in frequency to the band-edge where the quadratic dispersion approximation is good, in which case $\omega_q \approx \omega_p$ and $\delta_b \approx \delta_p$ (using $\omega_p^2 - \omega_q^2 =$

$(\omega_p + \omega_q)(\omega_p - \omega_q)$). Thus the spatial dependence of qubit coupling for these two different models agrees well.

We note we can also use the bound states model to get some mileage out of the circuit model. Reading off α instead from eq. (5.24), we find

$$\delta_b = a\sqrt{\beta/2}\sqrt{1/(1-\omega_q/\omega_b)} \tag{5.85}$$

This last result will apply not just to qubits in inductively shunted cavities for $r/a > 0.1$, but more generally to qubits in 2D coupled cavity arrays.

We identify two interesting features of the agreement between the waveguide and the bound states model: (1) Both models are valid in completely different qubit anharmonicity limits. The waveguide model was valid in the limit that qubits are weakly anharmonic, due to the use of the impedance formula eq. 2.87, whereas the bound states model assumed qubits that are perfect 2-level systems, i.e. infinitely anharmonic. (2) The waveguide model is valid for qubit frequencies $\omega_q < \omega_p$ (so long as $\lambda \gg a$), whereas the bound states model results are valid for qubit frequencies close to the cutoff ω_b (but not too close as $(\omega_b - \omega_q) \gg \beta$ must also be satisfied). That both models agree suggests that the K_0 form of the spatial decay of J and other cavity-mediated crosstalk quantities might be good approximations irrespective of qubit anharmonicities and detunings from the plasma/cutoff frequency.

5.6 FE simulations of cavity-mediated crosstalk

We performed FE simulations of a realistic superconducting circuit device, and compared the results with the predictions of the previous sections. The HFSS simulation model of the device is shown in Fig. (5.12). This model is based on the coaxmon architecture discussed in Chapter 4. For the purpose of simulating cavity-mediated crosstalk qubit coupling circuitry and readout circuitry are not included in the model, although we illustrate how a nearest neighbour capacitive coupling network might be implemented in Fig. 5.12(C).

The model consists of a 21×21 array of concentric transmon qubit islands on a silicon ($\epsilon_r = 11.9$ in this simulation) substrate measuring $\ell_x = 42\,\text{mm}$, $\ell_y = 42\,\text{mm}$, $\ell_z = 0.5\,\text{mm}$, enclosed by a perfectly conducting cavity, inductively shunted by a 20×20 array of perfectly conducting cylinders. The qubit islands and cylinders

Table 5.2: **Fundamental mode frequency of device enclosure:** Simulated and predicted fundamental frequency of the enclosure in Fig. 5.12 (GHz) as a function of the inductive shunt radius (mm).

	0[a]	0.05	0.1	0.15	0.2	0.25	0.3	0.35	0.4
FE[b]	1.49	11.89	13.95	15.78	17.58	19.42	21.37	23.44	25.14
Eq. (5.17)	1.46	11.34	13.43	15.39	17.47	19.82	22.68	26.40	31.74

[a] no inductive shunts [b] HFSS eigenmode simulation

are spaced by $a = 2\,\text{mm}$, and each pair of qubit islands is capacitively coupled to an off-chip coaxial control line. The qubits have $C_J \approx 100\,\text{fF}$ and $L_J \approx 10\,\text{nH}$ at $f_{01} = 5\,\text{GHz}$, corresponding to $E_J/E_C \approx 80$, well in the transmon regime [14].

The fundamental mode frequency of the cavity over a range of cylinder radii is summarised in Table 5.2. In the absence of any cylinders, the fundamental frequency of the enclosure is well below the typical range of transmon frequencies, which would result in a high density of cavity modes around qubit frequencies. However, in the presence of the considered shunting arrays, the fundamental mode frequency is in all cases greater than 11 GHz. For $r/a > 0.1$, eq. (5.17) diverges from the simulation result as it breaks down due to Bragg scattering. For $r/a < 0.1$, we attribute the difference to the vacuum regions in the simulation model introduced by the control lines, which are not considered in eq. (5.17). Removal of the qubit pads results in small ($< 1\%$) changes to simulated cavity mode frequencies.

A reference qubit (drive) $j = 0$ was defined at the centre of the array, and the transverse coupling (drive-line coupling) to qubit $i = 1, 2, ..., 10$ was found by using the simple impedance formulas in Ref. [92], discussed in Chapter 2. We note that while simulating these properties between qubit (drive) j and qubit i, the Josephson junctions in all other qubits are replaced by open circuits. We re-express our results using

$$\Gamma^Q_{i,0} = J_{i,0}/J_{1,0} \tag{5.86}$$

$$\Gamma^D_{i,0} = \varepsilon_{i,0}/\varepsilon_{1,0} \tag{5.87}$$

These expressions eliminate the unknown prefactors in eqs. (5.70) & (5.73) considering qubits which couple equally to the evanescent waveguide mode. In this case we expect $\Gamma^Q = \Gamma^D$, since both are then only a measure of the spatial decay of the waveguide mode.

We find good agreement between simulation and the plasma-model of inter-qubit coupling and drive-line coupling for a range of qubit frequencies and shunt radii (see Fig. 5.13). When calculating the plasma penetration depth (eq. 5.41), we used the fundamental cavity frequency found from eigenmode simulation (Table 5.2) as the plasma frequency, rather than that from eq. (5.15). With this choice, we indeed find that the plasma model of inter-qubit coupling still agrees well with simulation for $r/a > 0.1$.

We confirm that the plasma penetration depth is of the order of the shunt separation, and decreases significantly with increasing shunt radius. We also confirm that for qubits well below the plasma frequency, the plasma penetration depth has only a weak dependence on the qubit frequency.

Note that although we have used coaxial qubits in this simulation, we expect the qubit geometry to only affect the coupling strength g to the TM_{00} waveguide mode, which will remain the dominant mode, and therefore expect good agreement with the model for other qubit geometries.

5.7 Discussion

In this chapter, we have shown how inductively shunting a cavity with a periodic array of cylinders can allow it to scale to arbitrary size in two dimensions, while having a cutoff frequency below which no photonic modes can exist. For qubits below the cutoff frequency, expressions have been found for how cavity-mediated crosstalk between qubits decays exponentially with spatial separation at a rate proportional to the shunt separation. These are useful properties where the aim is to build large 2D superconducting qubit arrays with nearest neighbour couplings, which we will use in the following chapter.

We conclude by commenting on some of the limitations of the work in this chapter. First, only square periodic inductive shunt arrays have been considered. This simplified the analysis, however, it may be advantageous to introduce disorder into the inductive shunt array, for instance to reduce the effective penetration depth. Determining expressions for the penetration depth in the presence of disorder would be interesting.

Secondly, throughout this chapter it has been assumed the inductively shunted cavity has no internal losses. This is justified by the fact the inductively shunted cavity can be made of a superconducting material such as aluminium, but a more careful treatment would allow for internal losses. For the plasma model, one consequence of including internal losses is the plasma permittivity would take the adjusted form [160]

$$\epsilon_p(f) = 1 - \frac{f_p^2}{f(f + i\gamma/(2\pi))} \tag{5.88}$$

where γ represents a damping term on induced currents in the plasma.

Finally, any real superconducting circuit quantum processor will require coupling circuitry between qubits to facilitate entangling gates. This circuitry should only slightly perturb the mediating TM_{00} waveguide mode because it lies perpendicular to the electric field of this mode, and so we anticipate the cavity-mediated crosstalk results in this chapter will not be significantly affected. However, this circuitry will introduce its own circuit mediated crosstalk channels, which might result in long-range crosstalk between qubits. This circuit mediated crosstalk is contingent on the type of coupling circuitry being implemented, and is beyond the scope of this chapter. We note that in an idealised lumped element representation, circuit mediated crosstalk between qubits that are nearest neighbour coupled by bus resonators decays exponentially with qubit distance [92]. Further study of circuit mediated crosstalk, and its separability from cavity-mediated crosstalk, would be an interesting avenue for future research.

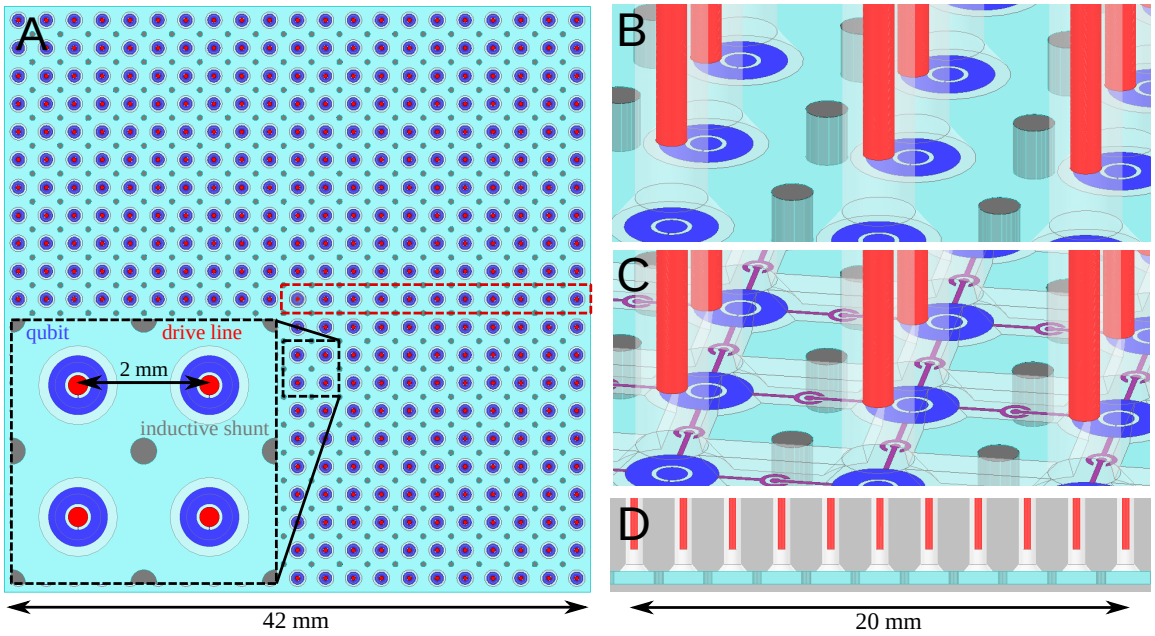

Figure 5.12: **Ansys Electronics Desktop FE simulation model:** (**A**) Top-down view of the model. The qubits for which J and drive-line cross-talk were simulated are indicated by the dashed red line. (**B**) View showing the drive lines (red) above each qubit, and the inductive shunts (gray, here shown with $r = 0.2\,\mathrm{mm}$) passing through the substrate. (**C**) Illustrating how the design can be modified to include a nearest-neighbor direct capacitive coupling network (purple) between qubits. (**D**) Cross-section of the dashed-red region in (a). The model is enclosed by perfect conductor (shown in gray), representing an ideal superconducting enclosure.

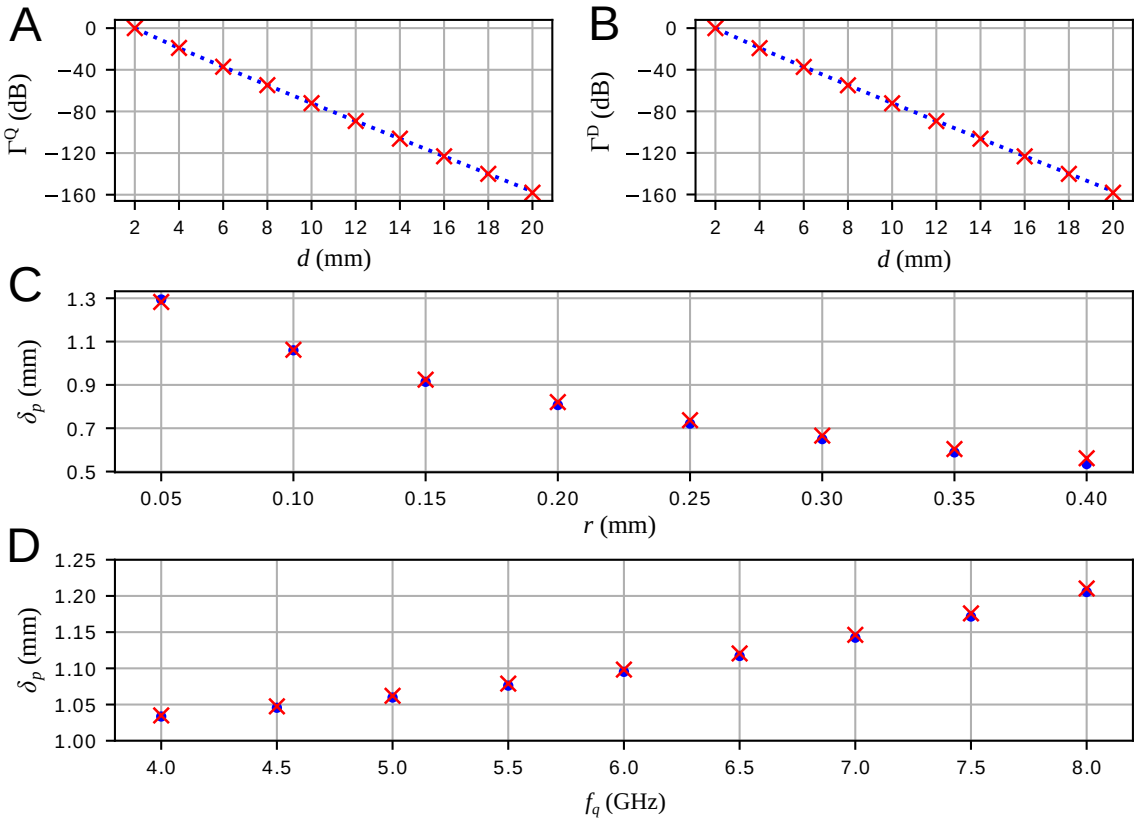

Figure 5.13: **Comparison of simulation results and analytical predictions for crosstalk decay:** (**A**) & (**B**) Inter-qubit and drive-line to qubit crosstalk for $r = 0.1\,\text{mm}$, $f_q = 5\,\text{GHz}$. Red crosses are FE simulation values, and blue dotted lines are the prediction of eqs. (5.70), (5.73)& (5.41). (**C**) & (**D**) Plasma penetration depth against shunt radius and qubit frequency. Red crosses are calculated using eq. (5.41) and blue dots are found by fitting eq. (5.70) to the FE simulation Γ^Q values, with δ_p as the sole fit parameter. In (C) $f_q = 5\,\text{GHz}$, and in (D) $r = 0.1\,\text{mm}$.

Chapter 6

Design and Construction of a Tileable Circuit

In this chapter, we present a methodology for designing and constructing tileable superconducting circuit devices that integrates the off-chip wiring and reverse-side readout of the coaxmon architecture presented in Chapter 4, with an inductively shunted cavity enclosure as described in Chapter 5. This involves the development of a novel enclosure design featuring CNC machined pillars, and the exploration of CNC drilling and laser drilling processes to make holes in superconducting circuit substrates. It further involves the development of a waferscale fabrication process for making coaxmon circuits featuring reverse-side resonators. The methodology is then applied to construct a four-qubit demonstration device that contains within it a single unit cell of the architecture.

6.1 Unit cell design

We start by looking at the Ansys HFSS simulation model in Fig. 6.1. In this model, a $2\,\text{mm} \times 2\,\text{mm} \times 0.475\,\text{mm}$ section of silicon substrate (light blue) is bounded above and below by the perfectly conducting walls of an enclosure (light gray). On the upper-side of the substrate (the qubit-side) the silicon is separated from the enclosure by a $0.125\,\text{mm}$ vacuum region, whereas on the lower side (the resonator-side) the substrate directly contacts the enclosure. The corners of four concentric transmon qubits (dark blue) and the corners of four reverse-side spiral resonators (green) are shown. These pads are all modelled as perfectly conducting sheets. The corners of the off-chip control wiring pins are shown in red and yellow for the qubit and resonator sides respectively. These are modelled as perfect conductors, and separated from the perfectly conducting enclosure by cylindrical vacuum regions. In the centre

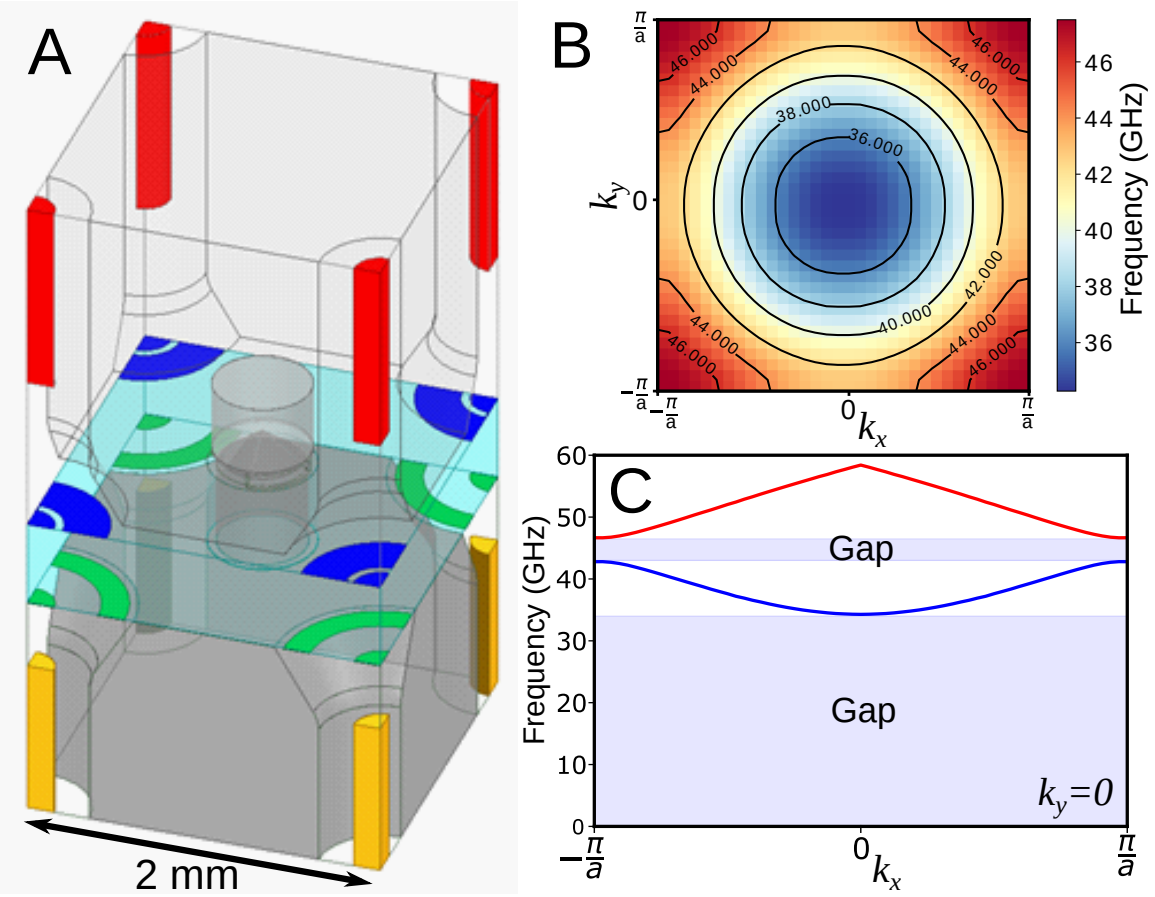

Figure 6.1: **HFSS unit cell simulation:** (**A**) HFSS model of a single unit cell of a tileable superconducting circuit design, described in the main text. (**B**) Simulated 2D band-structure of the infinite construct formed by tiling the plane with this unit cell, showing the lowest band. (**C**) Simulated band-structure of lowest two bands along $k_y = 0$ for this construct.

of the model, a perfectly conducting cylinder with radius 0.25 mm passes through the substrate and inductively shunts the lower and upper halves of the enclosure.

This model forms a unit cell, containing a single inductive shunt and a single $(4 \times 1/4)$ controllable and measurable qubit. By assigning linked boundary conditions [165] on the non-perfectly conducting boundaries of the model, the eigenmode solver in HFSS can map out the band-structure of the infinite construct formed by tiling the plane with this unit cell. In Fig. 6.1(B), the simulated band structure of the lowest band is shown along k_x and k_y. The band is characterised by a cutoff at 34.3 GHz with a band gap below extending to 0, with a quadratic dispersion around the cutoff frequency. This is in agreement with the results in Chapter 5, and we associate the cutoff fre-

quency with the plasma frequency of the meta-material formed by the periodic array of cylinders.

We can compare the cutoff frequency with the prediction of eq. 5.15. Ignoring the cylindrical vacuum regions due to the control wiring, we find the effective relative permittivity of the tiled construct to be $\epsilon_r = 3.6$ using eq. 5.8, using that $\epsilon_r = 11.45$ for the 0.475 mm thick silicon substrate layer, and $\epsilon_r = 1$ for the 0.125 mm thick vacuum layer between the qubit-side of the substrate and the enclosure. For $r = 0.25$ mm and $a = 2$ mm, the predicted plasma frequency is then 35.9 GHz, which differs from the cutoff frequency found in simulation by $\sim 5\%$. We can also compare the curvature of the simulated quadratic dispersion with that predicted by eq. 5.77. The predicted curvature is $\alpha = 2.45 \times 10^{-7}\text{m}^2$, using the predicted plasma frequency $\omega_p/2\pi = 35.9$ GHz, which differs from the simulated curvature $\alpha_{sim} = 2.20 \times 10^{-7}\text{m}^2$ by $\sim 10\%$, where the simulated curvature is found using

$$\alpha_{sim} = \frac{1}{2\omega_p} \frac{\partial^2 \omega}{\partial |\boldsymbol{k}|^2} \bigg|_{\boldsymbol{k}=\boldsymbol{k_0}} \tag{6.1}$$

here using the simulated cutoff frequency $\omega_p/2\pi = 34.3$ GHz. Fig. 6.1(C) shows the first two simulated bands plotted along $k_y = 0$. A second band gap is visible between 42.8 GHz and 46.7 GHz, followed by a second band that extends to 58.4 GHz.

In Fig. 6.2 we show a visualisation of the construct formed by tiling this unit cell. The off-chip wiring design is such that qubits and readout resonators remain individually addressable as the unit cell is tiled (Fig. 6.2(C)). Superconducting qubits and resonators typically operate in the frequency range $4-10$ GHz, and so $(\omega_{circuit}/\omega_p)^2 \ll 1$. As a result, eq. 5.75 will be a good approximation for the penetration depth δ_p. Inserting $\epsilon_r = 3.6$ and $\omega_p/2\pi = 34.3$ GHz, we predict the penetration depth for cavity mediated crosstalk to be $\delta_p = 0.73$ mm in this construct. The 2 mm qubit pitch means cavity mediated crosstalk is thus predicted to decay by over an order of magnitude for each increase in qubit separation.

Since there is a vacuum gap between the qubit-side of the substrate and the enclosure, and no on-chip wiring or readout-resonators on the qubit-side of the substrate, qubit coupling circuitry has relatively free rein on the substrate. The capacitance to ground of such circuitry can be adjusted by milling out tailored vacuum regions in the enclosure, without significantly affecting the plasma-frequency or penetration depth for

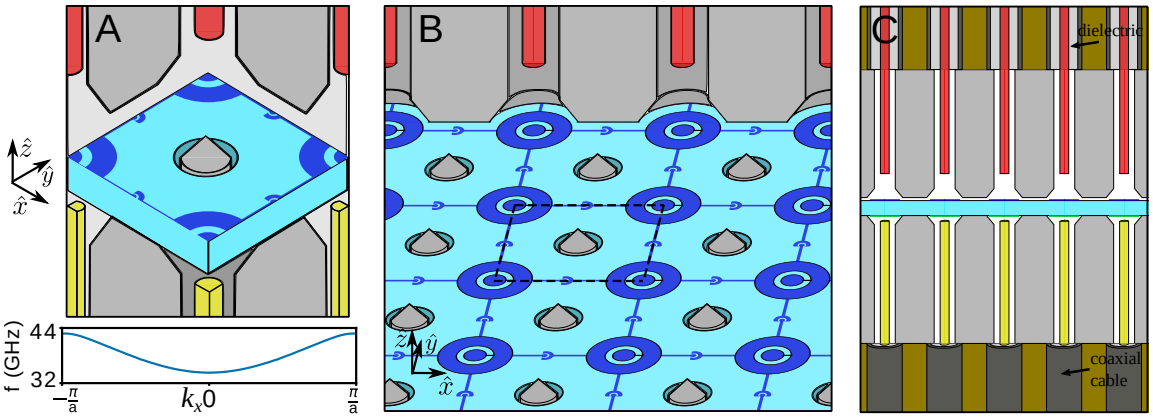

Figure 6.2: **Tileable construct:** (**A**) Visualisation of the unit cell shown in Fig. 6.1, here depicted with capacitive coupling circuitry; along with the band stucture of the lowest band along $k_y = 0$. (**B**). Cut-away of a construct formed by tiling this unit cell. (**C**) Cross-section showing the off-chip wiring, provided by coaxial cables.

cavity-mediated crosstalk. In Fig. 6.2(B), we depict a simple nearest-neighbour direct capacitive coupling network between qubits, although the design may accommodate more advanced coupling circuitry.

This construct is thus motivated as an architecture for creating large 2D arrays of nearest neighbour coupled superconducting qubits, that can be formed by simply tiling a unit cell.

6.2 Circuit design and fabrication

Here, we discuss the circuit design and fabrication process developed to be able to create coaxmon circuits featuring 2D arrays of qubits and reverse-side resonators, and featuring holes in the circuit substrate for compatibility with inductively shunted cavity enclosures.

In the following, we focus on designing a circuit without qubit-qubit couplers. This is with the aim of constructing a proof-of-principle device to characterise coherence and crosstalk in the architecture prior to the inclusion of coupling circuitry. Including coupling circuitry is not expected to significantly effect the form of enclosure mediated crosstalk between qubits (see Chapter 5), however it will introduce circuit mediated crosstalk. For a direct capacitive coupler network, the J coupling between qubits will cause ZZ crosstalk governed by eq. 7.27, and control line crosstalk $\vartheta_{ij} = (J_{ij}/\Delta_{ij})^2$ in the limit $J_{ij}/\Delta_{ij} \gg \varepsilon_{ij}/\varepsilon_{jj}$ (see eq. 7.16), where these equations are taken from

Chapter 7. Taking values $\Delta_{ij}/2\pi = 450\,\text{MHz}$ and $J/2\pi = 10.7\,\text{MHz}$ from the coupled coaxmon device in Ref. [140] limits nearest-neighbour qubit control line selectivity to $\vartheta \sim -30\,\text{dB}$, significantly worse than the $\vartheta \sim -55\,\text{dB}$ selectivity measured in Chapter 7. Taking the measured ZZ crosstalk in the same reference, $2\chi_{ZZ}/2\pi = -0.66\,\text{MHz}$, would introduce gate errors to simultaneous 20 ns single-qubit gates of $\sim 7 \times 10^{-4}$, using eq. 7.43, significantly higher than the $1.8(4) \times 10^{-4}$ simultaneous single-qubit gate errors measured in Chapter 7. To mitigate these issues, flux tunable couplers with a large on-off ratio [103, 133–137] could be used rather than fixed capacitive coupling circuitry. In this case, the device crosstalk would ideally approach that of the device without qubit-qubit couplers during single-qubit gate operations. This would require each coupler to have its own flux control line, necessitating $2n$ flux control lines in a device featuring a square array of n nearest-neighbour coupled qubits. Selective, off-chip flux control of concentric qubits has been previously demonstrated in the coaxmon architecture [144], making this a promising approach if the increased control electronics and fridge wiring overhead can be tolerated.

6.2.1 Circuit design

The circuit design was guided by the following general goals: (1) Reduce the qubit-resonator coupling g. As discussed in Chapter 4, previous concentric qubit and reverse-side spiral resonator pairs measured in our lab have had large coupling strengths up to $g/2\pi = 460$ MHz. Here, it was desired to target smaller coupling values $g/2\pi \approx 150\,\text{MHz}$. (2) Make use of the intrinsic Purcell filtering effect described in Chapter 4 to suppress qubit radiative decay through the resonator control line. (3) Ensure qubit relaxation times are not radiatively limited, by setting $T_{1,rad} \gg 100\,\mu\text{s}$. (4) Put qubits well into the transmon regime, by making $E_J/E_C \gtrsim 100$. (5) Achieve readout parameters typical of planar superconducting circuit designs, with external resonator decay rates $\kappa_{ext}/2\pi \sim 5\,\text{MHz}$; and $|\chi|/\kappa_{ext} \approx 0.5$ for optimum qubit readout fidelity (see Chapter 7, section 3). (6) Reduce the electric field energy participation p in interface layers.

To achieve these goals, we performed black-box quantisation (BBQ) simulations of a single qubit-resonator pair inside a four-qubit device model (Appendix B) while varying certain physical dimensions in the circuit. This process was carried out in a non-systematic way and could be improved. The varied dimensions common to all the qubits and resonators are listed in Table 6.1 along with the chosen values.

Table 6.1: **Common circuit dimensions:** Circuit dimensions common to all qubit-resonator pairs. A concentric qubit and spiral resonator with these dimensions are shown in Fig. 4.2 and Fig. 4.3 in Chapter 4. The pin distances are as defined in Fig. 4.5.

Dimension	Value (µm)
Qubit inner radius, r_i^q	150
Qubit middle radius, r_m^q	200
Qubit outer radius, r_o^q	450
Qubit pin distance, d_{pin}^q	900
Resonator inner radius, r_i^r	150
Resonator middle radius, r_m^r	400
Resonator outer radius, r_o^r	550
Resonator spiral width, w	5
Resonator pin distance, d_{pin}^r	200 (400*)

Table 6.2: **Simulated circuit parameters:** Simulated circuit parameters for a qubit-resonator pair, found by performing black box quantisation (BBQ) and solving the resultant Hamiltonian numerically. The resonator spiral coefficient a is 17 µm in this simulation.

Parameter	BBQ simulated value
Qubit frequency, $\omega_q/2\pi$ (GHz)	5.43
Junction inductance, L_J (nH)	6.5
Intrinsic purcell filter frequency, $\omega_f/2\pi$ (GHz)	5.45
Resonator frequency, $\omega_r/2\pi$ (GHz)	8.2
Anharmonicity, $\alpha/2\pi$ (MHz)	-163
Josephson to charging energy ratio, E_J/E_C	170
Qubit-resonator coupling, $g/2\pi$ (MHz)	129
Single-photon stark shift, $2\chi/2\pi$ (MHz)	- 0.37
Resonator external decay rate, $\kappa/2\pi$ (MHz)	4.5 (0.33*)
Qubit radiative relaxation time, $T_{1,rad}$ (µs)	~ 4000

Table 6.3: **Distinct circuit dimensions and desired circuit parameters:** Circuit dimensions distinct to each qubit-resonator pair for the four-qubit device in section 6.3, and the desired distinct circuit frequencies. The spiral shapes are related to the spiral coefficients using eq. 4.7.

	Q_1/R_1	Q_2/R_2	Q_3/R_3	Q_4/R_4
Junction areas (µm^2)	0.2323^2	0.2369^2	0.2408^2	0.2441^2
Resonator spiral coefficients, a (µm)	16.94	17.28	17.61	17.88
Qubit frequencies, ω_q (GHz)	5.76	5.87	5.97	6.04
Resonator frequencies, ω_r (GHz)	8.3	8.4	8.5	8.6
Purcell filter frequencies, ω_F (GHz)	5.76	5.87	5.97	6.04

Table 6.2 shows the simulated circuit parameters for this qubit-resonator pair, where the BBQ equivalent circuit has been found using the Fosters method [85] and the Hamiltonian has been solved numerically. We have fitted L_J to put the qubit on resonance with the Purcell filter.

The results show that in simulation this qubit-resonator pair broadly achieves goals (1)-(4), however (5) is not achieved as the single-photon Stark shift is significantly below the desired value with $|\chi|/\kappa_{ext} \approx 0.1$. We only qualitatively attempted to achieve goal (6), by increasing the surface area to perimeter ratio of the qubit pads compared to previous coaxmon designs [144], and by filleting all sharp edges to reduce electric field divergences.

For the four qubit device described in section 6.3, it was decided to stagger the four qubit and resonator frequencies in steps of 100 MHz to avoid frequency collisions. The dimensions distinct to each qubit-resonator pair are shown in Table 6.3, along with the desired qubit, resonator, and Purcell filter frequencies. Note that the desired qubit frequencies are resonant with the desired Purcell filter frequencies. We also note here that during the actual assembly of this device, the distance d^r_{pin} was set to 400 µm due using the wrong steel control pin alignment piece (having height 4.1 mm rather than 4.3 mm) during step F of the control plug assembly. This has the important consequence of significantly reducing the expected external decay rate of all resonators from $\kappa_{ext}/2\pi \approx 4.5$ MHz to $\kappa_{ext}/2\pi \approx 0.33$ MHz.

6.2.2 Circuit fabrication

Having chosen circuit dimensions for the qubits and spiral resonators, GDSII format files for the patterns for circuit fabrication were generated using Python code written in collaboration with Shuxiang Cao, making use of the gdspy Python module [175].

Circuits were fabricated using a waferscale fabrication process that was developed in collaboration with Shuxiang Cao, Giulio Camponaro and Simone Fasciati, based on a chip-scale fabrication process previously developed by Joseph Rahamim and Michael Peterer [144, 176]. A waferscale fabrication process was developed for the following reasons: (1) Performing circuit fabrication prior to dicing is anticipated to reduce interface losses. (2) The reproducibility and uniformity of spin coated resist layers is improved [177]. (3) A waferscale process is able to make large circuits containing 2D arrays of thousands of qubits.

The recipe is now summarised. First, a double-side polished silicon wafer was cleaned in hydrofluoric acid (HF), followed directly by aluminium evaporation onto both sides of the wafer using a Plassys MEB 550 S2 UHV with load-lock, with a base oxidation chamber pressure of $\sim 1 \times 10^{-8}$ mbar. All circuit features except for the Josephson junctions were then defined by submerging the wafer in aluminium etchant after performing photolithography in an EVG620 mask alignment system to define an etching mask. The Josephson junctions were formed using a standard Dolan bridge double angle evaporation technique [178], with the bridges defined in a bilayer resist stack using electron-beam lithography (EBL) with a Raith 30keV EBL system. Steep angle (60°) shadow evaporation and a 'T-style' resist bridge were used to reduce the sensitivity of the junction area to the bridge thickness [176, 179]. The full fabrication recipe is presented in Appendix C. We note that the recipe had to be specialised due to the need to fabricate circuits on both sides of the wafer. This meant both sides of the wafer had to remain clean throughout the process, and the patterns on both sides of the opaque silicon wafer had to be aligned.

The Josephson junctions were also redesigned as part of this project with the goals of preventing aluminium 'flags' that do not adhere to the silicon surface, and removing sharp corners to reduce dielectric relaxation. An example of a junction made using a previous design, and a junction made using the adjusted design are shown in Fig. 6.3. The chosen junction dimensions and a more detailed discussion of the adjusted junction design are provided in Appendix D.

In fixed frequency superconducting circuit devices, the ability to accurately produce Josephson junctions with the desired inductance L_J is an important consideration as it directly affects the accuracy with which qubit frequencies can be set by the experimenter. In Appendix D, we quantify our ability to produce nominally identical junctions across a wafer by measuring the room temperature resistance of $0.04\,\mu m^2$ area Josephson junctions fabricated across a 3 inch wafer. We find a small local standard deviation of junction resistances of 1.9% for junctions fabricated within $850\,\mu m \times 320\,\mu m$ areas, and a larger 9.1% standard deviation for junctions fabricated across a $20\,cm^2$ area of this particular wafer. These results compare to 1.9% standard deviation in a $1\,cm \times 1\,cm$ area and 3.5% standard deviation in a $49\,cm^2$ area achieved in Ref. [142], in a systematic study across 38 wafers.

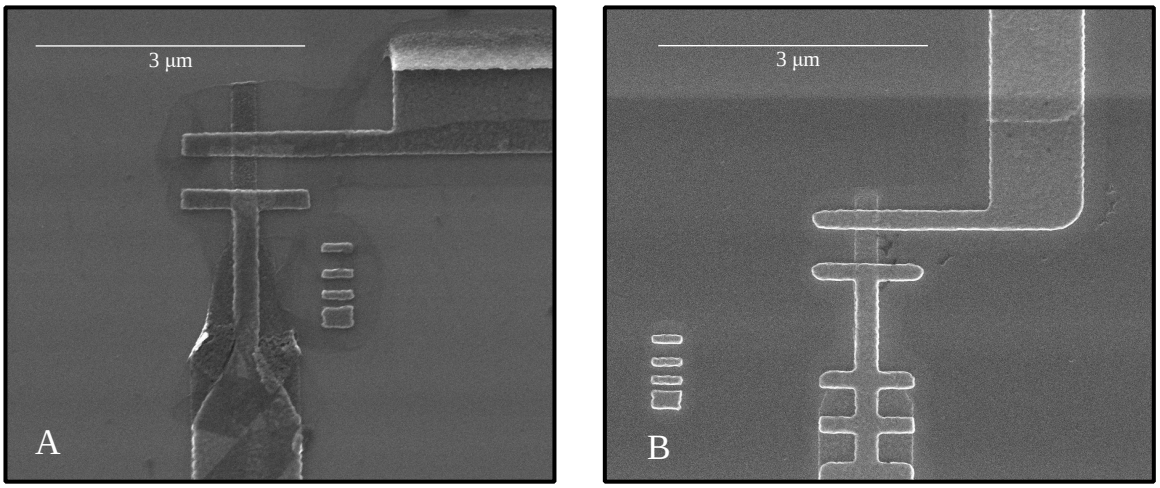

Figure 6.3: **Josephson junction design modifications:** SEM images (30keV) of double angle evaporation JJs. (**A**) Aluminium 'flags' that do not adhere to the silicon surface are visible in the lead-up to the junction and near the top right corner. (**B**) Adjusted design aimed at preventing these flags. The ridge features below the junction create undercuts that prevent flags, and the change in geometry prevents the flag visible in the top right corner of (A). A wide 375 μm resist bridge prevents tearing of the angle evaporated aluminium strip above the junction visible in (A). All edges are filleted to reduce sharp corners.

Another important consideration is systematic error leading to wafer to wafer variation in the junction inductance L_J. In the device measured in the next chapter, a large systematic error (that we attribute to exposing the oxidation chamber of the Plassys evaporator to atmosphere between evaporations) meant the junction inductance L_J of all four qubits was significantly higher than designed. The result was all qubit frequencies were in the $\sim 4-4.2$ GHz range rather than the desired $\sim 5.8-6$ GHz range in the circuit design. The main consequence of this is that the single-photon Stark shift of all resonators was significantly reduced compared to the value in Table 6.2.

A selection of images of qubits and spiral resonators taken at different stages of the waferscale fabrication process are shown in Fig. 6.4. Fig. 6.5 shows a wafer after the double sided fabrication process is complete. This particular wafer includes the circuit measured in the next chapter.

6.2.3 Substrate machining

CNC machining processes were used to both dice the wafer and to drill holes in the circuit substrate to make it compatible with an inductively shunted enclosure. This

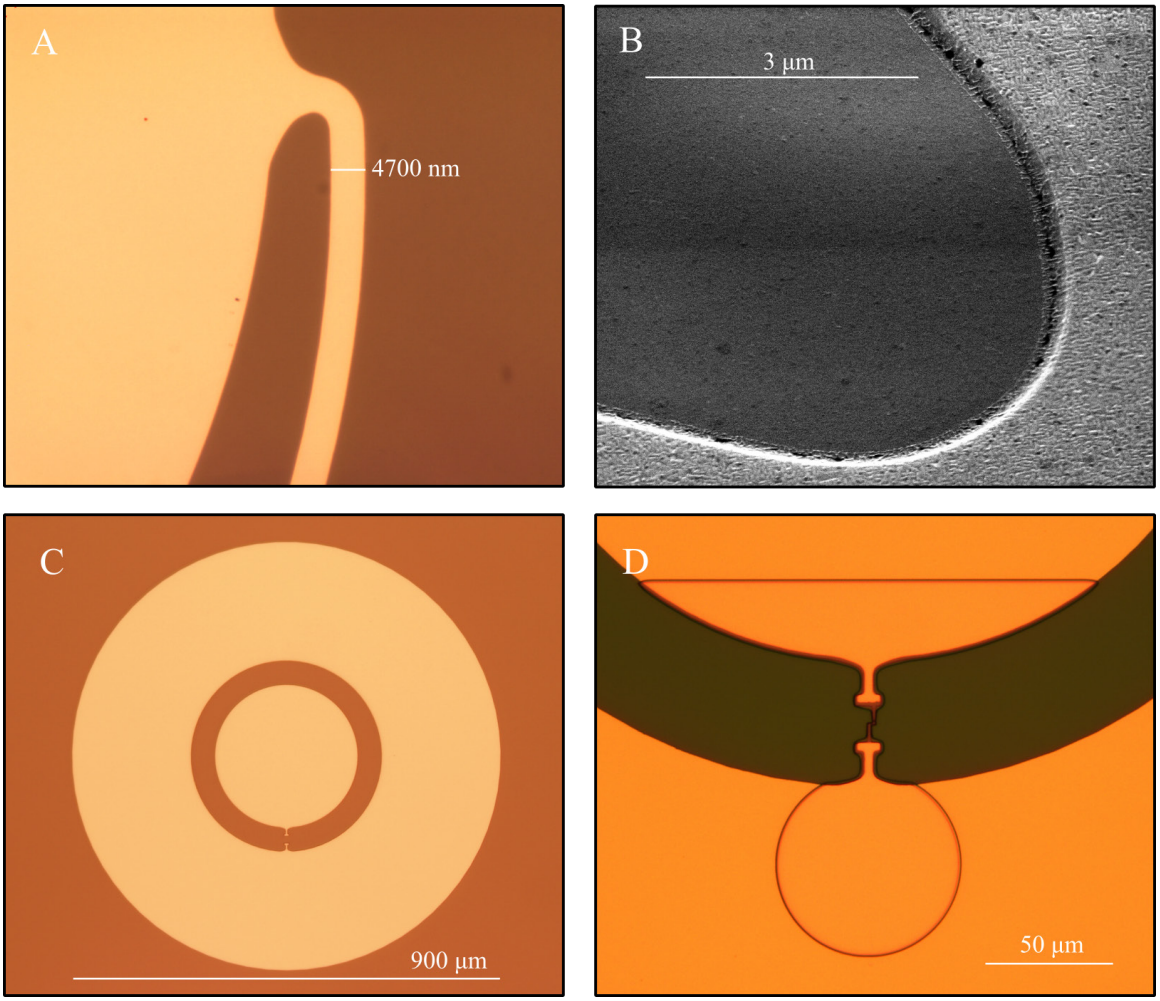

Figure 6.4: **Assorted waferscale fabrication images:** (**A**) Optical image (100x mag.) of spiral resonator post fabrication (prior to dicing). The smooth transition from the inner pad to the spiral is visible. The spiral thickness deviates from the desired 5 µm by $\sim$ 300 nm. (**B**) SEM image (20keV) of resonator spiral edge post fabrication (including dicing). Taken at angle so edge profile is visible. This image was taken by Simone Fasciati. (**C**) Optical image (5x mag.) of qubit pads prior to JJ fabrication. (**D**) Optical image (20x mag.) of EBL defined overlap pads and JJ after development and prior to double angle evaporation. These images are all taken from circuits on the wafer shown in Fig. 6.5.

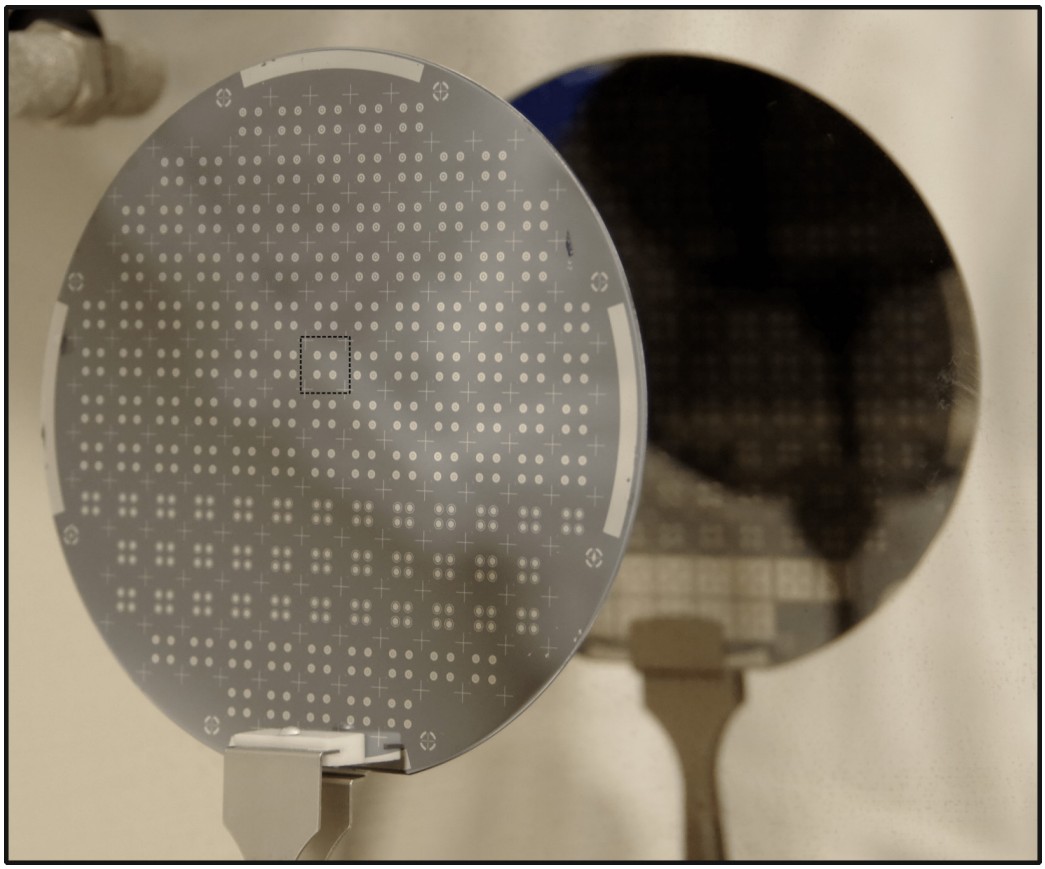

Figure 6.5: **Processed double-side wafer:** Optical image of wafer ready for dicing. Reverse-side resonator patterns are visible in the reflection. The four-qubit circuit measured in Chapter 7 is highlighted by the dashed square.

machining was performed in collaboration with James Gates, Lewis Carpenter, and Paul Gow at the University of Southampton, who have expertise in substrate machining to high $< 10\,\mu m$ tolerances for photonics applications [180]. We performed junction tests to ensure that drilling holes through silicon chips would not break Josephson junctions already fabricated on these chips. We also explored using femtosecond laser machining as an alternative method to drill these holes. The results of the drilling tests are discussed in the next section.

The CNC machining process was as following. First, a layer of S1805 Microposit photoresist was spun onto both sides of the wafer to act as a protective layer. The wafer was then diced using a DISCO DAD3430 Dicing Saw, with a $70\,\mu m$ kerf blade. The chips were separated and the protective resist was removed. After inspection and room temperature resistance measurements, a selection of chips were chosen. A new layer of protective resist was then spun onto these chips, and holes were drilled into

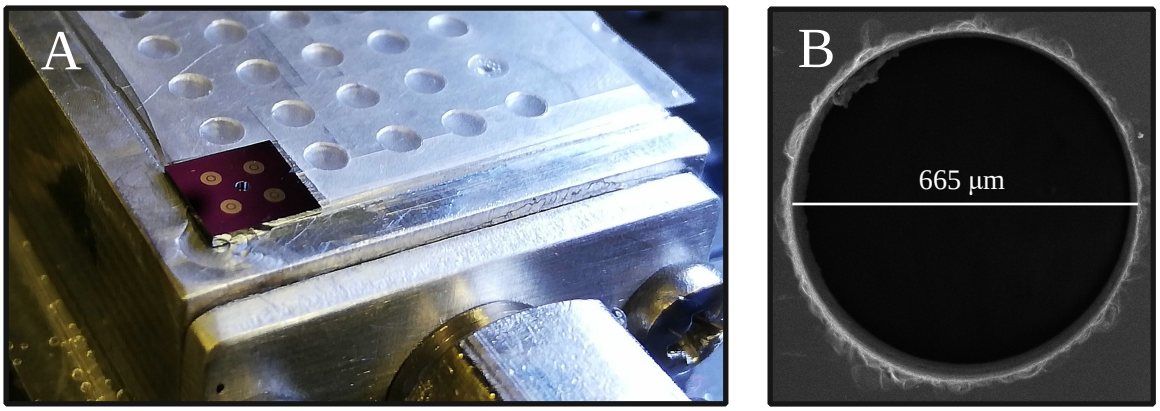

Figure 6.6: **CNC drilled hole in four-qubit device:** (**A**) Optical image of the four-qubit chip mounted on the Loxhom µ6 6-axis micro-machine, just after drilling the central hole. A protective layer of S1805 resist is visible on the chip. (**B**) SEM image (30keV) of this hole, after the protective resist has been removed.

each chip using a Loxham Precision µ6 Drill. The targeted diameter of the drilled holes was 650 µm. The drilled holes were aligned to markers in each chip using a custom optical alignment rig developed by our collaborators.

Fig. 6.6(A) shows an example four-qubit device with the same design as that measured in Chapter 7, mounted on the Loxham Precision µ6 Drill after a hole has been drilled in the centre of the chip. Fig. 6.6(B) shows an SEM of the drilled hole, having a diameter of 665 µm. The drilling parameters were not optimised, and we expect the visible damage to the silicon at the hole edge can be reduced. The protective resist was then removed. The recipe for preparing and removing the protective resist layer for both dicing and drilling processes is provided in Appendix C. In future, it would be advantageous to perform waferscale device drilling prior to dicing, to reduce the number of resist preparation and removal steps.

An HFSS eigenmode simulation of the electric field participation ratio p of qubits in the four-qubit model in Appendix B inside a cylindrical shell centred on the drilled hole, with inner-diameter 650 µm, outer-diameter 700 µm, and 475 µm thickness gives: $p_{shell} \approx 1 \times 10^{-7}$ at 4 GHz. This value is between three to four orders of magnitude smaller than the participation in the interface layers that are thought to play a major role in dielectric relaxation [59, 63, 66, 67]; illustrating that even if CNC drilling is quite destructive to the silicon within this volume as appears in Fig. 6.6(B), the effect on qubit coherence is suppressed.

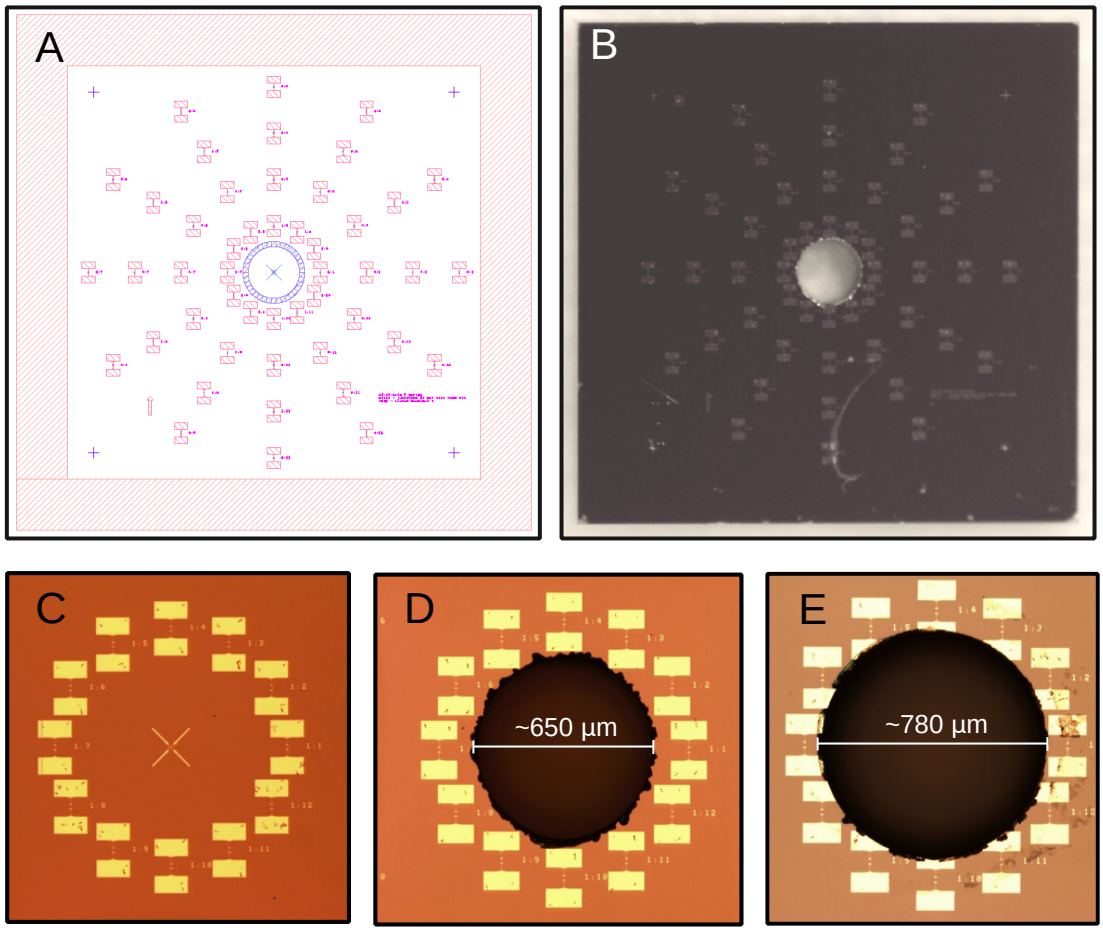

Figure 6.7: **Josephson junction drilling tests:** (**A**) 'Bullseye' pattern containing 46 junctions arranged in 4 rings, with radii of $\{450, 900, 1350, 1800\}$ µm from the chip centre. (**B**). Optical image of one of these chips, with a CNC drilled hole in the centre. Note that the scratch bottom centre of this chip was caused by probe tips and was not related to drilling. (**C**) Optical image of central ring of junctions prior to drilling. (**D**) Optical image of central ring of junctions after CNC drilling. (**E**) Optical image of central ring of junctions after femtosecond laser drilling.

6.2.4 Silicon drilling investigation

Four chips were fabricated with the 'bullseye' pattern shown in Fig. 6.7(A), each containing 48 Josephson junctions with 200 nm × 200 nm areas. The resistance of the junctions were measured at room temperature and a protective layer was spun onto both sides of each chip. A nominally 600 µm hole was then drilled through the centre of each chip, before the resist was removed and the resistances of the junctions measured again. In two of the chips, the hole was CNC drilled using the Loxham Precision µ6 Drill at the University of Southampton. In the remaining chips, the hole was drilled using a femtosecond laser by Laser Micromachining Ltd., with particular assistance from Nadeem Rizvi.

Before drilling, no shorted or open junctions were measured on any of the four chips. After drilling, no opens or shorts were measured on the CNC drilled chips (out of 96) and 3 shorts were measured on the laser drilled chips (out of 96). We did not see any correlation between position of shorted junctions and proximity to the drilled hole. There were two shortcomings to this experiment that prevent us from drawing strong conclusions, related to the probe station: (1) The resistance measurements were highly inaccurate due to significant static voltage offsets – it was possible to distinguish shorts and opens from finite resistances, but not possible to meaningfully record the finite resistances. This issue was later resolved by measuring the current at many different voltages and fitting to an I-V curve. (2) The probe station itself was known to cause junction shorts at this time. This problem was later greatly reduced after installing a surge protector and a deionising fan. Nevertheless, we interpret the small number of opens and shorts as evidence that the CNC drilling and laser machining of chips did not result in significant damage to Josephson junctions.

As seen in Fig 6.7(D)&(E), the laser hole diameter and CNC hole diameter exceeded the desired 600 µm by $\sim$ 180 µm and $\sim$ 50 µm respectively. In the case of the laser drilled hole, this was due to the significant $\sim 10^\circ$ side-wall angle of the drilling process. The junctions were on the laser entrance side, and so to achieve an exit diameter of 600 µm meant an entrance diameter of $\sim$ 780 µm. The CNC drilling process did not result in a side-wall angle, and the deviation from 600 µm was in this case due to non-optimised drilling parameters which were later improved (see Fig. 6.6(B)). Residual, partially removed resist is also visible in Fig. 6.7(E), due to the laser hard baking the protective resist to the substrate. Due to the significant side-wall angle and the issue of residual resist, along with practical cost considerations, CNC drilling was chosen as the method to drill holes in the four-qubit device described in the next section.

6.3 Four-qubit device design and assembly

Having motivated a unit cell design and developed a circuit fabrication recipe, we designed a device to demonstrate the key technologies at a small scale. A four-qubit device formed by expanding the unit cell allows us to measure the addressibility of nearest neighbour qubits and drive-lines, and involves a single inductive shunt. To keep the demonstration device as simple as possible, it was decided not to include

qubit coupling circuitry. This allows us to establish a lower bound on crosstalk in the architecture before introducing coupling circuitry.

6.3.1 Device design

Fig. 6.8 shows a cut-away model of the fully assembled device design, including the control wiring and circuit substrate (the circuit is not shown and is discussed separately in section 6.3). The circuit enclosure has two parts, the base and the lid, both made from aluminium 6061. Aluminium was chosen as it becomes a superconductor below 1.2K, and so provides a superconducting ground to the circuit. While etched high purity aluminium (5N5 99.9995% Al) has been shown to form higher Q superconducting cavities [181], aluminium 6061 ($\sim$ 97.9% Al) was chosen for its machinability. A $5\,\text{mm} \times 5\,\text{mm} \times 0.6\,\text{mm}$ recess cavity is formed at the centre of the enclosure and houses the circuit substrate. The $2\,\text{mm} \times 2\,\text{mm}$ central region of this recess cavity has the exact same dimensions as the unit cell discussed above and shown in Fig. 6.1, including the four tapered though holes which we from here on refer to as sockets.

The control wiring is provided by the two copper pieces on either side of the enclosure. We call these pieces the control plugs. These act as adaptors, taking control signals from coaxial cables in the dilution refrigerator and carrying them to the circuit. The control plugs consist of a circuit-side piece and a fridge-side piece, both made of oxygen free copper. This is to maximise the thermal link of these parts to the base plate of the fridge, with the aim of improving the thermalisation of the device. Each control plug contains four silver-plated copper (SPC) UT47 coaxial cables, with stripped back inner conductors protruding from the circuit-side and attached to SMP connectors on the fridge-side. SMP connectors (Rosenberger 19K107-270L5 female, RS PRO 878-2410 male) were chosen due to their small size, allowing for a higher packing density compared to SMA connectors.

The whole assembly is aligned by dowel pins that run through the device, which is held together by M3 fasteners. We used titanium fasteners due to their non-magnetic properties. Due to the difficulty of machining high precision titanium dowels, we used 303 A2 stainless-steel dowels, which are also non-magnetic.

Fig. 6.9 shows schematics of the circuit substrate inside the assembled enclosure. In Fig. 6.9(A) a cross-section of the circuit substrate inside the sealed enclosure is

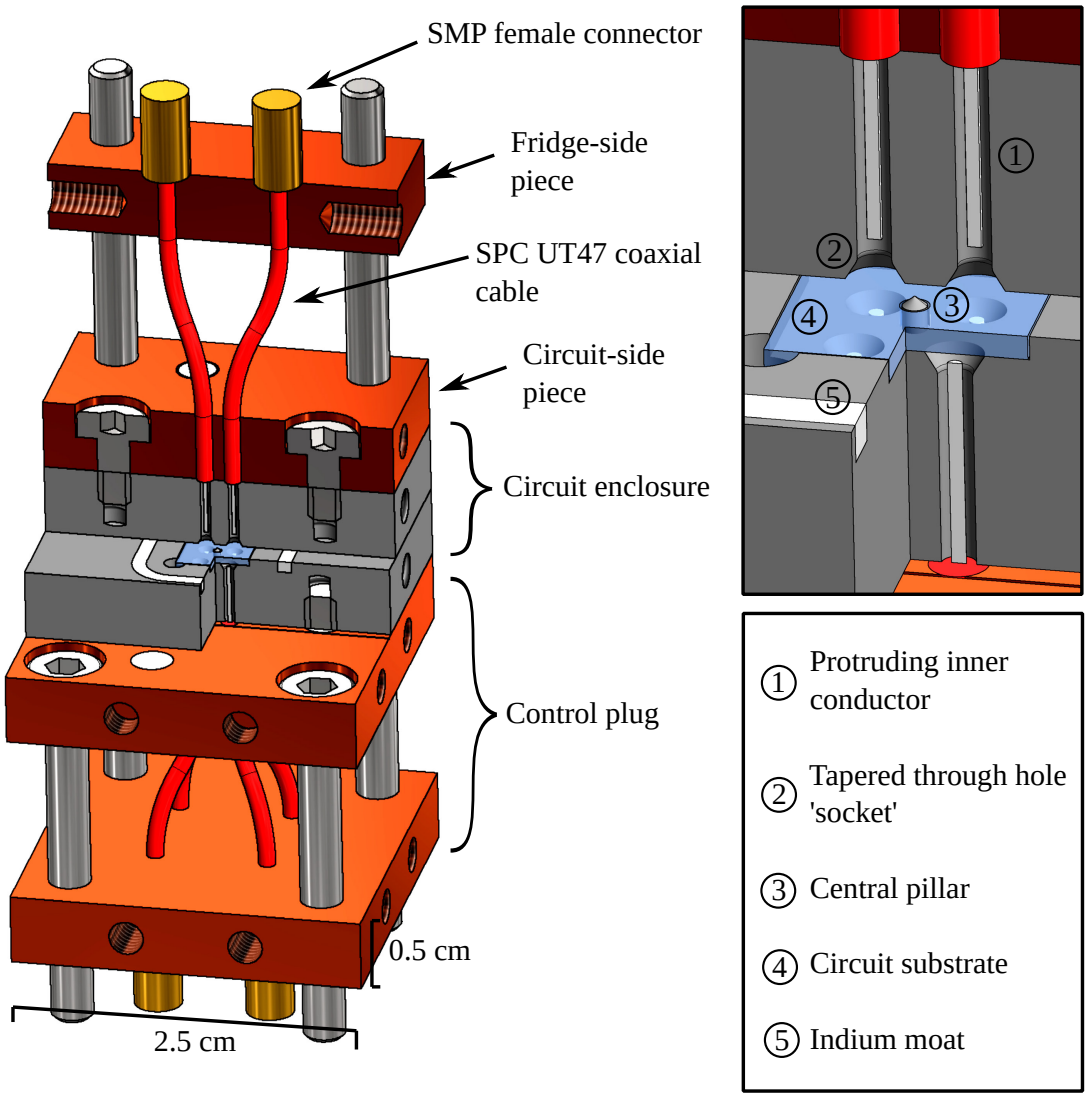

Figure 6.8: **Cut-away model of assembled device:** Render of the fully assembled device, showing the control plugs fastened onto the circuit enclosure. Fastener nuts are not shown.

shown. The substrate is not bonded to the enclosure in any way and the resonator-side of the substrate simply rests on the enclosure base. The tapered holes in the sockets have 1.2 mm maximum diameter which prevents the outer pads of the resonators from shorting to the enclosure.

In Fig. 6.9(B) a cross-section of the pillar is shown. The pillar is formed of a cylinder 0.5 mm height and 0.25 mm radius, topped by a 0.2 mm mm high cone. The cone protrudes into a cylindrical recess inside the enclosure lid, which we call the well. This well is filled with indium, which is a superconductor below 3.41 K. This is to ensure an inductive connection between the base and lid through the pillar. As discussed in

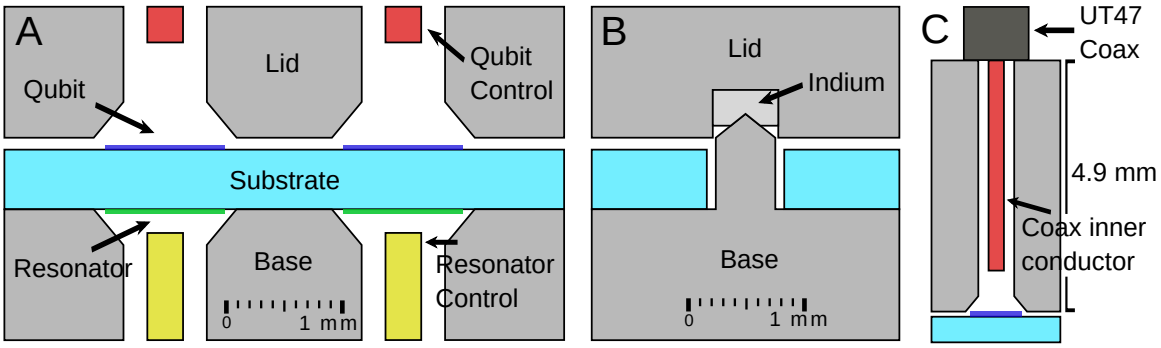

Figure 6.9: **Cross-sections of circuit in enclosure:** (**A**) Slice though qubits, resonators, and control lines. (**B**) Slice through pillar and indium-filled well. (**C**) The UT47 coaxial cables are separated from qubits by 4.9 mm.

Chapter 4, if an inductive connection is not made, the pillar will instead capacitively shunt the cavity, which would have the undesired effect of reducing the frequency of cavity modes.

We note here that superconducting inductive shunts could instead be formed by fabricating superconducting TSVs in the substrate and inductively connecting them to the enclosure in some manner, for instance with indium bump-bonds [127]. However, superconducting TSV fabrication is a multistage process, and generally performed before superconducting circuit fabrication [129, 152]. Since the pillar design does not require TSV fabrication or substrate-enclosure bonding, it may result in increased qubit relaxation times, by reducing the number of fabrication steps and so opportunities for wafer contamination.

In Fig. 6.9(C) a cross-section of the off-chip wiring for one of the qubits is shown. The UT47 coaxial cable outer-jacket and dielectric are flush with the top of the enclosure, and the exposed inner conductor protrudes 4 mm into the enclosure through one of the sockets. The protruding inner conductor and the socket holes in the enclosure have radii of 0.15 mm and 0.35 mm respectively and are separated by vacuum during measurement, thereby forming a coaxial waveguide with 50.8 Ω impedance. This is well matched to the 50 Ω impedance of the UT47 coaxial cable above, minimising reflections that could distort the shape of short control pulses sent to the qubits – which might reduce the fidelity of short qubit gates. The coaxial cable is separated from the circuit substrate by 4.9 mm, to suppress any interaction between the PTFE dielectric in the coaxial cable and the near-field of the qubit which could contribute to dielectric losses.

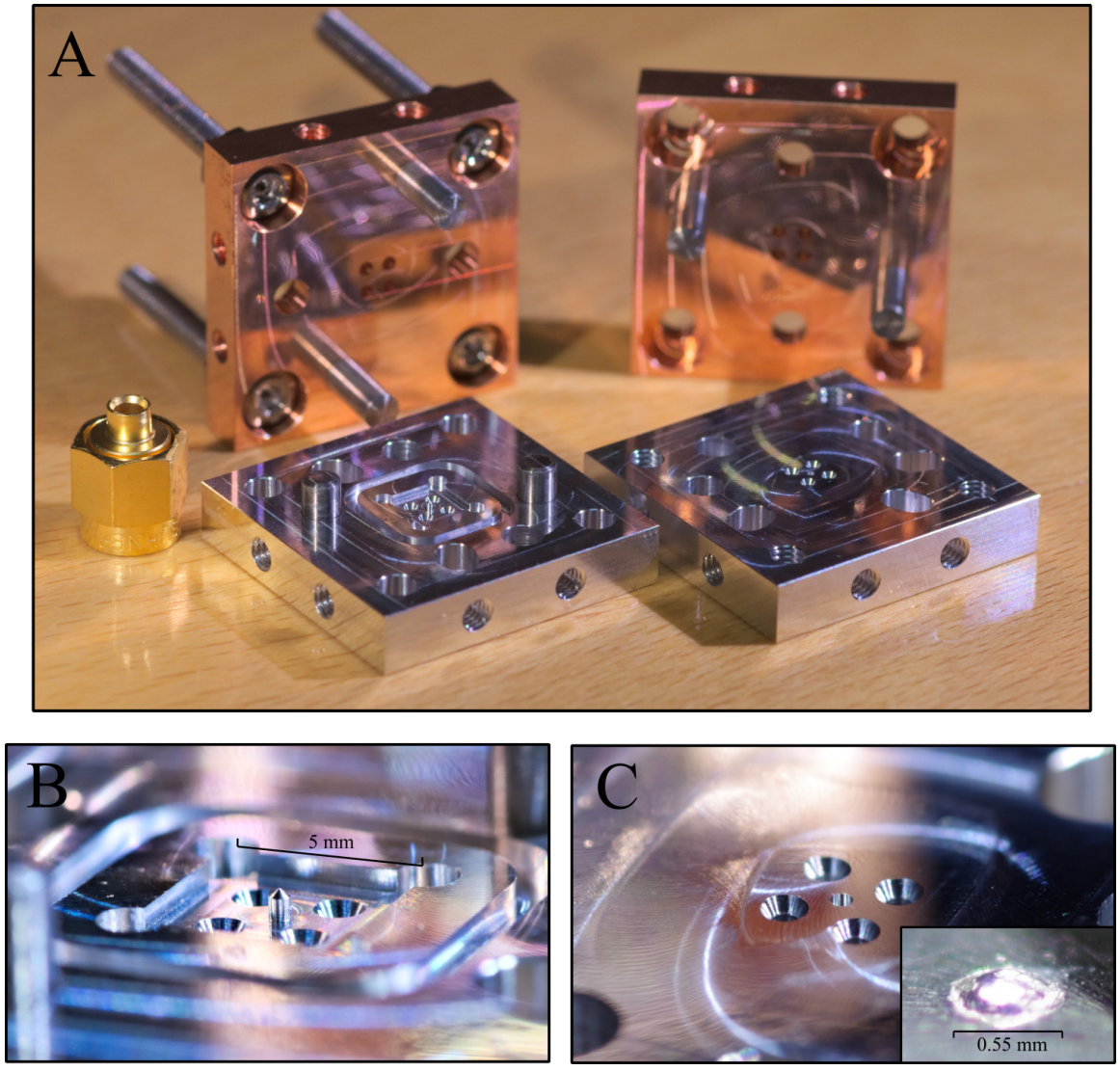

Figure 6.10: **Machined device parts:** Optical images of the machined parts. (**A**) The enclosure base and lid, and the qubit-side of both control plugs. Alignment dowels are visible in the base part and in the control plugs. An SMA connector is included for scale. (**B**) The enclosure base, showing the pillar and the four tapered through-holes for resonator control. (**C**) The enclosure lid, showing the well and the four tapered through-holes for qubit control. Inset shows an indium ball placed inside the well.

6.3.2 Machining and assembly

Fig. 6.10 shows some of the machined parts of the enclosure. These parts were designed using Autodesk Inventor [182] and machined at the Precision Development Facility at the Rutherford Appleton Laboratory (RAL) in Didcot. This facility specialises in precision CNC machining, in particular for space flight instrumentation. The facility has the capability to CNC machine parts to tolerances exceeding ±1 µm. For our parts, we requested the tolerance on all features to be ±10 µm. This choice was made as the circuit substrate rests in the enclosure base, and so the alignment of the off-chip control wiring to the qubits and resonators, and the alignment of the circuits to ground, is contingent on the accurate positioning of the enclosure features. For instance, the resonator outer pads are separated from the enclosure by only 50 µm in the nominal design, and so 50 µm misalignment would result in the outer resonator pad shorting to the enclosure, changing the circuit topology. Also, the small dimensions of the pillar and the requirement that it be inductively connected to the lid meant that the alignment and tolerances of these features was critical. The fridge-side copper plates of the control plugs, for which high machine tolerance was not required, were machined separately in-house to ±100 µm tolerance.

Fig. 6.11 shows the assembled enclosure. In Fig. 6.11(A) the qubit-side control plug is shown slotting into the lid of the enclosure. Notice that the alignment dowels in the control plug extend further than the protruding inner-conductors, aligning the control plug to the enclosure before the inner-conductors enter the sockets. This ensures that the delicate inner conductors are well aligned with the sockets before joining the two parts.

Fig. 6.11(B) shows a zoomed-in view of the protruding inner conductors. The sockets in the enclosure lid are also visible. The off-chip wiring will fail if the inner conductors contact the socket walls. This sets a maximum lateral misalignment threshold of 200 µm on the inner conductors.

Fig. 6.11(C) shows the fully assembled enclosure, with both control plugs attached.

6.3.3 Control plug assembly

The control plug assembly process was developed with the aim of improving the alignment alignment accuracy of the off-chip wiring to qubits and resonators over previous

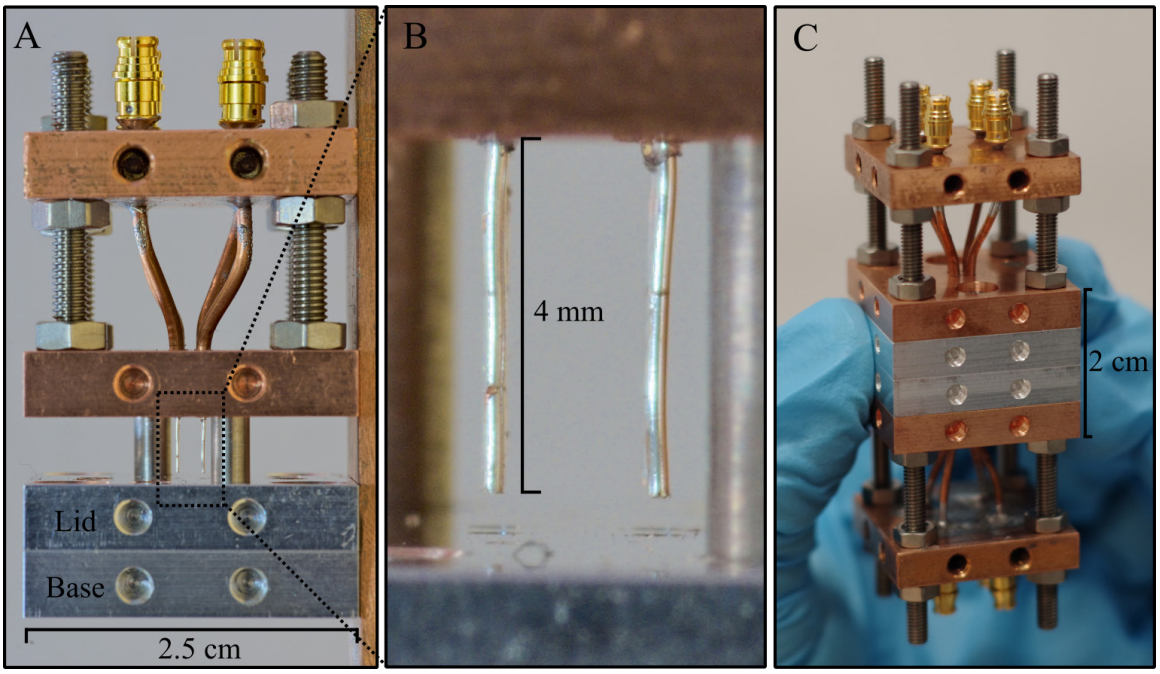

Figure 6.11: **Assembled device:** Optical images showing the control plug slotting into the sockets in the enclosure lid.

coaxmon devices. As discussed in Chapter 4, the coupling of qubits and resonators to the off-chip wiring in the coaxmon architecture has an exponential dependence on the wiring to circuit separation d_{pin}, making accurate alignment important. The steps are shown in Fig. 6.12 and described below:

A Prepare two coaxial cable assemblies consisting of $> 9\,\text{mm}$ sections of UT47 silver plated copper coaxial cable with female SMP connectors at the ends. Measure S parameters on VNA to ensure good transmission, which we defined as $S_{11}, S_{22} < 15\,\text{dB}$ up to $10\,\text{GHz}$.

B Cut cable assemblies into two $43.3\,\text{mm}$ long sections, and using a razor blade strip back outer jacket and dielectric to expose $15\,\text{mm}$ of inner conductor.

C Thread the stripped back cables through the fridge-facing copper plate of the control plug, and then apply solder paste as shown.

D Melt the solder paste using a heat gun. Then carefully bend the coaxial cables into shape using pliers.

E Thread the coaxial cables through the circuit-facing copper plate, until the outer jackets and dielectrics of the coaxial cables are flush to the surface of the copper

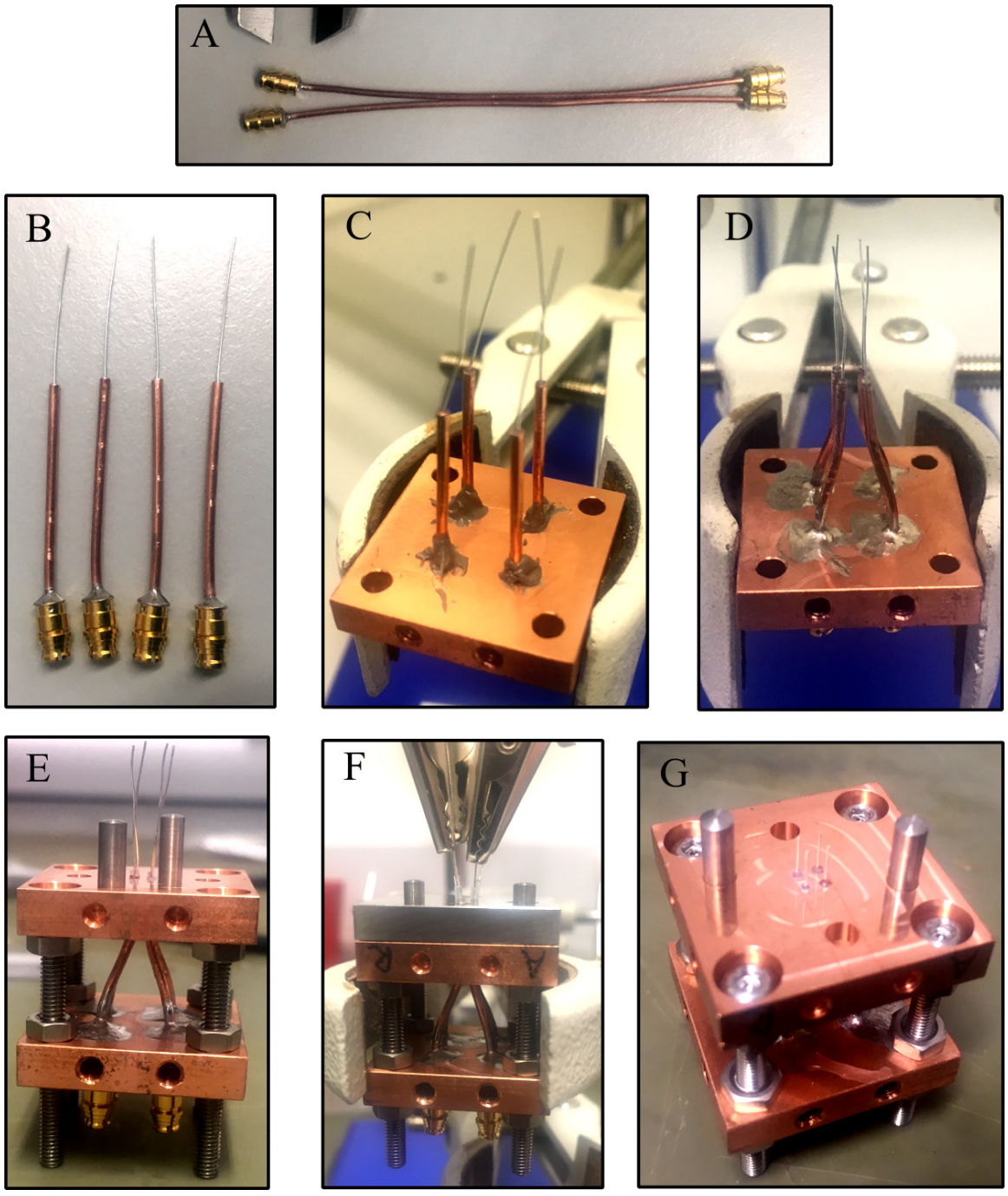

Figure 6.12: **Control plug assembly steps:** Optical images showing the control plug assembly process. The steps are described in the main text.

plate. Fasten the control plug together using titanium screws and nuts.

F Thread the inner conductors through the steel control pin alignment piece. Press this piece flush against the control plug. Apply tension to the inner conductors to straighten them, and then cut with a razor blade pressed flush to the alignment piece.

G Remove the alignment piece. The distance the inner conductors extend from the circuit-facing copper plate should now equal the height of the alignment piece – allowing d_{pin} to be set accurately. Lateral realignment of the inner conductors can be done carefully with tweezers after assembly.

Note that in Fig. 6.12(F), the dielectric has been re-threaded onto the inner conductors to align them laterally. This was later found to be unnecessary as lateral alignment can be adjusted after assembly with tweezers. One necessary adjustment to the control plug design was to include another copper plate to anchor the SMP connectors to prevent them from breaking off under force. This is shown in Fig. 7.1(B) in Chapter 7.

The four-qubit circuit measured in the next chapter is shown inside the enclosure base in Fig. 6.13. The circuit chip was diced to dimensions 475 ± 10 µm $\times$ 475 ± 10 µm, chosen to be very close to the 500 ± 10 µm $\times$ 500 ± 10 µm recess in the enclosure base in order to improve the alignment of the circuit to the enclosure.

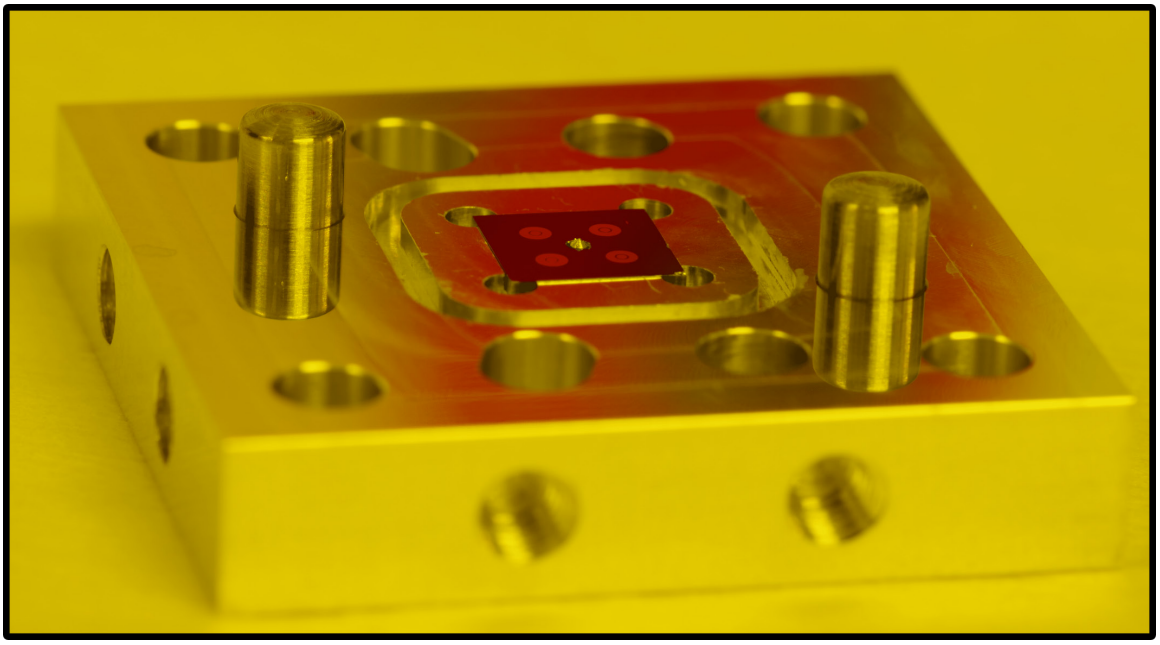

Figure 6.13: **four-qubit circuit in enclosure base:** Optical image of the four-qubit device measured in Chapter 7 resting inside the enclosure base. The four qubits are visible on the silicon substrate, as is the pillar protruding from the drilled hole in the substrate centre.

Chapter 7

Experimental Demonstration of a Tileable Circuit

In this chapter we present measurements on a four-qubit prototype tileable superconducting circuit. We outline the experimental setup, present the measurement results, and conclude with a discussion of the results.

7.1 Experimental setup

The four-qubit device described in the previous chapter was mounted inside an Oxford instruments dilution refrigerator and cooled to $\sim 10\,\mathrm{mK}$. We note that the circuit used in the experiment was stored in atmosphere for approximately six months prior to measurement. Fig. 7.1 shows the device mounted on to the base plate of the dilution refrigerator. The device was clamped from two sides to increase the thermal connection to the base plate. A cryoperm shield was fitted around the device to magnetically shield it and reduce magnetic flux trapping during the normal to superconducting phase transition. The open top of the cyroperm shield was covered with aluminium foil to reduce paths for IR light to reach the device.

Qubit control signals were generated using single side-band up-conversion of 2 GSs^{-1} sampling rate DAC signals with continuous $\sim 4\,\mathrm{GHz}$ LO signals, and qubit readout was performed with a standard cryogenic RF heterodyne detection setup, which notably did not include any quantum limited amplifiers. The control electronics and dilution refrigerator setup is described in more detail in appendix F.

We note here that the device was measured in five separate cooldowns, between

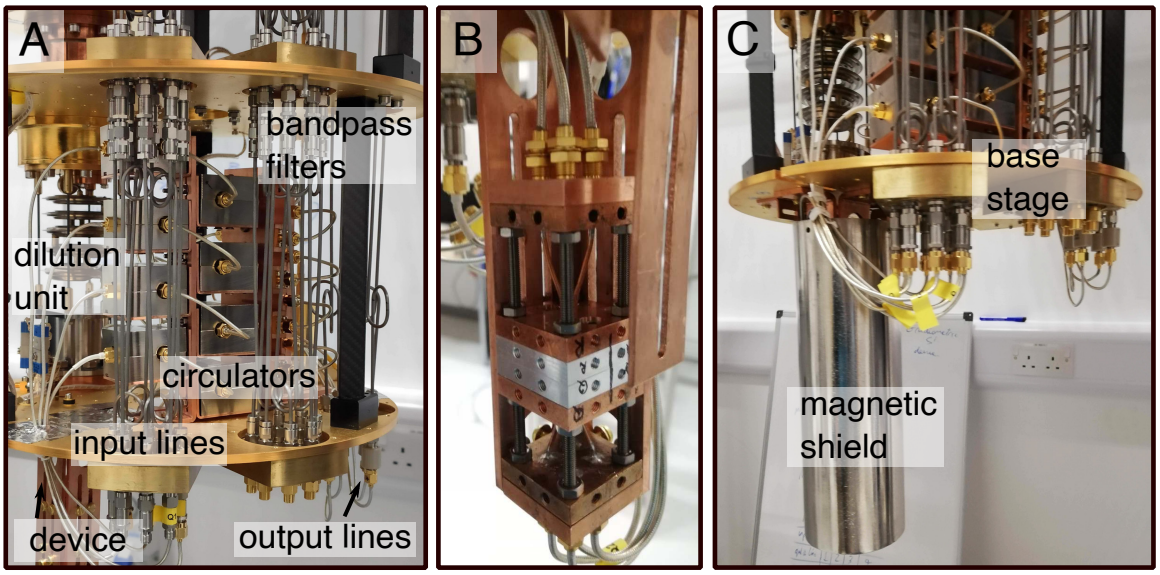

Figure 7.1: **Device mounted in fridge:** (**A**) Top of base stage of Triton 500 dilution refrigerator, showing cryogenic microwave components and dilution unit. Qubit control and resonator control input lines and circulators are clearly visible, and readout bandpass filters and output lines are partially visible. (**B**) four-qubit device mounted to base stage of fridge, with external control lines connected. (**C**) Underside of base stage showing device inside Cryoperm magnetic shield.

which the dilution refrigerator was warmed to room temperature and exposed to atmosphere. No evidence of warping or damage to the device was observed between these cooldowns, indicating it is robust to thermal cycling. Unless stated otherwise, the data presented in the following was all collected during the final cooldown.

7.2 Basic device characterisation

The following effective Hamiltonian is used to describe the four-qubit system (neglecting losses)

$$\hat{H}_{eff} = \hat{H}_d + \hat{H}_s \tag{7.1}$$

$$\begin{aligned}\hat{H}_d = \sum_{i=1}^{4} \omega_{q,i}\hat{a}_i^\dagger\hat{a}_i + \frac{\alpha_i}{2}\hat{a}_i^\dagger\hat{a}_i(\hat{a}_i^\dagger\hat{a}_i - 1) + \omega_{r,i}\hat{b}_i^\dagger\hat{b}_i + 2\chi_{ii}\hat{a}_i^\dagger\hat{a}_i\hat{b}_i^\dagger\hat{b}_i \\ +\varepsilon_{ii}^q(\hat{a}_i - \hat{a}_i^\dagger)V_i^q + \varepsilon_{ii}^r(\hat{b}_i - \hat{b}_i^\dagger)V_i^r\end{aligned} \tag{7.2}$$

$$\hat{H}_s = \sum_{i,j(i\neq j)}^{4} J_{ij}(\hat{a}_i^\dagger\hat{a}_j + \hat{a}_i\hat{a}_j^\dagger) + 2\chi_{ij}\hat{a}_i^\dagger\hat{a}_i\hat{b}_j^\dagger\hat{b}_j + \varepsilon_{ij}^q(\hat{a}_i - \hat{a}_i^\dagger)V_j^q + \varepsilon_{ij}^r(\hat{b}_i - \hat{b}_i^\dagger)V_j^r \tag{7.3}$$

Here, $\hat{H}_d$ contains the desirable Hamiltonian terms, and $\hat{H}_s$ contains the undesired, or spurious, interaction terms. This effective Hamiltonian is a slightly simplified version of that proposed in Ref. [92], to describe low-anharmonicity qubits with interactions in the dispersive limit – conditions which our device satisfies. $\hat{a}_i^\dagger(\hat{a}_i)$ and $\hat{b}_i^\dagger(\hat{b}_i)$ are the creation(annihilation) operators for qubits and resonators respectively; $\omega_{q,i}$ are the qubit transition frequencies; α_i are the qubit anharmonicities; $\omega_{r,i}$ are the resonator frequencies; $2\chi_{ii}$ are the single-photon Stark shifts between qubit i and resonator i; $\varepsilon_{ii}^q(\varepsilon_{ii}^r)$ are the couplings of qubit(resonator) i to qubit(resonator) control line i driven with voltage $V_i^q(V_i^r)$. J_{ij} are parasitic transverse couplings between qubits, $2\chi_{ij}$ are parasitic single-photon Stark shifts between qubits and resonators, and $\varepsilon_{ij}^q(\varepsilon_{ij}^r)$ are parasitic couplings between qubits(resonators) and qubit(resonator) control lines.

All interactions are in the dispersive limit in this device, and so we use a generalised version of eq. 2.46 to relate the χ shift to the transverse coupling strength between qubit i and resonator j

$$g_{ij} = \sqrt{-\frac{\chi_{ij}\Delta_{ij}(\Delta_{ij} - E_C/\hbar)}{E_C/\hbar}} \tag{7.4}$$

where $\Delta_{ij} = \omega_{q,i} - \omega_{r,j}$. In the following, the qubits and resonators are labelled Q_i and R_i. Their relative positions, as well as the interactions between them, are shown schematically in Fig. 7.2.

7.2.1 Spectroscopic characterisation

Resonator spectroscopy was used to find the resonator frequencies, as well as their internal and external quality factors. Pulsed resonator spectroscopy was performed, with and without prior π pulses on qubits, to find the single-photon Stark shift between qubits and resonators as well as the qubit thermal populations.

Fig 7.3(A)&(B) shows pulsed resonator spectroscopy on R_1, with and without a prior pi pulse on Q_1 (pulse schemes shown in inset). Each data point is composed of an average of 1500 measurements, with a delay of 1000 µs between each measurement to allow the qubit to relax to its equilibrium state. We first fit each response separately to a simple 7 free parameter circuit model which treats the resonator as an RLC circuit coupled to a lossless external line with a linear response [183]. The predicted

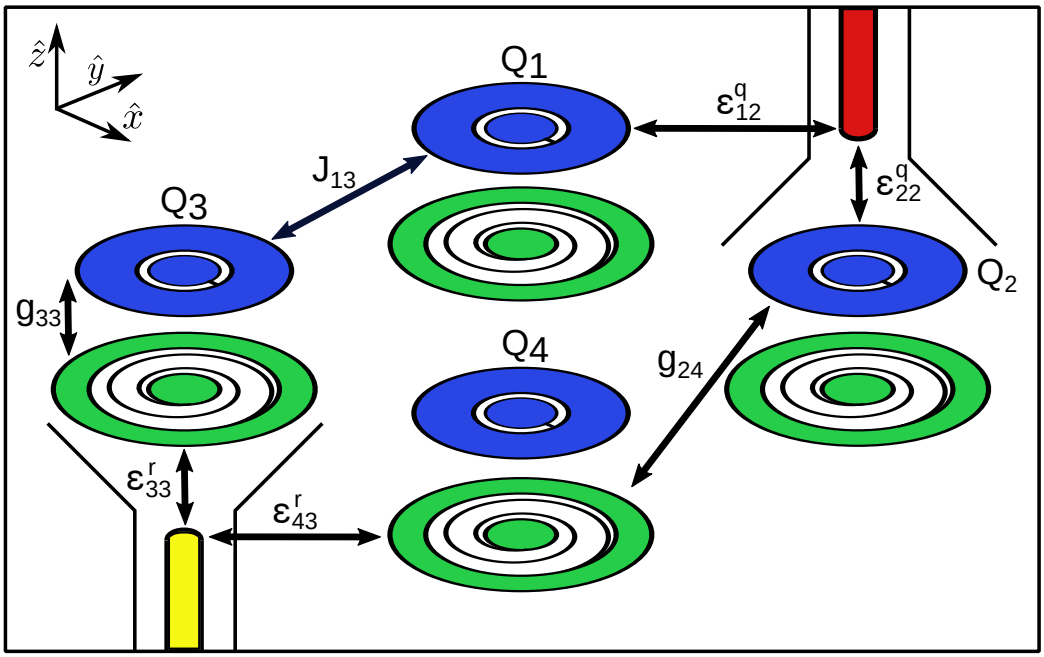

Figure 7.2: **Device interactions:** Visualisation of circuit arrangement and interactions in the four-qubit device.

reflected signal near resonance can be approximated as the product of two responses

$$S_{11}(f) = g_{cable}(f, ...) \times g_{resonator}(f, ...) \tag{7.5}$$

$$g_{cable}(f, c_1, c_2, c_3, c_4) = (c_0 + c_1(\frac{f - f_0}{f_0}))e^{i(c_2 + c_3(\frac{f-f_0}{f_0}))} \tag{7.6}$$

$$g_{resonator}(f, p_0, Q_L, f_0) = 1 - \frac{p_0}{1 + 2iQ_L(\frac{f-f_0}{f_0})} \tag{7.7}$$

g_{cable} models the linear response of the line, and $g_{resonator}$ models the response of the lossy RLC resonator. Only p_0, Q_L and f_0 are of physical interest to us. f_0 is the loaded resonator frequency, Q_L is the loaded quality factor of the resonator, and p_0 determines the size of the dip in $|S_{11}|$ caused by the resonator, relative to the background cable response. The internal and external quality factors are to a good approximation given by $Q_i = Q_L(1+k)$ and $Q_e = Q_L(1+k)/k$, where $k = p_0/(2-p_0)$.

Denoting the fit parameters for the reflection data taken with and without a prior π pulse as $\boldsymbol{p_\pi}$ and $\boldsymbol{p_0}$, we use the fitted parameters as an initial guess in the following fit to both datasets

$$S_{11}(f)_0 = p_g S_{11}(f, \boldsymbol{p_0}) + p_e S_{11}(f, \boldsymbol{p_\pi}) \tag{7.8}$$

$$S_{11}(f)_\pi = p_e S_{11}(f, \boldsymbol{p_o}) + p_g S_{11}(f, \boldsymbol{p_\pi}) \tag{7.9}$$

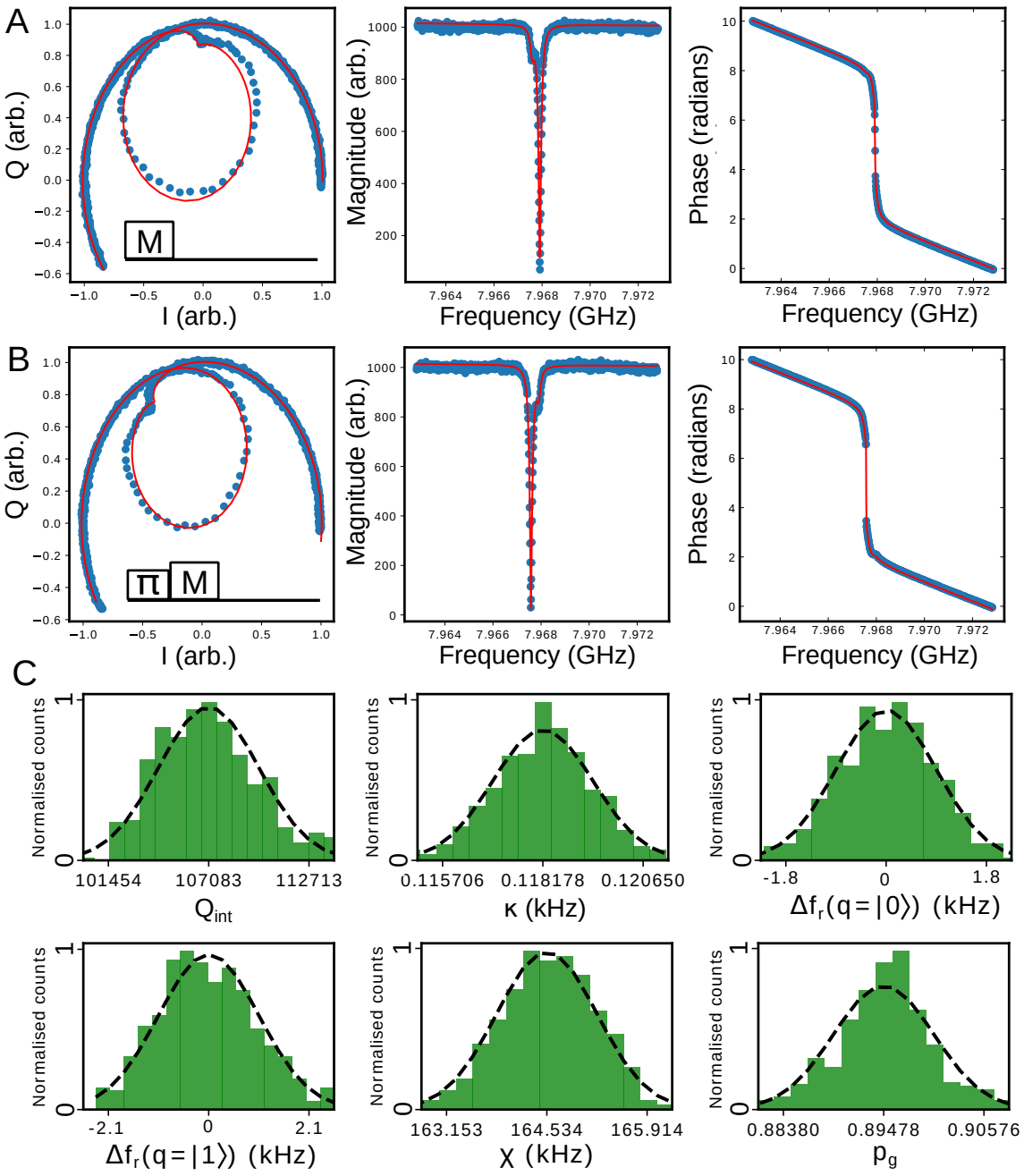

Figure 7.3: R_1 **spectroscopy:** IQ, magnitude, and phase response of R_1 sweeping drive frequency. (**A**) without any prior qubit pulse. (**B**) with a prior π pulse applied to Q_1. Pulse sequences shown in insets. Measurement pulse is a 5 µs square drive pulse with a concurrent integration window. Fit to the model described in main text is shown in red. (**C**) Variation in relevant fitting parameters found by bootstrapping (500 resamples).

Table 7.1: **Resonator spectroscopy parameters:** Resonator and qubit parameters determined from fitted resonator spectroscopy. Standard deviation on quantities in brackets.

	$\omega_r/2\pi$(GHz)	Q_{int}(x10^{-3})	$\kappa_{ext}/2\pi$(kHz)	$\chi/2\pi$(kHz)	$g/2\pi$(MHz)	p_g(%)
Q_1/R_1	7.968	107 (3)	118 (1)	165 (0.7)	124 (0.2)	87
Q_2/R_2	8.083	75 (2)	73 (1)	167 (0.8)	126 (0.3)	82
Q_3/R_3	8.183	513 (66)	749 (2)	169 (0.7)	128 (0.3)	87
Q_4/R_4	8.289	157 (5)	241 (1)	164 (0.6)	128 (0.2)	90

where p_g and p_e are the thermal population of the qubit ground and excited state, related by the Boltzmann factor

$$p_e = p_g \exp(\frac{-\hbar\omega_q}{k_b T}) \tag{7.10}$$

Here, the predicted response is a weighted sum of the response for a qubit in the ground and excited state. We assume a perfect π pulse that swaps these populations, and also assume negligible population in higher levels. We further assume negligible relaxation between the ground and excited states during measurement. The model has in total 11 free parameters, as we take the cable response parameters to be the same in both $\boldsymbol{p_0}$ and $\boldsymbol{p_\pi}$.

To estimate the variance on the fit parameters, we perform a bootstrapping technique. We resample 500 times from the reflection data, with replacement, and put each sample through our fitting routine. Fig. 7.3(C) shows the resultant distribution of the fit parameters, which closely resemble normal distributions, indicating the fitting routine is robust. We estimate the uncertainty in the fit parameters from the variance of the normal distributions. The fitted parameters, along with uncertainties, are presented in Table 7.1. Here, κ_{ext} is the external decay rate given by $\kappa_{ext} = \omega_r/Q_{ext}$. The phase responses for each resonator are shown in Fig. 7.4. As is clear in the phase response, resonators R_1, R_3 and R_4 are externally limited, whereas R_2 is internally limited.

The qubit frequencies are first determined by power spectroscopy. An example power spectroscopy plot for Q_1 is shown in Fig. 7.5. The f_{01} and f_{12} transitions are clearly visible, from which we find the qubit frequency and anharmonicity. We can then calculate the charging energy and inductive energy using eqs. 2.35 in Chapter 2, from which we can find the charge dispersion using eq. 2.28. The fitted qubit parameters are shown in Table 7.2.

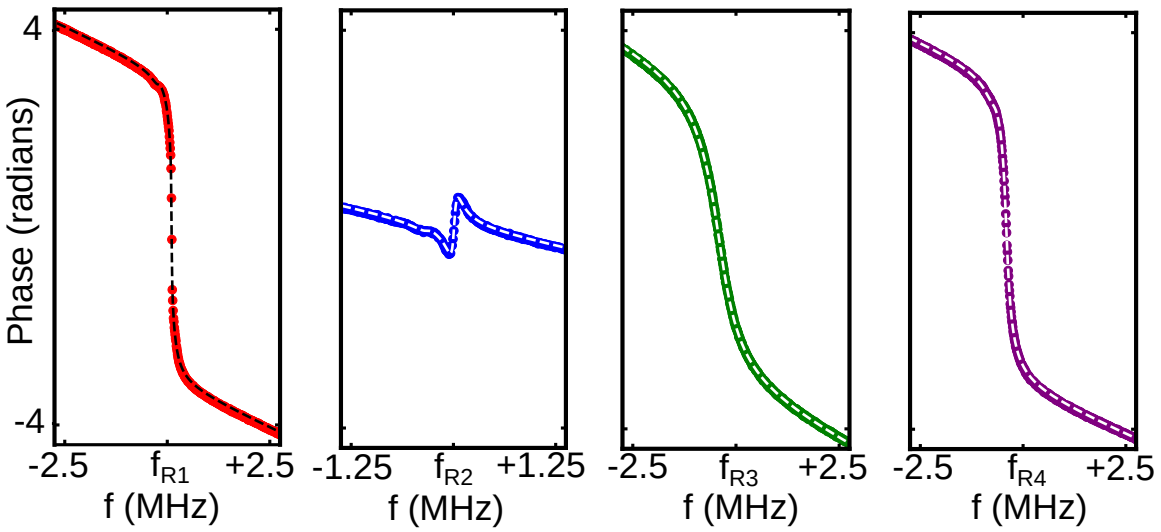

Figure 7.4: **Resonator phase responses:** Fitted phase response of the four readout resonators from reflection measurements.

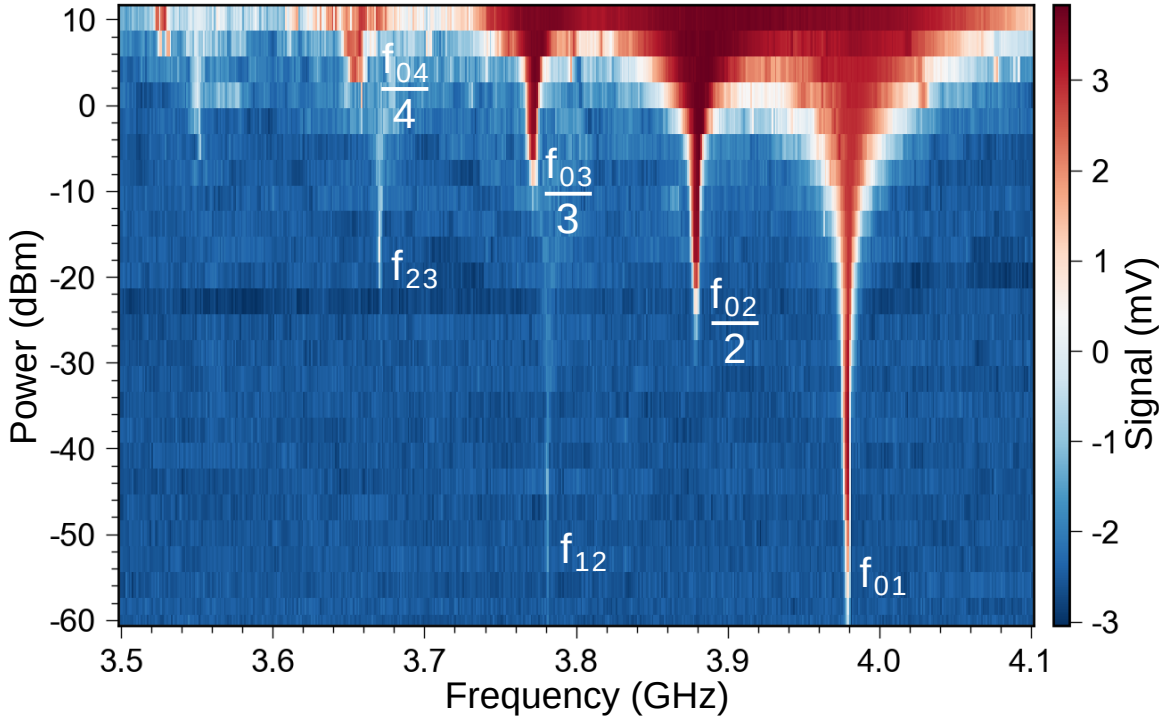

Figure 7.5: Q_1 **power spectroscopy:** Applying a continuous drive tone through Q_1's control line. At higher drive powers, multi-photon transitions are visible [184]. This data was taken during the first device cooldown (all other data in this chapter taken in cooldown 5).

Table 7.2: **Qubit parameters:** Qubit parameters determined from qubit spectroscopy. E_J and E_C (equivalently L_J and C_Σ) are determined from ω_q and α using eq. 2.35. ϵ_n is the charge dispersion of the nth level, defined in eq. 2.28. More precise values of ω_q and α are found from Ramsey interferometry experiments.

	$\omega_q/2\pi$(GHz)	$\alpha/2\pi$(MHz)	L_J(nH)	C_Σ(fF)	E_J/E_C	ϵ_0/h(Hz)	ϵ_1/h(Hz)
Q_1	3.981	-199	13.4	109	69	4.2	-394
Q_2	4.045	-199	13.0	109	71	3.1	-297
Q_3	4.130	-198	12.5	109	74	1.9	-185
Q_4	4.192	-197	12.1	109	76	1.3	-127

7.3 Qubit coherence metrology

To benchmark the relaxation times of the four qubits, we performed pulsed T_1 experiments on the four qubits simultaneously. Here, each T_1 experiment involved the following: (1) A resonant π pulse on the uninitialised qubit, followed by a delay time $\Delta\tau$ before a measurement of the qubit state. (2) Repetition of this experiment 1000 times to determine the qubit ground state population p_g at delay time $\Delta\tau$, with a 1100 µs delay between the start of each experiment to allow the qubit to relax back to its equilibrium state. (3) Repetition of this ensemble of experiments 41 times while logarithmically stepping the delay time $\Delta\tau$ from 3 µs to 1000 µs. The result is a T_1 experiment time trace like that shown in the inset in Fig. 7.6(D). The T_1 relaxation time is then found by fitting the exponential function $p_g = A\exp(-t/T_1) + B$ to these time traces. These T_1 experiments were repeated 251 times over a period of 12 hours. The consecutive extracted values of T_1 are shown in Fig. 7.6(A)&(B) and the resulting histograms of T_1 are shown in Fig. 7.6(C)&(D). The observed variation in relaxation times is consistent with relaxation dominated by coupling to one or more unstable, near-resonant coherent TLS [83, 185, 186]. The frequency of such coherent TLS has been found to fluctuate following a telegraphic noise profile with a sub-millihertz switching rate [83, 185]. The T_1 histograms in Fig. 7.6 show a fair fit to bimodal Gaussian distributions (a good fit in the case of Q_1), suggesting that we have only partially sampled from the telegraph noise of the relevant loss inducing coherent TLS over the 12 hour measurement period. It is expected that over longer ($\sim$ 100 hour) measurement periods, the T_1 measurements would sufficiently sample from the telegraph noise, in which case the histograms would tend to a single Gaussian distribution, as observed in Ref. [83].

To benchmark dephasing times on the four qubits, we performed pulsed T_2 Ramsey and T_2 Hahn Echo experiments on the four qubits separately. Here, each T_2 Ramsey

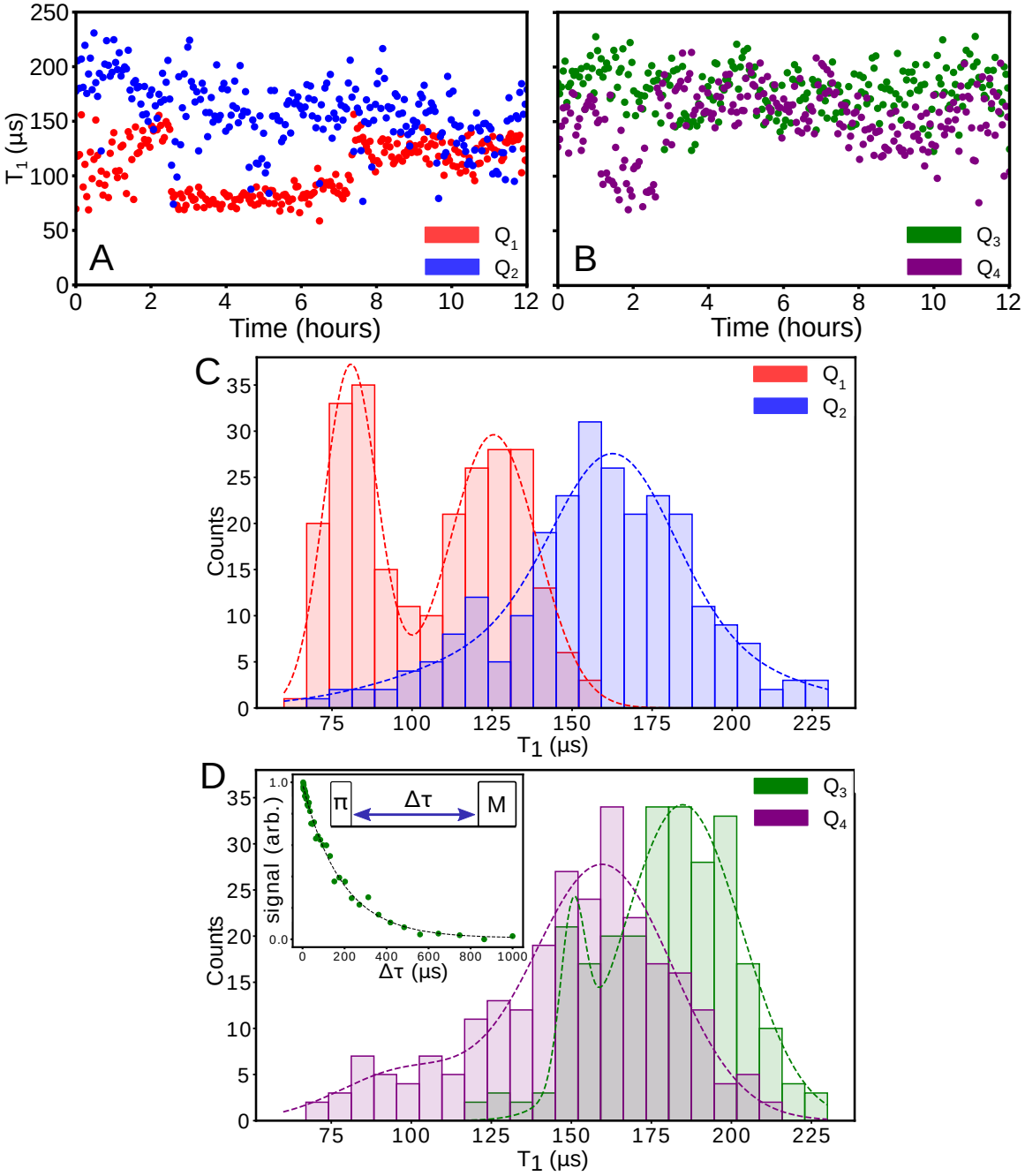

Figure 7.6: **Qubit relaxation characterisation (T_1):** (**A**) & (**B**) 251 consecutive T_1 measurements over a 12 hour period on the four qubits. (**C**) & (**D**) Resulting histograms of T_1. Dashed lines are fits to bimodal Gaussian distributions. Inset on (D) shows one example fitted T_1 time trace for Q_3. The four qubits were measured simultaneously; the results are shown on separate plots for legibility.

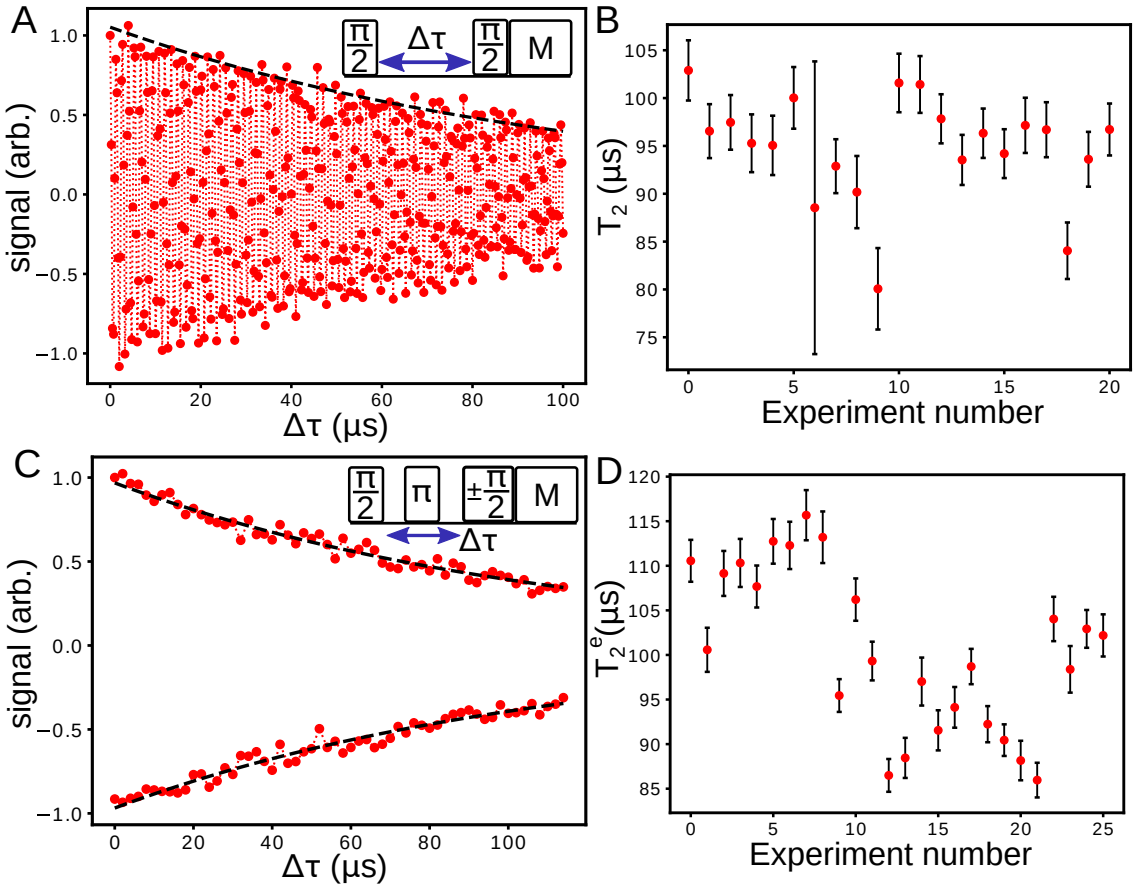

Figure 7.7: Q_1 **dephasing characterisation (T_2):** (**A**) Ramsey experiment time trace. (**B**) Fitted T_2 Ramsey times from 21 repeated time trace experiments. (**C**) Hahn echo experiment time trace. Each time step is measured twice, with opposite phase on the final $\pi/2$ pulse, to improve the fit accuracy. (**D**) Fitted T_2^e echo times from 26 repeated time trace experiments.

experiment involved the following: (1) An off-resonance $\pi/2$ pulse on the uninitialised qubit, with the pulse detuned from the qubit resonance by $\sim 0.75\,\text{MHz}$, followed by a delay time $\Delta\tau$ before a second identical off-resonant $\pi/2$ pulse, and immediately afterwards a measurement of the qubit state. (2) Repetition of this experiment 500 times to determine the qubit ground state population p_g at delay time $\Delta\tau$, with a 600 µs delay between the start of each experiment to allow the qubit to relax back to its equilibrium state. (3) Repetition of this ensemble of experiments 400 times while linearly stepping the delay time $\Delta\tau$ from 0 µs to 100 µs. The result is a T_2 Ramsey experiment time trace like that shown in Fig. 7.7(A). The T_2 Ramsey time is then found by fitting the function $p_g = A\exp(-t/T_2)\sin(\Delta\omega\Delta\tau + \phi) + B$ to these time traces. These T_2 Ramsey experiments were repeated 21 times taking approximately

Table 7.3: **Qubit coherence measurements:** Summary of qubit coherence results found from repeated measurements. Standard deviations in brackets.

	T_1 (µs)	T_2 (µs)	T_2^e (µs)	T_2^* (µs)
Q_1	106(24)	95(5)	101(9)	193(52)
Q_2	159(30)	104(9)	116(6)	183(25)
Q_3	179(21)	89(12)	128(9)	199(25)
Q_4	151(30)	99(8)	113(4)	181(24)
Avg.	149(38)	97(10)	115(12)	189(34)

two hours per qubit. The resulting T_2 Ramsey times for Q_1 are shown in Fig. 7.7(B).

Each T_2 Hahn Echo experiment involved the following: (1) A resonant $\pi/2$ pulse on the uninitialised qubit, followed by a delay time $\Delta\tau/2$ before a resonant π pulse, followed by another delay time $\Delta\tau/2$ before a final resonant $\pi/2$ pulse immediately followed by a measurement of the qubit state. (2) Repetition of this experiment 1000 times to determine the qubit ground state population p_g at delay time $\Delta\tau$, with a 600 µs delay between the start of each experiment to allow the qubit to relax back to its equilibrium state. (3) Repetition of this ensemble of experiments 58 times while linearly stepping the delay time $\Delta\tau$ from 0 µs to 114 µs. (4) Repetition of this entire time trace experiment with a π phase change to the central π pulse. This is to improve the final fit accuracy. The result is a T_2^e Hahn Echo experiment time trace like that shown in Fig. 7.7(C). The T_2^e time is then found by fitting the function $p_g = \pm A\exp(-t/T_2^e) + B$ to these time traces. These T_2^e experiments were repeated 26 times taking approximately two hours per qubit. The resulting T_2^e times for Q_1 are shown in Fig. 7.7(D). Note that the T_2 experiments were run separately due to software limitations at the time of measurement. The coherence results are summarised in Table 7.3, where T_2^* is the echoed pure dephasing time defined $1/T_2^* = 1/T_2^e - 1/(2T_1)$.

7.4 Crosstalk characterisation

As discussed in Chapter 6, the device we have measured is a reference device with no intentionally designed couplings except g_{ii} between qubit-resonator pairs, and so we identify any other interactions as undesired crosstalk. We consider four kinds of crosstalk: qubit control line crosstalk, resonator control line crosstalk, qubit-qubit crosstalk, and resonator-qubit crosstalk. These are highlighted in Fig. 7.2, and related to the spurious interactions defined in eq. 7.3.

Table 7.4: **Crosstalk bounds:** Experimentally found upper bounds on the magnitude of important crosstalk quantities in the device, along with predicted maximum values from FE simulations using the simple impedance formulas in Ref. [92].

Crosstalk quantity	Upper bound	FE simulation
Qubit-qubit coupling $J/2\pi$	250 kHz	10 kHz
Qubit-qubit ZZ shift $2\chi_{ZZ}/2\pi$	4 kHz	10 Hz
Parasitic qubit-resonator coupling $g/2\pi$	1500 kHz	50 kHz
Parasitic single-photon Stark shift $2\chi_p/2\pi$	40 Hz	0.06 kHz
Parasitic measurement induced dephasing[a] $\Gamma_p/2\pi$	0.5 Hz	0.1 µHz

[a] driving a neighbouring resonator with $n_{crit}/10$ photons

We express the control line crosstalk in terms of selectivities, which we define below, and are able to measure directly. We find average qubit control line selectivity of -56 ± 3 dB, and average resonator control line selectivity of -42 ± 8 dB. Conversely, we were unable to detect any parasitic qubit-qubit couplings J_{ij} or qubit-resonator dispersive shifts χ_{ij} at the sensitivity of our experiments, and instead put experimental bounds on the relevant quantities, which are summarised in Table 7.4 along with predicted values from FE simulations. The experiments performed to find these results are now described.

7.4.1 Qubit control line selectivity ϑ

We define the qubit control line selectivity ϑ_{ij} as the ratio of the power $P_j^q \propto (V_j^q)^2$ in qubit control line j required to induce equal frequency Rabi oscillations in qubits i and j, when driving the qubits on resonance. This definition differs from that in Refs. [92, 143], where the selectivity is defined as a ratio of the voltage. In the limit $|J_{ij}|, |\varepsilon_{jj}^q V_j^q| \ll |\Delta_{ij}|$, where $\Delta_{ij} = \omega_{q,i} - \omega_{q,j}$, the selectivity has a simple relation to the crosstalk parameters in eq. 7.3. This can be seen by considering that the drive configuration when resonantly driving qubit i from control line j is identical to that used to perform the two-qubit cross-resonance gate, mentioned in Chapter 3. Viewed in this light, qubit i forms the target qubit, and qubit j the control qubit. The effective driving Hamiltonian on the target qubit can be expressed as [36, 140]

$$\hat{H}_{drive} = \varepsilon_{jj}^q V_j^q [\mu \hat{Z}\hat{X} + \nu \hat{I}\hat{X} + \frac{\varepsilon_{ij}^q}{\varepsilon_{jj}^q}(\cos(\phi_{ij})\hat{I}\hat{X} + \sin(\phi_{ij})\hat{I}\hat{Y})] \tag{7.11}$$

$$\nu = \frac{J_{ij}}{\Delta_{ij}} \frac{\alpha_j}{\alpha_i - \Delta_{ij}} \tag{7.12}$$

$$\mu = \frac{J_{ij}}{\Delta_{ij}} \frac{-\Delta_{ij}}{\alpha_i - \Delta_{ij}} \tag{7.13}$$

The μ term describes a conditional rotation on the target qubit, the ν term describes an unconditional rotation on the target through the J_{ij} interaction, and the remaining terms describe unconditional rotations directly through the control line crosstalk ε_{ij}. In general, the two unconditional rotations will not be in phase, which we express with the phase variable ϕ_{ij}. If we assume that the control qubit is in the ground state during this drive, then $\hat{Z}\hat{X} \rightarrow \hat{I}\hat{X}$ and the driving Hamiltonian simplifies to

$$\hat{H}_{drive} = \varepsilon^q_{jj} V^q_j \{[\frac{J_{ij}}{\Delta_{ij}} + \frac{\varepsilon^q_{ij}}{\varepsilon^q_{jj}} \cos(\phi_{ij})]\hat{I}\hat{X} + \frac{\varepsilon^q_{ij}}{\varepsilon^q_{jj}} \sin(\phi_{ij})\hat{I}\hat{Y})\} \tag{7.14}$$

Notice that the dependence on the control qubit anharmonicity has dropped out. This drive will result in Rabi oscillations in the target qubit at frequency

$$\Omega_i = \varepsilon^q_{jj} V^q_j [(\frac{J_{ij}}{\Delta_{ij}})^2 + (\frac{\varepsilon^q_{ij}}{\varepsilon^q_{jj}})^2 + 2\frac{\varepsilon^q_{ij}}{\varepsilon^q_{jj}} \frac{J_{ij}}{\Delta_{ij}} \cos\phi_{ij}]^{\frac{1}{2}} \tag{7.15}$$

If the drive is instead resonant with the control qubit, it will undergo Rabi oscillations with frequency $\Omega_j = \varepsilon^q_{jj} V^q_j$ (under the assumtion that ε_{jj} is frequency independent). Thus we arrive at an expression for the qubit drive line selectivity in terms of the parameters in our device Hamiltonian

$$\vartheta_{ij} = (\frac{J_{ij}}{\Delta_{ij}})^2 + (\frac{\varepsilon^q_{ij}}{\varepsilon^q_{jj}})^2 + 2\frac{\varepsilon^q_{ij}}{\varepsilon^q_{jj}} \frac{J_{ij}}{\Delta_{ij}} \cos\phi_{12} \tag{7.16}$$

Experimentally, we find the selectivity ϑ_{ij} of qubit control line j to qubit i by driving resonant Rabi oscillations in qubit j at different drive voltages V^q_j and fitting the linear response $\Omega_j = k_{jj} V^q_j$. We subsequently drive resonant Rabi oscillations in qubit i and fit the linear response $\Omega_i = k_{ij} V^q_j$. The selectivity is then $\vartheta_{ij} = (k_{ij}/k_{jj})^2$, and can be expressed in dB as

$$\vartheta_{ij} \rightarrow 10 \log_{10}(\vartheta_{ij}) \tag{7.17}$$

The factor of 10 is due to ϑ_{ij} being a ratio of powers. All qubit control line selectivities are presented in Table 7.5. Plots of the fitted linear voltage responses used to determine θ_{21} are shown in Fig. 7.8(A)&(B).

We see that, in general, it is not possible to bound J_{ij}/Δ_{ij} or $\varepsilon^q_{ij}/\varepsilon^q_{jj}$ from measurements of ϑ_{ij} alone, since the phase ϕ_{ij} can cause destructive interference between them. For instance, in the case where $J_{ij}/\Delta_{ij} = \varepsilon^q_{ij}/\varepsilon^q_{jj}$ and $\phi_{ij} = \pi$: $\vartheta_{ij} = 0$ irrespective of the magnitude of these terms. However, from FE simulations of the device, we expect the $J/2\pi$ terms to be $\sim 10\,\text{kHz}$, while the measured $\Delta/2\pi$ terms

Table 7.5: **Qubit control line selectivity:** Experimental values for selectivity of qubit control lines to qubits, in dB. Errors are all < 0.1 dB.

	Drive Q_1	Drive Q_2	Drive Q_3	Drive Q_4
Q_1	-	-56.0	-55.4	-53.5
Q_2	-56.0	-	-54.8	-50.5
Q_3	-56.6	-56.1	-	-51.6
Q_4	-61.6	-59.7	-58.9	-

are ~ 100 MHz. Therefore, we expect the $(J_{ij}/\Delta_{ij})^2$ term to be order 10^{-8}, corresponding to 80 dB selectivity. This is far smaller than the measured selectivity values, implying $\varepsilon^q_{ij}/\varepsilon^q_{jj} \gg J_{ij}/\Delta_{ij}$. Further evidence for this is provided by the measurement data. Considering Fig. 7.8(B), the highest driving amplitude on Q_2 (the target) is ~ 2 V at the generator, corresponding to a drive strength on Q_1 (the control) of $\varepsilon^q_{11}V^q_1 \sim 300$ MHz, significantly larger than the detuning $\Delta_{12}/2\pi = 64$ MHz. If $J_{12}/\Delta_{12} \gg \varepsilon^q_{12}/\varepsilon^q_{11}$, we would in this case expect the Rabi rate to follow the green dashed curve shown in this figure, found using the semianalytical method introduced in Ref. [187]. We truncate the semianalytical model to the first 10 energy levels, using $\Delta_{12}/2\pi = 64$ MHz and $\alpha_1/2\pi = -199$ MHz, and then fit J_{12} to give agreement with the first data point (finding $J_{12}/2\pi = 0.115$ MHz). The obvious poor fit of this curve is clear experimental evidence that $\varepsilon^q_{12}/\varepsilon^q_{11} \gg J_{12}/\Delta_{12}$. Thus, in our device, we conclude that

$$\vartheta_{ij} \approx (\frac{\varepsilon^q_{ij}}{\varepsilon^q_{jj}})^2 \tag{7.18}$$

We will use this later to experimentally bound the value of J_{ij}.

7.4.2 Resonator control line selectivity φ

We define the selectivity φ_{ij} as the ratio of the drive power $P^r_j \propto (V^r_j)^2$ in resonator control line j required to put an equal steady-state population of photons n in resonators i and j, when driving the resonators at a detuning Δ_r from their bare resonance frequency, where $\Delta_r \gg \chi, \kappa$. The selectivity can be expressed in dB as

$$\varphi_{ij} \to 10\log_{10}(\varphi_{ij}) \tag{7.19}$$

The factor of 10 is due to φ_{ij} being a ratio of powers. The selectivity can be related to the cross-talk terms in eq. 7.3. We start from the expression for the steady state photon number in a resonator coupled to a single qubit under a continuous drive from a control line [188]

$$\bar{n}_\pm = \frac{(\varepsilon V)^2}{\kappa^2/4 + (\Delta_r \pm \chi)^2} \tag{7.20}$$

Here, εV is the drive amplitude on the resonator, κ is the total decay rate of the resonator, χ is half the single-photon Stark shift shift, and Δ_r is the detuning of the drive from the bare resonator frequency. The photon number depends on whether the qubit is in the excited (+) or ground (−) state. If we assume that $\chi_{ii} \gg \chi_{ij}$ for $i \neq j$, we can generalise eq. 7.20 to multiple resonators, qubits, and drives

$$\bar{n}_{i,\pm} = \frac{(\varepsilon^r_{ij} V^r_j)^2}{\kappa_i^2/4 + (\Delta_{r,i} \pm \chi_{ii})^2} \tag{7.21}$$

For a drive detuning $\Delta_{r,i} \gg \chi_{ii}$, the photon number becomes insensitive to the state of the qubit. If additionally $\Delta_{r,i} \gg \kappa_i$, the photon number is given by

$$\bar{n}_i = \frac{(\varepsilon^r_{ij} V^r_j)^2}{\Delta^2_{r,i}} \tag{7.22}$$

Using eq. 7.22, the ratio of the powers required to equally populate resonators i and j from resonator control line j, using a drive detuned from each resonator by Δ_r, is given by

$$\left.\frac{P^r_j(\text{driving resonator } j)}{P^r_j(\text{driving resonator } i)}\right|_{\bar{n}_i = \bar{n}_j} = (\frac{\varepsilon^r_{ij}}{\varepsilon^r_{jj}})^2 \tag{7.23}$$

The LHS is exactly our definition of the resonator control line selectivity, therefore we arrive at

$$\varphi_{ij} = (\frac{\varepsilon^r_{ij}}{\varepsilon^r_{jj}})^2 \tag{7.24}$$

Note that if we had instead defined the selectivity as the ratio drive powers when driving the resonators at their bare frequencies, it would be dependent on χ_{ii} and κ_i. The two definitions are related in the following manner

$$\varphi_{ij}(\text{bare resonance}) = \frac{\kappa_j^2 + 4\chi_{jj}^2}{\kappa_i^2 + 4\chi_{ii}^2} \times \varphi_{ij}(\text{far detuned}) \tag{7.25}$$

To experimentally measure the selectivity φ_{ij} of resonator control line j to resonator i, we off-resonantly drove resonator j continuously at varying drive powers P^r_j. We then measured the AC Stark-shift ω_{AC} induced in qubit j with a Ramsey interferometry experiment, and fitted to the linear response $\omega_{AC,j} = k'_{jj} P^r_j$. We subsequently off-resonantly drove resonator i, measured the AC-Stark shift in qubit i, and fitted the linear response $\omega_{AC,i} = k'_{ij} P^r_j$. We use that $\omega_{AC,i} = 2\chi_i n_i$ [188] to relate the AC Stark-shift in qubit i to the steady state photon number in resonator i. The selectivity is then given by $\varphi_{ij} = (\chi_j/\chi_i)(k'_{ij}/k'_{jj})$. Note that this experiment is only possible because the resonators are driven suitably far detuned that the induced dephasing rate is small. This is because the induced photon number scales as $n \propto 1/\Delta_r^2$, whereas the

Table 7.6: **Resonator control line selectivity:** Experimental values for selectivity of resonator control lines to resonators, in dB. Errors are all < 0.1 dB.

	Drive R_1	Drive R_2	Drive R_3	Drive R_4
R_1	-	-38.0	-51.6	-51.2
R_2	-39.6	-	-54.3	-45.3
R_3	-31.2	-32.2	-	-38.3
R_4	-39.8	-33.2	-47.0	-

induced dephasing rate scales as $\Gamma \propto 1/\Delta_r^4$ [188]). Small induced dephasing allows us to perform long Ramsey interferometry experiments and achieve better frequency resolution. We further increase the frequency resolution by using a Gaussian windowing and interpolation technique applied to the Fourier transform of the time traces, discussed in Appendix E.

All resonator control line selectivities are presented in Table 7.6. We detuned our continuous driving tone from resonators by $+5$ MHz in all cases, well in the limit $\Delta_{r,i} \gg \chi_{ii}, \kappa_i$. Plots of the fitted linear power responses used to determine φ_{21} are shown in Fig. 7.9(C)&(D).

7.4.3 Qubit qubit crosstalk

Bounds on the parasitic transverse coupling J_{ij} between qubits follow directly from the qubit control line selectivity results. We found that $J_{ij}/\Delta_{ij} \ll \varepsilon_{ij}/\varepsilon_{jj}$ and $\vartheta_{ij} \approx (\varepsilon_{ij}/\varepsilon_{jj})^2$. This immediately leads to the following experimental bound on J_{ij}

$$|J_{ij}| < [\min(\vartheta_{ij}, \vartheta_{ji})]^{\frac{1}{2}} |\Delta_{ij}| \tag{7.26}$$

This results in bounds ranging between $J_{34}/2\pi < 100$ kHz and $J_{13}/2\pi < 250$ kHz, resulting in bounds on the magnitude of the frequency shift in qubits due to the state of other qubits, $2\chi_{ZZ}$, ranging between $|\chi_{ZZ,34}|/2\pi < 0.1$ kHz, and $|\chi_{ZZ,14}|/2\pi < 2$ kHz, where we have used the following relation [36, 140]

$$\chi_{ZZ,ij} = J_{ij}^2 \frac{\alpha_i + \alpha_j}{(\Delta_{ij} + \alpha_i)(\Delta_{ij} - \alpha_j)} \tag{7.27}$$

7.4.4 Qubit resonator crosstalk

In order to bound the parasitic coupling g_{ij} between resonators and qubits, we resonantly drove each resonator to populate it with a steady-state number of photons, and attempted to measure parasitic AC Stark-shifts $\omega_{AC,p}$ in neighbouring qubits

with Ramsey interferometry experiments. We wish to populate each resonator with as many photons as possible to achieve the smallest bound on χ_p, however, for photon numbers near the critical photon number $n_{crit} = \Delta^2/4g^2$, where $\Delta = \omega_r - \omega_q$, the simple linear relationships between drive power and photon number and between photon number and AC Stark shift break down [188]. Therefore, as a compromise, we populated each resonator with at least $n_{crit}/10$ photons, under the approximation that the simple linear relations hold up to $n_{crit}/10$.

First, we must calibrate the power of a continuous resonant drive to the steady state number of photons in the resonator. We do this by measuring the T_2 Ramsey time of qubit i while applying a continuous resonant drive to resonator i, similar to Ref. [189]. The generalised measurement-induced dephasing rate Γ_m of qubit i due to this drive is given by [188]

$$\Gamma_{m,i} = \frac{(\bar{n}_{+,i} + \bar{n}_{-,i})\kappa_i \chi_{ii}^2}{\kappa_i^2/4 + \chi_{ii}^2 + \Delta_r^2} \tag{7.28}$$

We apply a continuous drive with power P_i^r to resonator i and measure the dephasing rate by fitting the exponential decay of a Ramsey time trace. We repeat at many powers and fit the data to $\Gamma_{m,i} = K_i P_i^r$, as shown in Fig. 7.9. If we define $\bar{n}_{-,i} = c_i P_i^r$, then for a drive applied at the ground state resonance frequency of resonator i we find

$$c_i = \frac{K_i(\kappa_i^2/4 + 2\chi_{ii}^2)}{\kappa_i \chi_{ii}^2 (1 + n_{+,i}/n_{-,i})} \tag{7.29}$$

where, using eq. 7.20

$$\frac{\bar{n}_{+,i}}{\bar{n}_{-,i}} = \frac{1}{1 + 16\chi_{ii}^2/\kappa_i^2} \tag{7.30}$$

For the four resonators, we find $c_i = \{1.5, 1.2, 0.45, 1.6\} \times 10^{10}\mathrm{W}^{-1}$.

Having calibrated the drive power to photon number $\bar{n}_-$ for a drive resonant with the ground state peak of the resonator, we measure the frequency of qubit i with a long Ramsey interferometry experiment. This is repeated four times, with either no continuous drive on any resonator, or a continuous drive on resonator j calibrated to populate it with its critical photon number, for all permutations $j \neq i$. This is shown for qubit Q_1 in Fig. 7.8(E). Note that we initially miscalibrated our c_i values due to incorrectly using the external decay rate κ_{ext} rather than the total decay rate κ , and also incorrectly calculated the ratio $\bar{n}_+/\bar{n}_-$. The result is that instead of populating resonators with $n_{crit}/10$ photons, we populated them with $\{39(1), 25(1), 37(1), 40(2)\}$ photons, where $n_{crit} = \{258, 257, 251, 256\}$ for the four resonators. This error does

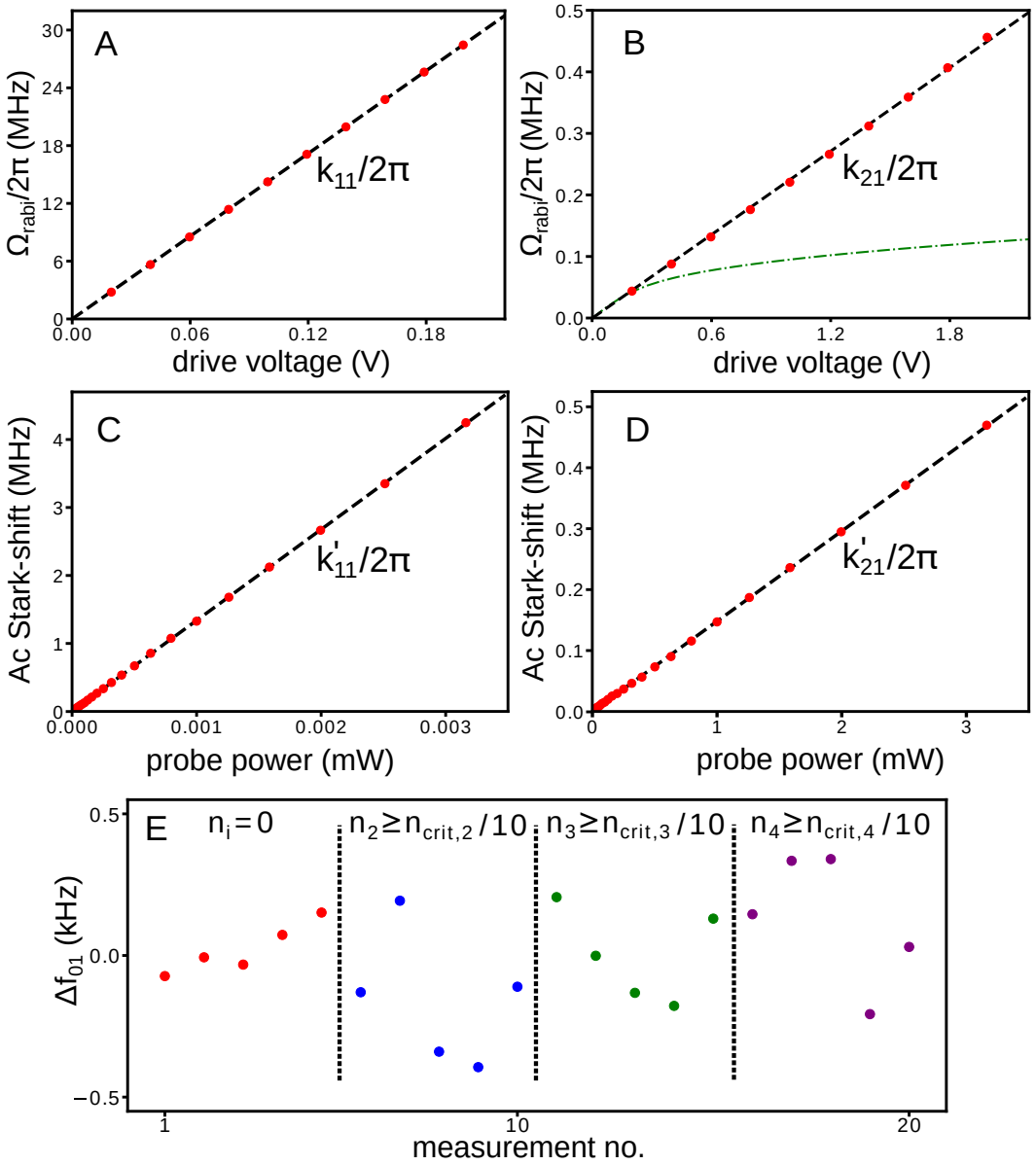

Figure 7.8: **Crosstalk characterisation measurements:** (**A**) & (**B**) Experimentally measured Rabi-oscillation frequencies in Q_1 and Q_2 respectively, driven resonantly though qubit control line 1. The squared ratio of the fitted gradients gives the qubit control line selectivity θ_{21}. Dashed green line in (B) shows prediction if $J_{21}/\Delta_{21} \gg \varepsilon^q_{21}/\varepsilon^q_{11}$. (**C**) & (**D**) Experimentally measured Ac Stark-shifts in Q_1 and Q_2, as a result of off-resonantly (+5 MHz) driving each qubit's readout-resonator through resonator control line 1. The ratio of the fitted gradients is proportional to the resonator control line selectivity φ_{21}. (**E**) Q_1 frequency from 20 repeated Ramsey measurements, either with no continuous drive on any resonator, or resonantly populating one of R_2, R_3, R_4 with at least $n_{crit}/10$ photons. From the observed distributions we assign an approximate bound on any induced Ac Stark-shift in Q_1 of $\omega_{AC,1}/2\pi < 1$ kHz.

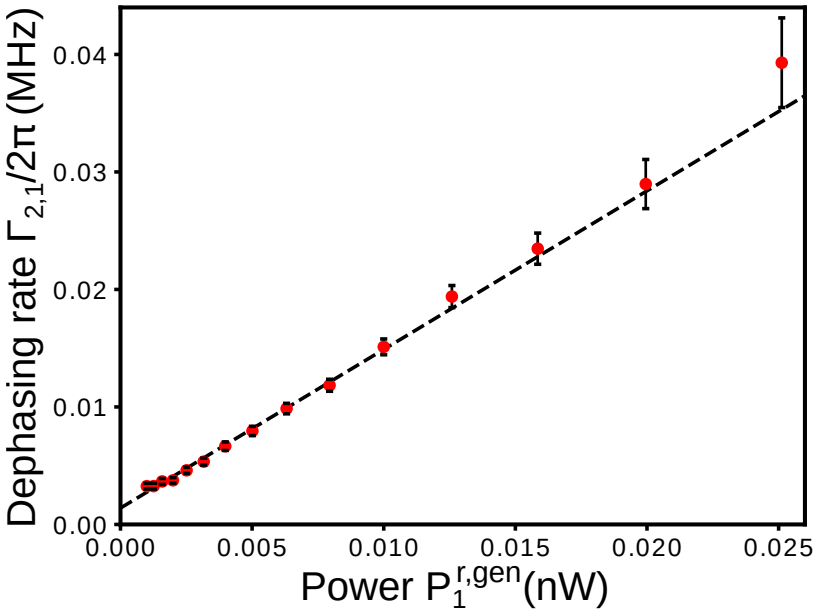

Figure 7.9: **Probe power to photon number calibration:** Dephasing rate in Q_1 extracted from Ramsey time traces vs. generator drive power, for a continuous drive applied resonant to the ground state peak of R_1. Dashed black line shows linear fit.

not affect the results.

From Fig. 7.8(E), it is clear that we are unable to resolve any AC Stark shift above the variation in the measured qubit frequency – which will be a combination of measurement noise and real variation. The standard deviation on the frequency of Q_1 is 0.2 kHz across these 20 measurements, which is consistent with the predicted charge noise on the first level $\epsilon_1 \approx 0.400$ kHz (Table 7.2). The frequency is determined from the Fourier transform of the Ramsey time trace, with the resolution improved by using the interpolation technique described in appendix E.

We were unable to detect any parasitic AC Stark shifts for any parasitically coupled qubit resonator pair using this method, with frequency resolution of approximately 1 kHz, from which we put approximate bounds on parasitic single-photon Stark-shifts $\chi_{p,ij}/2\pi \lesssim 20$ Hz, by using $\omega_{AC,i} = 2\chi_{p,ij}n_j$ (qubit i and resonator j). This results in a bound on $g_{ij}/2\pi \lesssim 1.5$ MHz, where we have used eq. 7.4. From the small bounds on χ_{ij}, we can put stringent bounds on the dephasing rate of qubits due to populating other resonators with up to $n_{crit}/10$ photons, using eq. 7.28, $\Gamma_{p,ij}/2\pi \lesssim 0.5$ Hz.

7.5 Single qubit gate errors

The ability to perform high fidelity quantum gates is crucial for any quantum processor. We characterised the fidelity of single qubit gates on our device using randomised benchmarking (RB) [190, 191]. In a single qubit RB experiment, the qubit is initialised in the ground state, and a random sequence of single qubit Clifford gates is applied to it. The inverse gate (also a Clifford gate) is then applied, and the qubit is measured. If the qubit preparation, Clifford gates, and measurement are all perfect, then the qubit will be measured in the ground state. Imperfect gates and decoherence will leave the qubit in a mixed state. As the number of Clifford gates m in the initial sequence is increased, the measured ground state population of the qubit will trace out the following exponential decay curve

$$p_g = A\alpha^m + B \tag{7.31}$$

The average error per physical gate (EPG) can be determined from the decay rate of this curve

$$\text{EPG} = \frac{1}{2}(1 - \alpha^{1/N_g}) \tag{7.32}$$

where N_g is the average number of physical gates per Clifford gate. Key properties of RB are: (1) it is insensitive to state preparation and measurement (SPAM) errors; (2) the Clifford gate that inverts the prior sequence of Clifford gates can always be found efficiently [192]; and (3) the method naturally generalises to the benchmarking of multi-qubit gates in larger qubit systems [193].

We performed single qubit RB on all four qubits both separately and simultaneously, and used two different physical gate decompositions of the Clifford group, one into $I, X_{\pi/2,\pi}, Y_{\pi/2,\pi}$ gates; and the other into physical $I, X_{\pi/2,\pi}$ and 'virtual' Z gates [194]. We call these decompositions XY and VZX respectively. The XY decomposition consists of $N_g = 45/24$ average physical gates per Clifford, and the VZX decomposition consists of $N_g = 28/24$ average physical gates per Clifford. The virtual Z gates are so called because they physically involve only a phase change to future physical qubit gates. As such, they have zero duration and are fully implemented in software. As a result, these gates are not coherence limited and have effectively perfect fidelity. By using a VZX decomposition, the error per Clifford gate can be significantly reduced, as each Clifford gate consists of significantly fewer physical gates. The software used to perform these RB experiments was written by Takahiro Tsunoda and Andrew Patterson, with some changes made to incorporate the VZX

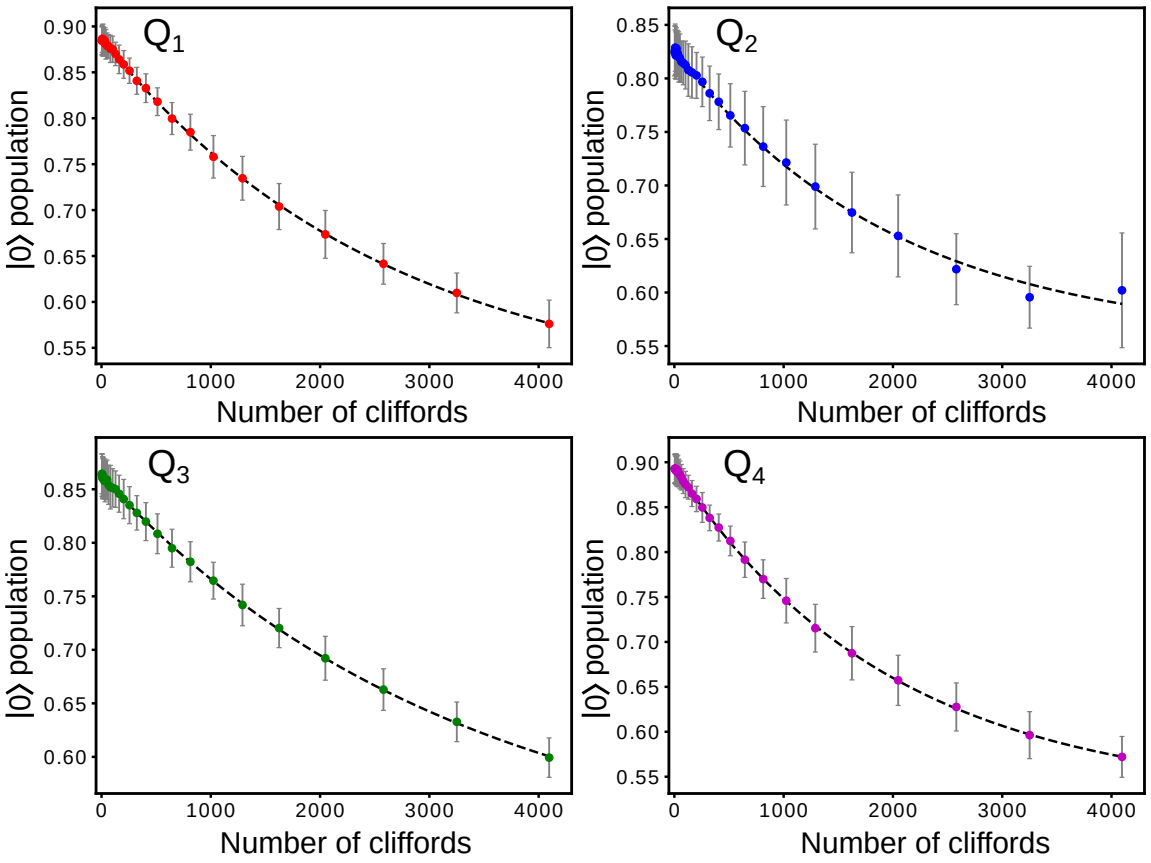

Figure 7.10: **Randomised benchmarking measurements:** RB curves from simultaneous single qubit RB on the four qubits, using the VZX Clifford decomposition. The error bars show the standard deviation across the 80 Clifford seeds. Dashed black lines show fit to eq. 7.31.

Clifford decomposition and to implement the virtual Z gate.

The EPG values found from our RB experiments are summarised in Table 7.7. The RB measurements used to determine e_{sim}^{VZX} are shown in Fig. 7.10. We find an average EPG of 1.81×10^{-4} across the four qubits in this measurement. Our physical gates all had Blackman window [195] pulse envelopes, 20 ns duration, and were spaced by a 4 ns buffer. We sampled 80 times from the Clifford group for each pulse sequence length, and took 5000 averages of each measurement. Each complete RB measurement took four hours. As described in the gate calibration section, we used single-shot readout in our RB experiments. As a consequence of this, we can study correlations between errors on the four qubits during simultaneous single qubit RB. This was first done in Ref. [43] to study crosstalk and correlated errors in a superconducting circuit with two transmon qubits. In Ref. [197], the protocol was extended to an arbitrary number

Table 7.7: **Single qubit gate errors:** Summary of error-per-physical gate found by RB. The coherence limited error-per-gate $e_{c.l.}$ is calculated as $(3 - e^{\tau_g/T_1} - 2e^{\tau_g/T_2^e})/6$ [196] where τ_g is the physical gate separation, here 24 ns.

	$e_{sep}^{XY}(\times 10^4)$	$e_{sim}^{XY}(\times 10^4)$	$e_{sep}^{VZX}(\times 10^4)$	$e_{sim}^{VZX}(\times 10^4)$	$e_{c.l.}(\times 10^4)$
Q_1	1.51(7)	2.28(9)	2.29(4)	1.64(4)	1.1(1)
Q_2	1.42(8)	1.50(7)	1.46(6)	2.15(8)	0.94(5)
Q_3	1.44(7)	1.28(6)	1.16(5)	1.31(5)	0.85(5)
Q_4	3.4(1)	3.1(1)	2.23(4)	2.16(4)	0.97(5)
Avg.	1.9(8)	2.0(7)	1.8(5)	1.8(4)	1.0(1)

of qubits, and was performed on a four superconducting transmon qubit device. The full protocol requires running all possible permutations of separate and simultaneous single qubit RB; i.e. on each qubit separately, then on qubit 1 and 2 simultaneously, then qubits 1 and 3, and so on. In the case of four qubits, this results in a total of 15 RB experiments. We ran a reduced protocol, where we performed separate single qubit RB experiments on the four qubits, and then simultaneous single qubit RB on all four qubits, for a total of 5 RB experiments.

Fig. 7.11 shows some of the expectation-of-products and product-of-expectations for the simultaneous RB experiment using the VZX decomposition, along with the fitted correlated multi-qubit depolarising parameters $\alpha_{\langle 12\rangle}$, $\alpha_{\langle 123\rangle}$, $\alpha_{\langle 1234\rangle}$. The fitted uncorrelated multi-qubit depolarising parameters $\alpha_{\langle 1\rangle\langle 2\rangle}$, $\alpha_{\langle 1\rangle\langle 2\rangle\langle 3\rangle}$, $\alpha_{\langle 1\rangle\langle 2\rangle\langle 3\rangle\langle 4\rangle}$ can also be found from this data, although they are not shown on the graph for the sake of legibility. These quantities allow us to look for correlated errors. Sources of such correlated errors could be spurious interactions between qubits, or decoherence events that affect all qubits simultaneously. For instance, $\Delta\alpha_{12} = \alpha_{\langle 12\rangle} - \alpha_{\langle 1\rangle\langle 2\rangle} > 0$ is a clear signature of correlated errors between Q_1 and Q_2, whereas $\Delta\alpha_{12} = 0$ implies no significant correlated errors between these qubits [197]. This applies to all the multi-qubit depolarising parameters, $\Delta\alpha_{12} = \alpha_{\langle 12\rangle} - \alpha_{\langle 1\rangle\langle 2\rangle}$, $\Delta\alpha_{13} = \alpha_{\langle 13\rangle} - \alpha_{\langle 1\rangle\langle 3\rangle}$, ..., $\Delta\alpha_{1234} = \alpha_{\langle 1234\rangle} - \alpha_{\langle 1\rangle\langle 2\rangle\langle 3\rangle\langle 4\rangle}$. If all of these correlated 'error heralds' $\Delta\alpha$ are zero, it implies that correlated errors between qubits are insignificant compared to other error sources. In Fig. 7.11(B) & (C) we plot histograms of all these calculated error heralds $\Delta\alpha$, found by a bootstrapping technique, for simultaneous single-qubit RB performed with the VZX and XY gate sets respectively. Here, we have resampled 500 times from the 80 Clifford seeds, with replacement, to generate 500 resampled single shot data sets. Correlations are preserved by this resampling as we preserve the time ordering of the single shot measurements within each seed. We then fit all

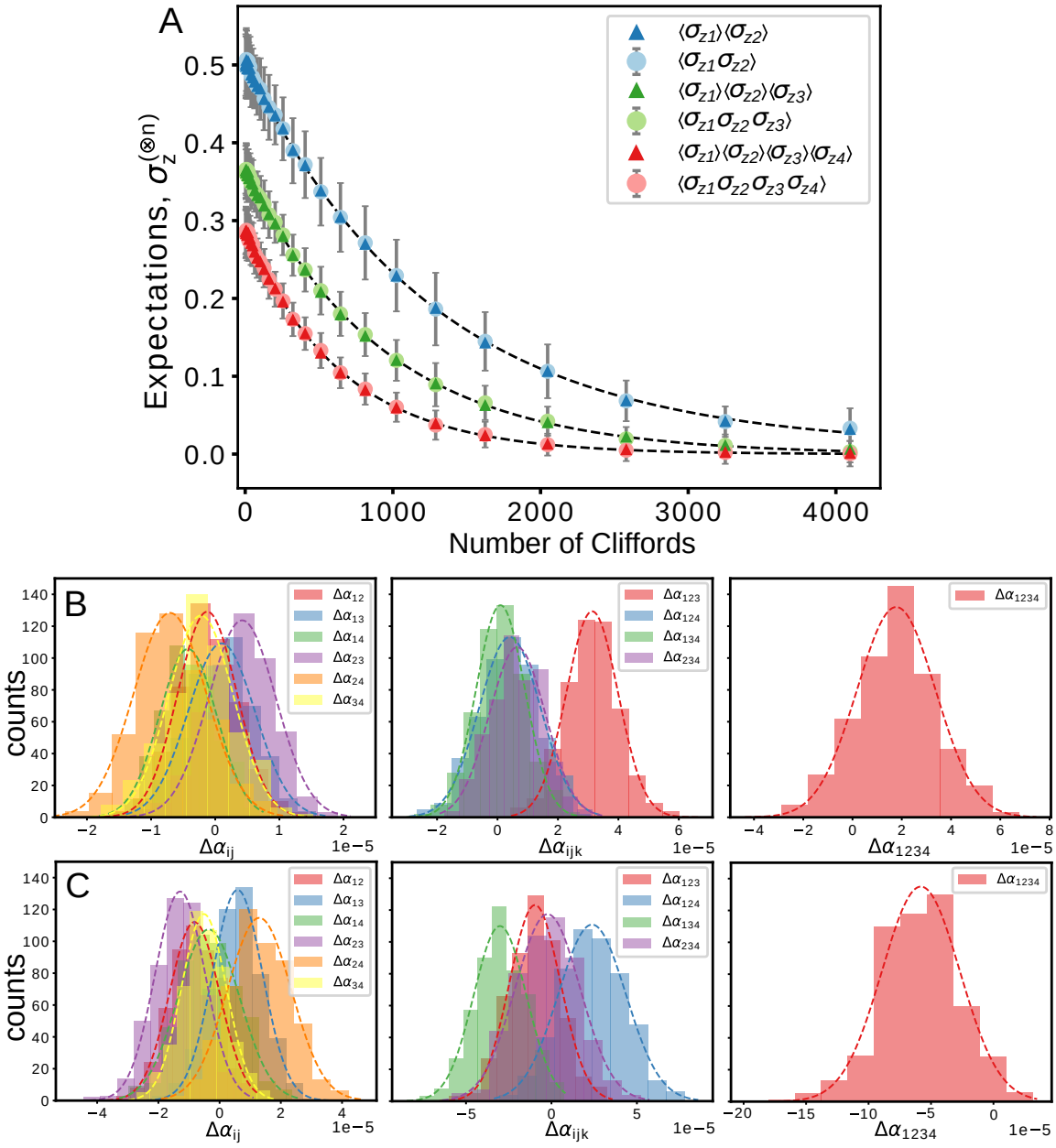

Figure 7.11: **Randomised benchmarking correlated errors:** (**A**) Plotting some of the $\langle\sigma_z\rangle$. (**B**) Histograms of all the resultant correlated error heralds $\Delta\alpha$ for the simultaneous single qubit RB measurement using the VZX decomposition, found by a bootstrapping technique using 500 resamples. (**C**) Correlated error herald histograms using the XY decomposition.

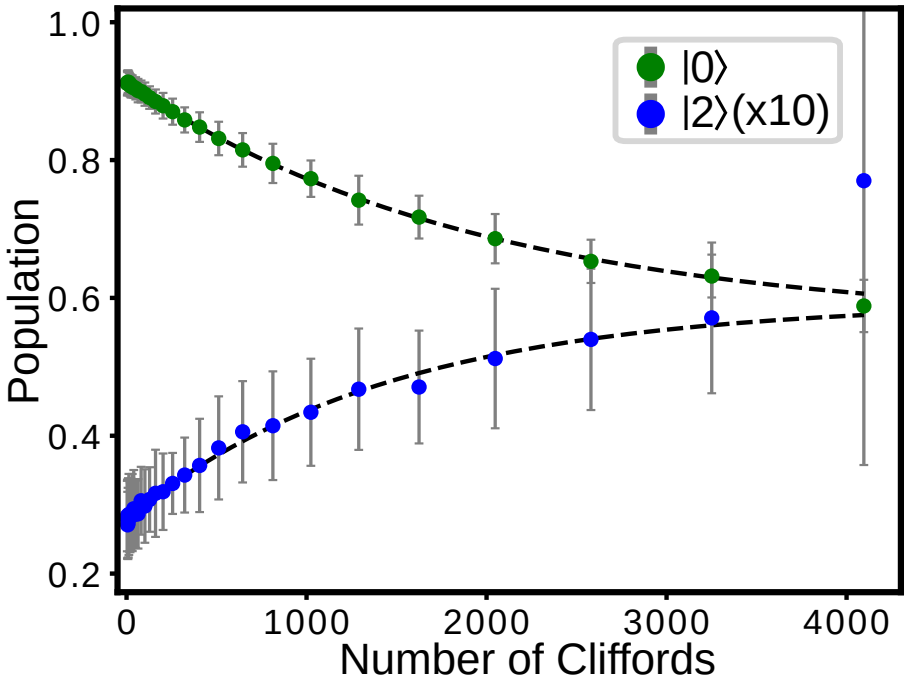

Figure 7.12: **Leakage randomised benchmarking:** RB measurement performed on Q_3, tracking the population of the first three energy levels of the qubit (g and f shown). Both populations are fit to eq. 7.31. Notice the anomalous final measurement value for the f state population, which we exclude from the fit.

of these resampled data-sets to determine the multi-qubit α parameters and build the distributions shown in the figure. The distributions all point to no statistically significant correlated errors - except for $\Delta\alpha_{123}$ in the measurement using the VZX gateset, where the expectation is 3.8 times greater than the standard deviation. This result is surprising as we would not expect 3 qubit correlated errors. We suspect this outlier is a consequence of using a bootstrapping method to determine the errors. It would be better to repeat the experiment many times to generate the statistics, in which case we expect this outlier would disappear. However, as each full RB experiment performed here took 4 hours, this would be time intensive.

An assumption of RB is that the qubits being benchmarked are indeed true two-level systems. As such, the determined errors-per-gate do not in general include leakage out of the qubit basis, and only provide limited information regarding such leakage [198]. Adjusted leakage randomised benchmarking (LRB) protocols have been developed to address this [199]. In our system, we characterised leakage out of the qubit basis on Q_3 by tracking the second excited state population of the qubit during measurement. We choose Q_3 as the readout SNR was sufficient for us to distinguish

the second excited state (the f state) in single-shot measurements. The g state and f state populations during RB are shown in Fig. 7.12. The leakage data is fit to the same RB curve as in eq. 7.31, with the leakage per physical gate (LPG) given by

$$\text{LPG} = (1 - \alpha)B/N_g \tag{7.33}$$

This expression is valid when EPG$\gg$LPG [199]. We find an EPG of $1.98(5) \times 10^{-4}$ and LPG $3.6(3) \times 10^{-5}$. Notice the anomalous final measured value in this experiment, for the 4096 Clifford gate pulse sequence, which we excluded from the fit. This value does not follow the exponential decay curve, and has a much larger standard deviation than the other values. Unfortunately, we are unable to determine a satisfactory cause. In future, a more careful study of leakage should be performed, with the DRAG parameter tuned up specifically to reduce leakage, as in Ref. [194]. In that work, we note that the authors were able to reduce the LPG to $3.1(6) \times 10^{-6}$. Here, we at least determine that in this experiment the LPG is approximately five times smaller than the EPG.

We now present the calibration procedure we used to tune-up single qubit gates for these RB experiments.

7.5.1 Single qubit gate calibration

Our calibration procedure consisted of eight steps, shown in Fig. 7.13. The first step consisted of calibrating single shot qubit readout. We were able to achieve single shot readout without the use of any quantum-limited amplifiers such as Josephson parametric amplifiers (JPAs) [200] or travelling wave parametric amplifers (TWPAs) [201] due to the long coherence times of our qubits. We could use long 5 µs measurement integration windows on the four qubits, which was enough to achieve single shot readout SNR. Histograms of the readout signal for 20000 repeated qubit readout measurements, with no prior state preparation, are shown in Fig. 7.14. Two distinguishable Gaussian-like distributions are visible for all four qubits. We associate these with the thermal ground and excited state populations of the qubits. In the case of Q_3, a third distribution is visible, which we attribute to the second excited state (f state) of the qubit. From the number of counts in each distribution, we can estimate the thermal ground state population of each qubit. We find $p_g = \{84, 84, 94, 90\}\%$, which are consistent with the values found from resonator spectroscopy (Table 7.1), except for Q_3, where the ground state population is anomalously high. This may reflect real variation in qubit temperature over time, or have another cause we cannot

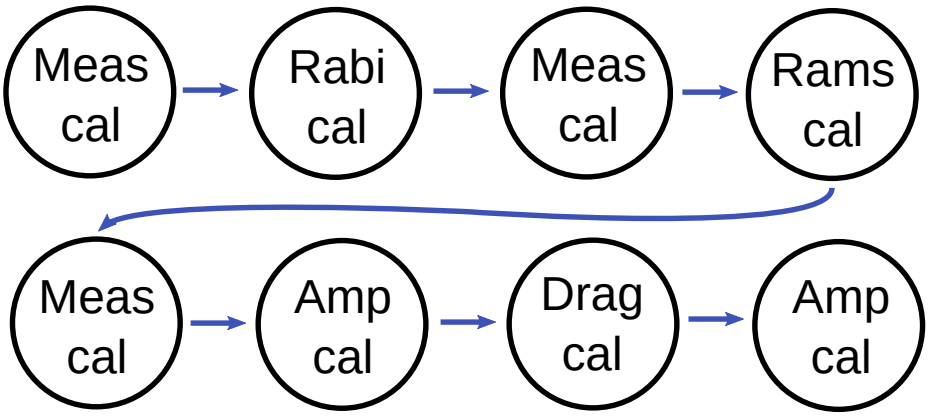

Figure 7.13: **Gate calibration procedure:** Flow diagram of gate calibration process.

identify. We note that the ground state populations measured in other single shot measurements are consistent with those in Table 7.1 (see the ground population in Fig. 7.10(C) for example). We repeated these measurements with a prior π pulse on the qubit, and then used a clustering algorithm (GaussianMixture from the scikit [202] machine learning python package) to categorise individual measurements as corresponding to the qubit being in the ground state or the excited state. This single shot readout functionality was implemented by Shuxiang Cao.

To determine the measurement fidelity of our readout, we simulated readout signals using the measured distribution of the ground and excited state readout signals, and categorised them with our clustering algorithm. We also included the effect of excited qubit decay during the measurement integration time in our model. By counting how many times the simulated ground state measurements are falsely assigned as excited $p(e|g)$, and how many times simulated excited state measurements are falsely assigned as ground $p(g|e)$, we can assign measurement fidelities to each qubit. We use the following definition for the measurement fidelity [45, 54]

$$F = 1 - p(e|g) - p(g|e) \tag{7.34}$$

In this definition, zero readout fidelity corresponds to 50% assignment accuracy (i.e. worst measurement fidelity corresponds to a random coin toss). If eq. 7.34 returns a negative value then swapping the ground and excited state categorisations will result in a positive value between 0 and 1. We find simultaneous readout fidelities of $F = \{97.8, 97.7, 98.5, 98.4\}\%$ for the four qubits in our device, using 5 µs measurement integration windows. Note that our model for calculating the fidelity does not take

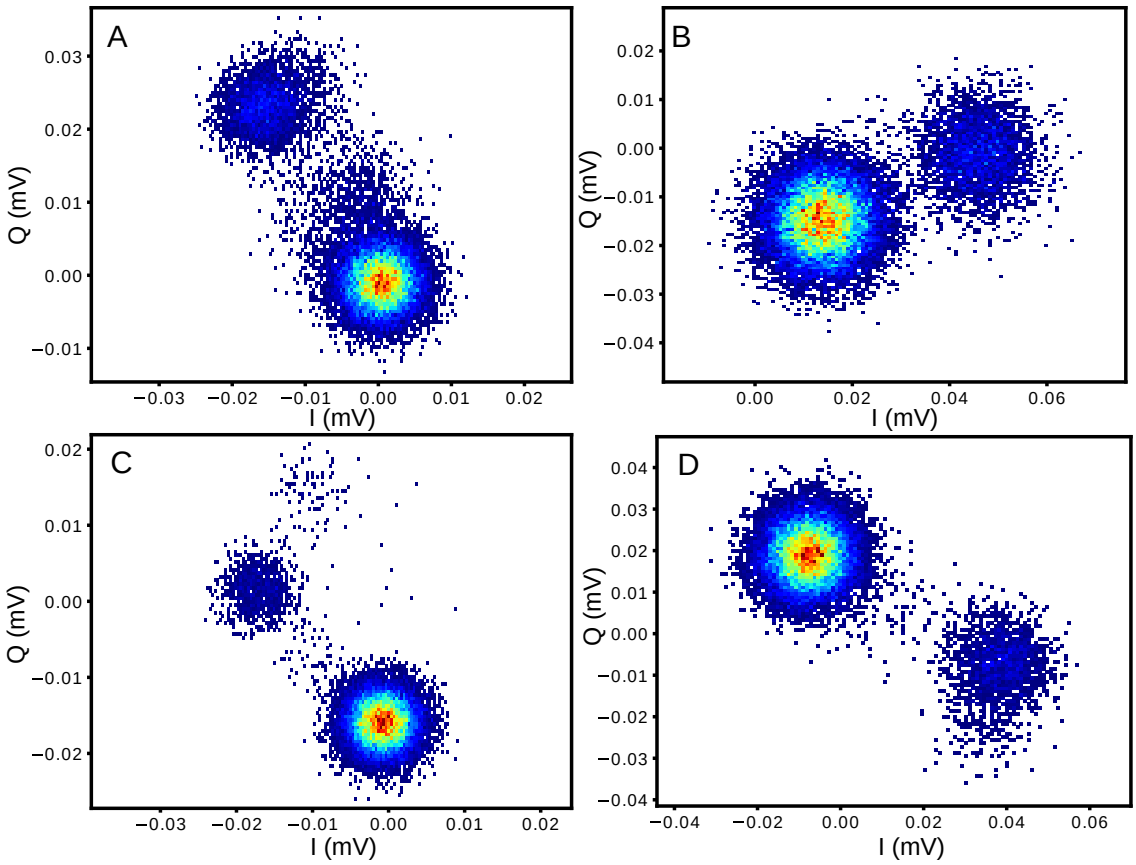

Figure 7.14: **Single shot readout:** Histograms of 20000 single shot readout signals on the 4 qubits, with no prior qubit preparation pulses.

into account thermal excitation events, and so these fidelities will be an overestimate. However, since thermal excitation events are approximately 10 times less frequent than decay events in our device (considering the thermal populations), we expect it to be a good estimate.

After performing single shot readout calibration, which is carried out simultaneously on the four qubits, we calibrated the amplitude of single qubit gates by performing simultaneous time Rabi experiments on the four qubits, from which we calibrate the pulse amplitude required to drive 20 ns π pulses for the four qubits. An example measurement is shown in Fig. 7.15(A). Each qubit was driven with nominally identical power. Under this drive, the qubits underwent a π rotation in $\{8.7, 9.45, 10.5, 14.1\}$ ns respectively.

We repeated single shot readout calibration using these improved π pulses. Next, we

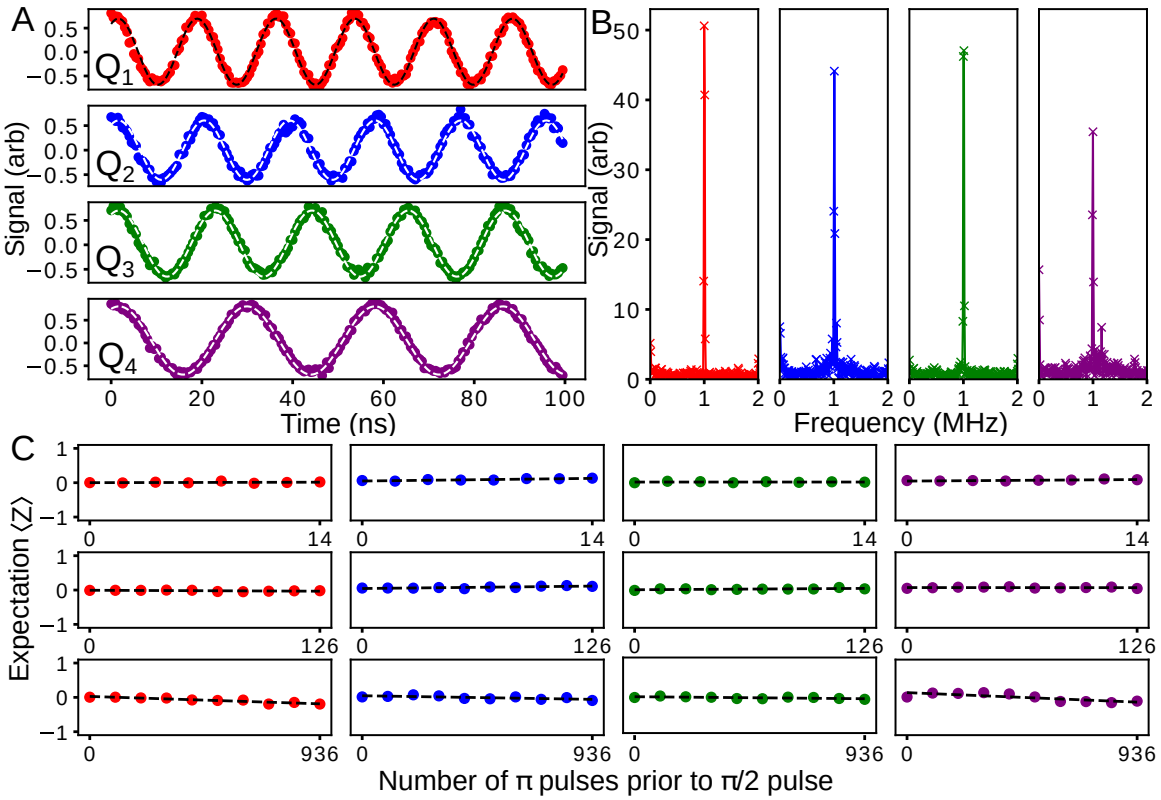

Figure 7.15: **Gate calibration measurements:** Each experiment was performed simultaneously on the four qubits. (**A**) Rabi time trace experiment data. (**B**) Fourier transforms of Ramsey time trace experiment. (**C**) 'ping-pong' π pulse amplitude tune-up experiment. The amplitude error is taken from the gradient of the line fit.

calibrated the frequency of qubit control pulses by performing simultaneous 100 µs long Ramsey interferometry experiments on the four qubits. We detuned the Ramsey pulses by 1 MHz from the recorded values of qubit frequency, and from the measured Ramsey fringe frequency infer the offset of the real qubit frequency from the recorded value. The Fourier transform of these four interferometry experiments are shown in Fig. 7.15(B). In this case, the measured offsets were $\{3.2, 9.1, 4.8, -2.3\}$ kHz.

Having accurately calibrated the frequency and roughly calibrated the amplitude of single qubit gates, we repeated the single shot readout calibration. This was likely unnecessary, but since it took ~ 1 minute, we included it. We then performed a more accurate calibration of the amplitude of single qubit gate control pulses. We did this using a method described in the Appendix of Ref. [203], and which we colloquially refer to as 'ping-pong' calibration. Here, pulse trains containing $2n$ X_π pulses are applied to the qubit ('pinging' the state back and forth between the poles of the

Bloch sphere), before finally applying an $X_{\pi/2}$ pulse ('ponging' the state onto the equator of the Bloch sphere) and measuring. Small errors will result in the final state being slightly over or under rotated from the equator of the Bloch sphere. Crucially, the projected measurement onto the Z axis is first order sensitive to these errors, whereas it would only be second order sensitive if the state was near the poles of the Bloch sphere. For sufficiently small errors ϵ, where $\pi \to \pi(1+\epsilon)$, the measurement expectation $\langle \boldsymbol{Z} \rangle$ after the pulse train is given by [203]

$$\langle \boldsymbol{Z} \rangle = -(2n\pi + \frac{\pi}{2})\epsilon \tag{7.35}$$

By measuring $\langle \boldsymbol{Z} \rangle$ for various values of n, ϵ can be inferred from a line fit, and gate amplitudes adjusted accordingly to correct it. In our calibration, we repeatedly measured progressively longer pulse trains (more sensitive to errors), and corrected the amplitude after each train. Example ping-pong calibration results are shown in Fig. 7.15(C). In this particular example, the pulse amplitudes were adjusted by $\{-1.37, -0.02, -0.95, -0.67\}\%$ due to this ping-pong calibration. The code to perform the ping-pong calibration was written by Takahiro Tsunoda, and was edited to be run simultaneously on the four qubits.

Next, we calibrated the DRAG pulse shape parameter. Briefly, the goal of this DRAG correction is to reduce leakage out of the qubit subspace [204]. In our software, DRAG correction and calibration were implemented by Takahiro Tsunoda. We did not adjust this software to implement the DRAG correction simultaneously on the four qubits, and ran it sequentially on each qubit instead.

Adjusting the DRAG parameter will change the pulse envelope of gates, and so we must again perform amplitude calibration, which we do by repeating the ping-ping calibration. This will itself change the optimal DRAG parameter, and so ideally we would repeatedly iterate between DRAG and amplitude calibration to find the optimum gate parameters. However, as the calibration process gets longer, slow drifts in qubit and measurement instrument parameters can render such fine tuning redundant. For example, we observed that the frequency of our qubits can change by $\sim 10\,\text{kHz}$ on hour long timescales. The output of our qubit generators is also likely to drift with the temperature of the laboratory, which we did not monitor or control during these experiments. Because of these considerations, we finish the calibration procedure after the second ping-pong calibration, at which point the whole calibration process takes 25 minutes.

7.6 Discussion

We now discuss the device in the context of the results. We first summarise the circuit parameters. The measured qubit anharmonicities $|\alpha|/2\pi \approx 200\,\text{MHz}$ were 20% larger than the simulated values of 163 MHz from the BBQ simulation results in Table 6.2, while the average measured qubit-resonator coupling $g/2\pi = 126.5\,\text{MHz}$ was just 2% smaller than the predicted value. The average measured resonator frequency was 319 MHz lower than the desired values in Table. 6.3, while the average frequency step between resonators was 107 MHz as opposed to the desired 100 MHz. The average qubit frequency was 1.82 GHz lower than desired, while the average frequency step between qubits was 70 MHz compared to the desired 100 MHz. Nevertheless, the qubits were still well into the transmon regime, with $E_J/E_C \geq 69$ and charge dispersion on the first level $\epsilon_1 < 400\,\text{Hz}$, corresponding to dephasing times $\gtrsim 250\,\text{ms}$ (see Chapter 2). The average measured single-photon Stark shift $2\chi/2\pi$ was $-332\,\text{kHz}$. The average resonator external decay rate $\kappa_{ext}/2\pi$ was 274 kHz, far below the desired value of 4.5 MHz, with a large standard deviation 269 kHz. The average resonator internal quality factor was 2.13×10^5, similarly having a large standard deviation 1.76×10^5.

7.6.1 Readout

The consequence of the low χ and κ_{ext} values was to negatively impact qubit readout. Following closely Ref. [148], we can use the Fisher separation as a metric of how well dispersive readout can distinguish between the ground and excited states of qubits. If readout signals corresponding to the ground and excited states have averages $\langle S_0 \rangle$ and $\langle S_1 \rangle$, and equal variance $\text{var}(S_0)$, then the Fisher separation is given by

$$R = \frac{(\langle S_0 \rangle - \langle S_1 \rangle)^2}{var(S_0)} \tag{7.36}$$

For dispersive readout of qubits with infinite T_1 times and in the steady-state, using resonators that are externally limited such that $\kappa_{ext} \gg \kappa_{int}$, and in the low photon number limit $n \ll n_{crit}$ the Fisher separation takes the following form [148]

$$R = \frac{8\kappa_{ext} t_m \chi^2 \eta n}{\kappa_{ext}^2/4 + \chi^2} \tag{7.37}$$

where t_m is the measurement time, η is the efficiency of the amplification chain, and n is the number of photons in the resonator. This expression is maximised for $\kappa_{ext} = 2\chi$, to give the simple result

$$R = 4\kappa_{ext} t_m \eta n \tag{7.38}$$

We see that for the best ground and excited state separability, large values of κ_{ext} and χ are favourable given that $\chi = \kappa_{ext}/2$. For fast readout not in the steady-state, this general conclusion remains true, although the optimal ratio of χ/κ_{ext} reduces to below 0.5 [54]. In Ref. [54] 98.25% fidelity single-shot readout was achieved with $t_m = 48\,\text{ns}$, due to very large $\kappa_{ext}/2\pi = 37.5\,\text{MHz}$ and $\chi/2\pi = -7.9\,\text{MHz}$ values. We note that the device in this reference also included a quantum limited amplifier. In our device, we were only able to achieve single shot readout due to the long T_1 times, allowing for long measurement times $t_m = 5\,\mu\text{s}$.

The large variation in κ_{ext} in our device could be due to either poor control pin alignment, or an impedance mismatch on the readout lines inside the dilution refrigerator. Experiments subsequently performed on this device in a different dilution refrigerator by James Wills and Brian Vlastakis reveal that the significant variation in κ remains, making it likely that poor pin alignment is responsible. R_3 had the best performance, with $\kappa_{int}/2\pi \approx 16\,\text{kHz}$ and $\kappa_{ext}/2\pi \approx 750\,\text{kHz}$. This at least establishes that the reverse-side resonator design is capable of operating well into the externally limited regime. More work is needed to improve the reproducibility of high internal quality factor resonators, and to increase the pin alignment accuracy to reduce the variability of κ_{ext} seen in this device.

7.6.2 Qubit coherence

We next discuss the coherence results summarised in Table 7.3. The device had average measured T_1 times of 149 µs and echoed pure dephasing times T_2^* of 189 µs. These results establish that the architecture, featuring off-chip control wiring, reverse-side readout, and inductively shunting pillar are compatible with high transmon qubit coherence times, see e.g. Ref [12]. This is an important consideration for any 3D-integrated architecture and is one of the key results of this thesis. Cautiously, we attribute the high relaxation times to four main factors: (1) The circuit fabrication process, in particular the lack of substrate processing prior to the first metal evaporation, that may introduce contaminants to the substrate and increase dielectric losses. (2) The large physical size of our qubits, which will reduce the participation ratio of the qubits in the lossy interfaces that contribute to dielectric relaxation [59, 63, 67, 69]. (3) The 3D transmon nature of our architecture, with no wire-bonds, bump-bonds, epoxy, or fibreglass PCB's or other lossy materials in proximity to the qubits. (4) The low frequency of our qubits, since dielectric relaxation models predict a frequency independent quality factor $Q_{dielectric}$ [59, 63, 67, 69] and $T_{1,dielectric} = Q_{dielectric}/\omega_q$.

The significant excited state population of the qubits suggests that qubit coherence was not purely dielectic loss limited, and that further increases in qubit coherence could have been made by improving the infra-red (IR) filtering of the device, by reducing quasiparticle related decoherence channels [15].

The pure dephasing times show that the qubit dephasing was not solely limited by qubit relaxation. A thermal photon population in the resonator will cause qubit dephasing at a rate given by eq. 2.75, restated below [81]

$$\Gamma^{th} = \frac{\bar{n}_{th}\kappa\chi^2}{\kappa^2/4 + \chi^2} \tag{7.39}$$

Assuming the dephasing is entirely due to thermal resonator photons sets a bound on the photon number and temperature of our four resonators: $\bar{n}_{th} \leq \{5.7, 6.1, 6.3, 5.4\} \times 10^{-3}$, $T \leq \{71, 73, 74, 73\}$ mK. Here we have used $\bar{n}_{th} = 1/(e^{\hbar\omega_r/k_BT} - 1)$ [205] (valid for $\bar{n}_{th} \ll 1$). The close upper bounds on resonator temperatures is suggestive that thermal photons might indeed have been the dominant dephasing mechanism, as was determined to be the case for the transmon qubit in Ref. [81]. If so, the $\sim$ 70 mK resonators are significantly hotter than the $\sim$ 20 mK base stage of the dilution refrigerator, consistent with 'hot' control lines [81].

7.6.3 Crosstalk

Moving onto the characterisation of crosstalk in the device, the average qubit control line selectivity ϑ_{ij} is -56 dB, with a small standard deviation of ± 3 dB. We concluded the selectivity was dominated by the direct parasitic drive coupling to the qubits $\vartheta_{ij} \approx (\varepsilon^q_{ij}/\varepsilon^q_{ij})^2$. The results demonstrate that the off-chip wiring design is compatible with high qubit selectivity. For comparison, in a superconducting qubit device featuring a quantum chip wirebonded to an interposer PCB, crosstalk between neighbour planar transmission lines on the interposer was ~ -40 dB at 5 GHz, in transmission measurements [104]. In simulations, transmission crosstalk between the wirebonds routing signals from the interposer to the device substrate were -30 dB at 8 GHz [104]. This crosstalk will result in effective $(\varepsilon^q_{ij}/\varepsilon^q_{ij})^2$ values between -30 dB to -40 dB due to the direct coupling of the control lines, before accounting for additional coupling through spurious interactions at the device itself. An advantage of the coaxial off-chip wiring is that, away from the quantum device, direct spurious couplings between the control lines are suppressed, because signals are carried in closed coaxial

cables – with limited routes for EM fields to leak out and cause spurious interactions with other control lines. From the qubit control line crosstalk values, we predict a 20 ns X_π or Y_π gate on any qubit would induce AC Stark shifts in the other qubits $|\omega_{AC,ij}|/2\pi < 30\,\text{Hz}$, which will have a negligible effect on gate errors. This is found from the AC-Stark shift ω_{AC} in the qubit frequency due to an off resonant drive on the qubit [197]

$$\omega_{AC} = \frac{\Omega^2}{2\Delta_{q,d}} \tag{7.40}$$

Here, Ω is the Rabi drive strength on this qubit, $\Delta_{q,d} = \omega_q - \omega_d$ is the detuning of the drive, and it has been assumed that $|\Delta_{q,d}| \gg \Omega$. Labelling this qubit i and assuming the drive is through qubit control line j and resonant with qubit j, then in the case $\vartheta_{ij} \approx (\varepsilon^q_{ij}/\varepsilon^q_{jj})^2$ we expect

$$\omega_{AC,i} = \frac{\Omega_j^2}{2\Delta_{i,j}}\vartheta_{ij} \tag{7.41}$$

where Ω_j is the frequency of Rabi oscillations in qubit j. Approximating the 20 ns X_π and Y_π gates as portions of Rabi oscillations ($\Omega_j/2\pi = 25\,\text{MHz}$) then leads to the above bounds.

The experimental bound the qubit control line selectivity measurements place on qubit-qubit ZZ shifts, $2\chi_{ZZ}/2\pi < 4\,\text{kHz}$, implies that the frequency shift of qubits due to changing the state of other qubits would introduce error-per-gates $< 1 \times 10^{-7}$ for 20 ns physical gates comprising X_π and Y_π rotations. This number is found using a simple Rabi model of the gates. For a qubit initialised in the ground state, the population of the excited state under an continuous off-resonant drive $\Delta_d = \omega_d - \omega_q$ with Rabi drive strength Ω, at time $t = \pi/\Omega$, is given by

$$p_e = \frac{\Omega^2}{\Delta_d^2 + \Omega^2}\sin^2[\frac{\sqrt{\Delta_d^2 + \Omega^2}}{2}t] \tag{7.42}$$

$$= 1 - (\frac{\Delta_d}{\Omega})^2 + \mathcal{O}((\frac{\Delta_d}{\Omega})^4) \tag{7.43}$$

from which the above bound follows.

The average readout control line selectivity φ_{ij} in the device was $-42\,\text{dB}$, which we directly associate with the parasitic drive coupling $\varphi_{ij} = (\varepsilon^r_{ij}/\varepsilon^r_{jj})^2$. From the resonator control line crosstalk, we predict that resonantly populating any of the resonators with up to its critical photon number would result in negligible photon numbers in other resonators, using eq. 7.22.

The very stringent experimental bounds on parasitic single-photon Stark-shifts $\chi_p/2\pi < 40\,\text{Hz}$ (corresponding to $g_p/2\pi < 1.5\,\text{MHz}$) and on parasitic dephasing rates $\Gamma_p/2\pi < 0.5\,\text{Hz}$ (at $n_{crit}/10$ photons where n_{crit} is the critical photon number) imply qubit readout will have a negligible effect on neighbouring qubit dynamics. This is an indication that the reverse-side readout design is compatible with selective qubit readout that minimally disturbs neighbouring qubits. It is also an improvement on a previous four-qubit coaxmon device, where values of g_p up to $g_p/2\pi = 19\,\text{MHz}$ were directly measurable [144]. We attribute this to the greater qubit pitch in our device, and to the different qubit and resonator pad dimensions.

7.6.4 Single qubit gates

Simultaneous single-qubit RB on the four qubits provides a strong overall figure of merit for the device, since it is sensitive to qubit coherence, crosstalk, and the ability of the off-chip wiring to transmit undistorted control pulses to qubits. The high coherence and low crosstalk in our device are reflected in high [12, 112, 194] single qubit gate fidelities (avg. $> 99.98\%$) measured by simultaneous RB. The low crosstalk is consistent with the small differences in the separate and simultaneous RB gate errors, and by the fact we are unable to find statistically significant signatures of correlated errors in the simultaneous RB data. In the case of Q_3 (XY gateset) and Q_1 (VZX gateset), the error-per-gate was in fact significantly higher in the RB experiment that was run separately, which we attribute to variability in both our gate tune-up procedure and in qubit coherence on hour-long timescales. Our physical gate errors were approximately 40-70% coherence limited. Two plausible remaining error channels are X errors due to non-idealities with our amplitude tune-up, and Z errors due to Stark shifting of our low anharmonicity qubits by the 20 ns control pulses [194] (due to off resonantly driving the $|1\rangle \leftrightarrow |2\rangle$ qubit transition). Software improvements to increase single qubit gate fidelities should include calibrating a phase correction to correct for these Stark shifts [194], which could be implemented using a virtual Z gate [194]. Interestingly, since we do not perform such phase correction, our DRAG correction may in fact be dominantly mitigating phase errors and not leakage errors [194]. Tuning up a phase correction with virtual Z gates before tuning up DRAG correction may also therefore significantly reduce the leakage per gate (LPG), as demonstrated in Ref. [194].

7.6.5 Limitations

We conclude the chapter with a discussion of the limitations of our device. We identify two main limitations: (1) The readout parameters of our device were not ideal and should be improved in future devices. (2) The functional benefit of the pillar was not conclusively demonstrated in these experiments due to the small enclosure size. In HFSS eigenmode simulations, the fundamental cavity mode frequency of the device is 30 GHz with the pillar, and 21 GHz without it, both well above the circuit mode frequencies. We were unable to experimentally detect clear signatures of this cavity mode in cryogenic experiments due to the high attenuation of our readout lines outside the 8 GHz − 12 GHz band. To convincingly demonstrate the effect of the pillar on crosstalk will require a larger enclosure where cavity modes would interact more strongly with qubits in the absence of the pillar array. This limitation is addressed in the conclusions.

Chapter 8

Conclusions

In this thesis, we have reviewed some of the major scaling challenges faced by superconducting circuits and proposed circuit tileability as a useful property for a scalable circuit architecture. We have reviewed the coaxmon architecture and motivated it as a promising scaling architecture, with the aid of HFSS simulations and analytical results. We have discussed how in its original form, this architecture cannot tile due to the emergence of low frequency spurious cavity modes in the enclosure. We have then developed models to show how inductively shunting cavities can allow them to scale arbitrarily in two dimensions while possessing a cutoff frequency below which no cavity modes can exist, and shown good agreement between these models and HFSS simulations. In particular, we have applied a plasma meta-material model [160] for cylinder arrays to model the cavity in the limit that the cylinder radii are suitably small, and have used a circuit model in the large radii limit where the inductively shunted cavity can be modelled as a 2D coupled-cavity array. We have used these models to predict the exponential decay of cavity-mediated crosstalk between superconducting qubits enclosed in such cavities, finding agreement between an approach that considers the transfer impedance between enclosed qubits, and one that considers a bounds states interaction between enclosed qubits.

We have then integrated an inductively shunted cavity into the coaxmon architecture to form a unit cell containing a single addressable and measurable qubit and a single inductive shunt. We have shown in HFSS simulations that the cutoff frequency and band-structure of the infinite construct formed by tiling this unit cell agree well with those predicted by the plasma meta-material model. We have designed and constructed a four-qubit device that contains within it this unit cell, and demonstrated high coherence times (avg. $T_1 = 149\,\mu s$, $T_2^* = 189\,\mu s$) and single qubit gate fidelities (avg. $> 99.98\%$) comparable to the state-of-the-art in transmon circuits [12], along with high control wiring selectivity. The device construction involved the fabrication of reverse-side circuits and the use of novel CNC drilling of the silicon circuit substrate.

It is anticipated that this architecture can be tiled to build 2D arrays of hundreds or thousands of nearest-neighbour coupled qubits, and so provide a useful testbed of algorithms suited to this connectivity, such as the surface codes for quantum error correction [94–96]. More generally, it is hoped that application of the plasma meta-material model of Ref. [160] to inductively shunted cavities as described in this thesis will prove fruitful in the design of large-scale superconducting circuit device enclosures [153].

8.1 Future directions

Towards these goal, there are plenty of directions for further work. In the near-term, the architecture is planned to be demonstrated at the 16 qubit scale. Fig. 8.1 shows an enclosure that has been made for this purpose. The enclosure is a simple copy-paste extension of the four-qubit device enclosure demonstrated in this thesis (recesses have also been milled out in the lid to reduce the capacitance to ground of nearest-neighbour coupling circuitry). Importantly, the simulated fundamental mode frequency in this enclosure is found to be 10.9 GHz in the case where the pillar array is not inductively shunted to the enclosure lid with indium, and 34.8 GHz when the pillar array is inductively shunted to the enclosure lid. This is close to the fundamental frequency of the infinite array simulated in Chapter 6: 34.3 GHz. Thus it should be easier to experimentally verify the effect of the pillar on enclosure modes. It will also be possible to measure, or at least bound, distance 2 (next-nearest neighbour) and distance 3 crosstalk in this device. Prior to circuit fabrication, measurements of S parameters between different control ports in the enclosure should be able to test the predicted form of the exponential decay of crosstalk found in this thesis.

Further work should be invested into improving readout parameters in future devices over those found in this thesis. A demonstration of high fidelity $\sim 99\%$, fast ~ 100 ns readout would establish that the architecture is able to perform qubit readout on par with the state-of-the-art in planar superconducting circuit designs [53, 54]. This is particularly important for surface code experiments, where the state of ancillary qubits must be readout and reset at the end of each stabilisation cycle [94]. Furthermore, work should be undertaken to multiplex readout in this architecture to improve its scalability.

Associated with improving readout parameters, the alignment of the off-chip control wiring should be improved. While the assembly process presented in this thesis to make the 'control plug' wiring parts was viable for the purposes of a demonstration device, in future it would be sensible to collaborate with industry partners to create reproducible, bespoke control plug parts with higher tolerances. This will become a necessity at larger scales.

Improved light-tight shielding [15, 73] should be employed in future devices to reduce the high (avg. $> 10\%$) residual excited state populations measured in this thesis. It is anticipated this will also improve qubit relaxation times.

Lastly, ZX gates between two directly capacitively coupled transmons have already been demonstrated in the architecture [140] (without the inductive shunt) using the cross-resonance gate, with fidelity = 97%. It will be necessary to demonstrate higher fidelity two qubit gates in larger qubit arrays, while maintaining the ability to perform high fidelity single qubit gates and selective readout.

We conclude on a speculative note, by asking: how many qubits can this architecture accommodate? If we limit ourselves to monolithic devices fabricated on a single substrate, then the unit cell in this thesis (having 2 mm qubit pitch) could tile to an array of 2000 qubits in a 9 cm $\times$ 9 cm area, or to an array of 8000 qubits in a 18 cm $\times$ 18 cm area. Such circuits could be fabricated on a 6 inch and a 12 inch silicon wafer respectively. We see no obvious roadblocks to building the device enclosures for these circuits with the same CNC methods as used in this thesis, and such enclosures could comfortably fit inside a dilution refrigerator. The scaling bottleneck would instead be the space and cost requirements of the cryogenic control setup, the control electronics, and the heat load on the dilution refrigerator [57] during circuit operation. In the near-term, it should be possible to characterise subsets of qubits in such devices, to measure or bound crosstalk between distant qubits, and to study correlated errors over larger spatial distances than have previously been accessible. For instance, correlated relaxation errors between qubits separated at the $\sim$ cm scale due to radiation induced quasiparticles have been indicated as a potentially serious threat to error correction with superconducting qubits [74, 77]. It is our hope that this architecture could be a promising testbed for probing questions such as this on the road to fault tolerant quantum computation.

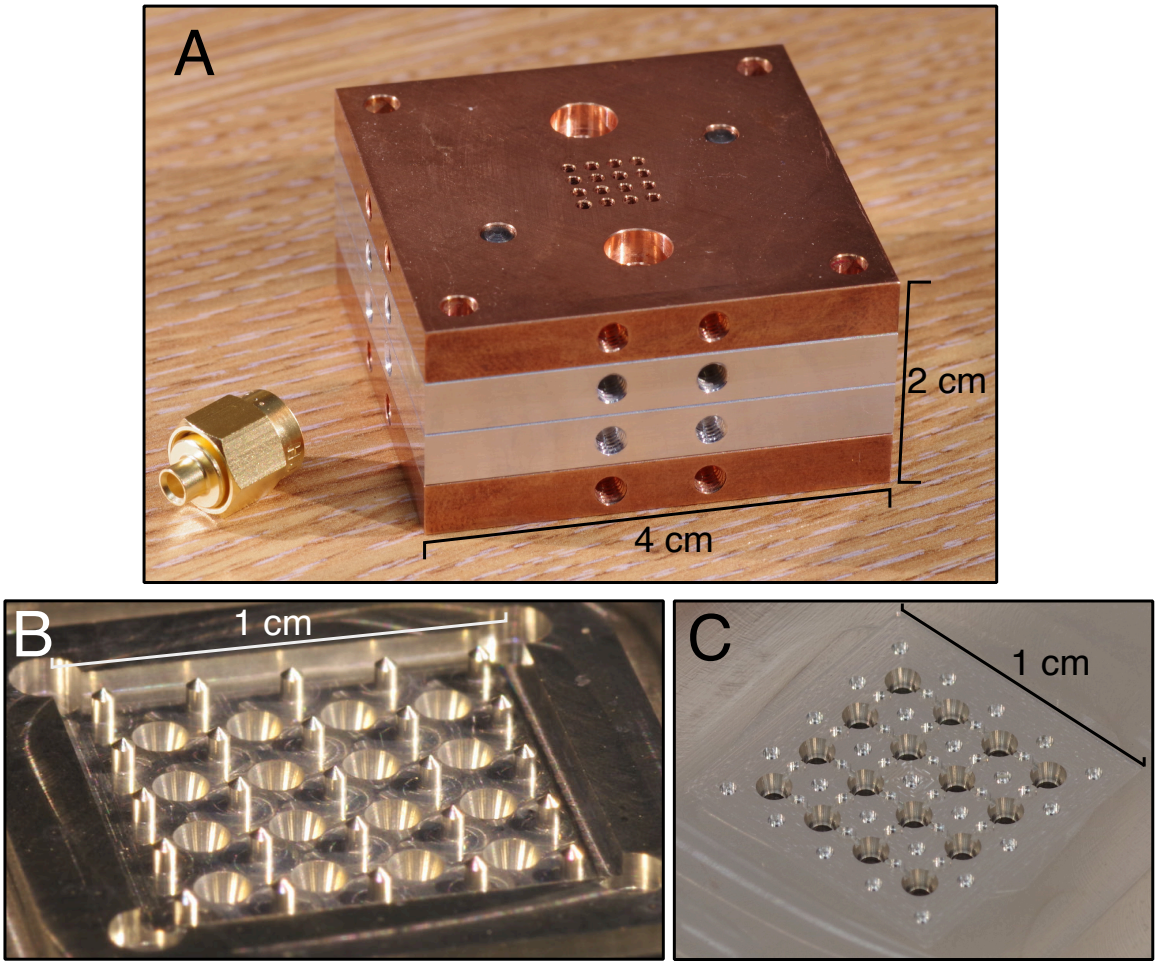

Figure 8.1: **16 qubit device enclosure:** Optical images of CNC machined enclosure for a 16 qubit circuit on a 10 mm × 10 mm substrate. (**A**) Closed enclosure with circuit-facing halves of the unassembled control plugs attached, and SMA connector for scale. (**B**) Close up of the enclosure base, featuring a 5×5 array of micro-machined pillars and 16 tapered through holes for readout resonator control wiring. (**C**) Close up of enclosure lid, featuring a 5×5 array of wells for the pillars to enter, 16 tapered through holes for qubit control wiring, and milled out recesses between the tapered through holes to reduce the capacitance of qubit coupling circuitry to ground.

Appendices

Appendix A

Mapping 2D Coupled Cavity Circuit to 1D Circuit

Using mesh analysis [206], the currents i_i in Fig. 5.5 of the main text must satisfy

$$\mathbf{Z_{2D}} \begin{bmatrix} i_1 \\ \vdots \\ i_i \\ \vdots \\ i_{nm} \end{bmatrix} = \begin{bmatrix} V_1 \\ \vdots \\ V_i \\ \vdots \\ V_{nm} \end{bmatrix} \tag{A.1}$$

where $\mathbf{Z_{2D}}$ is an $nm \times nm$ impedance matrix defined below, i_i is the current through mesh i and V_i is the voltage applied to mesh i. At the resonant mode frequencies of this circuit, currents can oscillate in the absence of any excitations ($V_i = 0$), which will occur when $\mathbf{Z_{2D}}\boldsymbol{i} = \lambda \boldsymbol{i}$, $\lambda = 0$.

$\mathbf{Z_{2D}}$ can be expressed as a diagonal block matrix. For a nearest neighbour coupling model this block matrix is tridiagonal, while for a next-nearest neighbour coupling model it is pentadiagonal, and so on. We will consider the cases of nearest neighbour and next-nearest neighbour couplings. Expressed in block form, $\mathbf{Z_{2D}}$ is a $m \times m$ matrix of $n \times n$ matrices. For nearest neighbour coupling, it takes the form

$$\mathbf{Z_{2D_{m\times m}}} = \begin{bmatrix} \mathbf{Z}\alpha & \mathbf{Z_G} & & & \cdots & & \mathbf{0} \\ \mathbf{Z_G} & \mathbf{Z}\beta & \mathbf{Z_G} & & & & \\ & \mathbf{Z_G} & \mathbf{Z}\beta & \mathbf{Z_G} & & & \\ & & \ddots & \ddots & \ddots & & \\ & & & \mathbf{Z_G} & \mathbf{Z}\beta & \mathbf{Z_G} & \\ & & & & \mathbf{Z_G} & \mathbf{Z}\beta & \mathbf{Z_G} \\ \mathbf{0} & & \cdots & & & \mathbf{Z_G} & \mathbf{Z}\alpha \end{bmatrix}$$

where

$$\mathbf{Z}\alpha_{\mathbf{n\times n}} = \begin{bmatrix} Z_{\alpha_1} & -Z_g & & & \cdots & & 0 \\ -Z_g & Z_{\alpha_2} & Z_b & & & & \\ & -Z_g & Z_{\alpha_2} & -Z_g & & & \\ & & \ddots & \ddots & \ddots & & \\ & & & -Z_g & Z_{\alpha_2} & -Z_g & \\ & & & & -Z_g & Z_{\alpha_2} & -Z_g \\ 0 & & \cdots & & & -Z_g & Z_{\alpha_1} \end{bmatrix}$$

$$Z_{\alpha_1} = Z_0 + 2Z_g + 2Z_b$$
$$Z_{\alpha_2} = Z_0 + 3Z_g + Z_b$$

$$\mathbf{Z}\beta_{\mathbf{n\times n}} = \begin{bmatrix} Z_{\beta_1} & -Z_g & & & \cdots & & 0 \\ -Z_g & Z_{\beta_2} & Z_b & & & & \\ & -Z_g & Z_{\beta_2} & -Z_g & & & \\ & & \ddots & \ddots & \ddots & & \\ & & & -Z_g & Z_{\beta_2} & -Z_g & \\ & & & & -Z_g & Z_{\beta_2} & -Z_g \\ 0 & & \cdots & & & -Z_g & Z_{\beta_1} \end{bmatrix}$$

$$Z_{\beta_1} = Z_0 + 3Z_g + Z_b$$
$$Z_{\beta_2} = Z_0 + 4Z_g$$

$$\mathbf{Z_{G_{n\times n}}} = -Z_g\mathbf{I_{n\times n}}$$

and

$$Z_0 = i\omega L_0 - \frac{i}{\omega C_0} \qquad Z_g = i\omega L_g \qquad Z_b = i\omega L_b$$

It can be verified by expansion that $\mathbf{Z_{2D}}$ can be written

$$\mathbf{Z_{2D_{nm\times nm}}} = \mathbf{Z_{1D_{n\times n}}} \oplus \mathbf{Z_{1D_{m\times m}}} - Z_0\mathbf{I_{nm\times nm}} \tag{A.2}$$

where $\oplus$ is the Kronecker sum and

$$\mathbf{Z_{1D_{n\times n}}} = \begin{bmatrix} Z_1 & -Z_g & & \cdots & 0 \\ -Z_g & Z_2 & -Z_g & & \\ & \ddots & \ddots & \ddots & \\ & & -Z_g & Z_2 & -Z_g \\ 0 & \cdots & & -Z_g & Z_1 \end{bmatrix}$$

$$Z_1 = Z_0 + Z_g + Z_b$$
$$Z_2 = Z_0 + 2Z_g$$

$\mathbf{Z_{1D_{n\times n}}}$ is exactly the impedance matrix of the circuit in Fig. 5.6 of the main text. This mapping makes solving the eigenvalues of $\mathbf{Z_{2D}}$ much easier, since it immediately follows that

$$\lambda(\mathbf{Z_{2D}})_{ij} = \lambda(\mathbf{Z_{1D}})_i + \lambda(\mathbf{Z_{1D}})_j - Z_0 \tag{A.3}$$

Therefore, finding the mode frequencies of the 2D circuit is reduced to the problem of solving the eigenvalues of the 1D circuit, inserting these into eq. (A.3), and solving for $\lambda(\mathbf{Z_{2D}})_{ij} = 0$.

$\mathbf{Z_{1D}}$ is a tridiagonal matrix that is also a toeplitz matrix except for the 'boundary' elements $\mathbf{Z_{1D}}_{11}$ and $\mathbf{Z_{1D}}_{nn}$. Exact, simple closed-form solutions for this type of matrix are known to exist for particular values of these boundary elements [207], in our case for the three values $L_b = 0, L_g, 2L_g$. Using these solutions and substituting into eq. (A.3) leads to the following mode frequencies for the circuit in Fig. (5.5) of the main text

$$f_{ij} = \frac{f_0}{\sqrt{1 + 4\beta(1 + \frac{1}{2}\gamma_{ij})}} \tag{A.4}$$
$$\gamma_{ij} = \cos(\frac{i\pi}{n}) + \cos(\frac{j\pi}{m}) \quad (L_b = 0)$$
$$\gamma_{ij} = \cos(\frac{j\pi}{n+1}) + \cos(\frac{j\pi}{m+1}) \quad (L_b = L_g)$$
$$\gamma_{ij} = \cos(\frac{(i-1)\pi}{n}) + \cos(\frac{(j-1)\pi}{m}) \quad (L_b = 2L_g)$$

Notice that increasing the boundary inductance L_b lowers the frequency of all modes in these solutions.

We find it interesting that the 2D circuit can be mapped directly into the far simpler 1D circuit. This is only true for the special case of identical inductances and capacitances across all unit cells, and in general is not possible.

We now consider the next-nearest neighbour coupling case, to demonstrate the effect of including further couplings. Here, next nearest neighbour couplings include horizontal and vertical next-nearest neighbour couplings, and do *not* include diagonal

next-nearest neighbour couplings. In this case, it can again be verified by expansion that $\mathbf{Z_{2D}}$ can be written in the same form as eq. (A.2), where now

$$\mathbf{Z_{1D_{n\times n}}} = \begin{bmatrix} Z_1 & -Z_g & -Z_{g_2} & & \cdots & & 0 \\ -Z_g & Z_2 & -Z_g & -Z_{g_2} & & & \\ -Z_{g_2} & -Z_g & Z_3 & -Z_g & -Z_{g_2} & & \\ & & \ddots & \ddots & \ddots & & \\ & & & & & & \\ & & -Z_{g_2} & -Z_g & Z_3 & -Z_g & -Z_{g_2} \\ & & & -Z_{g_2} & -Z_g & Z_2 & -Z_g \\ 0 & & \cdots & & -Z_{g_2} & -Z_g & Z_1 \end{bmatrix}$$

$$\begin{aligned} Z_1 &= Z_0 + Z_g + Z_{g_2} + Z_b \\ Z_2 &= Z_0 + 2Z_g + Z_{g_2} \\ Z_3 &= Z_0 + 2Z_g + 2Z_{g_2}. \end{aligned}$$

This is again the impedance matrix of the circuit in Fig. 5.6 of the main text, now with next nearest neighbour couplings included. Simple closed form solutions to $\mathbf{Z_{1D_{n\times n}}}$ no longer exist in this case, however the problem has still been greatly simplified from one of finding the eigenvalues of a $\mathbf{mn} \times \mathbf{mn}$ matrix to one of finding the eigenvalues of one $\mathbf{m} \times \mathbf{m}$ matrix and one $\mathbf{n} \times \mathbf{n}$ matrix.

Appendix B

HFSS Models for Inductively Shunted Cavities

All FE simulations for Chapter 5 were carried out in ANSYS HFSS using the eigenmode solver. Fig. B.1 shows the model used to simulate the mode frequencies shown in Fig. 5.4 of the main text. $\ell_z = 10r$ in this model to reduce the mesh volume for smaller values of r. This is justified by the fact we expect the solutions to be independent of ℓ_z. 35 adaptive passes were done in the simulation to improve the result accuracy. The total number of mesh elements was $\sim 1 \times 10^6$ in the final pass.

Fig. B.2(A) shows the model used to simulate the fundamental mode frequency of the inductively shunted cavity taking $\ell_x, \ell_y \to \infty$, also shown in Fig. 5.4 of the main text. In this simulation, the total number of mesh elements was $\sim 1 \times 10^5$. Fig. B.2(B) shows the simulated fundamental mode frequency of this infinite structure for different values of ℓ_z. The relative standard deviation of the frequency is 0.005% between $\ell_z = 0.1\,\text{mm}$ and $1\,\text{mm}$, which could be entirely attributable to simulation error, demonstrating that the fundamental mode frequency is largely independent of ℓ_z over this range.

Fig. B.3 shows the model used to simulate the mode frequencies shown in Fig. 5.7 of the main text for $n = 6$. The cavity contains a 6×6 array of effective coupled cavities, formed between a 5×5 inductive shunt array. Inductive shunts are also embedded into the boundary walls in this model. This was done in order to justify the assumption $L_b = 0$ in the circuit model. In this simulation, the number of adaptive passes was 24, and the number of mesh elements was $\sim 0.5 \times 10^6$.

Fig. B.4 shows the model used to simulate the four qubit circuit parameters in Table. 6.2 of the main text; and also to simulate the Purcell filter response in Fig. 4.8 of the main text.

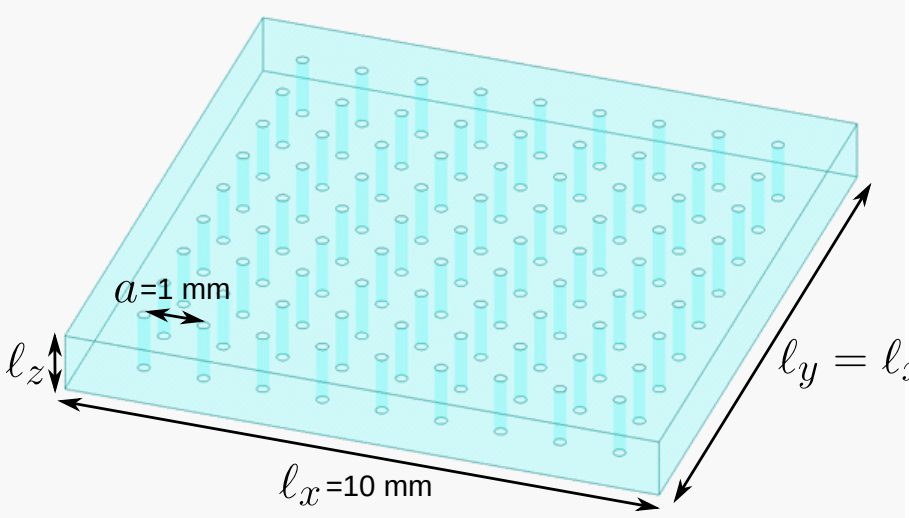

Figure B.1: **HFSS model to test plasma model predictions:** HFSS model featuring a 9×9 array of perfectly conducting shunts through a $10\,\text{mm} \times 10\,\text{mm}$ lossless dielectric with permittivity $\epsilon_r = 11.9$ and bounded on all sides by perfect conductor. In this image, $r = 0.1\,\text{mm}$.

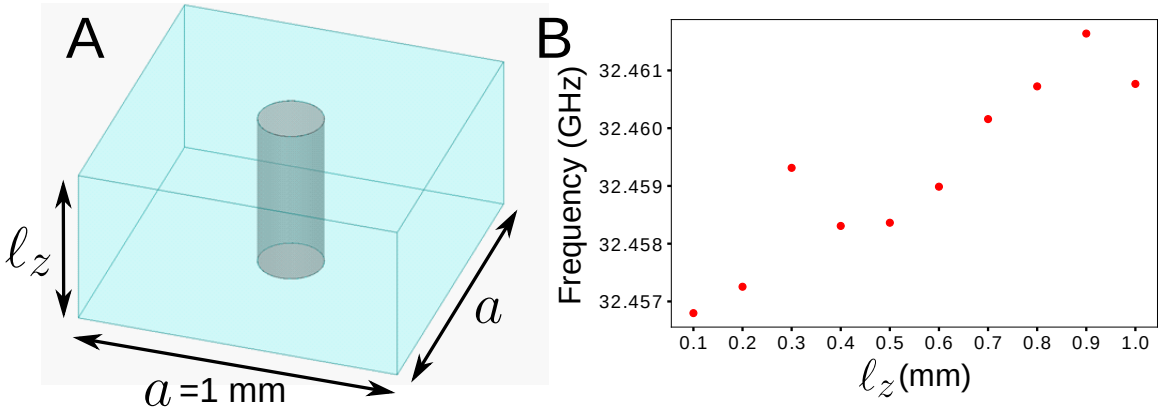

Figure B.2: **HFSS model of infinite cylinder array:** (**A**) HFSS model of an infinite 2D array of perfectly conducting cylinders in a lossless dielectric with permittivity $\epsilon_r = 11.9$. Linked boundary conditions (so called 'Master' and 'Slave' boundaries) are assigned on the side walls to simulate the fundamental mode of the infinite structure. The upper and lower walls are assigned as perfect conductor. In this image $r = 0.1\,\text{mm}$. (**B**) The simulated fundamental mode frequency for different values of ℓ_z, for $r = 0.1\,\text{mm}$.

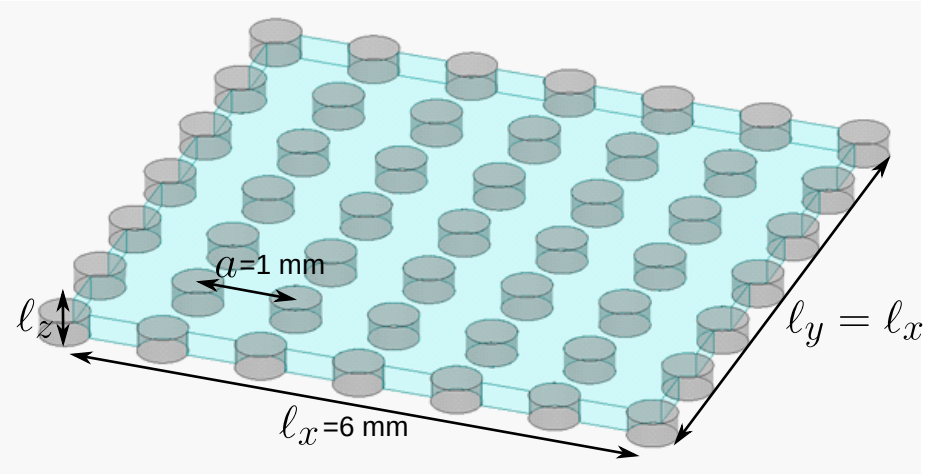

Figure B.3: **HFSS model to test circuit model predictions:** HFSS model featuring a 5×5 array of perfectly conducting shunts through a $10\,\text{mm} \times 10\,\text{mm}$ lossless dielectric with permittivity $\epsilon_r = 11.9$ and bounded on all sides by perfect conductor. $r = 0.25\,\text{mm}$ in this image.

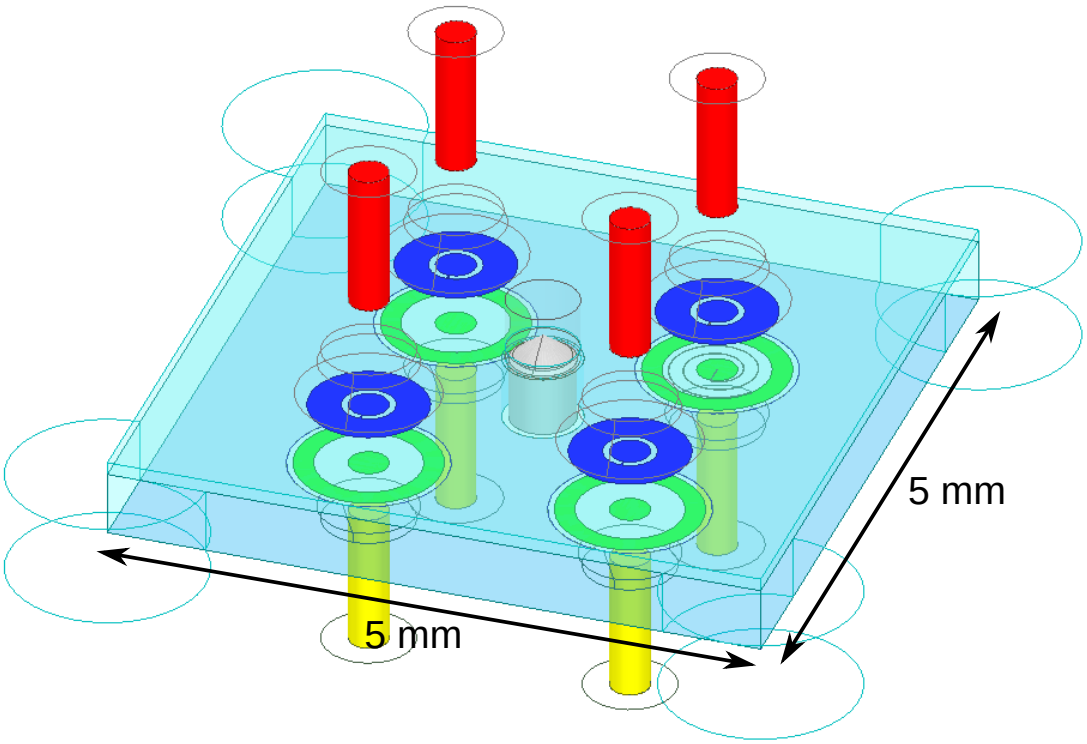

Figure B.4: **HFSS model of four qubit device:** Used to simulate the properties of a single qubit-resonator pair. A single lumped port is placed across the top right qubit and the concentric resonator pads are joined by a perfectly conducting spiral. All other resonator pads are open circuited to reduce the simulation complexity.

Appendix C

Fabrication Recipe

Wafer clean & evaporation

1 2 minute HF dip in 10:1 buffered oxide etchant (BOE 10:1, Chemstech), using the wafer dipper shown in Fig. C.3(A) to prevent backside contact with the fresh wafer.

2 Clean in two large beakers of deionised (DI) water: 30 s each beaker.*

3 Load wafer into loadlock of PLASSYS evaporator (Fig. C.2)(B) within 5 minutes (to limit oxide regrowth) with qubit-side exposed, using the wafer cassette shown in Fig. C.3(E) to prevent backside contact.

4 Transfer to oxidation chamber, pressure $\approx 2 \times 10^{-8}$ mbar, and bake for 12 hours at $\sim 100\,^{\circ}$C using UV bulb (to remove water traces from substrate).

5 Evaporate 100 nm of aluminium onto the qubit-side of the wafer using 1 nm/s evaporation rate, evaporation chamber pressure $\approx 2 \times 10^{-8}$ mbar.

6 Unload wafer, turn over to expose resonator-side, reload, and evaporate 100 nm of aluminium using the same evaporation rate.

* The HF dip removes the oxide layer on the silicon. As a result, the surface becomes hydrophobic and the DI water beads and rolls off, making a nitrogen dry unnecessary. However, the surface also becomes highly reactive and attracts particulates [208], making the wafer particularly vulnerable to contamination at this stage. The DI water used to remove the HF should therefore be very pure. Fig. C.1 shows optical images of sections of different wafers before (A) and after the HF dip, cleaned using (B) particulate filtered DI water from the cleanroom tap and (C) ultra-pure DI water (19391 - Spectrophotometric Grade - Alfa Aesar). As is clear, using the DI water from

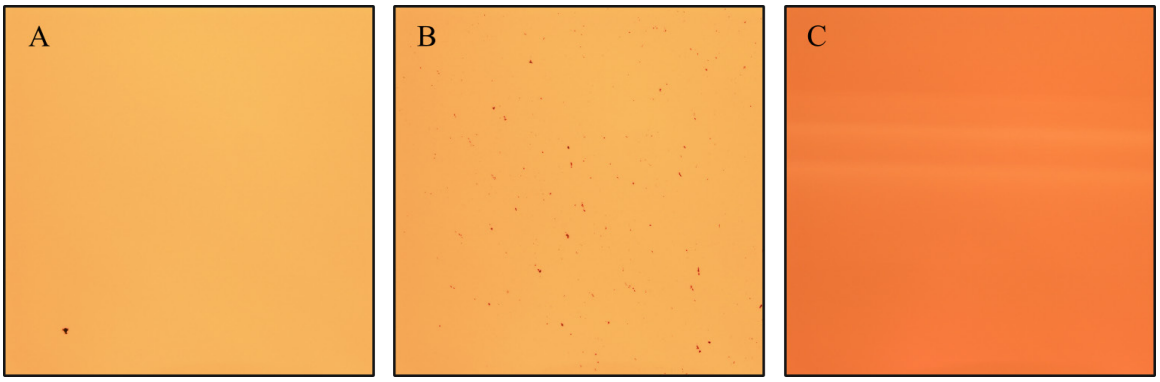

Figure C.1: **DI clean post HF dip:** Optical images under 5x magnification of silicon wafer (**A**) Before any processing. (**B**) After HF dip and clean in DI water from cleanroom tap. (**C**) After HF dip and clean in ultra-pure DI water. (Change in colour due to different microscope lighting settings in final image.)

the cleanroom tap results in significant surface contamination whereas the ultra-pure DI water does not. After determining this, ultra-pure DI water was used at all stages of our fabrication process that required DI water.

Large feature fabrication

The large qubit and resonator features are all patterned on the wafer by a photolithography and etching process. In this recipe, the resonator-side is patterned first, though the order is likely not essential.

1 Spin coat (Fig. C.2(D)) the qubit-side of the wafer with a protective layer of Microchemicals AZ1514 H photo-resist: 4000 rpm, 50s. Use the non-backside contact chuck shown in Fig. C.3.

2 Softbake on hotplate (Fig. C.2(E)) with qubit-side up: 100 °C, 50s. Use the the metal ring shown in Fig. C.3(D) during all hotplate bakes to prevent contamination of the wafer backside.

3 Let cool for 2 minutes.

4 Spin coat active layer of AZ1514 H photo-resist onto resonator-side: 4000 rpm, 50s. Now use a standard vacuum chuck for improved resist uniformity compared to the non-vacuum chuck.

5 Softbake on hotplate with resonator-side up: 100 °C, 50s.

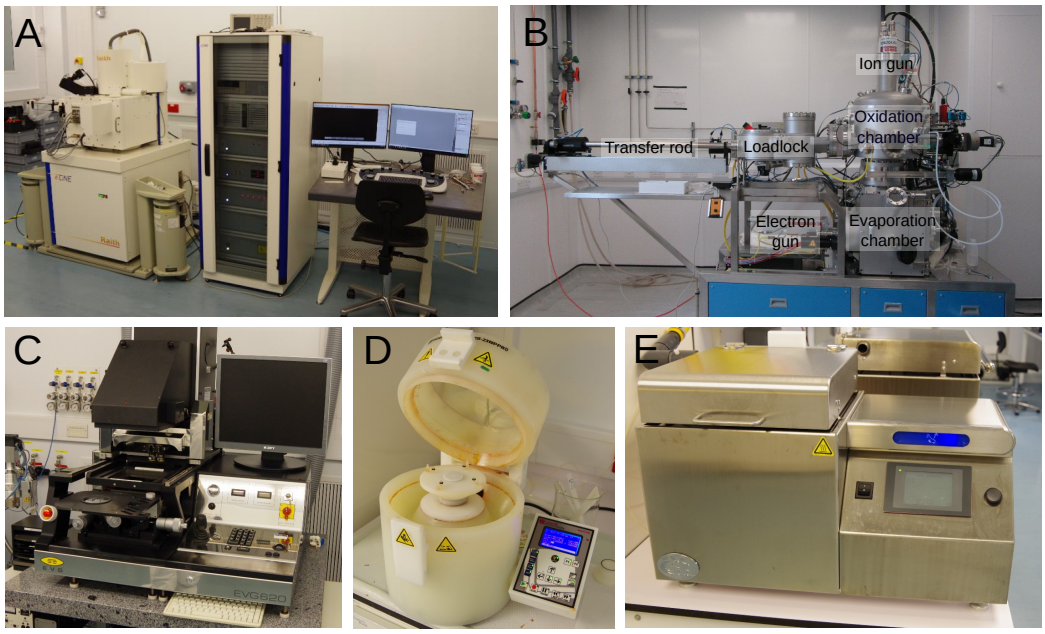

Figure C.2: **Cleanroom Equipment:** (**A**) Raith 30keV EBL system. (**B**) PLASSYS with loadlock and ion gun and. (**C**) EVG620 mask aligner system. (**D**) Laurell Technologies WS-650HZB-23NPPB spin coater. (**E**) Brewer Science 1300 hotplate.

6 Load wafer into the EVG620 pattern aligner system, with the mask defining the reverse-side resonator patterns loaded.

7 Align wafer to mask and expose wafer: exposure dose $20\,\mathrm{mJ/cm^2}$.

8 Unload wafer and develop in a beaker of Microchemicals AZ 727 developer: 23 °C, 80 s. Provide strong manual agitation to wafer during development.

9 Stop development in two beakers of DI water: 30 s each beaker with agitation.

10 Blow dry gently with a nitrogen gun.

11 Etch in Alfa Aesar aluminium etchant: 23 °C, 130 s, without agitation. (Pattern should become visible near the 2 minute mark).

12 Stop etching in beaker of DI water: 30 s. Then clean under flowing DI water to remove etchant residue. (Pour directly from the ultra-pure DI water bottle).

13 Blow dry with nitrogen.

14 Strip photoresist (including protective layer on qubit-side) in beaker of Dimethyl Sulfoxide (DMSO): 80 °C, 15 minutes. No agitation.

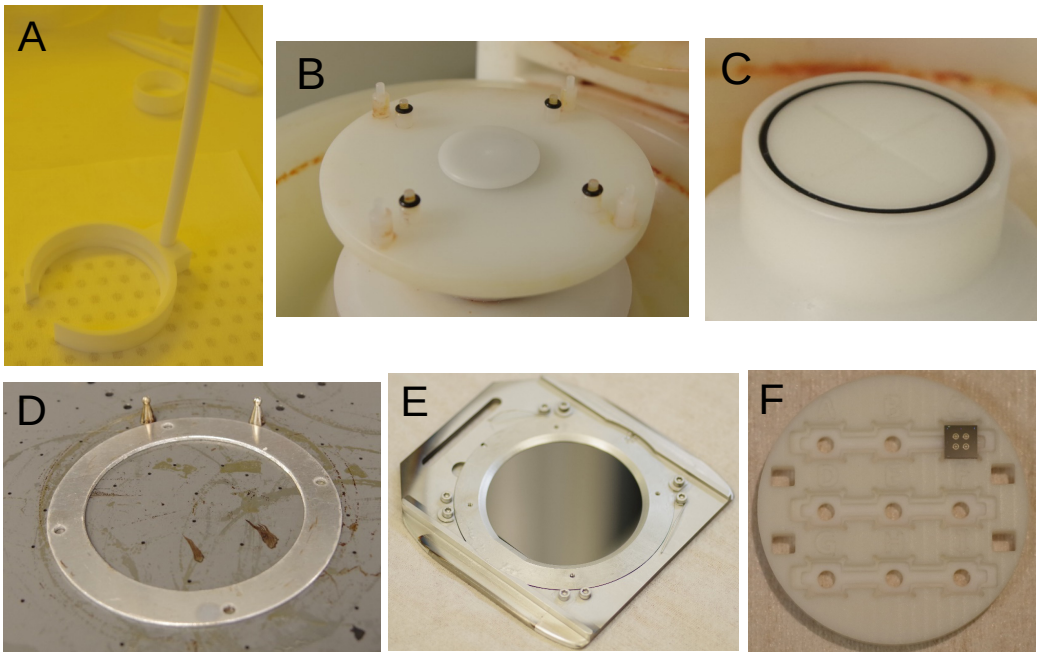

Figure C.3: **Double-sided fabrication equipment:** (**A**) PTFE wafer dipper to minimise backside contact. (**B**) Non-contact spin coater chuck to to minimise backside contact. (**C**) Standard vacuum spin coater chuck. (**D**) Metal ring on hotplate to avoid backside contact. (**E**) Evaporator wafer cassette featuring recess (not visible) to avoid backside contact. (**F**) PTFE chip holder with recesses to avoid backside contact during chip cleaning and storage (5 mm × 5 mm Si chip visible).

15 Clean in beaker of DI water: 1 minute. Then clean under flowing DI water to remove DMSO residue.

16 Blow dry with nitrogen.

At this stage, the resonator-side circuits have been fabricated. A spiral-resonator made by this process, and an SEM of the metal edge are shown in Fig. 6.4(A)&(B) of the main text.

17 Repeat steps 1-16 with exact same parameters, now with the protective layer spun on the resonator-side of the wafer and the patterns defined on the qubit-side of the wafer. Use the backside optics and overlay mode of the EVG620 to align the qubit-side pattern with the resonator-side pattern.

Fig. 6.4(C) in the main text shows a pair of qubit pads made by this process. After the qubit-side large features have been etched, the wafer is ready for Josephson junction fabrication.

Josephson junction fabrication

The $\mathcal{O}(200\,\text{nm} \times 200\,\text{nm})$ Josephson junctions are fabricated using electron beam lithography to define Dolan bridges [178] in a bilayer of resist, and then performing steep angle evaporation. In particular, we use the 'T' style bridge and the steep angle evaporation technique developed in Ref. [179]. In this variant, the junction dimensions become independent of the width of the Dolan bridge. This reduces by one the number of parameters the junction area depends on, which is anticipated to improve the resultant junction resistance statistics.

Resist bilayer preparation

A copolymer-PMMA bilayer resist stack is spun before EBL. The copolymer layer is activated by a far lower flux of electrons than the PMMA layer, meaning that it can be developed away to leave free standing PMMA structures like a Dolan bridge.

1 Bake wafer on hotplate to remove water residue: 180 °C, 5 minutes, qubit-side up. Again use the metal ring to prevent contamination of the resonator-side.

2 Spin coat protective layer of copolymer resist (Allresist AR-P 617.08) onto resonator-side: 4000 rpm, 50 s. Use non-contact chuck to prevent contamination of the qubit-side.

3 Bake on hotplate: 180 °C, 5 minutes, resonator-side up.

4 Let cool for 5 minutes.

5 Spin coat active layer of copolymer resist (AR-P 617.08) onto qubit-side: 4000 rpm, 50 s. Use vacuum chuck to improve resist uniformity.

6 Bake on hotplate: 180 °C, 5 minutes, qubit-side up.

7 Let cool for 5 minutes.

8 Spin coat active layer of PMMA 950k resist (Allresist AR-P 672.045) onto qubit-side: 4000 rpm, 50 s. Use vacuum chuck to improve resist uniformity.

9 Bake on hotplate: 180 °C, 5 minutes, qubit-side up.

10 Let cool for 5 minutes.

Electron beam lithography & development

1 Load wafer into Raith 30 keV EBL system, qubit-side up. Turn on electron gun to 30 keV and leave for 2 hours to allow gun to thermalise and minimise focus drift. Set beam aperture to 30 µm^2.

2 Calibrate coordinate system with 3 point alignment to features at wafer edges. Calibrate focus by burning contamination spots near wafer centre (should be possible to burn 20 nm diameter spots). Perform write-field alignment using 100 µm × 100 µm write-field.

3 Read current in the Faraday cup (should be ~ 0.3 nA).

4 Apply automatic focus correction using charge coupled device (CCD) laser.*

5 Load JJ pattern file and write the junctions: dose 550 µC/cm^2, beam step size 8 nm (beam speed should be ~ 7 mm/s).

6 Change gun energy to 20 keV and set beam aperture to 120 cm^2. (This is to increase write speed: lower doses are needed at lower beam voltages due to increased electron scattering angles inside the resist).

7 Calibrate focus by burning contamination spots. Perform write-field alignment using 250 µm × 250 µm write-field.

8 Read current in the Faraday cup (should be ~ 4.5 nA).

9 Apply automatic focus correction using charge coupled device (CCD) laser.

10 Load overlap pattern file and write the overlaps**: dose 400 µC/cm^2, beam step size 200 nm (beam speed should be ~ 5 mm/s).

11 Unload wafer from Raith.

12 Develop exposed resist in beaker containing 1:3 mixture of MIBK:IPA: 25 °C, 45 s. No agitation (to improve reproducibility), qubit-side of the wafer down (may help to clear resist residue).

13 Immediately transfer to a beaker of IPA to stop development: 15 s with gentle agitation. Transfer to second beaker of IPA: 1 minute with gentle agitation.

14 Blow dry gently with nitrogen gun.

15 Load wafer into PT7160 RF plasma barrel etcher and O_2-plasma ash (to remove resist residue prior to evaporation): power 45 W, 20 s (including ~ 7 s transient power ramp up), O_2 pressure 0.5 mbar.

* By measuring the intensity of the laser light reflected off the wafer, the height map of the wafer can be inferred, and focus correction applied. Performing this correction is essential when patterning junctions across a wafer in this Raith system. Without it, poor focus would preclude viable Dolan bridges across most of the wafer.
** This is to reduce dielectric losses at this interface. We perform ion milling (described later) to remove the oxide layer on the large aluminium pads before evaporating the junction leads, however, even after a milling process there may be a small oxide layer separating them. By greatly increasing the overlapping surface area of these layers, the participation ratio in any remaining insulating oxide is minimised. Correlations between the qubit relaxation time and overlap area have been reported [69]. We chose a total overlap area of 10 000 µm, 5000 µm for each pad.

Fig 6.4(D) in the main text shows an image of a developed junction with overlap features before junction evaporation.

Double angle evaporation

1 Load wafer into evaporator, qubit-side exposed and junction bridges correctly aligned.

2 Ion mill with Argon (to remove the oxide layer that had grown on the aluminium pads of the qubit): ion mill voltage 400 V, acceleration voltage 90 V, ion current 15 mA, 1 min.

3 Evaporate 60 nm of aluminium at a steep 60° angle (w.r.t wafer normal vector) with an evaporation rate 0.5 mm/s, oxidation & evaporation chamber pressures $\approx 2 \times 10^{-8}$ mbar.

4 Flood chamber with O_2 (to form junction oxide layer): 5 mbar, 10 min.

5 Pump both chambers to $\approx 2 \times 10^{-8}$ mbar and evaporate 70 nm of aluminium at a rate 0.5 mm/s, 0° angle.

6 Unload wafer.

Lift-off

1 Perform aluminium lift-off in beaker of acetone: 65 °C, 30 minutes.

2 'Blow' acetone over wafer with pipette and sonicate at 80 kHz for 2 minutes to aid lift-off.

3 Clean in IPA beaker: 1 minute.

4 Blow dry with nitrogen.

Circuit fabrication is now complete. A wafer with circuits made by this recipe is shown in Fig. 6.5 of the main text.

Future improvements to fabrication recipe

The main improvements we identify are with the resist development processes performed after photolithography and EBL. The photolithography development process currently requires strong manual agitation which is hard to do reproducibly. Alternatives should be pursued, such as developing with the exposed side of the wafer face down while agitating with sonication. The temperature and time of development could also be further optimised.

The junction development at 25 °C in 1:3 MIBK:IPA is known to be non-optimal. Superior development has been achieved by cold development (< 0 °C) and by using a IPA:DI water mixture as the developer [209, 210]. This should improve JJ statistics.

Finally, performing lift-off in acetone at 65 °C must be carefully supervised as acetone boils at 56 °C. It may be advisable to replace acetone with DMSO - which has a much higher boiling point of 189 °C.

Protective resist recipe

The protective resist recipe for drilling and dicing was as follows:

1 Spin coat protective layer (Microposit S1805 photoresist) onto one side of the wafer/chip: 4000 rpm, 1 minute. In the case of wafer, use non-contact chuck to protect backside.

2 Softbake resist: 115 °C, 1 minute. Use metal ring to protect backside.

3 Repeat on second side of wafer/chip.

4 Perform dicing/drilling

5 Remove resist in DMSO at 80 °C, using PTFE non-contact chip holder (Fig. C.3(F)).

6 Clean chip in beaker of DI water: 30 s.

7 Blow dry with nitrogen.

Appendix D

Josephson Junction Design & Statistics

Junction design

The junction design used in this thesis is shown in Fig. D.1(A). Qualitatively, the corners are all filleted to reduce electric field divergences and so reduce the qubit participation in lossy interfaces. The dimensions are chosen to prevent loose aluminium 'flags' forming during junction fabrication. Fig. D.1(B) shows a cross section taken along the ridge features during angle evaporation. The approximate thickness of the copolymer resist and PMMA resist layers were found experimentally from SEM imaging. The two 0.3 µm wide ridges prevent the aluminium layer formed on the silicon surface from contacting the copolymer wall. Fig. D.1(C) shows the same cross-section with the ridges removed. Now the aluminium layer on the silicon surface connects to the side wall of the copolymer layer of resist. This will result in a loose 'flag' of aluminium after lift-off, which connects to the aluminium layer on the silicon but does not itself adhere to the silicon. Such flag features are visible in Fig. 6.3 of the main text. The dimension C in Fig. D.1(A) is similarly chosen to prevent a flag from forming above the Josephson junction.

Junction statistics

It is important for the local resistance variation between nominally identical junctions to be small, to be able to accurately set the relative frequencies between qubits on each chip. Global variation across the whole wafer is also an important parameter. For our purposes, global variation is tolerable, as we actually want resistance variation between chips so that we can select those with optimal resistances. However,

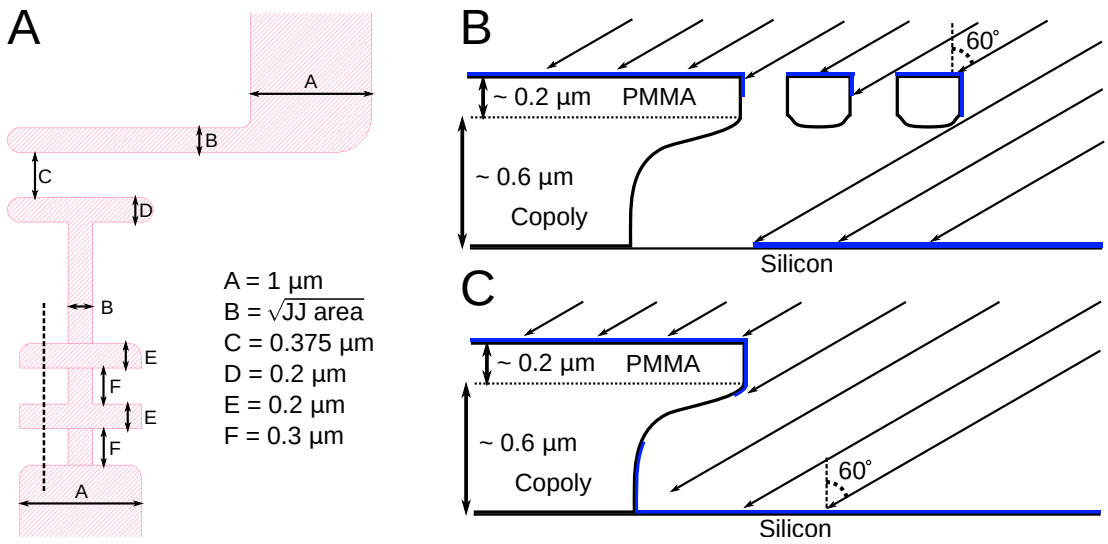

Figure D.1: **Josephson junction design:** (**A**) Resist pattern design for Josephson junctions with annotated dimensions. The corners are filleted to circles radius 0.1 µm. (**B**) Cross-section of resist profile along the dashed line in (A), during angle evaporation. (**C**) Same cross-section without the ridge features.

for larger devices with qubits spread across appreciable fractions of the wafer, global variation must also be minimised to ensure qubit frequency accuracy across devices. Fig. D.2 shows the pattern we used to test both local and global resistance variation. Fig. D.2(A) shows the whole pattern, consisting of a central pattern, and a repeated outer pattern written at 16 different locations on the wafer. The central pattern, shown in fig. D.2(B), consists of an array of 90 junctions. Each column contains 10 metal pads connected by a JJ with an identical area. The side lengths of the square junctions vary between columns. The outer pattern, shown in fig. D.2(C), consists of 10 junctions with identical 200 nm side lengths.

We wrote this pattern onto four 3 inch wafers using the junction fabrication recipe presented above, including the ion milling step to faithfully reproduce the conditions that junctions on device wafers would experience. We subsequently measured the room temperature resistance of all 250 junctions, soon after fabrication, and then again after a few days sitting in atmosphere, to measure junction ageing [211].

Fig. D.3 shows the results of these measurements on the final wafer. Fig. D.3(A) shows the measured resistance on the central pattern as a function of the junction side length, both before and after ageing. The resistances are fitted to the following

expression

$$R = \frac{\rho \times h}{(l + \delta_{ash})^2} \tag{D.1}$$

where ρ is the resistivity of the junction oxide layer, h is the thickness of the oxide layer, l is the targeted side length of the junctions, and δ_{ash} accounts for resist being isotropically etched away during the oxygen plasma ash and Argon mill steps prior to junction evaporation. We find $\delta_{ash} = 27.3\,\text{nm}, \rho \times h = 3.05 \times 10^{-10}\ \Omega\text{m}^2$ before ageing and $\delta_{ash} = 26.7\,\text{nm}, \rho \times h = 3.22 \times 10^{-10}\ \Omega\text{m}^2$ after ageing. Assuming the thickness of the oxide layer is $h = 3\,\text{nm}$ gives a junction resistivity of $\rho = 0.102\,\Omega\,\text{m}$ before ageing and resistivity of $\rho = 0.107\,\Omega\,\text{m}$ after ageing, a 6% increase. The small 2% variation in the fitted δ_{ash} parameter is consistent with the junction area not changing during the ageing process. The value of $\delta_{ash} \sim 27\,\text{nm}$ suggests oxygen plasma and argon milling do have a significant effect on junction area, and so this should be accounted for when designing junctions with targeted resistances. The average standard deviation of resistance between equal area junctions was 3.3%.

Fig. D.3(B) shows the measured resistances of all nominally $200\,\text{nm} \times 200\,\text{nm}$ area junctions on the wafer, plotted against position on the wafer. We find an average local standard deviation in the measured resistance between the 10 junctions in the 16 $320\,\mu\text{m} \times 850\,\mu\text{m}$ area outer patterns of 1.9%, and a much larger 9.1% standard deviation in the average resistance of each of these patterns, which are spread across a $20\,\text{cm}^2$ area. As shown, this global variation across the wafer is well fitted to a plane. This strongly suggests a miscalibration between the wafer height calculated by the CCD laser and the focus correction applied to the electron gun in the Raith EBL system. Subtracting the plane of fit from the average resistances, the standard deviation in the average resistance of each outer pattern is greatly reduced to 1.2%. This suggests that the global variation can be corrected for, and that once corrected junction resistance variation of $1\% - 2\%$ should be possible across whole wafers. This is consistent with results of Ref. [142], where global resistance variations of 3.5% were achieved across a larger $49\,\text{cm}^2$ area silicon wafer, and is an important consideration for future devices that may take up entire wafers.

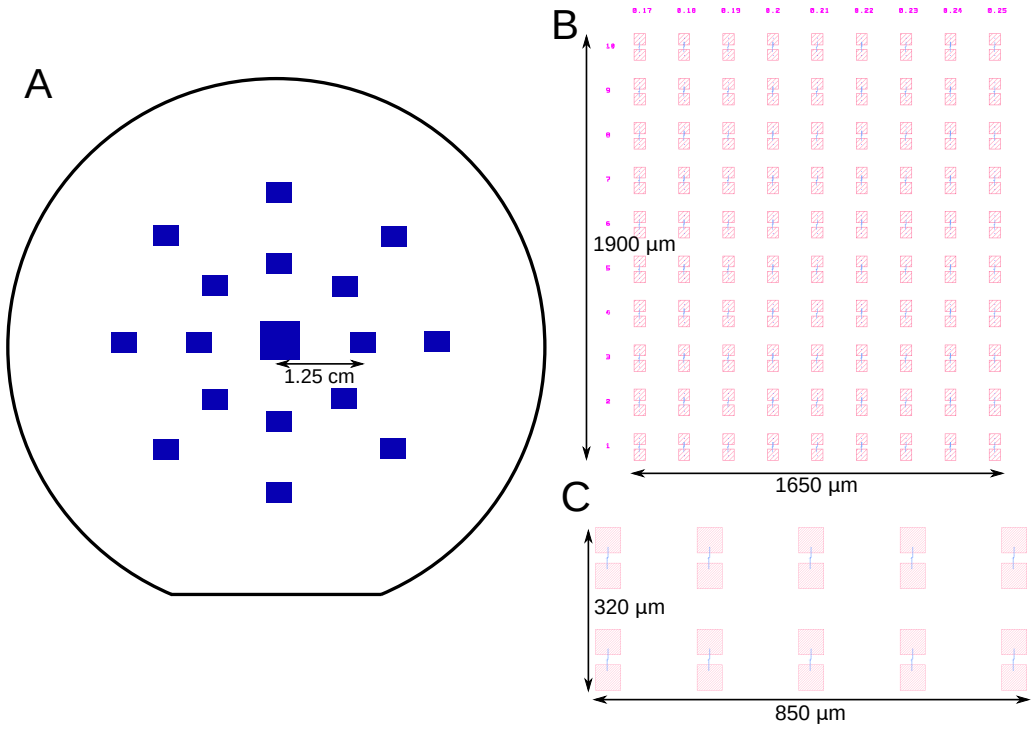

Figure D.2: **Waferscale junction test pattern:** (**A**) Illustration of pattern layout on 3 inch wafer, featuring a central pattern and 16 outer patterns arranged in a circular grid. (**B**) Central pattern featuring 90 junctions. Each column consists of ten nominally identical junctions joined by 50 µm × 50 µm probe-tip contact pads. Nominal junction areas range from 170 nm × 170 nm to 250 nm × 250 nm across the nine columns. (**C**) Outer pattern, consisting of ten nominally identical 200 nm × 200 nm area junctions joined by contact pads.

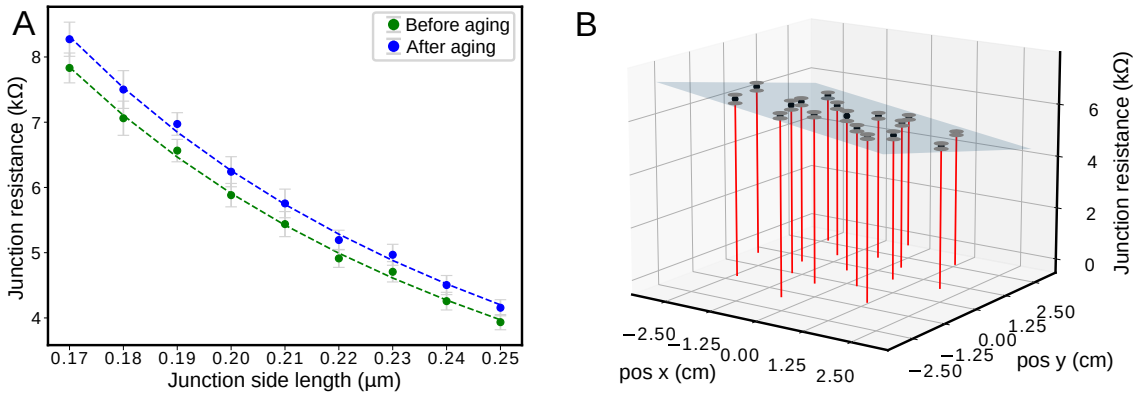

Figure D.3: **Junction resistance variation:** (**A**) Measured room temperature resistances of the central pattern, both before and after ageing. Each point shows the average and standard deviation of the ten nominally identical junctions in each column. (**B**) Measured room temperature resistances of all nominally 200 nm × 200 nm area junctions on the wafer, plotted against position on the wafer. Each point shows average and standard deviation of ten nominally identical junctions.

Appendix E

FFT Interpolation to Improve Ramsey Interferometry Resolution

In Chapter 7, it was often required to find the frequency of oscillations in Ramsey time trace measurement data. Extracting the frequency by directly fitting the time trace data to sinusoidal functions was found to be insufficiently robust, due to noise and the possibility of multiple frequency components in the time trace data.

Instead, we extracted the frequency by taking the fast-Fourier transform (fft) of the time trace data. Fig. E.1(A) shows the fft of a $T = 20\,\mu s$ long Ramsey time trace measured on Q_1 (inset). The principle peak (with index p) in the fft corresponds to the Ramsey oscillation frequency. The frequency spacing between signals in the fft, Δf, is given by $1/T$, in this case 50 kHz. Therefore, the frequency of the Ramsey oscillations can be estimated as $\Delta f \times p$, with frequency resolution $\Delta f/2 = 25\,\text{kHz}$.

Following Ref. [212], the frequency resolution can be greatly improved by windowing the time trace data and interpolating the frequency using the fft signal values at indices $p-1, p, p+1$, denoted S_{p-1}, S_p, S_{p+1}. In this method, the frequency is given by $f = \Delta f(p + \Delta p)$, where

$$\Delta p = \frac{\ln(\frac{S_{p+1}}{S_{p-1}})}{2\ln(\frac{S_p^2}{S_{p+1}S_{p-1}})} \tag{E.1}$$

Fig. E.1(B) shows the fft of the same 20 µs Ramsey time trace data as shown in Fig. E.1(A), now windowed with a 4 µs standard deviation Gaussian. Notice that S_{p-1} and S_{p+1} are much larger in Fig. E.1(B) than in Fig. E.1(A). This is due to the nature of the fft of a Gaussian windowing function compared to a rectangular windowing function [212]. Fig. E.1(C) plots the Ac Stark shifted frequency of Q_1 while

applying a continuous drive tone to R_1 through the control line of R_4, with the frequency found by principle peak selection and by the Gaussian interpolation method. The lowest power data points correspond to the data in Fig. E.1(A)&(B). By eye, the Gaussian interpolation method achieves a frequency resolution of $\sim 1\,\mathrm{kHz}$, compared to $25\,\mathrm{kHz}$ for the principle peak selection method.

Assuming the time trace data is a perfect sine wave with frequency f_0, the frequency error of the Gaussian interpolation technique can be directly computed [212]

$$E = (f_0 - f_{Gaus})/\Delta f = -\frac{\ln(\frac{W_{\Delta p+1}}{W_{\Delta p-1}})}{2\ln(\frac{W_{\Delta p}^2}{W_{\Delta p+1}W_{\Delta p-1}})} - \Delta p \tag{E.2}$$

where

$$W_p = \sqrt{\frac{\pi}{2}}\rho e^{-2(\pi\rho p)^2}|\mathrm{erf}(\frac{1+i4\pi\rho^2 p}{2\sqrt{2}\rho}) + \mathrm{erf}(\frac{1-i4\pi\rho^2 p}{2\sqrt{2}\rho})| \tag{E.3}$$

The result depends on Δ_p and on the ratio $\rho = \sigma/T$, where σ is the standard deviation of the Gaussian windowing function. In Fig. E.1(D), we compute the frequency error as a function of Δp for $\rho = 0.2$. The maximum error occurs at $\Delta p = \pm 0.284$, with a value $0.009\Delta_f$. This corresponds to a frequency resolution of approximately $0.5\,\mathrm{kHz}$ for $T = 20\,\mu\mathrm{s}$, consistent with the results in Fig. E.1(C). This is over 50 times greater than the resolution of the peak selection method.

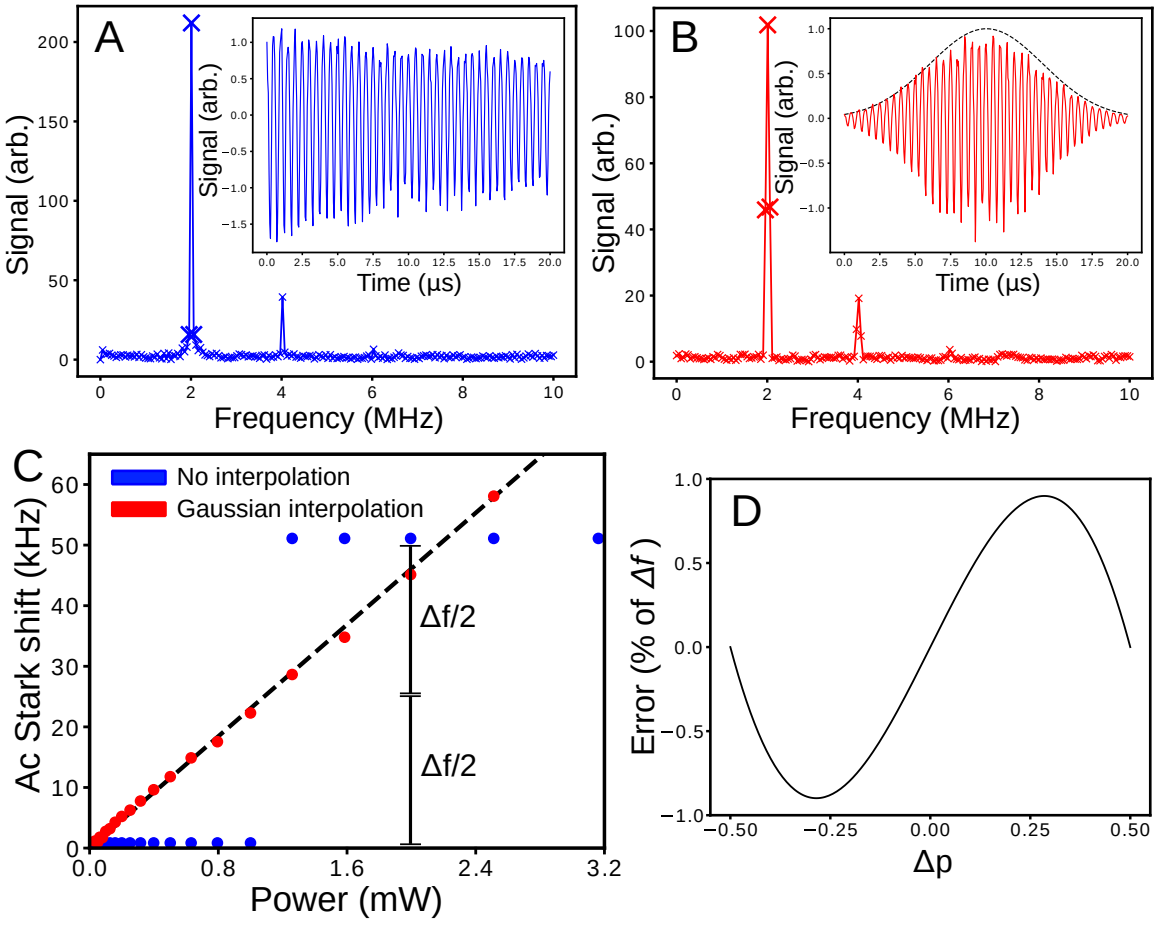

Figure E.1: **Frequency resolution improvement of FFT using Gaussian interpolation:** Ramsey interferometry of Q_1 while continuously driving R_1 through control line of R_4. (**A**) Fast Fourier transform (fft) of 20 µs Ramsey time trace shown in inset (continuous drive power 0.032 mW). Crosses corresponding to principle peak index p and side indices $p-1$ and $p+1$ are enlarged. (**B**) Fft of same 20 µs Ramsey time trace windowed with a 4 µs standard deviation Gaussian as shown in inset. (**C**) Ac Stark shift vs continuous drive power as found by: (1) peak selection of unwindowed fft data (2) Gaussian interpolation of windowed fft data. The gradient of the line fit, k'_{14}, was used to determine the resonator control line crosstalk φ_{14}. (**D**) Frequency error of Gaussian interpolation method for different values of Δp, assuming the fft is performed on a perfect sine wave windowed with a $0.2T$ standard deviation Gaussian.

Appendix F

Control Electronics and Dilution Refrigerator Setup

The electronic control setup and fridge wiring diagram is shown in Fig. F.1. All the signal generators and signal processors shared a common 10 MHz external clock, which allowed them to be phase-locked. Table F.1 provides a list of the RF electronics and components used.

Readout resonator control Resonator spectroscopy and qubit readout were performed using a standard RF heterodyne detection setup. A continuous RF tone (R LO gen) is split and sent to the LO ports of two IQ mixers. In the up-conversion mixer, the LO is combined with ~ 100 MHz signals at the I and Q ports produced by a digital-to-analogue converter (DAC). Given the following LO, I and Q input signals

$$s_{LO} = a\cos(\omega_{LO}t) \tag{F.1}$$

$$s_I = b(t)\sin(\omega_{IF}t + \phi) \tag{F.2}$$

$$s_Q = b(t)\cos(\omega_{IF}t + \phi) \tag{F.3}$$

the RF output signal of an ideal IQ mixer is given by [213]

$$s_{RF} \propto b(t)\cos((\omega_{LO} + \omega_{IF})t + \phi) \tag{F.4}$$

This is known as single side-band up-conversion, as the outputted RF signal has only one frequency component. Considering eq. F.4, it is clear that short RF pulses can be generated by rapidly modulating the amplitude of the I and Q signals. The frequency of the signal can be adjusted by changing ω_{LO}. In this way, a DAC with a 2 GSs^{-1} sampling rate can produce short ~ 10 ns pulse envelopes for ~ 10 GHz frequency signals – far higher than the DAC sampling rate. The DAC output is controlled by

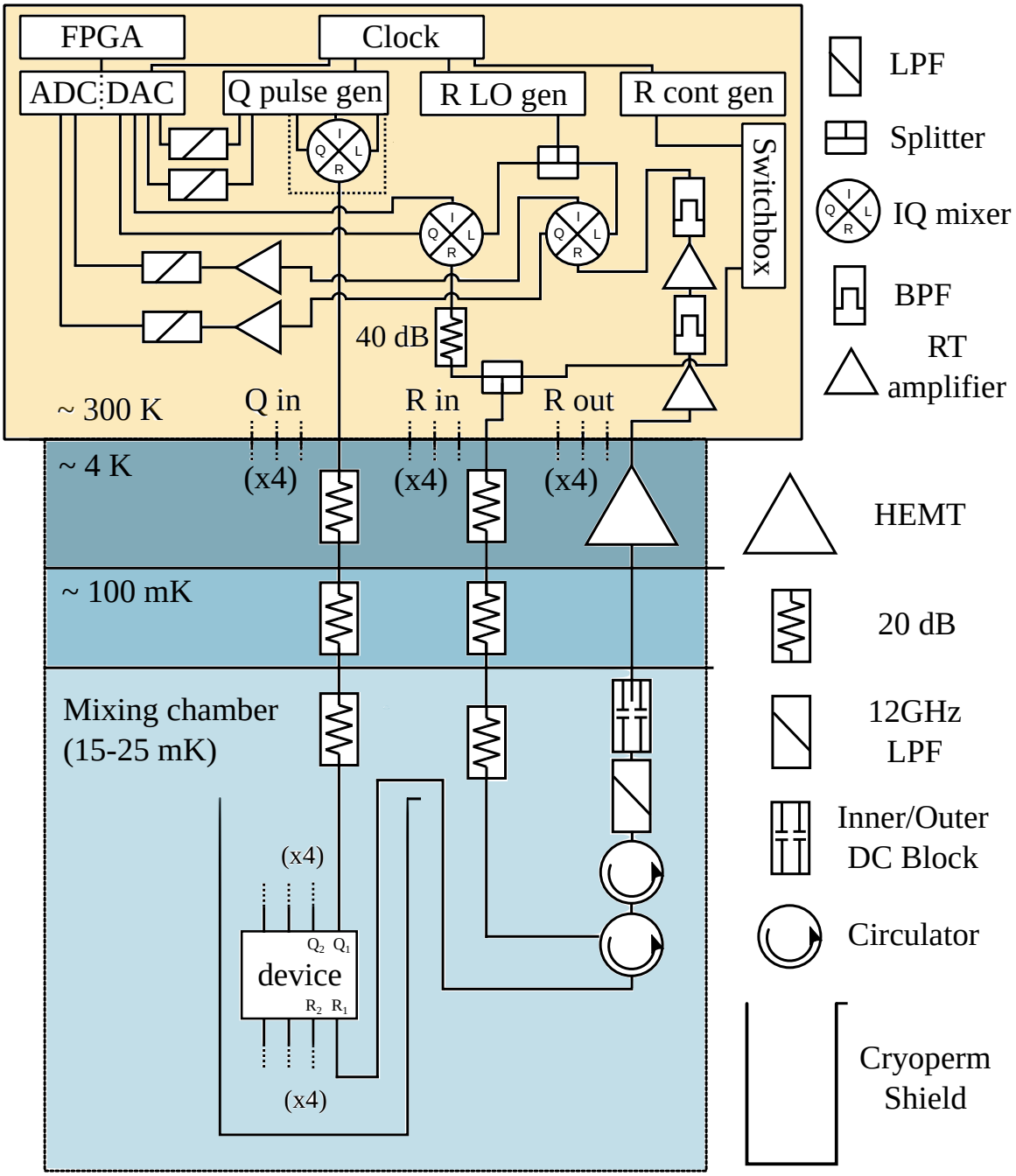

Figure F.1: **Experimental setup wiring diagram:** Schematic diagram of room temperature electronics and dilution refrigerator wiring. Manufacturer and part numbers for the components are given in Table F.1

Table F.1: **Equipment list:** Summary of equipment used for these experiments.

Category	Generator/Part	Manufacturer & Model
RF generators & electronics	Q pulse gen	R&S SGS100A SGMA (×4)
	R LO gen	Anapico APMS20G-4-ULN (×1)
	R cont gen	R&S SMA100A (×1)
	Switchbox	Pickering 60-801-208 8 GHZ 6CH (×1)
	DAC&ADC	Abaco Systems FMC110 (×4)
	DAC&ADC trigger	Abaco Systems FMC230 (×4)
	FPGA	4DSP PC821 (×1)
	Clock	Stanford Research Systems FS725 (×1)
Room temperature components	Splitter	Mini-Circuits ZX10-2-1252+S+ (×4)
	IQ mixer	Marki IQ-0618MXP (×8)
	BPF	Keelion Microwave KBF-8/12-Q7S (×4)
	Attenuator	Mini-Circuits BW-S20-2W263+ (×8)
	RT amplifier (1)	Mini-Circuits ZX60-183A+ (×4)
	RT amplifier (2)	Mini-Circuits ZVA-183+ (×4)
	LPF	Mini-Circuits VLF-160+ (×8)
Cryogenic components	20dB attenuator	XMA 20 dB 2082-6418-20-Cryo (×24)
	HEMT (Q_1 & Q_3)	Low Noise Factory LNC6_20C (×2)
	HEMT (Q_2 & Q_4)	Low Noise Factory LNC4_16A (×2)
	12 GHz LPF	K&L Microwave 6L250-00089 (×4)
	Circulator	Raditek 8-12-Cryo S23-1WR-b (×8)
	DC Block	API/Inmet 8039 (×4)
	Cyroperm Shield	Magnetic Shields MuCan (×1)
Dilution refrigerator	-	Oxford Instruments Triton 500

an FPGA (field-programmable gate array). This FPGA ran custom firmware written by Andrew Patterson, with some adjustments made by Shuxiang Cao.

The RF signal is routed through the dilution refrigerator to a readout resonator control port in the device. It is attenuated by 40 dB at room temperature to suppress the amplitude of any direct LO leakage into the RF output, and then by a further 20 dB at the 4 K stage, the 100 mK stage, and the 15 mK mixing chamber stage; a total attenuation of 100 dB. These staggered 20 dB attenuators reduce the power of the signal to levels commensurate with driving single photon transitions in superconducting circuit resonators.

After interacting with the device, the reflected signal is routed through two circulators, a low pass filter, and a DC block, to a HEMT applifier at the 4 K stage. Two circulators are used to improve the isolation of the device from any backwards trav-

elling noise generated by the HEMT. The DC block protects the HEMT from DC noise, which could break it. The DC block and the HEMT are connected by a single niobium-titanium (NbTi) coaxial cable that is a superconductor below 10 K. This serves two purposes: it reduces the attenuation of the output signal and so increases the signal to noise (SNR) of qubit readout, and it reduces the thermal link between the 4 K stage and mixing chamber stage. These HEMT amplifiers amplify the signal by ~ 35 dB. Outside the fridge, the signal is further amplified by ~ 50 dB and filtered to suppress noise outside the $8\,\text{GHz} - 12\,\text{GHz}$ range. This amplified signal is then sent to the RF port of the second, down-conversion mixer. Here, the RF signal is combined with the same (up to a phase) LO signal that was sent to the up-conversion mixer. The signals are given by

$$s_{LO} = a\cos(\omega_{LO}t + \phi') \tag{F.5}$$

$$s_{RF} = b'(t)\cos((\omega_{LO} + \omega_{IF})t + \phi'') \tag{F.6}$$

For an ideal IQ mixer, the outputted I and Q signals are then given by

$$s_I \propto b'(t)\sin(\omega_{IF}t + \Delta\phi) \tag{F.7}$$

$$s_Q \propto b'(t)\cos(\omega_{IF}t + \Delta\phi) \tag{F.8}$$

$$\Delta\phi = \phi'' - \phi' \tag{F.9}$$

If both of these signals are recorded, then both $b'(t)$ (up to a constant scale factor) and $\Delta\phi$ can be determined. In this way, the amplitude and phase response of superconducting circuit resonators at $\sim 10\,\text{GHz}$ are transferred to signals at $\sim 100\,\text{MHz}$, which can be digitised with ~ 100 times greater resolution of the waveform, allowing accurate determination of $b'(t)$ and $\Delta\phi$. This digitisation is performed by an analogue-to-digital converter (ADC) with a 2 GSs^{-1} sampling rate, and the digitised I and Q signals are finally processed and saved by the FPGA. The stored signal can be represented on an Argand diagram by

$$S = f(s_I) + ig(s_Q) \tag{F.10}$$

where $f(x)$ and $g(x)$ are processing functions performed on the two quadratures by the FPGA – ideally some form of weighted integration [189, 214] to take account of the time dependent response of the resonator to the measurement pulse. In our case, we performed simple unweighted integration for all of our experiments on this device.

Some of the experiments we performed to characterise readout crosstalk required

us to also simultaneously send a continuous drive tone to a resonator. To achieve this, we used a splitter to combine the up-converted RF signal with the output of a signal generator (R cont gen) configured to produce a continuous single-frequency drive. This generator had only one output port, and so we used a room temperature switcher (Switchbox) to allow the output to be remotely switched between the four resonator control lines.

Qubit control Qubit control signals were generated in the same fashion as the readout input signals, using single side-band up-conversion. The only difference is we used IQ mixers housed inside the qubit control pulse generators (Q pulse gen). Inside the dilution refrigerator, the signals were also attenuated in an identical manner to readout input signals.

Bibliography

1. Nielsen, M. A. & Chuang, I. *Quantum computation and quantum information* 2002.
2. Shor, P. W. Polynomial-time algorithms for prime factorization and discrete logarithms on a quantum computer. *SIAM review* **41,** 303–332 (1999).
3. Calderbank, A. R. & Shor, P. W. Good quantum error-correcting codes exist. *Physical Review A* **54,** 1098 (1996).
4. Steane, A. M. Simple quantum error-correcting codes. *Physical Review A* **54,** 4741 (1996).
5. Shor, P. W. *Fault-tolerant quantum computation* in *Proceedings of 37th Conference on Foundations of Computer Science* (1996), 56–65.
6. DiVincenzo, D. P. The physical implementation of quantum computation. *Fortschritte der Physik: Progress of Physics* **48,** 771–783 (2000).
7. Takeda, S. & Furusawa, A. Toward large-scale fault-tolerant universal photonic quantum computing. *APL Photonics* **4,** 060902 (2019).
8. Bruzewicz, C. D., Chiaverini, J., McConnell, R. & Sage, J. M. Trapped-ion quantum computing: Progress and challenges. *Applied Physics Reviews* **6,** 021314 (2019).
9. Saffman, M. Quantum computing with atomic qubits and Rydberg interactions: progress and challenges. *Journal of Physics B: Atomic, Molecular and Optical Physics* **49,** 202001 (2016).
10. Petit, L. *et al.* Universal quantum logic in hot silicon qubits. *Nature* **580,** 355–359 (2020).
11. Loss, D. & DiVincenzo, D. P. Quantum computation with quantum dots. *Physical Review A* **57,** 120 (1998).
12. Kjaergaard, M. *et al.* Superconducting qubits: Current state of play. *Annual Review of Condensed Matter Physics* **11,** 369–395 (2020).
13. Ladd, T. D. *et al.* Quantum computers. *Nature* **464,** 45–53 (2010).
14. Koch, J. *et al.* Charge-insensitive qubit design derived from the Cooper pair box. *Physical Review A* **76,** 042319 (2007).
15. Serniak, K. *et al.* Hot nonequilibrium quasiparticles in transmon qubits. *Physical review letters* **121,** 157701 (2018).

16. Vepsäläinen, A. *et al.* Impact of ionizing radiation on superconducting qubit coherence. *arXiv preprint arXiv:2001.09190* (2020).

17. Girvin, S. M. Superconducting qubits and circuits: Artificial atoms coupled to microwave photons. *Lectures delivered at Ecole d'Eté Les Houches* (2011).

18. Reagor, M. J. *Superconducting cavities for circuit quantum electrodynamics* (Yale University, 2016).

19. Pozar, D. M. *Microwave engineering* (John wiley & sons, 2011).

20. Wang, C. *et al.* Measurement and control of quasiparticle dynamics in a superconducting qubit. *Nature communications* **5,** 1–7 (2014).

21. Tinkham, M. *Introduction to superconductivity* (Courier Corporation, 2004).

22. Mattis, D. & Bardeen, J. Theory of the anomalous skin effect in normal and superconducting metals. *Physical Review* **111,** 412 (1958).

23. Zmuidzinas, J. Superconducting microresonators: Physics and applications. *Annu. Rev. Condens. Matter Phys.* **3,** 169–214 (2012).

24. Solgun, F. & DiVincenzo, D. P. Multiport impedance quantization. *Annals of physics* **361,** 605–669 (2015).

25. Joesphson, B. Possible new effects in superconductive tunneling. *Phys. Lett* **1,** 251 (1962).

26. Feynman, R. P. *The Feynman Lectures on Physics Vol 3* (Narosa, 1965).

27. Dolan, G. Offset masks for lift-off photoprocessing. *Applied Physics Letters* **31,** 337–339 (1977).

28. Waldram, J. R., Pippard, A. B. & Clarke, J. Theory of the current-voltage characteristics of SNS junctions and other superconducting weak links. *Philosophical Transactions of the Royal Society of London. Series A, Mathematical and Physical Sciences* **268,** 265–287 (1970).

29. Vystavkin, A. *et al.* ScS junctions as nonlinear elements of microwave receiving devices. *Revue de Physique Appliquée* **9,** 79–109 (1974).

30. Ambegaokar, V. & Baratoff, A. Tunneling between superconductors. *Physical Review Letters* **10,** 486 (1963).

31. Fagaly, R. Superconducting quantum interference device instruments and applications. *Review of scientific instruments* **77,** 101101 (2006).

32. Vool, U. & Devoret, M. Introduction to quantum electromagnetic circuits. *International Journal of Circuit Theory and Applications* **45,** 897–934 (2017).

33. Burkard, G., Koch, R. H. & DiVincenzo, D. P. Multilevel quantum description of decoherence in superconducting qubits. *Physical Review B* **69,** 064503 (2004).

34. Caldeira, A. & Leggett, A. J. Quantum tunnelling in a dissipative system. *Annals of physics* **149,** 374–456 (1983).

35. Sakurai, J. J. & Commins, E. D. *Modern quantum mechanics, revised edition* 1995.

36. Gambetta, J. *Quantum Information Processing: Lecture Notes of the 44th IFF Spring School* (Forschungszentrum Jülich, 2013).

37. Nakamura, Y., Pashkin, Y. A. & Tsai, J. S. Coherent control of macroscopic quantum states in a single-Cooper-pair box. *nature* **398,** 786–788 (1999).

38. Bouchiat, V., Vion, D., Joyez, P., Esteve, D. & Devoret, M. Quantum coherence with a single Cooper pair. *Physica Scripta* **1998,** 165 (1998).

39. Didier, N., Sete, E. A., da Silva, M. P. & Rigetti, C. Analytical modeling of parametrically modulated transmon qubits. *Physical Review A* **97,** 022330 (2018).

40. Blais, A., Huang, R.-S., Wallraff, A., Girvin, S. M. & Schoelkopf, R. J. Cavity quantum electrodynamics for superconducting electrical circuits: An architecture for quantum computation. *Physical Review A* **69,** 062320 (2004).

41. Blais, A., Grimsmo, A. L., Girvin, S. & Wallraff, A. Circuit Quantum Electrodynamics. *arXiv preprint arXiv:2005.12667* (2020).

42. Shore, B. W. & Knight, P. L. The jaynes-cummings model. *Journal of Modern Optics* **40,** 1195–1238 (1993).

43. Gambetta, J. M. *et al.* Characterization of addressability by simultaneous randomized benchmarking. *Physical review letters* **109,** 240504 (2012).

44. Wallraff, A. *et al.* Approaching unit visibility for control of a superconducting qubit with dispersive readout. *Physical review letters* **95,** 060501 (2005).

45. Gambetta, J., Braff, W., Wallraff, A., Girvin, S. & Schoelkopf, R. Protocols for optimal readout of qubits using a continuous quantum nondemolition measurement. *Physical Review A* **76,** 012325 (2007).

46. Krantz, P. *et al.* A quantum engineer's guide to superconducting qubits. *Applied Physics Reviews* **6,** 021318 (2019).

47. Jackson, J. D. *Classical electrodynamics* (John Wiley & Sons, 2007).

48. Houck, A. *et al.* Controlling the spontaneous emission of a superconducting transmon qubit. *Physical review letters* **101,** 080502 (2008).

49. Chow, J. M. *Quantum information processing with superconducting qubits* (Yale University, 2010).

50. *Ansys HFSS (High Frequency Structural Simulator)* `https://www.ansys.com`.

51. *COMSOL* `https://www.comsol.com`.

52. Paik, H. *et al.* Observation of high coherence in Josephson junction qubits measured in a three-dimensional circuit QED architecture. *Physical Review Letters* **107,** 240501 (2011).

53. Heinsoo, J. *et al.* Rapid high-fidelity multiplexed readout of superconducting qubits. *Physical Review Applied* **10,** 034040 (2018).

54. Walter, T. *et al.* Rapid high-fidelity single-shot dispersive readout of superconducting qubits. *Physical Review Applied* **7,** 054020 (2017).

55. Reed, M. D. *et al.* Fast reset and suppressing spontaneous emission of a superconducting qubit. *Applied Physics Letters* **96,** 203110 (2010).

56. Bronn, N. T. *et al.* Broadband filters for abatement of spontaneous emission in circuit quantum electrodynamics. *Applied Physics Letters* **107,** 172601 (2015).

57. Krinner, S. *et al.* Engineering cryogenic setups for 100-qubit scale superconducting circuit systems. *EPJ Quantum Technology* **6,** 2 (2019).

58. Kono, S. *et al.* Breaking the trade-off between fast control and long lifetime of a superconducting qubit. *Nat Commun* **11** (2020).

59. Wang, C. *et al.* Surface participation and dielectric loss in superconducting qubits. *Applied Physics Letters* **107,** 162601 (2015).

60. Martinis, J. M. *et al.* Decoherence in Josephson qubits from dielectric loss. *Physical review letters* **95,** 210503 (2005).

61. Müller, C., Cole, J. H. & Lisenfeld, J. Towards understanding two-level-systems in amorphous solids: insights from quantum circuits. *Reports on Progress in Physics* **82,** 124501 (2019).

62. Krupka, J. *et al.* Measurements of permittivity, dielectric loss tangent, and resistivity of float-zone silicon at microwave frequencies. *IEEE Transactions on microwave theory and techniques* **54,** 3995–4001 (2006).

63. Woods, W. *et al.* Determining interface dielectric losses in superconducting coplanar-waveguide resonators. *Physical Review Applied* **12,** 014012 (2019).

64. Melville, A. *et al.* Comparison of dielectric loss in titanium nitride and aluminum superconducting resonators. *Applied Physics Letters* **117,** 124004 (2020).

65. Calusine, G. *et al.* Analysis and mitigation of interface losses in trenched superconducting coplanar waveguide resonators. *Applied Physics Letters* **112,** 062601 (2018).

66. Gambetta, J. M. *et al.* Investigating surface loss effects in superconducting transmon qubits. *IEEE Transactions on Applied Superconductivity* **27,** 1–5 (2016).

67. Dial, O. *et al.* Bulk and surface loss in superconducting transmon qubits. *Superconductor Science and Technology* **29,** 044001 (2016).

68. Earnest, C. T. *et al.* Substrate surface engineering for high-quality silicon/aluminum superconducting resonators. *Superconductor Science and Technology* **31,** 125013 (2018).

69. Nersisyan, A. *et al. Manufacturing low dissipation superconducting quantum processors* in *2019 IEEE International Electron Devices Meeting (IEDM)* (2019), 31–1.

70. Chu, Y. *et al.* Suspending superconducting qubits by silicon micromachining. *Applied Physics Letters* **109,** 112601 (2016).

71. Catelani, G., Schoelkopf, R. J., Devoret, M. H. & Glazman, L. I. Relaxation and frequency shifts induced by quasiparticles in superconducting qubits. *Physical Review B* **84,** 064517 (2011).

72. Serniak, K. *et al.* Direct dispersive monitoring of charge parity in offset-charge-sensitive transmons. *Physical Review Applied* **12,** 014052 (2019).

73. Barends, R. *et al.* Minimizing quasiparticle generation from stray infrared light in superconducting quantum circuits. *Applied Physics Letters* **99,** 113507 (2011).

74. Wilen, C. *et al.* Correlated Charge Noise and Relaxation Errors in Superconducting Qubits. *arXiv preprint arXiv:2012.06029* (2020).

75. Riwar, R.-P. *et al.* Normal-metal quasiparticle traps for superconducting qubits. *Physical Review B* **94,** 104516 (2016).

76. Riwar, R.-P. & Catelani, G. Efficient quasiparticle traps with low dissipation through gap engineering. *Physical Review B* **100,** 144514 (2019).

77. Martinis, J. M. Saving superconducting quantum processors from qubit decay and correlated errors generated by gamma and cosmic rays. *arXiv preprint arXiv:2012.06137* (2020).

78. Martinis, J. M., Nam, S., Aumentado, J., Lang, K. & Urbina, C. Decoherence of a superconducting qubit due to bias noise. *Physical Review B* **67,** 094510 (2003).

79. Nakamura, Y., Pashkin, Y. A., Yamamoto, T. & Tsai, J.-S. Charge echo in a Cooper-pair box. *Physical review letters* **88,** 047901 (2002).

80. Zorin, A. *et al.* Background charge noise in metallic single-electron tunneling devices. *Physical Review B* **53,** 13682 (1996).

81. Wang, Z. *et al.* Cavity attenuators for superconducting qubits. *Physical Review Applied* **11,** 014031 (2019).

82. Clerk, A. & Utami, D. W. Using a qubit to measure photon-number statistics of a driven thermal oscillator. *Physical Review A* **75,** 042302 (2007).

83. Burnett, J. J. *et al.* Decoherence benchmarking of superconducting qubits. *npj Quantum Information* **5,** 1–8 (2019).

84. Schlör, S. *et al.* Correlating decoherence in transmon qubits: Low frequency noise by single fluctuators. *Physical review letters* **123,** 190502 (2019).

85. Nigg, S. E. *et al.* Black-box superconducting circuit quantization. *Physical Review Letters* **108,** 240502 (2012).

86. Solgun, F., Abraham, D. W. & DiVincenzo, D. P. Blackbox quantization of superconducting circuits using exact impedance synthesis. *Physical Review B* **90,** 134504 (2014).

87. Foster, R. M. A reactance theorem. *Bell System technical journal* **3,** 259–267 (1924).

88. Gustavsen, B. & Semlyen, A. Rational approximation of frequency domain responses by vector fitting. *IEEE Transactions on power delivery* **14,** 1052–1061 (1999).

89. Brune, O. *Synthesis of a Finite Two-Terminal Whose Driving-Point Impedance is a Function of Frequency* PhD thesis (Ph. D. thesis, Department of Electrical Engineering, Massachusetts Institute . . ., 1931).

90. Anderson, B. & Moylan, P. The brune synthesis in state-space terms. *International Journal of Circuit Theory and Applications* **3,** 193–199 (1975).

91. Burkard, G. Circuit theory for decoherence in superconducting charge qubits. *Physical Review B* **71,** 144511 (2005).

92. Solgun, F., DiVincenzo, D. P. & Gambetta, J. M. Simple impedance response formulas for the dispersive interaction rates in the effective Hamiltonians of low anharmonicity superconducting qubits. *IEEE transactions on microwave theory and techniques* **67,** 928–948 (2019).

93. Andersen, C. K. *et al.* Repeated quantum error detection in a surface code. *Nature Physics* **16,** 875–880 (2020).

94. Fowler, A. G., Mariantoni, M., Martinis, J. M. & Cleland, A. N. Surface codes: Towards practical large-scale quantum computation. *Physical Review A* **86,** 032324 (2012).

95. Barends, R. *et al.* Superconducting quantum circuits at the surface code threshold for fault tolerance. *Nature* **508,** 500–503 (2014).

96. DiVincenzo, D. P. Fault-tolerant architectures for superconducting qubits. *Physica Scripta* **2009,** 014020 (2009).

97. Bravyi, S. B. & Kitaev, A. Y. Quantum codes on a lattice with boundary. *arXiv preprint quant-ph/9811052* (1998).

98. Tuckett, D. K., Bartlett, S. D., Flammia, S. T. & Brown, B. J. Fault-tolerant thresholds for the surface code in excess of 5% under biased noise. *Physical review letters* **124,** 130501 (2020).

99. Aharonov, D., Kitaev, A. & Preskill, J. Fault-tolerant quantum computation with long-range correlated noise. *Physical review letters* **96,** 050504 (2006).

100. Voinigescu, S. *High-frequency integrated circuits* (Cambridge University Press, 2013).

101. Loubet, N. *et al. Stacked nanosheet gate-all-around transistor to enable scaling beyond FinFET* in *2017 Symposium on VLSI Technology* (2017), T230–T231.

102. Krinner, S. *et al.* Demonstration of an All-Microwave Controlled-Phase Gate between Far-Detuned Qubits. *Physical Review Applied* **14,** 044039 (2020).

103. Arute, F. *et al.* Quantum supremacy using a programmable superconducting processor. *Nature* **574,** 505–510 (2019).

104. Huang, S. *et al.* Microwave Package Design for Superconducting Quantum Processors. *arXiv preprint arXiv:2012.01438* (2020).

105. Wenner, J. *et al.* Wirebond crosstalk and cavity modes in large chip mounts for superconducting qubits. *Superconductor Science and Technology* **24,** 065001 (2011).

106. Wadell, B. C. *Transmission line design handbook* (Artech House, 1991).

107. Chen, Z. *et al.* Fabrication and characterization of aluminum airbridges for superconducting microwave circuits. *Applied Physics Letters* **104,** 052602 (2014).

108. McConkey, T. *et al.* Mitigating leakage errors due to cavity modes in a superconducting quantum computer. *Quantum Science and Technology* **3,** 034004 (2018).

109. Linke, N. M. *et al.* Experimental comparison of two quantum computing architectures. *Proceedings of the National Academy of Sciences* **114,** 3305–3310 (2017).

110. Chamberland, C., Zhu, G., Yoder, T. J., Hertzberg, J. B. & Cross, A. W. Topological and subsystem codes on low-degree graphs with flag qubits. *Physical Review X* **10,** 011022 (2020).

111. Córcoles, A. D. *et al.* Challenges and opportunities of near-term quantum computing systems. *arXiv preprint arXiv:1910.02894* (2019).

112. Jurcevic, P. *et al.* Demonstration of quantum volume 64 on a superconducting quantum computing system. *arXiv preprint arXiv:2008.08571* (2020).

113. Otterbach, J. *et al.* Unsupervised machine learning on a hybrid quantum computer. *arXiv preprint arXiv:1712.05771* (2017).

114. Hertzberg, J. B. *et al.* Laser-annealing Josephson junctions for yielding scaled-up superconducting quantum processors. *arXiv preprint arXiv:2009.00781* (2020).

115. Jerger, M. *et al.* Frequency division multiplexing readout and simultaneous manipulation of an array of flux qubits. *Applied Physics Letters* **101,** 042604 (2012).

116. Chen, Y. *et al.* Multiplexed dispersive readout of superconducting phase qubits. *Applied Physics Letters* **101,** 182601 (2012).

117. Hornibrook, J. *et al.* Cryogenic control architecture for large-scale quantum computing. *Physical Review Applied* **3,** 024010 (2015).

118. Lecocq, F. *et al.* Control and readout of a superconducting qubit using a photonic link. *arXiv preprint arXiv:2009.01167* (2020).

119. Sliwa, K. *et al.* Reconfigurable Josephson circulator/directional amplifier. *Physical Review X* **5,** 041020 (2015).

120. Chapman, B. J. *et al.* Widely tunable on-chip microwave circulator for superconducting quantum circuits. *Physical Review X* **7,** 041043 (2017).

121. Magnard, P. *et al.* Microwave quantum link between superconducting circuits housed in spatially separated cryogenic systems. *Physical Review Letters* **125,** 260502 (2020).

122. Bronn, N. T. *et al.* High coherence plane breaking packaging for superconducting qubits. *Quantum science and technology* **3,** 024007 (2018).

123. Béjanin, J. *et al.* Three-dimensional wiring for extensible quantum computing: The quantum socket. *Physical Review Applied* **6,** 044010 (2016).

124. Yost, D.-R. W. *et al.* Solid-state qubits integrated with superconducting through-silicon vias. *npj Quantum Information* **6,** 1–7 (2020).

125. Rosenberg, D. *et al.* 3D integrated superconducting qubits. *npj quantum information* **3,** 1–5 (2017).

126. Brecht, T. *et al.* Multilayer microwave integrated quantum circuits for scalable quantum computing. *npj Quantum Information* **2,** 1–4 (2016).

127. Foxen, B. *et al.* Qubit compatible superconducting interconnects. *Quantum Science and Technology* **3,** 014005 (2017).

128. Bardin, J. C., Slichter, D. H. & Reilly, D. J. Microwaves in Quantum Computing. *arXiv preprint arXiv:2011.01480* (2020).

129. Alfaro-Barrantes, J. *et al.* Superconducting High-Aspect Ratio Through-Silicon Vias with DC-Sputtered Al for Quantum 3D integration. *IEEE Electron Device Letters* (2020).

130. Brecht, T. *et al.* Demonstration of superconducting micromachined cavities. *Applied Physics Letters* **107,** 192603 (2015).

131. Lei, C. U., Krayzman, L., Ganjam, S., Frunzio, L. & Schoelkopf, R. J. High coherence superconducting microwave cavities with indium bump bonding. *Applied Physics Letters* **116,** 154002 (2020).

132. Brecht, T. *et al.* Micromachined integrated quantum circuit containing a superconducting qubit. *Physical Review Applied* **7,** 044018 (2017).

133. Mundada, P., Zhang, G., Hazard, T. & Houck, A. Suppression of qubit crosstalk in a tunable coupling superconducting circuit. *Physical Review Applied* **12,** 054023 (2019).

134. Noguchi, A. *et al.* Fast parametric two-qubit gates with suppressed residual interaction using the second-order nonlinearity of a cubic transmon. *Physical Review A* **102,** 062408 (2020).

135. Yan, F. *et al.* Tunable coupling scheme for implementing high-fidelity two-qubit gates. *Physical Review Applied* **10,** 054062 (2018).

136. Collodo, M. C. *et al.* Implementation of Conditional-Phase Gates based on tunable ZZ-Interactions. *Physical Review Letters* **125,** 240502 (2020).

137. Zhao, P. *et al.* High-Contrast Z Z Interaction Using Superconducting Qubits with Opposite-Sign Anharmonicity. *Physical Review Letters* **125,** 200503 (2020).

138. Sheldon, S., Magesan, E., Chow, J. M. & Gambetta, J. M. Procedure for systematically tuning up cross-talk in the cross-resonance gate. *Physical Review A* **93,** 060302 (2016).

139. Chow, J. M. *et al.* Simple all-microwave entangling gate for fixed-frequency superconducting qubits. *Physical review letters* **107,** 080502 (2011).

140. Patterson, A. *et al.* Calibration of a cross-resonance two-qubit gate between directly coupled transmons. *Physical Review Applied* **12,** 064013 (2019).

141. Viola, L., Knill, E. & Lloyd, S. Dynamical decoupling of open quantum systems. *Physical Review Letters* **82,** 2417 (1999).

142. Kreikebaum, J., O'Brien, K., Morvan, A. & Siddiqi, I. Improving wafer-scale Josephson junction resistance variation in superconducting quantum coherent circuits. *Superconductor Science and Technology* **33,** 06LT02 (2020).

143. Rahamim, J. *et al.* Double-sided coaxial circuit QED with out-of-plane wiring. *Applied Physics Letters* **110,** 222602 (2017).

144. Rahamim, J. *Development of a coaxial circuit QED architecture for quantum computing* PhD thesis (University of Oxford, 2019).

145. Braumüller, J. *et al.* Concentric transmon qubit featuring fast tunability and an anisotropic magnetic dipole moment. *Applied Physics Letters* **108,** 032601 (2016).

146. Wolfram Research, I. *Mathematica, Version 12.2* Champaign, IL, 2020. `https://www.wolfram.com/mathematica`.

147. Göppl, M. *et al.* Coplanar waveguide resonators for circuit quantum electrodynamics. *Journal of Applied Physics* **104,** 113904 (2008).

148. Bronn, N. T. *et al.* Reducing spontaneous emission in circuit quantum electrodynamics by a combined readout/filter technique. *IEEE Transactions on Applied Superconductivity* **25,** 1–10 (2015).

149. Koester, S. J. *et al.* Wafer-level 3D integration technology. *IBM Journal of Research and Development* **52,** 583–597 (2008).

150. Suntives, A., Khajooeizadeh, A. & Abhari, R. *Using via fences for crosstalk reduction in PCB circuits* in *2006 IEEE International Symposium on Electromagnetic Compatibility, 2006. EMC 2006.* **1** (2006), 34–37.

151. Spiesshoefer, S. *et al.* Process integration for through-silicon vias. *Journal of Vacuum Science & Technology A: Vacuum, Surfaces, and Films* **23,** 824–829 (2005).

152. Vahidpour, M. *et al.* Superconducting through-silicon vias for quantum integrated circuits. *arXiv preprint arXiv:1708.02226* (2017).

153. Spring, P., Tsunoda, T., Vlastakis, B. & Leek, P. Modeling Enclosures for Large-Scale Superconducting Quantum Circuits. *Physical Review Applied* **14,** 024061 (2020).

154. Montgomery, C. G., Dicke, R. H., Purcell, E. M. & Purcell, E. M. *Principles of microwave circuits* (Iet, 1987).

155. Gong, X. *et al.* Precision fabrication techniques and analysis on high-Q evanescent-mode resonators and filters of different geometries. *IEEE transactions on microwave theory and techniques* **52,** 2557–2566 (2004).

156. Clark, T., Vadakkumbatt, V., Souris, F., Ramp, H. & Davis, J. Cryogenic microwave filter cavity with a tunability greater than 5 GHz. *Review of Scientific Instruments* **89,** 114704 (2018).

157. Nicorovici, N., McPhedran, R. & Botten, L. Photonic band gaps for arrays of perfectly conducting cylinders. *Physical Review E* **52,** 1135 (1995).

158. Smith, D. *et al.* Experimental and theoretical results for a two-dimensional metal photonic band-gap cavity. *Applied Physics Letters* **65,** 645–647 (1994).

159. Guida, G., Maystre, D., Tayeb, G. & Vincent, P. Mean-field theory of two-dimensional metallic photonic crystals. *JOSA B* **15,** 2308–2315 (1998).

160. Pendry, J. B., Holden, A., Stewart, W. & Youngs, I. Extremely low frequency plasmons in metallic mesostructures. *Physical review letters* **76,** 4773 (1996).

161. Belov, P., Tretyakov, S. & Viitanen, A. Dispersion and reflection properties of artificial media formed by regular lattices of ideally conducting wires. *Journal of electromagnetic waves and applications* **16,** 1153–1170 (2002).

162. Krynkin, A. & McIver, P. Approximations to wave propagation through a lattice of Dirichlet scatterers. *Waves in Random and Complex Media* **19,** 347–365 (2009).

163. Pendry, J. B., Holden, A., Robbins, D. & Stewart, W. Low frequency plasmons in thin-wire structures. *Journal of Physics: Condensed Matter* **10,** 4785 (1998).

164. Murray, C. E. & Abraham, D. Predicting substrate resonance mode frequency shifts using conductive, through-substrate vias. *Applied Physics Letters* **108,** 084101 (2016).

165. Remski, R. Analysis of photonic bandgap surfaces using Ansoft HFSS. *Microw. J.* **43,** 190–199 (2000).

166. Hartmann, M. J., Brandao, F. G. & Plenio, M. B. Strongly interacting polaritons in coupled arrays of cavities. *Nature Physics* **2,** 849–855 (2006).

167. Nagle, D., Knapp, E. & Knapp, B. Coupled resonator model for standing wave accelerator tanks. *Review of Scientific Instruments* **38,** 1583–1587 (1967).

168. Wangler, T. P. *RF Linear accelerators* (John Wiley & Sons, 2008).

169. Russer, P. *Electromagnetics, microwave circuit and antenna design for communications engineering* (Artech House, 2003).

170. Belov, P. *et al.* Strong spatial dispersion in wire media in the very large wavelength limit. *Physical Review B* **67,** 113103 (2003).

171. Marcuvitz, N. *Waveguide handbook* (Iet, 1951).

172. Marcuvitz, N. & Schwinger, J. On the representation of the electric and magnetic fields produced by currents and discontinuities in wave guides. I. *Journal of Applied Physics* **22,** 806–819 (1951).

173. Douglas, J. S. *et al.* Quantum many-body models with cold atoms coupled to photonic crystals. *Nature Photonics* **9,** 326–331 (2015).

174. González-Tudela, A., Hung, C.-L., Chang, D. E., Cirac, J. I. & Kimble, H. Subwavelength vacuum lattices and atom–atom interactions in two-dimensional photonic crystals. *Nature Photonics* **9,** 320–325 (2015).

175. Gabrielli, L. H. *gdspy* `https://github.com/heitzmann/gdspy`. 2020.

176. Peterer, M. *Experiments on multi-level superconducting qubits and coaxial circuit QED* PhD thesis (University of Oxford, 2016).

177. Scriven, L. Physics and applications of dip coating and spin coating. *MRS Online Proceedings Library (OPL)* **121** (1988).

178. Dolan, G. & Dunsmuir, J. Very small ($\lesssim$ 20 nm) lithographic wires, dots, rings, and tunnel junctions. *Physica B: Condensed Matter* **152,** 7–13 (1988).

179. Kelly, J. S. *Fault-tolerant superconducting qubits* (University of California, Santa Barbara, 2015).

180. Nedeljkovic, M. *et al.* Germanium-on-silicon waveguides operating at mid-infrared wavelengths up to 8.5 μm. *Optics express* **25,** 27431–27441 (2017).

181. Reagor, M. *et al.* Reaching 10 ms single photon lifetimes for superconducting aluminum cavities. *Applied Physics Letters* **102,** 192604 (2013).

182. *Autodesk. Autodesk Inventor* `https://www.autodesk.co.uk/products/inventor`. San Rafael, CA, 2020.

183. Kajfez, D. & Hwan, E. J. Q-factor measurement with network analyzer. *IEEE transactions on microwave theory and techniques* **32,** 666–670 (1984).

184. Braumüller, J. *et al.* Multiphoton dressing of an anharmonic superconducting many-level quantum circuit. *Physical Review B* **91,** 054523 (2015).

185. Klimov, P. *et al.* Fluctuations of energy-relaxation times in superconducting qubits. *Physical review letters* **121,** 090502 (2018).

186. Müller, C., Lisenfeld, J., Shnirman, A. & Poletto, S. Interacting two-level defects as sources of fluctuating high-frequency noise in superconducting circuits. *Physical Review B* **92,** 035442 (2015).

187. Tripathi, V., Khezri, M. & Korotkov, A. N. Operation and intrinsic error budget of a two-qubit cross-resonance gate. *Physical Review A* **100,** 012301 (2019).

188. Gambetta, J. *et al.* Qubit-photon interactions in a cavity: Measurement-induced dephasing and number splitting. *Physical Review A* **74,** 042318 (2006).

189. Bultink, C. C. *et al.* General method for extracting the quantum efficiency of dispersive qubit readout in circuit QED. *Applied Physics Letters* **112,** 092601 (2018).

190. Knill, E. *et al.* Randomized benchmarking of quantum gates. *Physical Review A* **77,** 012307 (2008).

191. Chow, J. *et al.* Randomized benchmarking and process tomography for gate errors in a solid-state qubit. *Physical review letters* **102,** 090502 (2009).

192. Gottesman, D. Stabilizer codes and quantum error correction. *arXiv preprint quant-ph/9705052* (1997).

193. Gaebler, J. P. *et al.* Randomized benchmarking of multiqubit gates. *Physical review letters* **108,** 260503 (2012).

194. McKay, D. C., Wood, C. J., Sheldon, S., Chow, J. M. & Gambetta, J. M. Efficient Z gates for quantum computing. *Physical Review A* **96,** 022330 (2017).

195. Weisstein, E. W. *Blackman Function. From MathWorld–A Wolfram Web Resource.* Available at `https://mathworld.wolfram.com/BlackmanFunction.html`.

196. IBM. *QISKit, open-source quantum computing software* Available at `https://qiskit.org/documentation/_modules/qiskit/ignis/verification/randomized_benchmarking/rb_utils.html#coherence_limit` (01/02/2020). Here the coherence limit is defined as in QISKit.

197. Balasiu, S. *Characterization of Multi-Qubit Algorithms with Randomized Benchmarking* (ETH Zürich, 2018).

198. Epstein, J. M., Cross, A. W., Magesan, E. & Gambetta, J. M. Investigating the limits of randomized benchmarking protocols. *Physical Review A* **89,** 062321 (2014).

199. Wood, C. J. & Gambetta, J. M. Quantification and characterization of leakage errors. *Physical Review A* **97,** 032306 (2018).

200. Krantz, P. *et al.* Single-shot read-out of a superconducting qubit using a Josephson parametric oscillator. *Nature communications* **7,** 1–8 (2016).

201. Macklin, C. *et al.* A near–quantum-limited Josephson traveling-wave parametric amplifier. *Science* **350,** 307–310 (2015).

202. Pedregosa, F. *et al.* Scikit-learn: Machine learning in Python. *the Journal of machine Learning research* **12,** 2825–2830 (2011).

203. Vlastakis, B. M. *Controlling coherent state superpositions with superconducting circuits* (Yale University, 2015).

204. Motzoi, F., Gambetta, J. M., Rebentrost, P. & Wilhelm, F. K. Simple pulses for elimination of leakage in weakly nonlinear qubits. *Physical review letters* **103,** 110501 (2009).

205. Yan, F. *et al.* The flux qubit revisited to enhance coherence and reproducibility. *Nature communications* **7,** 1–9 (2016).

206. Hayt, W. H., Kemmerly, J. E. & Durbin, S. M. *Engineering Circuit Analysis* (McGraw-Hill, 1993).

207. Losonczi, L. Eigenvalues and eigenvectors of some tridiagonal matrices. *Acta Mathematica Hungarica* **60,** 309–322 (1992).

208. Kern, W. The evolution of silicon wafer cleaning technology. *Journal of the Electrochemical Society* **137,** 1887 (1990).

209. Cord, B., Lutkenhaus, J. & Berggren, K. K. Optimal temperature for development of poly (methylmethacrylate). *Journal of Vacuum Science & Technology B: Microelectronics and Nanometer Structures Processing, Measurement, and Phenomena* **25,** 2013–2016 (2007).

210. Yasin, S., Hasko, D. & Ahmed, H. Comparison of MIBK/IPA and water/IPA as PMMA developers for electron beam nanolithography. *Microelectronic engineering* **61,** 745–753 (2002).

211. Pop, I. M. *et al.* Fabrication of stable and reproducible submicron tunnel junctions. *Journal of Vacuum Science & Technology B, Nanotechnology and Microelectronics: Materials, Processing, Measurement, and Phenomena* **30,** 010607 (2012).

212. Gasior, M. & Gonzalez, J. *Improving FFT frequency measurement resolution by parabolic and gaussian interpolation* tech. rep. (CERN-AB-Note-2004-021, 2004).

213. Abadal, A. *Calibration of an IQ mixer for continuous and pulsed modulation* 2014.

214. Ryan, C. A. *et al.* Tomography via correlation of noisy measurement records. *Physical Review A* **91,** 022118 (2015).